UNIVERSITÄT
BERN

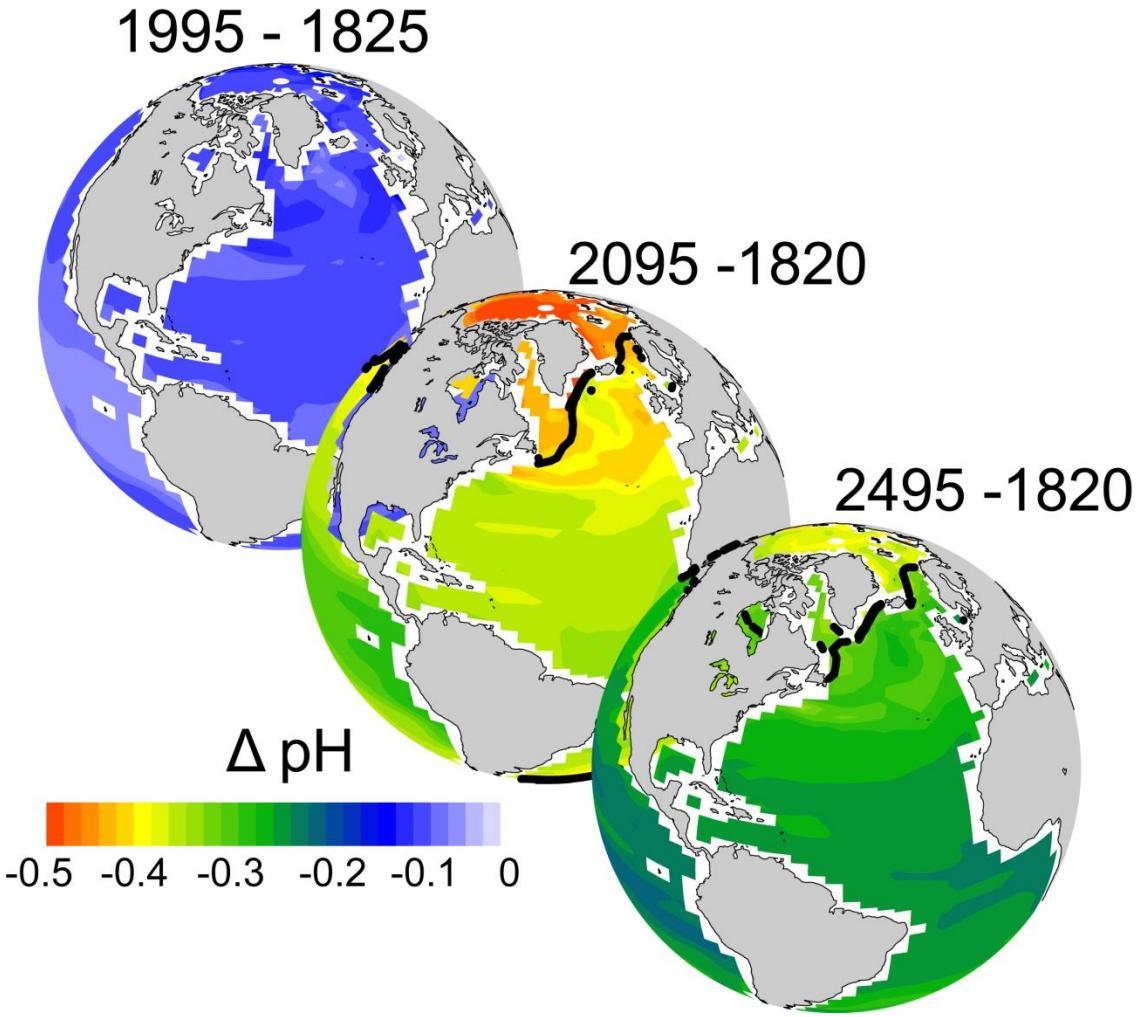

Carbon Cycle

Fortunat Joos, Renato Spahni
Physics Institute
University of Bern

2015

Table of Contents

B. Stocker is acknowledged for the translation of the German version of this manuscript and A. Bozbiyik for help with the formatting.

1 Introduction

The global cycles of carbon (C), oxygen (O) and of various other elements (N, P, Si, Fe, etc.) form a global **biogeochemical cycle.** This means that biological, geological, chemical and physical processes play a role. The cycles of the different elements are linked to each other, e.g. C, H_2O and O. For several reasons, the carbon cycle plays a key role in the Earth system:

- It affects the buildup and turnover rates of the entire **biosphere**. Carbon cycle, water cycle, oxygen cycle and the energy budget are coupled by the exchange of CO_2, O_2 and water with the biosphere.
- It affects the global radiation balance. Two most important greenhouse gases, but ranking after water vapor in importance, are carbon dioxide (CO_2) and methane (CH_4). Both contain carbon and their atmospheric concentration has been growing at an increasing rate since the industrial revolution (starting at around 1800 AD).
- A change of the radiation balance may cause irreversible changes in the climate system. Out of 1,000 g carbon, added to the atmosphere by burning fossil fuels, over 70 g remain in the atmosphere for several millennia (1st order irreversibility). In the non-linear climate system, an altered temperature regime can lead to a shift of its equilibrium (2nd order irreversibility) and hence to considerably different distributions of temperature, precipitation, etc.
- It affects the distribution of nutrients and oxygen in the ocean. The distribution of tracers, the ocean circulation and the carbon cycle are tightly coupled.
- Past variations of the atmospheric CO_2 and CH_4 concentrations and of the oceanic distribution of nutrients and carbon isotopes are recorded in Antarctic ice and ocean sediments. Measuring these variables in ice cores and oceanic sediment cores reveals quantitative information about past states of the climate system.

This lecture is concerned with two key questions:

1. How will the atmospheric CO_2 concentration, the climate and the interaction between climate and CO_2 evolve in the future?
2. How can we explain past variations in atmospheric CO_2 and climate?

1.1 The anthropogenic disturbance of the climate system

1.1.1 The observed increase of greenhouse gases

Throughout the past 200 years and particularly since World War II, human activities have caused an enormous disturbance of global biogeochemical cycles and climate. The increase in atmospheric CO_2 and other greenhouse gases is well documented thanks to a combination of atmospheric and ice core data. Over the course of the last millennium and before the industry-alization, the atmospheric concentrations of CO_2, CH_4 und N_2O were roughly constant.

Today, concentrations of these greenhouse gases are higher than during the past 800'000 years.

The atmospheric CO_2 concentration is commonly expressed as a molar ratio in units of ppm (parts per million in dry air: 10^{-6}). 1 ppm corresponds to an atmospheric inventory of 2.123 10^{12} kg C. The molar ratio of CH_4 and N_2O is given in ppb (parts per billion, 10^{-9}).

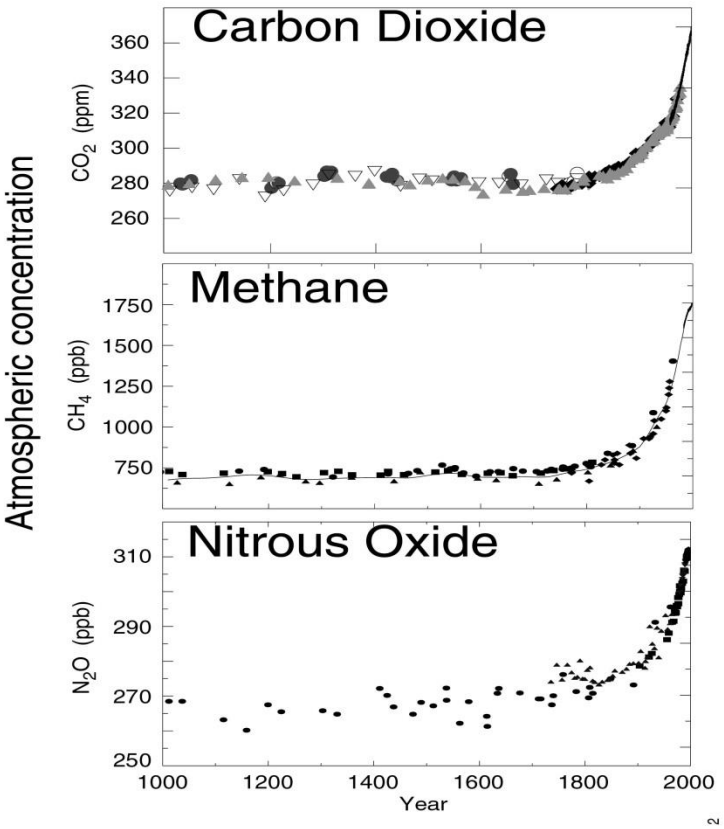

Figure 1.1: The rise in greenhouse gases CO_2, CH_4, und N_2O. In the past decades, the increase in the atmosphere has been directly measured with air samples, e.g., since 1958, regular measurements of CO_2 have been conducted on Mauna Loa (Hawaii). For earlier periods, measurements of air extracted from Antarctic ice cores are available (The Physical Institute of the University of Bern is involved in such measurements).

1.1.2 Effect of the increase in greenhouse gas concentrations on the radiation balance

The rise in atmospheric greenhouse gas concentrations and aerosols is associated with a considerable disturbance of the radiation balance of the Earth-surface/troposphere system. This disturbance of the radiation balance is referred to as Radiative Forcing. The Radiative Forcing of the surface-troposphere system by a perturbation, e.g., an increase in greenhouse gases, is equal to the change in net radiation (incident minus outgoing, short- and long-wave) that would pass the tropopause if the temperature and the state of the troposphere and the

Earth surface remained unchanged. The Radiative Forcing by well-mixed greenhouse gases is well known, whereas uncertainties in Radiative Forcing for other drivers are larger and particularly the effects of aerosols are relatively poorly understood.
As a first order approximation, the Radiative Forcing is a good indicator for the resulting change in the global mean temperature at the Earth surface. After attaining a new equilibrium, the change in the global mean temperature, $\Delta T_{s,\infty}$ and the Radiative Forcing, *RF* are linked by the climate sensitivity λ:

$$RF + \lambda \cdot \Delta T_{s,\infty} = 0 \qquad \text{and thus} \quad \lambda \equiv \frac{-RF}{\Delta T_{s,\infty}} \qquad \text{Eq. 1.1}$$

A change in Radiative Forcing leads to an altered radiation balance and the corresponding radiative response is given by $\lambda \, \Delta T_S$. The climate sensitivity is not accurately known due to numerous complex feedback mechanisms, e.g. an increase in *RF* leads to more water vapor in the atmosphere due to warming (positive feedback), changed cloud cover (positive as well as negative feedbacks) and a decrease of the snow- and ice cover (positive feedback).

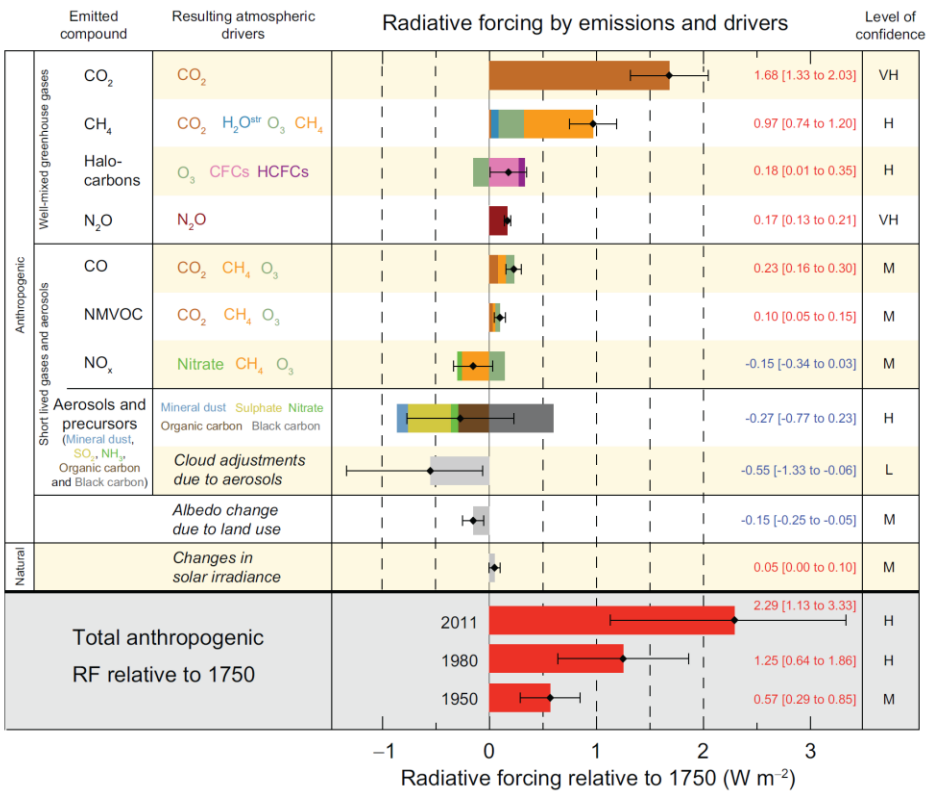

Figure 1.2: Estimates for the global mean Radiative Forcing in 2011 relative to 1750 for different drivers. (IPCC WGI, 2013, Figure SPM.5)

Radiative transfer models that resolve the 3-dimensional structure of the atmosphere, as well as the absorption of individual bands, yield the following (parameterized) relationship between atmospheric CO_2 and global Radiative Forcing:

$$RF(t) = 5.35\ \mathrm{W\,m^{-2}} \cdot \ln \frac{CO_2(t)}{CO_2(t_0)} \qquad \text{Eq. 1.2}$$

$CO_2(t_0)$ represents the preindustrial reference concentration. For a doubling of the atmospheric CO_2 concentration, the Radiative Forcing is equal to 3.7 W m^{-2} with an uncertainty of around 10%. Similar parameterizations exist for other anthropogenic greenhouse gases and aerosols. The CO_2 forcing increases with the logarithm of its concentration, due to 'self-shading'. Similarly, the Radiative Forcings of CH_4 and N_2O increases with the square root of their concentrations. Thus, an identical increase in concentration leads to a higher Radiative Forcing at low concentrations than at high concentrations. In contrast, for gases occurring at low concentrations (e.g. CFCs) the Radiative Forcing increases linearly with the atmospheric concentration.

agent	equation	C_o
CO_2	RF = 5.35 W m^{-2} $\ln(CO_2/CO_{2,o})$	278 ppm
CH_4	RF = 0.036 W m^{-2} $\left(\sqrt{CH_4} - \sqrt{CH_{4,0}}\right) - \left(f\left[CH_{4,}, N_2O_0\right] - f\left[CH_{4,0,}, N_2O_0\right]\right)$	742 ppb
N_2O	RF = 0.12 W m^{-2} $\left(\sqrt{N_2O} - \sqrt{N_2O_0}\right) - \left(f\left[CH_{4,o,}, N_2O\right] - f\left[CH_{4,0,}, N_2O_0\right]\right)$	272 ppb
CFC-11	RF = 0.25 W m^{-2} ($CFC\text{-}11 - CFC\text{-}11_0$)	0 ppt
CFC-12	RF = 0.32 W m^{-2} ($CFC\text{-}12 - CFC\text{-}12_0$)	0 ppt

Table 1.1: Equations for the calculation of the Radiative Forcing for different greenhouse gases, relative to a preindustrial (1750 A.D.) reference concentration (C_0). The overlap of the absorption bands of N_2O und CH_4 is accounted for by the function $f(M,N)=0.47 \ln(1+2.01\text{x}10^{-5} (MN)^{0.75}+5.31\text{x}10^{-15} M(MN)^{1.52})$. However, this term is small.

Often, the climate sensitivity is expressed as the increase of the equilibrium temperature, ΔT ($2\text{x}CO_2$), in response to a doubling of the atmospheric CO_2 content. Once the climate system has attained a new equilibrium, the change in the global surface temperature is equal to

$$\Delta T_{s,\infty} = \Delta T_{2x} \frac{RF}{RF(2xCO_2)} \qquad \text{Eq. 1.3}$$

It follows:

$$\lambda = \frac{-RF(2xCO_2)}{\Delta T_{2x}} \qquad \text{Eq. 1.4}$$

The 'warming commitment' by today's Radiative Forcing from well-mixed anthropogenic greenhouse gases can be derived by the equations above. For a mean climate sensitivity of 3^oC and a current Radiative Forcing of about 2.5 W m^{-2}, we expect an equilibrium warming of 2^oC relative to the preindustrial global mean surface temperature. We note that a considerable part of the greenhouse forcing is compensated by the cooling effect of aerosols and the climate system is currently not in equilibrium. The warming lags the forcing due to the large thermal inertia of the ocean.

The geographical distribution of the Radiative Forcing is different for well-mixed atmospheric gases (CO_2, CH_4, N_2O, CFCs) and for short-lived substances with regionally

variable concentrations (ozone, aerosols). For well-mixed gases, the disturbance of the radiation balance is largest in the subtropical zone and lowest at the poles, corresponding to the distribution of the long-wave outgoing radiation. The annual mean Radiative Forcing is slightly reduced at the Equator compared to the subtropics due to high cloud cover in the intertropical convergence zone.

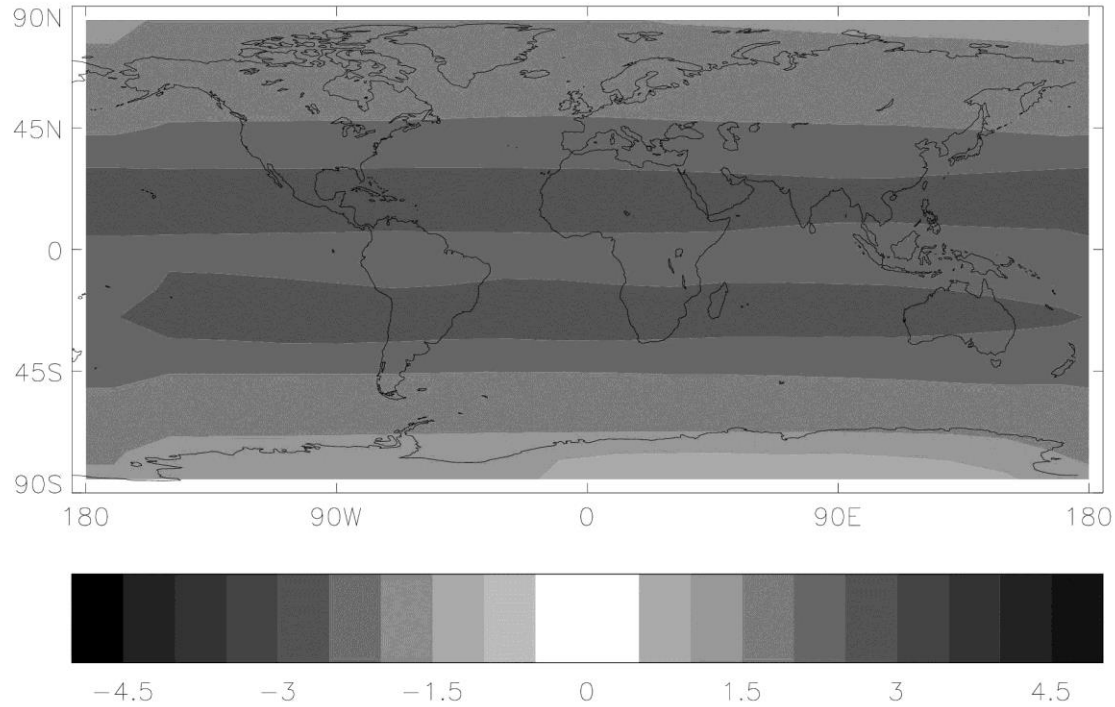

Figure 1.3: Geographical distribution of the annual mean Radiative Forcing (1750 to 2000) by the well mixed greenhouse gases CO_2, CH_4, N_2O, CFC-11 and CFC-12 in W m^{-2}.

Box 1.1

By how much would global mean surface temperature rise for a doubling of atmospheric CO_2?

a) Planetary radiation temperature. Let us consider the Earth as a black body with radius r_p. According to the Stefan-Boltzmann law, the emitted radiation for a body with temperature T is:

$h_{Planck} = -\sigma T^4$ black body radiation per unit area; sign indicates outgoing

In equilibrium: absorbed incident radiation = emitted planetary radiation :

$S_0 \cdot \pi r_p^2 \cdot (1-\alpha_p) - \sigma T_{e,0}^4 \cdot 4\pi r_p^2 = 0$, it follows:

$$\sigma T_{e,0}{}^4 = \left(\frac{S_0}{4}\cdot(1-\alpha_p)\right) \text{ and further: } T_{e,0} = \left(\frac{S_0}{4}\cdot(1-\alpha_p)\cdot\sigma^{-1}\right)^{\frac{1}{4}}$$

For the Earth:

$\alpha_p = 0.3$ Planetary albedo: 30% of the incoming radiation is reflected.

S_0 =1367 W m^{-2} Solar irradiance at the top of the atmosphere (TOA)

$\sigma = 5{,}57 \cdot 10^{-8}$ W m^{-2} K^{-4} Stefan Boltzmann constant

$T_{e,0}$ = 255 K planetary radiation temperature (calculated).

b) climate sensitivity λ, The equilibrium change in outgoing radiation in response to a Radiative Forcing, *RF,* balances *RF* and it holds at equilibrium: $RF+\Delta h=0$.

We linearize the response in h as a function of ΔT:

$$\Delta h = \left.\frac{\partial h}{\partial T}\right|_{T=T_{e,0}} \cdot \Delta T_{s,\infty}^* + f((\Delta T_{s,\infty}^*)^2)+.. \quad \text{and define} \quad \lambda \equiv \left.\frac{\partial h}{\partial T}\right|_{T=T_{e,0}}$$

It follows: $RF+\lambda \cdot \Delta T_{s,\infty}=0$, and thus $\Delta T_{s,\infty} = \frac{RF}{-\lambda}$

The climate sensitivity with regard to the black body radiation, λ_{Planck}, is:

$$\lambda_{Planck} \equiv \left.\frac{\partial h_{Planck}}{\partial T}\right|_{T=T_{e,0}} = -4\sigma T_{e,0}^3$$ and evaluation in 3-d yields: λ_{Planck}= –3.1 (W m^{-2}) K^{-1}

c) Equilibrium change in surface temperature, ΔT_S, for a doubling of atmospheric CO_2.

The Radiative Forcing is calculated according to:

$$RF(CO_2) = 5.35 \cdot \ln\frac{CO2(t_\infty)}{CO2(t_0)} \text{ W m}^{-2} = 5.35 \cdot \ln 2 \text{ W m}^{-2} = 3.7 \text{ W m}^{-2}$$

This yields when considering only the Planck feedback:

$$\Delta T_{s,\infty}^* = -RF / \lambda_{Planck} = (3.7 \text{ W m}^{-2}) / (3.1 \text{ W m}^{-2}\text{K}^{-1} = 1.2 \text{ K}$$

Feedback mechanisms: Other feedback mechanisms such as an increase in water vapor and a decrease in planetary albedo due to reduced ice and snow extent as well as changes in cloud properties affect the climate sensitivity. The confidence interval for the climate sensitivity is:

ΔT_{2xCO2} = [1.5 - .4.5 K] equilibium surface temperature change for a doubling of CO_2, or a Radiative Forcing of 3.7 W m$^{-2.}$

1.1.3 Impact of the greenhouse gas increase on the surface temperature

The largest portion of the observed warming of the last 50 years is probably due to the increase in greenhouse gases. The global mean temperature at the Earth surface has been increasing ever since instrumental records are available. The global temperature increase of the 20th century is 0.6±0.2 °C. The warming was strongest in continental regions of the northern hemisphere, while the ocean and the southern hemisphere have witnessed a smaller warming. The observed mean northern hemispheric temperatures of the past years appear to lie outside the range of variability of the past millennium. Preindustrial temperature changes are reconstructed based on proxy data (tree rings, ice cores, sediments).

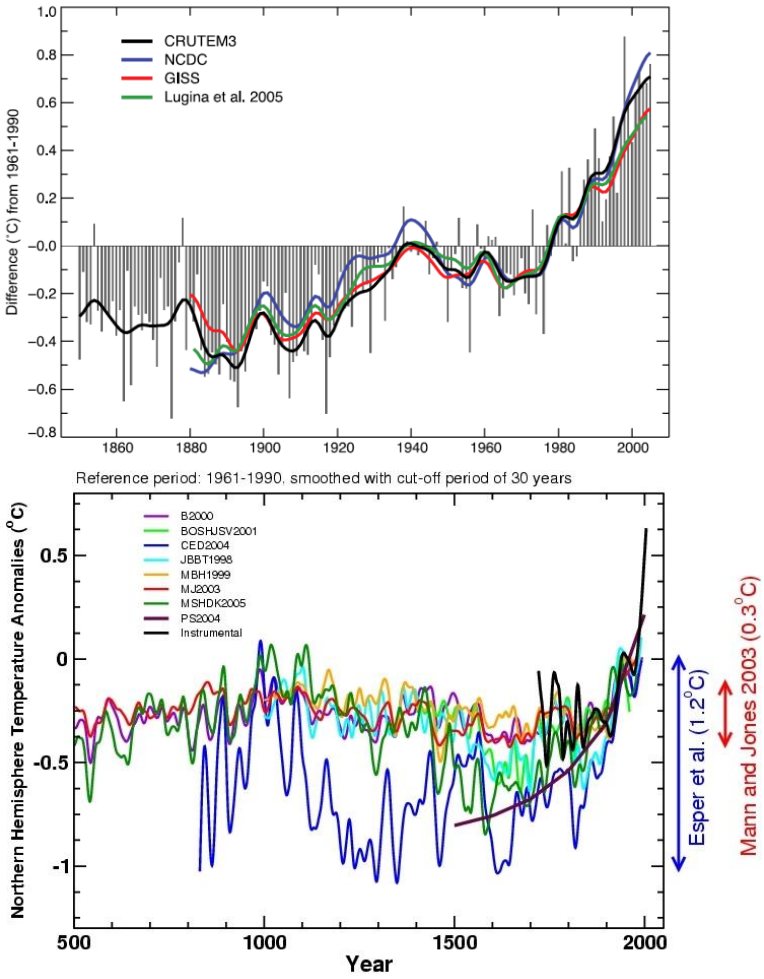

Figure 1.4: Increase of the global mean temperature (above) and the mean temperature of the northern hemisphere (below). Sufficient instrumental data for a reconstruction of the mean global temperature exists since 1860. The temperature before 1860 is reconstructed based on proxy data, predominantly tree ring analyses. These reconstructions are subject to different uncertainties and in some cases the different reconstructions disagree strongly.

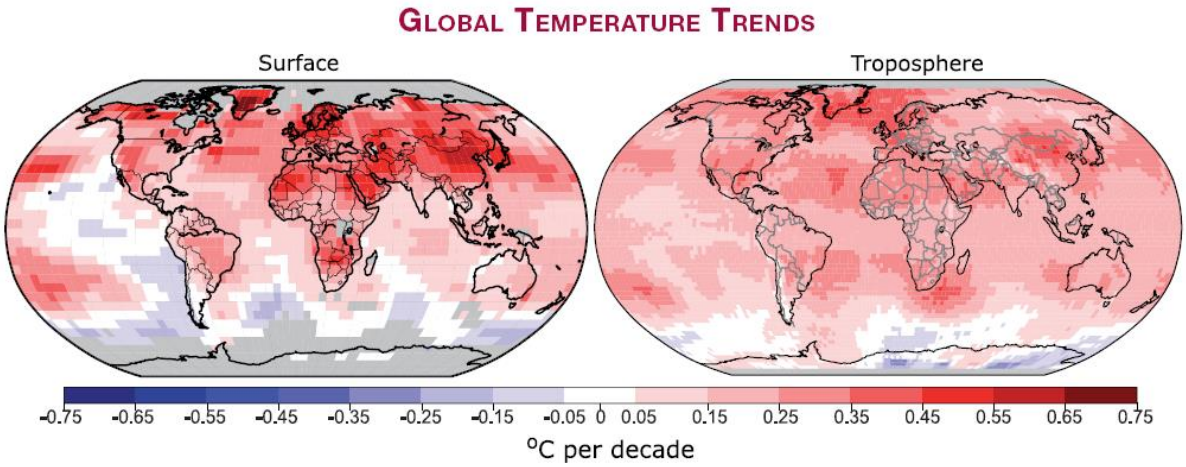

Figure 1.5: Patterns of estimated linear global temperature trends over the period 1979 to 2005 for the surface (left), and for the mid-troposphere from satellite records (right). Grey indicates areas with incomplete data. Rates of increase are generally larger over land than over ocean. (IPCC, 2007)

1.1.4 What to expect in the future?

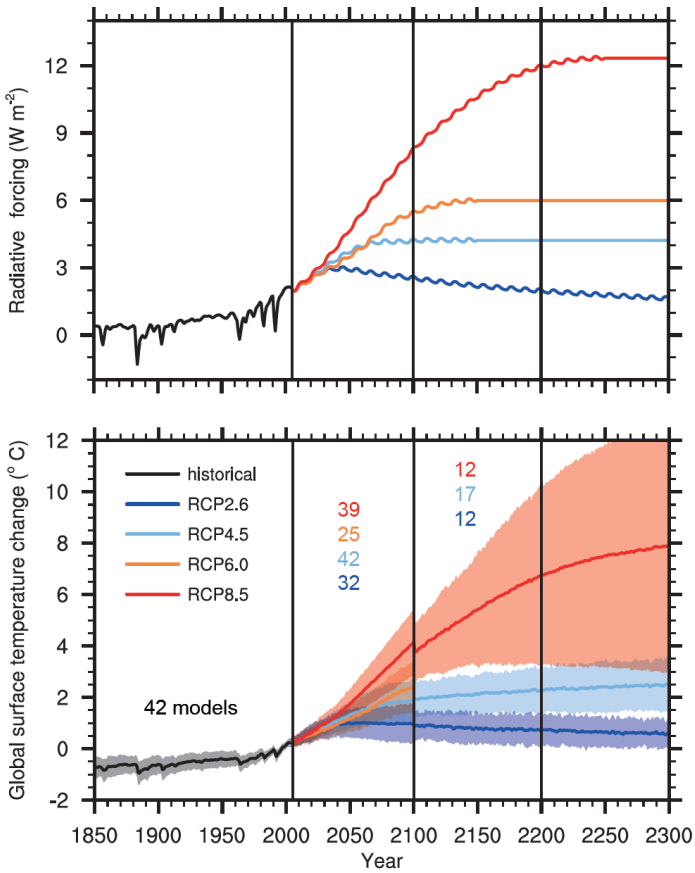

Figure 1.6: Radiative forcing and projected change in global means surface temperature (relative to 1986-2005) for the Representative Concentration Pathways (RCP) used by the Intergovernmental Panel on Climate Change (WGI, 2013, Figure TS.15). Solid lines are multi-model mean and the shading indicates the 5-95% interval across the distribution of models. RCP8.5 and RCP6 are pathways assuming no climate-policy intervention. Radiative forcing is assumed to stabilize after 2100 in all scenarios.

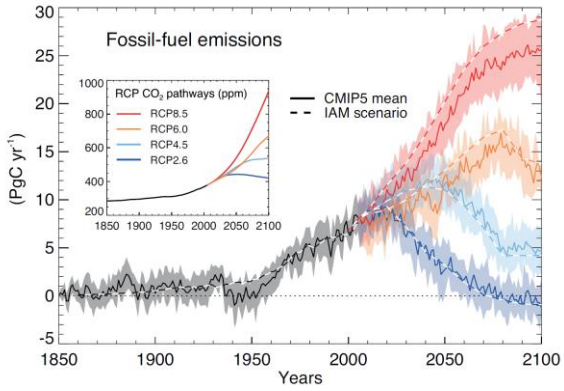

Figure 1.7: Compatible fossil-fuel emissions simulated by the CMIP5 models for the four Representative Concentration Pathways. The inset shows prescribed CO_2 concentrations. Solid lines are multi-model means; shading denotes the ±1 standard deviation range of individual model annual averages. (IPCC WGI, 2013, Figure TS.19)

Business as Usual: Without any climate-policy measures, greenhouse gas concentrations in the atmosphere will continue to increase and the rate of climate change is going to increase compared to the 20th century. Non-intervention scenarios for different possible development pathways of population, economy and technology point to sustained high CO_2 emissions. The emissions cause a further CO_2 increase in the atmosphere, an increase of global surface temperature, sea level rise, altered precipitation patterns, an increase in ocean acidity and a reduction in Arctic sea ice extent.

The modeled temperature and precipitation responses to the scenarios of the Inter-governmental Panel on Climate Change differ significantly depending on the season and region. The modeled temperature increase is the largest in continental regions and stronger in the northern than in the southern hemisphere. This is consistent with the observed trends of the past decades. While most models reveal a consistent picture of the temperature increase, results regarding to the projected precipitation changes show a stronger disagreement. However, an increase in the amount of precipitation is very likely in high latitudes, while a decrease is likely in most subtropical continental regions.

Many changes increase (approximately linearly) with cumulative carbon emissions:

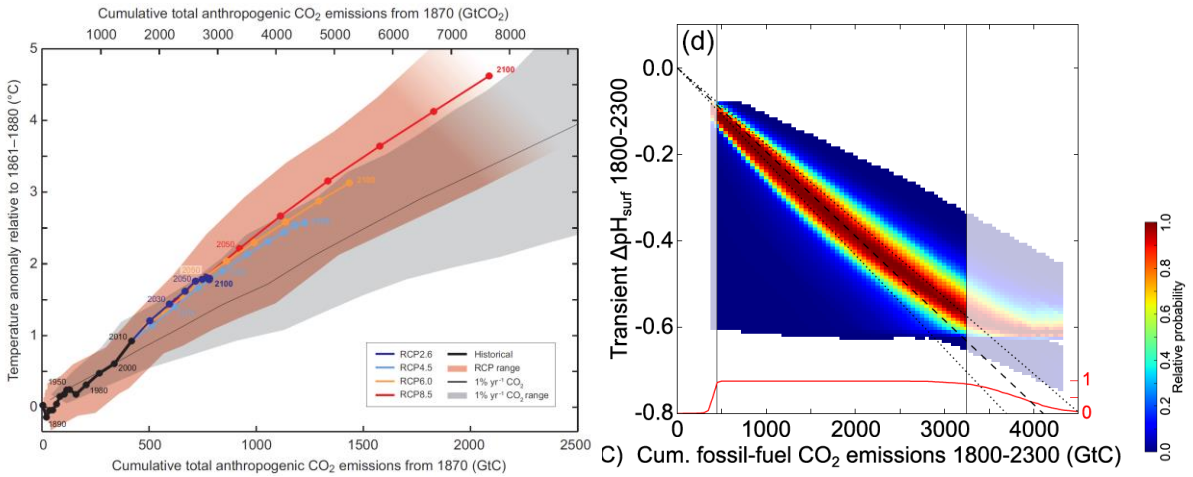

Figure 1.8: Relationship between cumulative carbon emissions and changes in global mean (left) surface air temperature and (right) surface ocean pH (IPCC WGI, 2013, Figure SPM.10 and Steinacher and Joos, BGD, 2015).

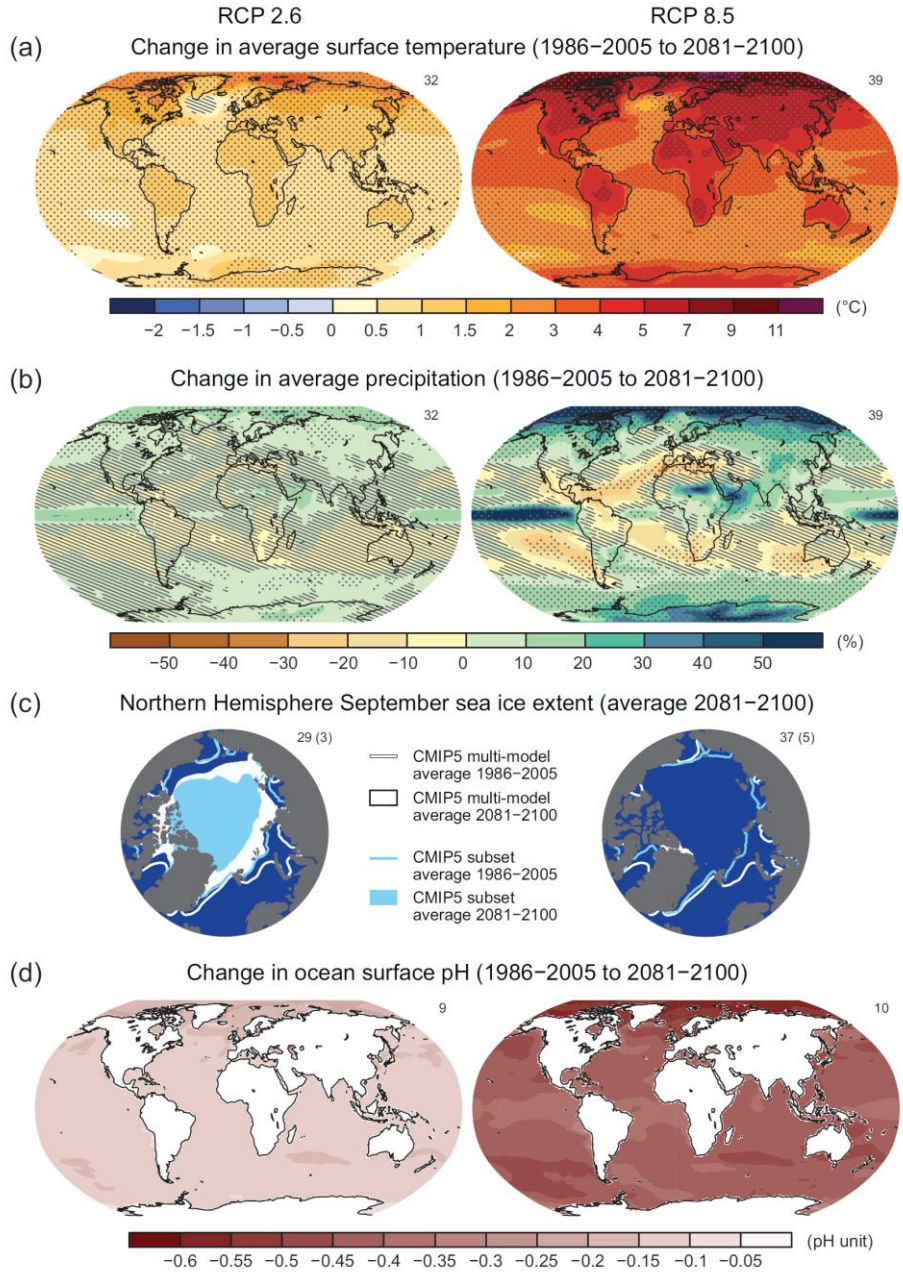

Figure 1.9: Maps of CMIP5 multi-model mean results for the scenarios RCP2.6 and RCP8.5 in 2081–2100 of (a) annual mean surface temperature change, (b) average percent change in annual mean precipitation, (c) Northern Hemisphere September sea ice extent, and (d) change in ocean surface pH. Changes in panels (a), (b) and (d) are shown relative to 1986–2005. For panels (a) and (b), hatching indicates regions where the multi-model mean is small compared to natural internal variability (i.e., less than one standard deviation of natural internal variability in 20-year means). Stippling indicates regions where the multi-model mean is large compared to natural internal variability (i.e., greater than two standard deviations of natural internal variability in 20-year means) and where at least 90% of models agree on the sign of change. In panel (c), the lines are the modelled means for 1986−2005; the filled areas are for the end of the century. The CMIP5 multi-model mean is given in white colour, the projected mean sea ice extent of a subset of models (number of models given in brackets) that most closely reproduce the climatological mean state and 1979 to 2012 trend of the Arctic sea ice extent is given in light blue colour. (IPCC WG, 2013, Figure SPM.8).

Stabilization of the greenhouse gas concentrations: Article 2 of the United Nations Framework Convention on Climate Change (UNFCC, Rio 1992) requires a stabilization of greenhouse gases in the atmosphere in order to prevent a dangerous anthropogenic disturbance of the climate system. CO_2 emitted by the combustion of fossil fuels accumulates in the climate system. A stabilization of CO_2 concentration in the atmosphere and thereby a slowdown and a long-term stabilization of anthropogenic temperature and climate changes requires a trend reversal with respect to the emissions and a reduction of carbon emissions below today's rate.

Anthropogenic warming and sea level rise would continue for centuries due to the time scales associated with climate processes and feedbacks, even if greenhouse gas concentrations were to be stabilized.

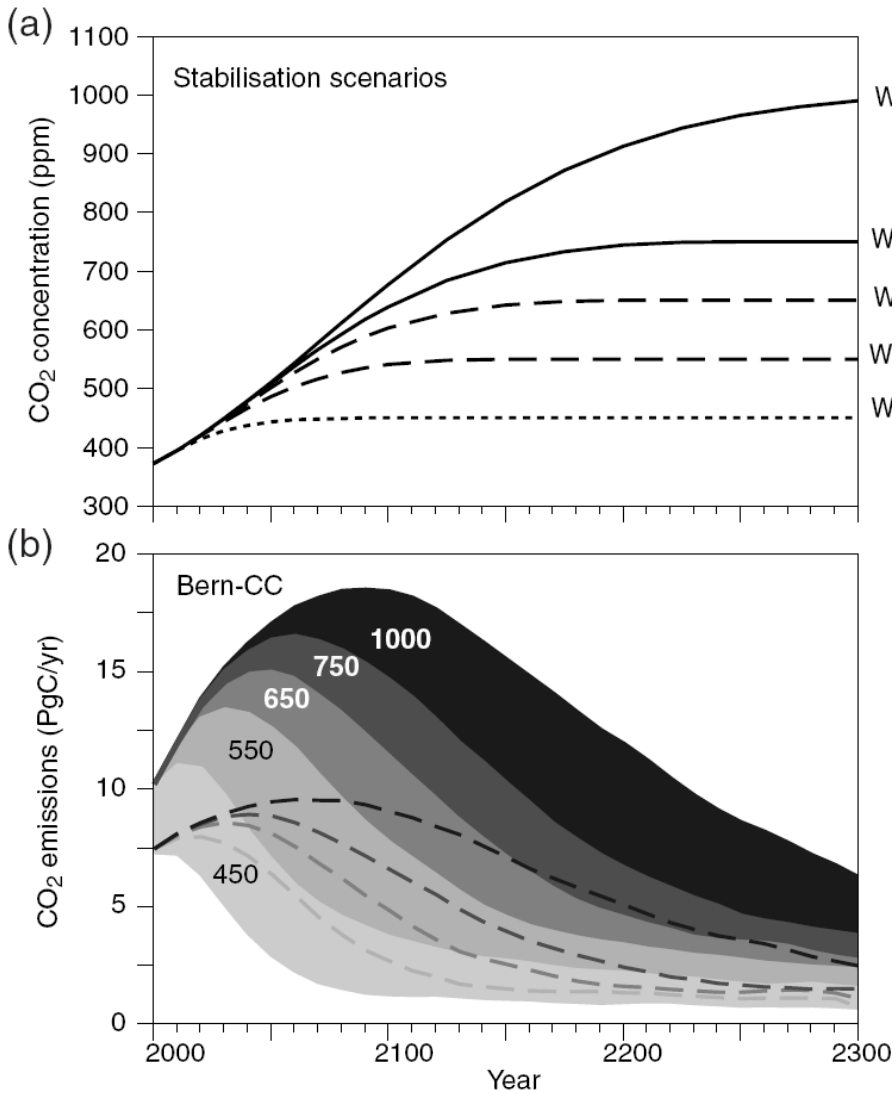

Figure 1.10: Projected CO_2 emissions leading to a stabilization at different CO_2 concentrations. Stabilization pathways (upper panel) were prescribed in a carbon cycle model (lower panel). The ranges represent the uncertainties resulting from different extreme model assumptions. For all stabilization scenarios, carbon emissions need to be reduced below today's level (From IPCC Third Assessment Report, Technical Summary, WGI).

Box 1.2

What fraction of fossil fuel resources could be combusted over the next 1000 years if atmospheric CO_2 were to be stabilized at twice the preindustrial concentration?

Conservative estimates of the fossil fuel reserves amount to some 5000 GtC (without accounting for the huge reserves of methane clathrates). On a time scale of several hundred years, ocean and atmosphere carbon inventories equilibrate and after 1000 years, about 20 % of the fossil emissions remain in the atmosphere (the possible C-uptake of the biosphere is small compared to the long-term ocean uptake). This results in a fraction *r* of the fossil fuel reserves that could be combusted, in order to stabilize CO_2 at around 560 ppm:

$$r = \frac{\text{Emission}}{\text{Resources}} = \frac{(560\ \text{ppm} - CO_{2,0}) \cdot \gamma \cdot \frac{1}{\alpha}}{\text{Resources}} = \frac{280\ \text{ppm} \cdot 2.123\ \text{GtC ppm}^{-1} \cdot \frac{1}{0.2}}{5000\ \text{GtC}} = 0.6$$

$CO_{2,0}$	280 ppm	preindustrial CO_2 concentration
γ	2.123 GtC ppm^{-1}	conversion factor (1 ppm in the entire atmosphere is equivalent to an atmospheric inventory of 2.123 GtC.)
α	~0.2	airborne fraction (fraction of the emissions that remains in the atmosphere)

Abrupt and irreversible climate change: The possibility of abrupt and irreversible changes in the climate system is real. From palaeodata, we know that a complete shut-down of the deep water formation in the North Atlantic is possible (Figure 1.11).

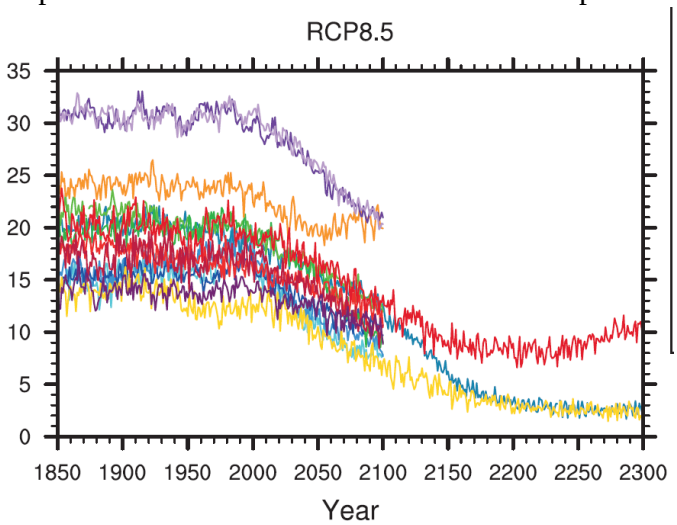

Figure 1.11: Multi-model projections of Atlantic Meridional Overturning Circulation (AMOC) strength at 30°N from 1850 through to the end of the RCP8.5 extension (IPCC WGI, 2013, Figure 12.35).

Models show a reduction of the deep water formation during the 21st century in the North Atlantic, which results in a decreased meridional heat transport. For constantly high greenhouse gas concentrations, some models simulate a complete and irreversible collapse of the North-Atlantic circulation.

1.2 Variability of the atmospheric CO_2 concentration in the past

Measurements of the CO_2 concentration provide valuable information about the climate in the past. To understand past changes in the climate system consistently, qualitatively and quantitatively remains a major challenge in climate physics. CO_2 concentrations and climate have been varying on all time scales throughout the Earth's history.

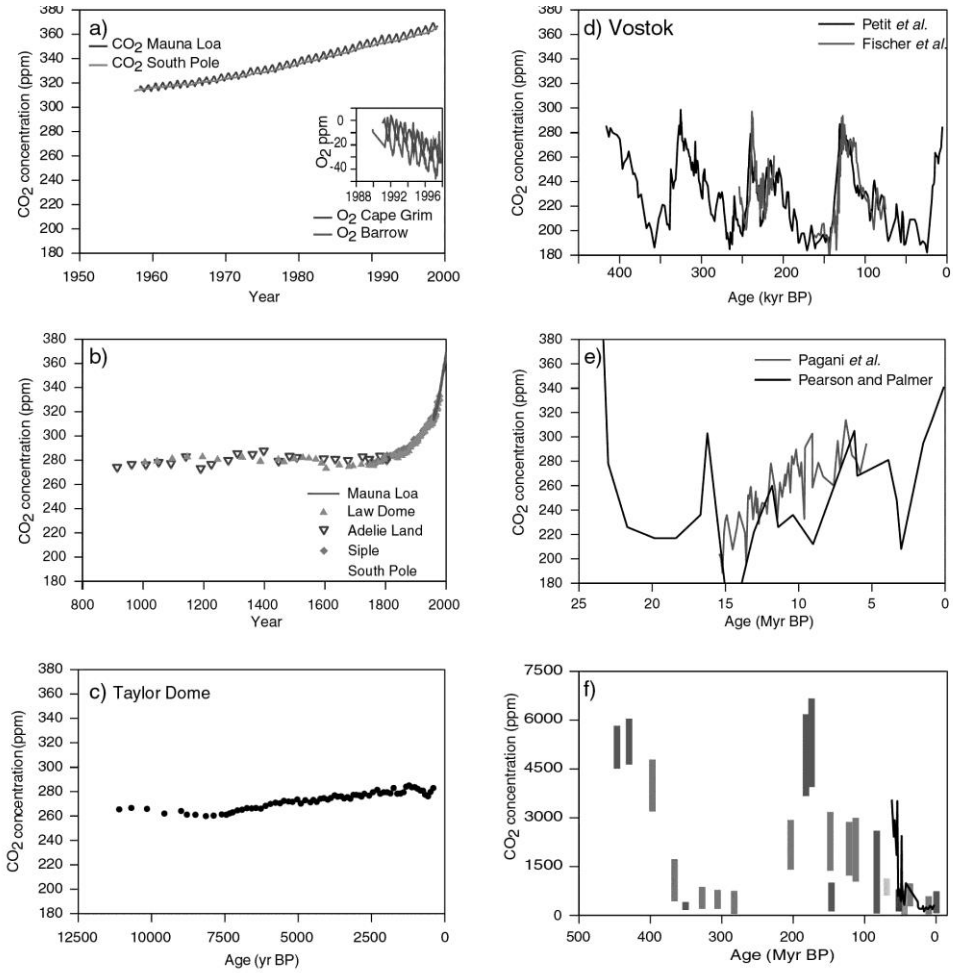

Figure 1.12: Variations of the atmospheric CO_2 concentration on different time scales.

Geological time scale: The CO_2 concentration was very high (> 3'000 ppm) between 600 and 400 million years before present (BP) and between 200 and 150 million years BP. On very long time scales, the atmospheric concentration is governed by the balance between geochemical source and sink processes, such as sedimentation of organic carbon in the ocean, erosion and volcanism. The formation of the terrestrial biosphere increased the erosion rate of silicate rocks which is a sink of CO_2. The net effect of this slight disequilibrium in the carbon cycle that was maintained over hundreds of millions of years was a reduction of the atmospheric CO_2 concentration. In the geologically younger past, the CO_2 concentration decreased further and there is evidence that the concentrations during the last 20 million years did not exceed 300 ppm.

Glacial-interglacial: Past atmospheric CO_2 concentrations can be reconstructed from measurements on air trapped in Arctic and Antarctic ice cores. The atmospheric CO_2 concentration varied between 180 and 300 ppm. The lowest concentrations are associated with periods of maximum glaciation and the highest values to warm periods. Variations of the Earth's orbital parameters (Milankovic Theory) are assumed to be the ultimate driver of the Glacial-Interglacial cycles. CO_2 is one of the different parameters of the Earth system that exhibits the typical Milankovic frequencies of the orbital parameters. The variation in the greenhouse gas concentrations amplified the glacial-interglacial climate change.

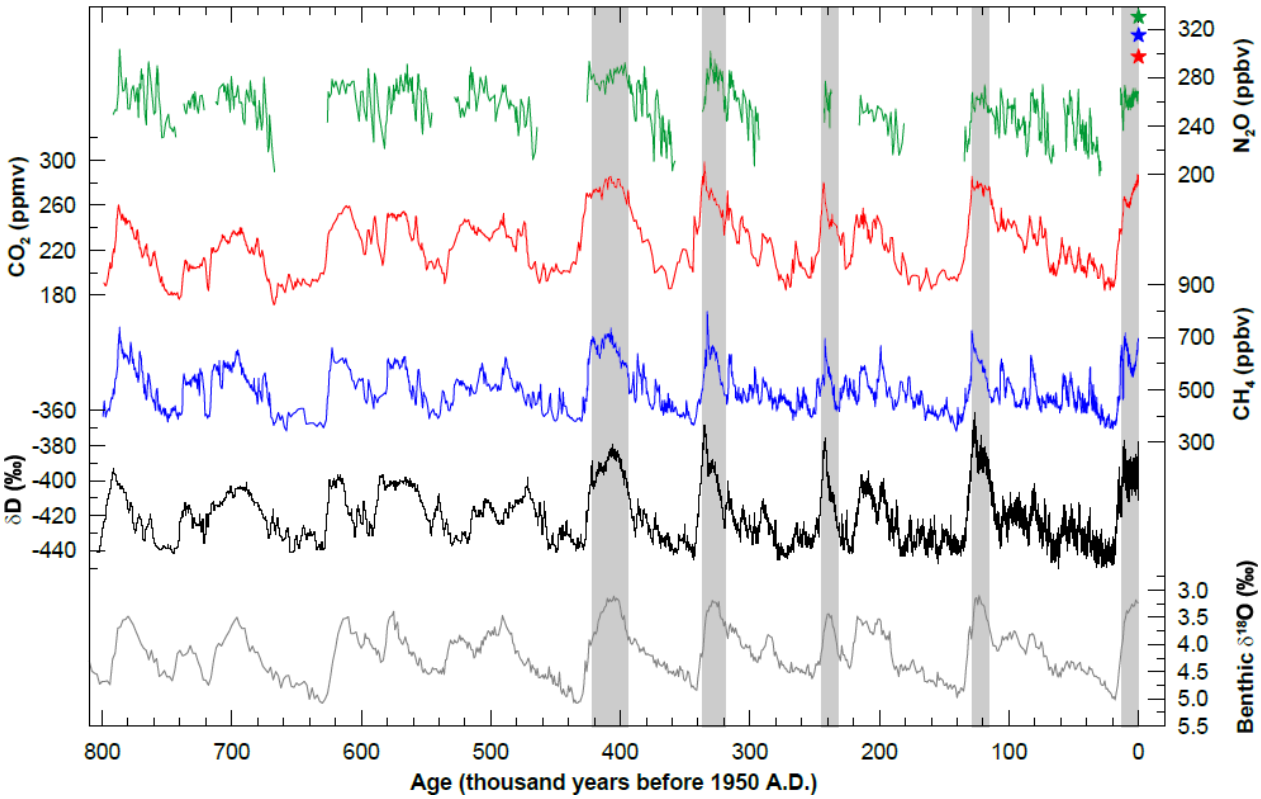

Figure 1.13: Variations of the greenhouse gases N_2O, CO_2 and CH_4, Deuterium in ice (a proxy for temperature) and δ18O in shells of bottom-dwelling organisms preserved in marine sediments (a proxy for ice volume/sea level) over the past 800'000 years. The data was retrieved from ice cores of Vostok, Antarctica and Dome Concordia (Antarctica) and from a stack of marine sediments (Lisiecki and Raymo, 2005). For a comparison, the greenhouse gas records were extended with data of the anthropogenic increase of the past 200 years (stars). The last five interglacials are highlighted with grey bands. The CO_2 and deuterium records correlate strongly. The somewhat colder warm phases between 450'000 and 800'000 years BP are associated with lower CO_2 concentrations than during the more recent, warmer interglacials.

Variations during the glacial period: Detailed measurements show that the CO_2 concentration also varied on shorter time scales. Variations in the CO_2 concentrations of up to 20 ppm are found. These are related to warm period in the Antarctica and the so-called Dansgaard-Oeschger warm-cold oscillations. These climate shifts are linked to changes in the ocean circulation and the heat transport in the North Atlantic, which lead to opposite temperature changes in the two hemispheres.

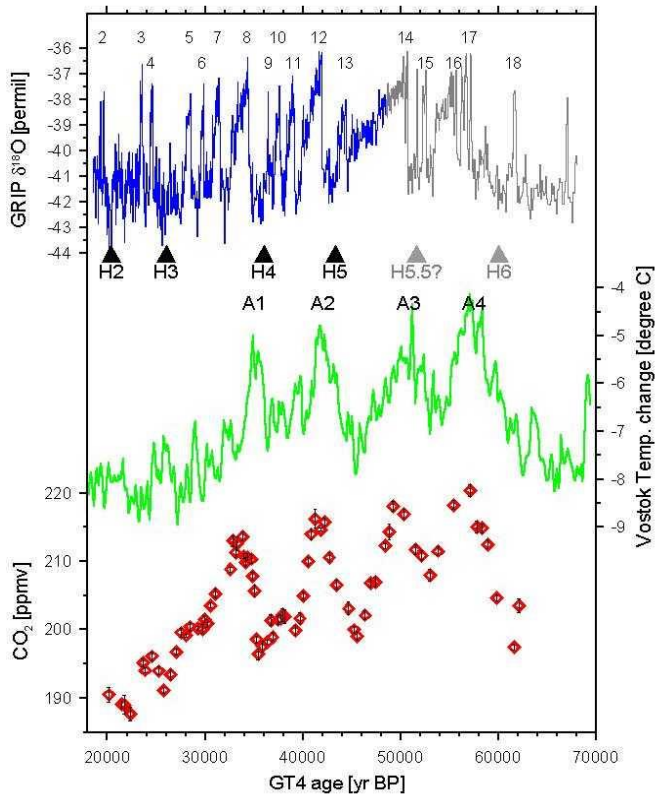

Figure 1.14: Variations of the temperature indicator $\delta^{18}O$ in Greenland ice (Greenland Ice Core Project, GRIP), the temperature as derived form $\delta^{18}O$ measurements on an Antarctic Ice core (Vostok) and the CO_2 content in the atmosphere. Arrows (H2 and H6) represent Heinrich Events (input of ice/freshwater into the North Atlantic) and the numbers represent (relative) warm phases in Greenland (Interstadials 2-18) and in Antarctica (A1-A4).

The catastrophic discharge of large ice masses (freshwater of low density) into the North Atlantic, recorded by the so-called Heinrich-layers in oceanic sediments, probably led to a temporary collapse of the deep water formation in the North Atlantic and to a reduction in the pole-ward heat transport. Increased CO_2 concentrations are found during the warm phases in Antarctica. Also during the last glacial-interglacial transition, different trends in CO_2 are detected. The CO_2 variations during the last glacial period are relatively small and demonstrate that under natural conditions, the CO_2 concentration is well buffered against abrupt climate change, in particular against a shut-down of the North Atlantic deep water formation.

Event, Stadial	Estimated age in 1000 years before present (kyr BP)
Holocene (current interglacial period)	10 kyr BP until today
Transition glacial-Holocene	18 to 10 kyr BP
Termination 1	14 kyr BP
Younger Dryas (YD)	12.7 to 11.5 kyr BP
Antarctic cold reversal	14 to 13 kyr BP
Bölling-Alleröd warm period	14.5 to 13 kyr BP
Last Glacial	74 to 14 kyr BP
Last Glacial Maximum (LGM)	25 to 18 kyr BP
Eemian/Marine Isotope Stadial 5e	128 to 118 kyr BP
Peak of the last Interglacial	124 kyr BP
Termination 2	130 kyr BP
Heinrich event	Large amounts of 'ice rafted debris' in marine sediments, reoccurrence after 7-10 kyr
Dansgaard-Oeschger cycles	Warm-cold oscillations during the last glacial, period with a duration of a few kyrs, detected in Greenland ice cores
Termination	Period of fast ice retreat

Table 1.2: Terminology used in paleoclimatic studies covering the past 150'000 years.

Variations during the Holocene: Measurements on ice of Taylor Dome and Dome C in Antarctica show that the CO_2 concentration at the beginning of the present warm period decreased slightly and increased again between 7 kyr BP and preindustrial by about 20 ppm. Measurements of the stable isotope ^{13}C constrain possible mechanisms responsible for this increase. The CO_2 concentration varied by a few ppm during the last millennium before the anthropogenic increase. The low natural variability of CO_2 and other greenhouse gases during the last millennium points to relatively small global climate variations.

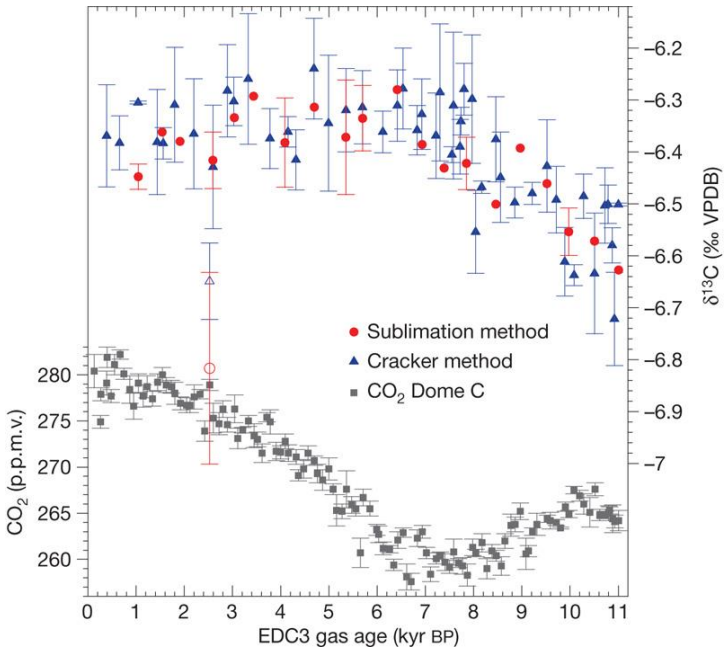

Figure 1.15: Variations of the atmospheric CO_2 concentration and of the ^{13}C:^{12}C isotope ratio during the Holocene (Note reversed age scale). The isotope ratio permits the quantification of different carbon source and sinks with different isotopic signatures.

Interannual and seasonal variations: Today, CO_2 measurements on atmospheric air are conducted routinely at around 40 stations worldwide. Considerable variability in the annual rate of atmospheric CO_2 increase is detected. The seasonal variation has an amplitude of a few ppm. The seasonal signal is mainly caused by the exchange with the land biosphere and decreases from north to south. This gradient is linked to the larger land fraction in the northern compared to the southern hemisphere.

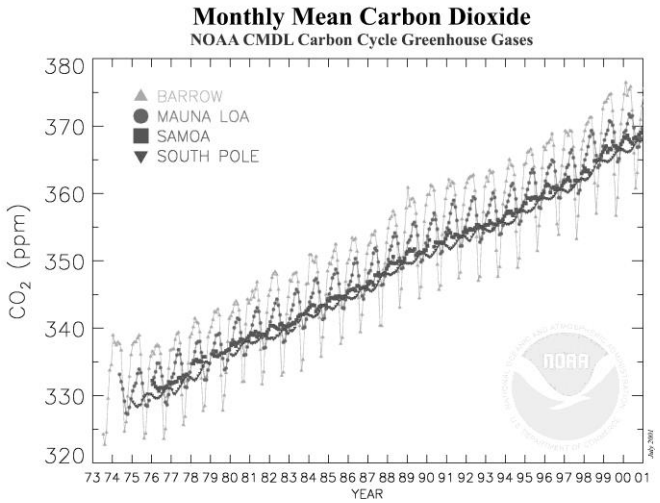

Figure 1.16: CO_2 concentration in air as recorded at stations located in different latitudes. The amplitude of the seasonal variability decreases from south to north.

1.3 Rates of change and Radiative Forcing during the past 20'000 years

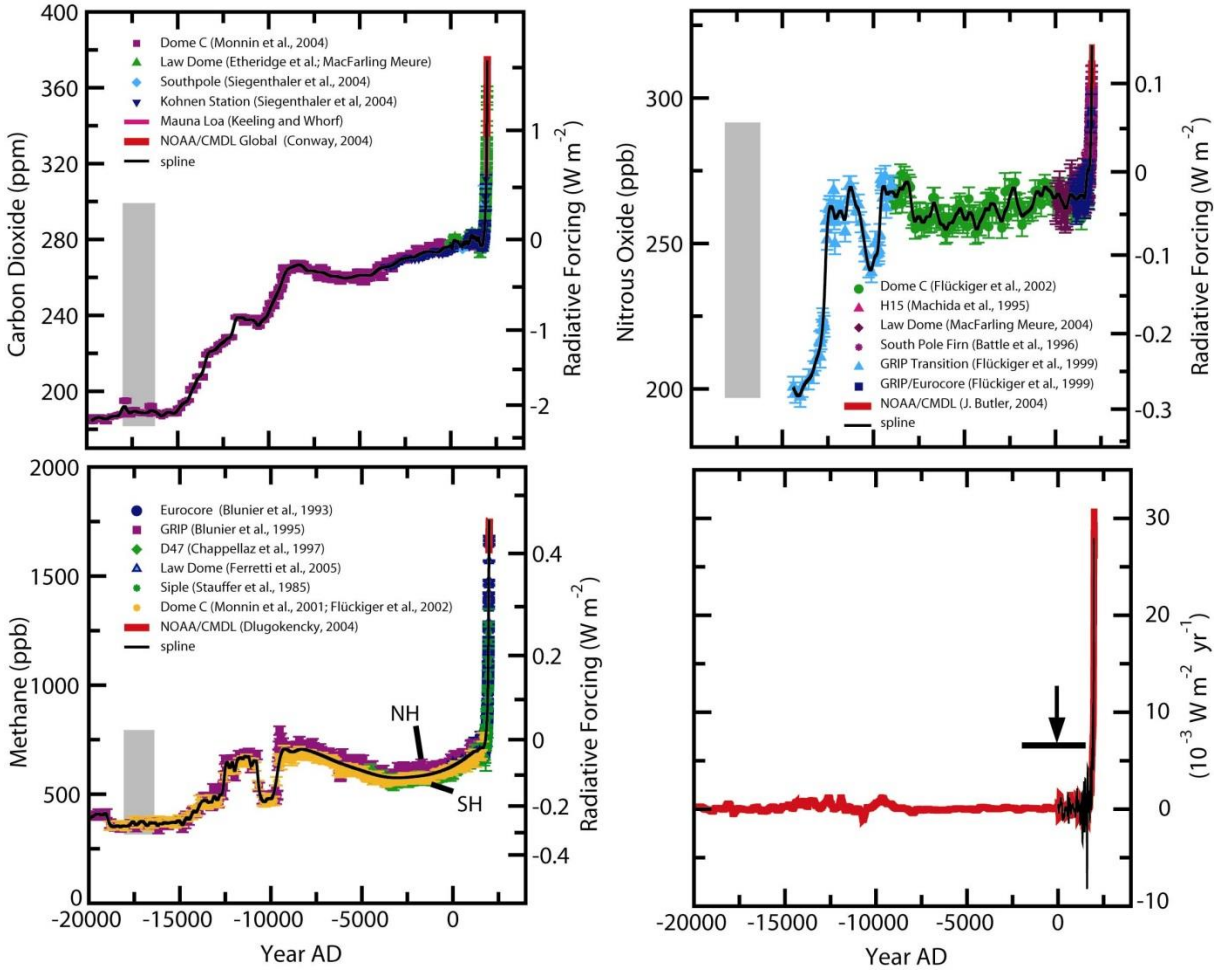

Figure 1.17: Changes in the atmospheric concentration of CO_2, CH_4, N_2O and rates of change of their combined Radiative Forcing during the past 20'000 years. Records from different ice cores from Antarctica and Greenland (symbols) are extended with direct atmospheric measurements. Radiative Forcing relative to 1750 is given on a non-linear scale on the right side. The grey bars represent measured values for the past 650'000 years. Variations in the atmospheric CO_2 dominate the Radiative Forcing of all three gases combined. The mean decadal rate of increase in Radiative Forcing (lower right) is six times larger than at any time during the past 20'000 years. Air trapped in ice reveals a smoothing of the atmospheric signal. The range of the age distribution of the air trapped in ice varies between 20 years in regions with a high accumulation of snow and 200 years for regions with low accumulation rates. The rates determined from the high-resolution Law Dome ice and firn records of the past 2000 years are given by the thin black line in the lower right figure. The arrow shows how the anthropogenic peak would be damped in places with low accumulation.

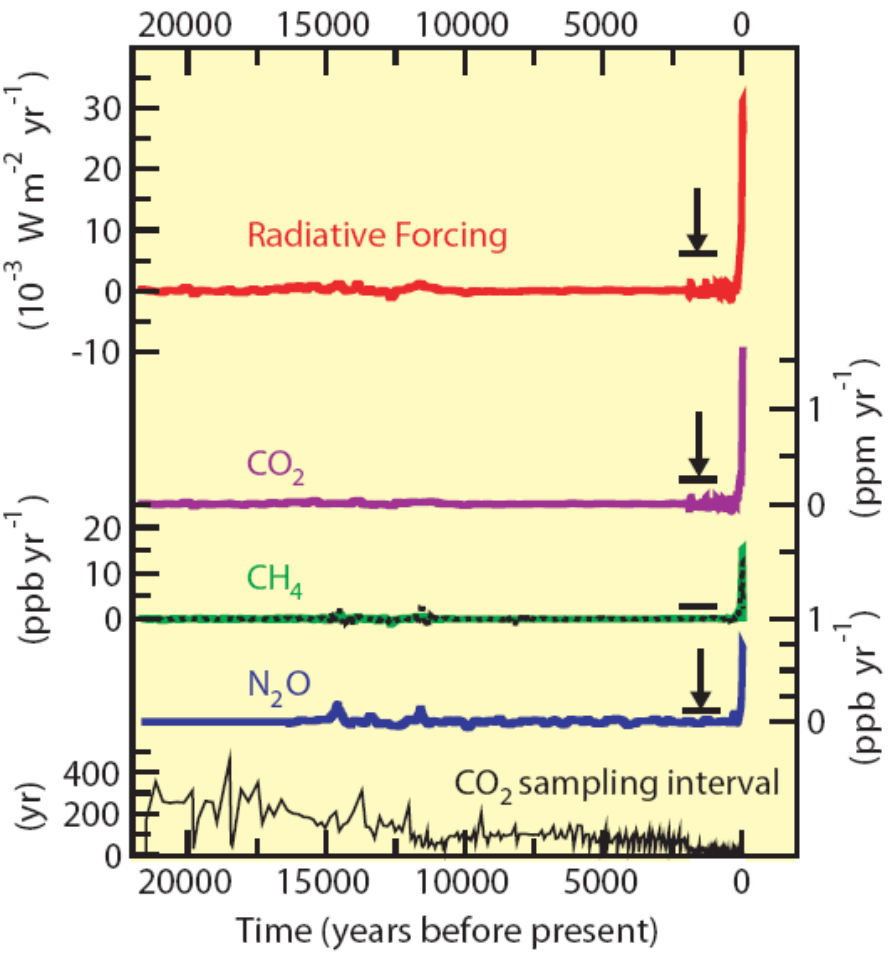

Figure 1.18: Rates of change for the three greenhouse gases, N_2O, CH_4, CO_2 and their combined radiative forcing for the last 22 ka. The Greenland CH_4 data represent decadal-scale variations and inferred rates of change (dash) are directly comparable for different periods. The black lines/arrows show the peak in the rate of change in radiative forcing and concentrations after the anthropogenic signals of CO_2, CH_4 (no arrow shown), and N_2O have been smoothed with a model describing the enclosure process of air in ice.

The rate of increase in concentrations and in Radiative Forcing of the three greenhouse gases CO_2, CH_4, N_2O is accelerating. Radiative Forcing of CO_2 varied by less than 0.1 milliwatt m^{-2} yr^{-1} during the past 6000 years before the Industrialization, but already by about 12 milliwatt m^{-2} yr^{-1} during the 20th century and by about 27 milliwatt m^{-2} yr^{-1} during the past decade (1994 to 2003).

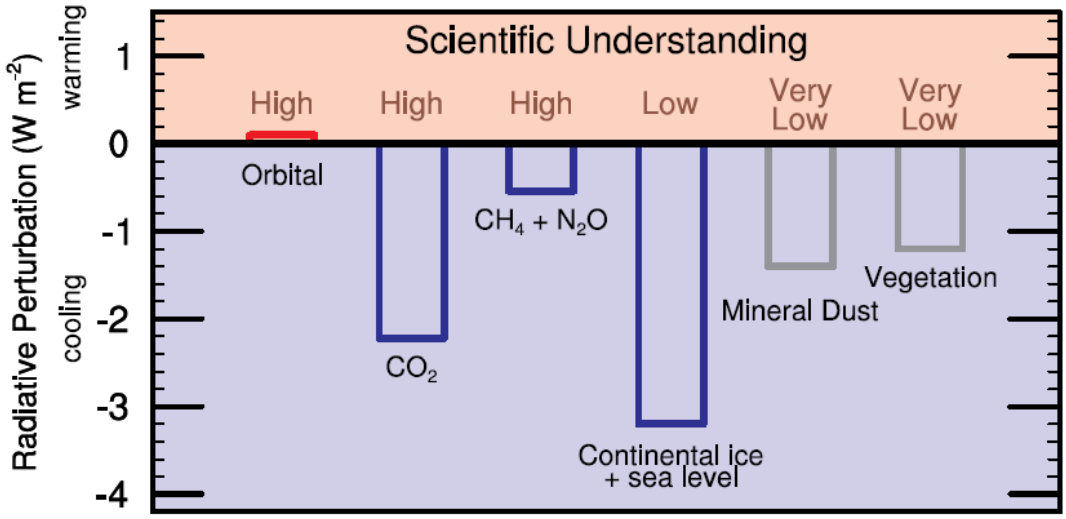

Figure 1.19: Radiative perturbations for the Last Glacial Maximum (21'000 years BP) relative to 1750 A.D. for different forcings/feedbacks (from Jansen et al., 2007).

Figure 1.2 and Figure 1.19 allow us to compare the well-known forcings of the radiation balance for today and the period of the LGM. The glacial-interglacial cycles were most likely driven by the changes of the Earth's orbit around the sun. However, the change in global mean radiation is too small to explain the reconstructed temperature change between today and the LGM. Other mechanisms amplified the orbital forcing. The increase in albedo due to the extent of ice sheets is the largest individual forcing at the LGM. The drivers linked to the biogeochemical system (greenhouse gases, dust, vegetation cover) are responsible for more than half of the LGM-forcing. This highlights the central role of biogeochemical cycles in the climate system.
The changes of the Earth orbit cause relatively small changes in the total solar energy input. However, at the LGM, the energy was distributed differently between seasons and latitude.
The Radiative Forcing today is the result of the partly cancelling contributions from well-mixed greenhouse gases (CO_2, CH_4, N_2O and CFCs), stratospheric and tropospheric ozone, different aerosols and changes in land use and solar energy output. In the near future, the CO_2 forcing will gain importance since emitted CO_2 is accumulating in the atmosphere, sulphur emissions are decreasing and methane concentrations are not increasing at this point of time.

From Sections 1.1, 1.2 and 1.3 the following conclusions emerge:

1. The 20th century increase in CO2 and its radiative forcing occurred more than an order of magnitude faster than any sustained change during the past 22,000 years.
2. Today's atmospheric CO_2 concentration is higher than ever during the past 800'000 years and probably the past 20 million years.
3. Greenhouse gases and the biogeochemical system play a central role for past and future climate change.

Literature:

Excellent book on the ocean carbon cycle:

Sarmiento, J. & Gruber, N. (2006) *Ocean Biogeochemical Dynamics* (Princeton University Press).

Reviews:

T. F. Stocker *et al.*, in *Climate Change 2013: The Physical Science Basis. Contribution of Working Group I to the Fifth Assessment Report of the Intergovernmental Panel on Climate Change*, T. F. Stocker *et al.*, Eds. (Cambridge University Press, Cambridge, United Kingdom and New York, NY, USA, 2013), pp. 33-115. http://www.ipcc.ch/report/ar5/wg1/

Solomon, S., Qin, D., Manning, M., Alley, R., Berntsen, T., Bindoff, N. L., Chen, Z., Chidthaisong, A., Gregory, J., Hegerl, G., Heimann, M., Hewitson, B., Hoskins, B., Joos, F., Jouzel, J., Kattsov, V., Lohmann, U., Matsuno, T., Molina, M., Nicholls, N., Overpeck, J., Raga, G., Ramaswamy, V., Ren, J., Rusticucci, M., Somerville, R., Stocker, T. F., Stouffer, R. J., Whetton, P., Wood, R. A. & Wratt, D. (2007) in *Climate Change 2007: The Physical Science Basis. Contribution of Working Group I to the Fourth Assessment Report of the Intergovernmental Panel on Climate Change*, eds. Solomon, S., Qin, D., Manning, M., Chen, Z., Marquis, M., Averyt, K. B., Tignor, M. & Miller, H. L. (Cambridge University Press, Cambridge United Kingdom and New York, NY, USA), pp. 19-91.http://www.ipcc.ch

Prentice, I. C., G. D. Farquhar, M. J. Fasham, M. I. Goulden, M. Heimann, V. J. Jaramillo, H. S. Kheshgi, C. LeQuéré, R. J. Scholes, and D. W. R. Wallace. 2001. The carbon cycle and atmospheric CO_2. Pp. 183–237 in Climate change 2001: The scientific basis (Contribution of Working Group I to the third assessment report of the Intergovernmental Panel on Climate Change), edited by J. T. Houghton, Y. Ding, D. Griggs, M. Noguer, P. van der Linden, X. Dai, K. Maskell, and C. A. Johnson. Cambridge: Cambridge University Press. http://www.proclim.ch/IPCC2001.html; http://www.ipcc.ch

Joos F. and I. C. Prentice. A paleo-perspective on changes in atmospheric CO2 and climate. In Towards Stabilization of Atmospheric CO2, C. Field and M. Raupach (Eds.), SCOPE/GCP rapid assessment of the carbon cycle, Island Press, in press, 2004. http://www.climate.unibe.ch/~joos/publications.html

Stocker, T. F. 2000. Past and future reorganisations in the climate system. *Quaternary Science Reviews* 19:301–319. http://www.climate.unibe.ch/publications.html

Others (results from ice cores)

Elsig, J., Schmitt, J., Leuenberger, D., Schneider, R., Eyer, M., Leuenberger, M., Joos, F., Fischer, H. and Stocker, T. F.: 2009, Stable isotope constraints on Holocene carbon cycle changes from an Antarctic ice core, *Nature* 461: 507–510. http://www.climate.unibe.ch/~joos/publications.html

Petit, J. R., J. Jouzel, D. Raynaud, N. I. Barkov, J.-M. Barnola, I. Basile, M. Bender, J. Chappellaz, M. Davis, G. Delayque, M. Delmotte, V.M. Kotlyakov, M. Legrand, V.Y. Lipenkov, C. Lorius, L. Pépin, C. Ritz, E. Saltzman, and M. Stievenard. 1999. Climate and atmospheric history of the past 420,000 years from the Vostok ice core, Antarctica. *Nature* 399:429–436.

Lüthi, D., et al. (2008), High-resolution carbon dioxide concentration record 650'000-800'000 years before present, *Science*, *453*, 379-382

Monnin, E., A. Indermühle, A. Däallenbach, J. Flückiger, B. Stauffer, T. F. Stocker, D. Raynaud, and J. Barnola. 2001. Atmospheric CO_2 concentrations over the last glacial termination. *Science* 291:112–114. http://www.climate.unibe.ch/publications.html

Siegenthaler, U., Stocker, T. F., Monnin, E., Luthi, D., Schwander, J., Stauffer, B., Raynaud, D., Barnola, J. M., Fischer, H., Masson-Delmotte, V. & Jouzel, J. (2005) *Science* **310,** 1313-1317.

2 The modern carbon cycle

2.1 Distribution of carbon in different reservoirs

Quantities and exchange fluxes of the most important carbon reservoirs are summarized in Figure 2.1 and Table 2.1. The carbon cycle is considerably disturbed by the carbon release from fossil fuel burning and deforestation and other land use activities. The reservoirs atmosphere, biosphere, ocean and sediments are characterized as follows:

Atmosphere: Carbon in the atmosphere is most commonly present in the form of carbon dioxide (CO_2; 2000: 368 ppmv), methane (CH_4, 2000: 1.7 ppmv = 1700 ppbv; parts per billion by volume) and carbon monoxide (CO; 50...100 ppbv). The atmospheric CO_2 concentration affects the radiation balance and thus physical climate. The CH_4 concentration has more than doubled during the past 200 years. The greenhouse effect of a single CH_4 molecule is much higher than that of a CO_2 molecule. However, its atmospheric concentration is two orders of magnitude smaller than CO_2.

Box 2.1

Units: Global amounts of carbon are commonly quantified in GtC (gigatons of carbon 1 GtC = 10^9 tC = 10^{15} g C) or in mol (1 mol-C=12.01 gram). Independent from its chemical form, only the amount of C-atoms are quantified. The atmospheric CO_2 concentration is usually given as a mixing ratio in ppm (parts per million (volume)= 1 CO_2 molecule per 10^6 molecules of dry air). A mean mixing ratio of 1 ppm corresponds to an atmospheric inventory of 2.123 GtC.

Biosphere: A highly simplified formula for organic material is CH_2O, or $C_6H_{12}O_6$ (glucose). The fluxes passing the terrestrial and marine biosphere are of similar magnitude, but the mean residence times differ markedly due to different reservoir sizes (see Table 2.1): they are ~10 years for the living terrestrial biosphere (without soils) and 1 month for the marine biosphere.

Box 2.2

Residence time: A useful first order measure to characterize the time scale of exchange processes is the residence time of carbon in a reservoir. The mean residence time, τ, of a substance in a reservoir of mass M and discharge F is:

$$\tau = \frac{M}{F}$$

Ocean: With its 40'000 GtC, the ocean is the largest rapidly exchanging carbon reservoir ('rapid' in this context means < 1000 years). Carbon is most abundant in the form of dissolved inorganic carbon. The denomination $\sum CO_2$ or DIC refers to the sum of bicarbonate (HCO_3^-; about 90%), carbonate (CO_3^{2-}; about 10%) and dissolved gaseous CO_2 (about 0.5%). A small amount of the total carbon in the ocean (a few percent) is in the form of dissolved organic carbon, DOC.

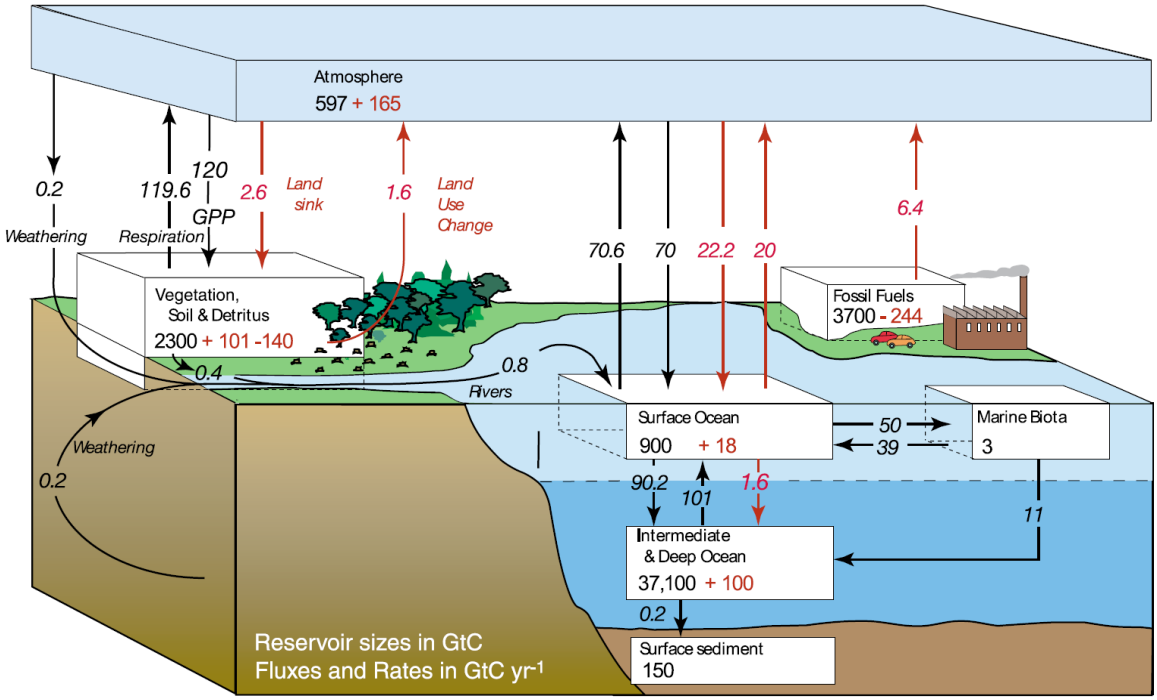

Figure 2.1: The global carbon cycle for the 1990s, showing the main annual fluxes in GtC yr^{-1}: pre-industrial 'natural' fluxes in black and 'anthropogenic' fluxes in red (modified from Sarmiento and Gruber (1), with changes in pool sizes from Sabine et al. (2)). The net terrestrial loss of –39 GtC is inferred from cumulative fossil fuel emissions minus atmospheric increase minus ocean storage. The loss of –140 GtC from the 'vegetation, soil and detritus' compartment represents the cumulative emissions from land use change (3), and requires a terrestrial biosphere sink of 101 GtC (in Sabine et al., given only as ranges of –140 to –80 GtC and 61 to 141 GtC, respectively; other uncertainties given in their Table 1). Net anthropogenic exchanges with the atmosphere are from Column 5 'AR4' in Table 7.1. Gross fluxes generally have uncertainties of more than ±20% but fractional amounts have been retained to achieve overall balance when including estimates in fractions of GtC/yr for river transport, weathering, deep ocean burial, etc. 'GPP' is annual gross (terrestrial) primary production. Atmospheric carbon content and all cumulative fluxes since 1750 are as of end of 1994. Figure from Denman et al. (4).

Sediments: A giant reservoir which exchanges carbon very slowly (on geological time scales) with the ocean. Carbon is most commonly present as $CaCO_3$ (calcite and aragonite) and $MgCO_3$, while around 1% is in the form of organic matter. Sediments are important when considering time scales longer than a few 1000 years, e.g. glacial-interglacial transitions.

Major global carbon reservoirs and fluxes
Main sources: Denman et al., 2007, Sabine et al., 2004, Tarnocai et al., 2009

Reservoirs			**10^{15} g C**
Atmosphere			
CO_2	1800	~280 ppm	594
	2007	383 ppm	813
Other Gases	CH_4 (2005)	1,774 ppm	4
	CO	0,1 ppm	
(Troposphere: 80 %, stratosphere 20 % of atmospheric mass)			
Oceans:	Inorganic C (ΣCO_2)		38,000
	Dissolved organic matter		<. 700
	Biomass		3
Land biosphere	Living		650
	Soil, humus, including frozen soil		ca 3200
Groundwater			450
Sediments	Inorganic C		ca. 60,000,000
	Organic C		ca. 12,000,000
Fossil fuels (conventional resources)			ca. 5,000

Fluxes	**10^{15} g C/yr**
Atmosphere - ocean, gross CO_2 exchange (preind.)	70
Atmosphere - land biota, net photosynthesis/respiration (NPP)	60
Marine photosynthesis	50
Net sedimentation in oceans/weathering	0,2
Volcanism	ca. 0.07
Fossil fuel combustion, 2007	8.5
Net land use flux, 2007	ca. 1.5

Residence times: τ = mass/flux		
Atmosphere (pre-industrial)	total exchange	4.6 yr
	exchange with ocean only	8.5 yr
	exchange with biosphere only	10 yr
Living land/biosphere: photosynthesis/respiration		11 yr
Marine biosphere: photosynthesis/respiration		0.06 yr
Oceans: exchange with atmosphere, total flux		540 yr
sedimentation only		200,000 yr
Atmosphere + biosphere + oceans: sedimentation		212,000 yr

Table 2.1: Global carbon reservoirs, fluxes, and mean residence times.

2.2 The anthropogenic CO_2 perturbation

The concentration of CO_2 has risen from a pre-industrial value of 280 ppm (prior to 1800) to today's value of approximately 385 ppm, an increase of about 40%. This increase can be attributed to the burning of fossil fuels (coal, oil, gas), as well as the clearing and burning of forests and other land use change activities.

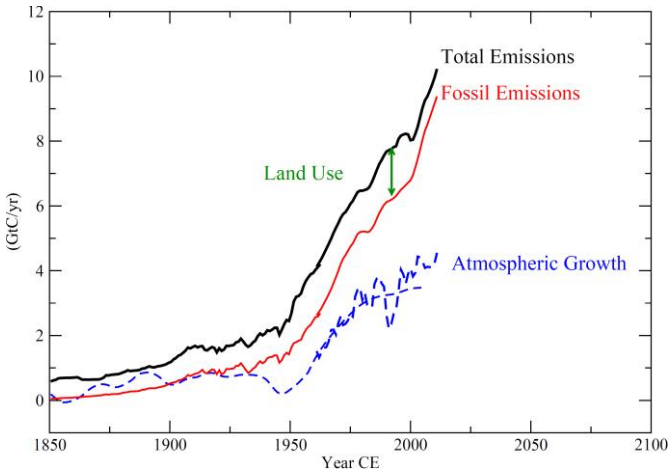

Figure 2.2: Emissions due to the burning of coal, oil and gas, deforestation and land use exceed the increase in the atmospheric inventory by about a factor of two. 5-yr running means are shown after 1961 for atmospheric growth.

Between 1860 and World War I, as well as after World War II until the present, CO_2 emissions due to fossil fuel burning have risen exponentially. This continuous growth has been interrupted during the two world wars, the Great Depression, the oil crisis in 1973 and the period of higher oil prices since 1980. Today the world-wide emissions of fossil fuels accounts for approximately 9 GtC/yr. Deforestation in the tropics and land use (ploughing leads to accelerated oxidation of the soil) are also major sources of CO_2. Estimates range between 0.5 and 2.7 GtC/yr, although it is difficult to estimate this quantity due to the heterogeneity of the biosphere. Open questions include: Which areas are affected? What is the carbon density per unit area? What is the effect of re-growth in cleared areas?

Currently the total emissions are ~10 GtC/yr. If all of the emitted CO_2 stayed in the atmosphere, the atmospheric concentration of CO_2 would rise by approximately 5 ppm per year (1 ppm = 2.12 GtC). The observed increase is only about half as large. The ocean and the land biosphere have taken up the other half. The 50% that stays in the atmosphere is referred to as the *airborne fraction.* The estimated oceanic CO_2 absorption today is about 2 GtC/yr and is somewhat smaller than the difference between emissions and the atmospheric growth. This implies that the land biosphere is responsible for taking up a large amount of carbon.

The airborne fraction exhibits considerable interannual variability. This may be caused by variations in the strength of land use emissions and variations in the global air-to-land and air-to-ocean net carbon fluxes. The air-to-biosphere net flux exhibits much larger interannual variability than the air-to-sea net flux. Usually more carbon is released during so called El Niño/Southern Oscillation (ENSO) events when human land use activities and dry climatic conditions cause large release of carbon by forest fires. An example is the Indonesian fires in 1998.

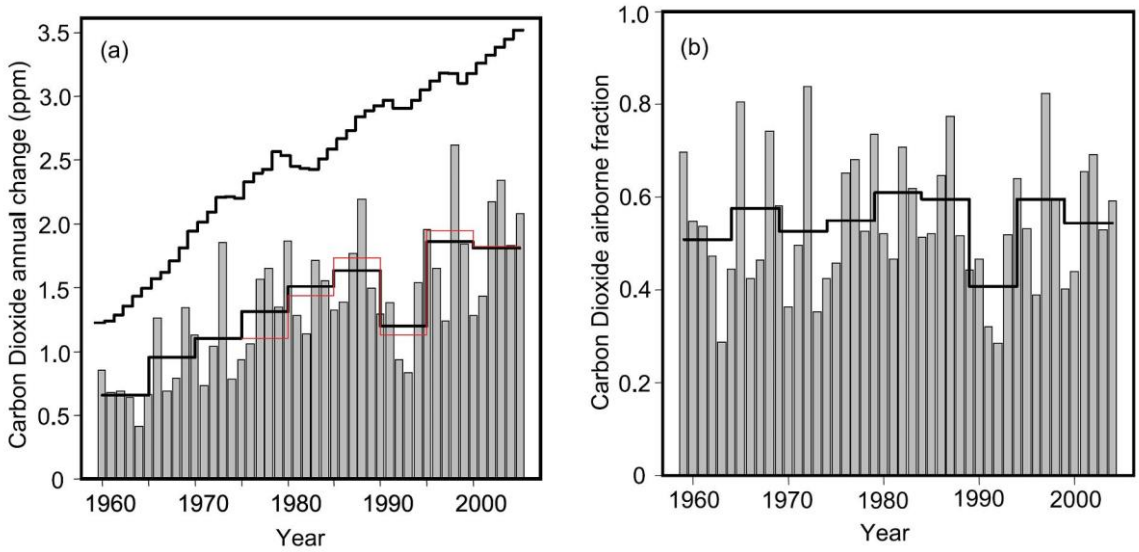

Figure 2.3: Comparison of annual fossil fuel emissions (black line) and annual (bar) and five-year mean changes in the atmospheric CO_2 inventory (left). Fraction of fossil emissions that remains in the atmosphere (right).

The carbon budget: Oceanic models are used to calculate the strength of the oceanic sink. The land sink is then calculated as a difference from the atmospheric balance equation. The equation is as follows:

$$\frac{dNa}{dt} = E - F_{a,oc;net} - F_{a,b;net} \qquad \text{Eq. 2.1}$$

Where, $F_{a,i;net}$ signifies the net carbon flux from the atmosphere into reservoir *i* and *Na* represents the atmospheric inventory. The total emissions, *E,* are equal to the sum of the change in the carbon inventory of the atmosphere, ocean and the land biosphere.

The net flux in the biosphere is the difference between the release of CO_2 due to deforestation and land use, F_{def}, and an implicit carbon sink, F_{sink}:

$$\frac{dNb}{dt} = F_{a,b;net} = F_{sink} - F_{def}. \qquad \text{Eq. 2.2}$$

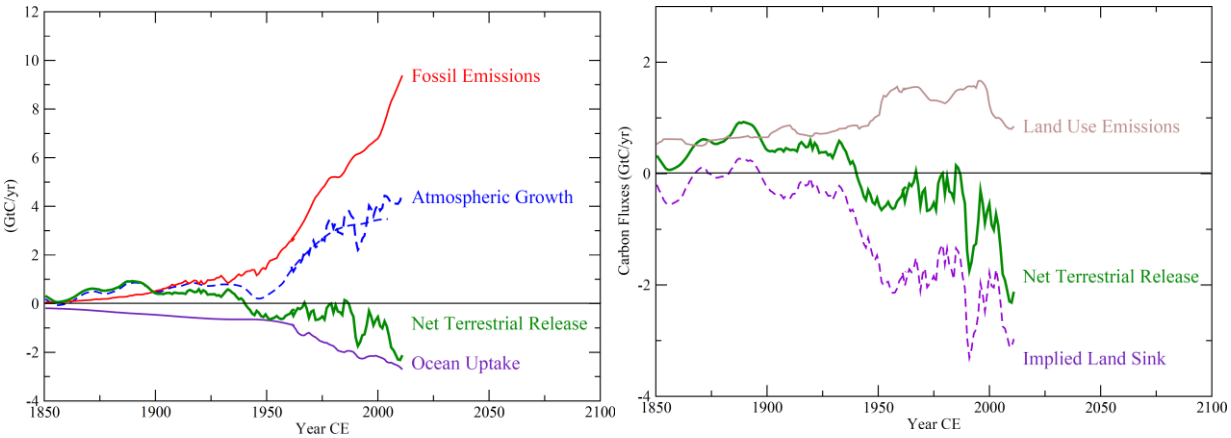

Figure 2.4: Anthropogenic fluxes between the various carbon reservoirs. Right panel shows the fossil fuel emissions deduced from the consumption and supply rate of oil, coal and gas, while the increase in the atmospheric C inventory is directly measured. The ocean fluxes are calculated with a model. The terrestrial release, $F_{a,b;net}$, is derived from the atmospheric balance equation. Left panel shows the difference between the release of CO_2 due to deforestation and land use change and the net flux into the biosphere, which implies a global terrestrial carbon sink (i.e. $F_{sink} > F_{def}$). The magnitudes of these sinks are poorly constrained since the land use changes are not well known. Possible causes of this implied sink are CO_2 fertilization of plants, anthropogenic nitrogen emissions, re-growth of forests in the northern hemisphere and climate change. Data represent 5-yr running means after 1961 and decadally smoothed values before.

The carbon and oxygen budget: The net fluxes in the ocean and the biosphere can also be estimated due to the decrease in atmospheric oxygen content and the rise in atmospheric CO_2. The burning of fossil fuels results in an increase in CO_2 and a decrease in O_2 in the atmosphere. The oceanic uptake of CO_2 does not result in any change in atmospheric oxygen content, while for every mol of carbon stored by the land biosphere, 1.1 mol of O_2 is released.

Atmospheric increase	4.0 ± 0.2 GtC/a
Fossil fuel emissions	7.8 ± 0.6 GtC/a
Net flux: Ocean-to-Atmosphere	-2.3 ± 0.7 GtC/a
Net flux: Land-to-Atmosphere	-1.5 ± 0.9 GtC/a
Components:	
Land use change & deforestation	1.1 ± 0.8 GtC/a
Implied terrestrial sink	-2.6 ± 1.2 GtC/a

Table 2.2: Balance of the anthropogenic CO_2 perturbation for the period 2000 to 2009 (IPCC WGI, 2013, Table 6.1).

Box 2.3

Is the increase in atmospheric carbon dioxide during the industrial period caused by human activities?

Yes, there are a number of observational constraints that clearly show that the recent CO_2 increase is man made:

- During each decade since 1900, CO_2 emitted by fossil fuel burning is larger than the atmospheric growth. Since the beginning of industrialization, emissions from land use activities and fossil emissions are larger than the atmospheric increase. The observed atmospheric CO_2 increase accounts only for 55% of the carbon released by human activities since 1959. The rest has been taken up by the ocean and the land biosphere.
- The ratio of heavy (^{13}C, ^{14}C) to light (^{12}C) isotopes has changed in a way that is only consistent with a fossil carbon source and a source from the land biosphere. ^{13}C is depleted in organic carbon as the light isotope ^{12}C is preferentially assimilated during photosynthesis. ^{14}C is not present in old, fossil carbon as the ^{14}C initially present is decayed with a half-life of 8200 years. Both, the $^{13}C/^{12}C$ and the $^{14}C/^{12}C$ ratio (before the atomic bomb tests in the 1950s and 1960s that produced ^{14}C) have decrease in the atmosphere mainly as a result of the release of isotopically light fossil carbon. A release of carbon from the ocean or from volcanoes, rocks and geothermal sources would have increased the $^{13}C/^{12}C$ isotopic ratio.
- The ratio of oxygen to nitrogen has declined as expected from oxidation of fossil or organic material.
- Measurements of the partial pressure of CO_2 in surface water and of carbon and other tracers within the ocean yield an uptake of carbon by the ocean (and not a release)
- The North-South inter-hemispheric gradient has increased in parallel with fossil emissions, as the fossil sources are mainly over land in the Northern Hemisphere.
- CO_2 concentration varied only within 20 ppm during the past ten thousand years before the onset of the industrialization and only within 10 ppm during the last millennium. This suggests that the carbon cycle was close to equilibrium before industrialization started.

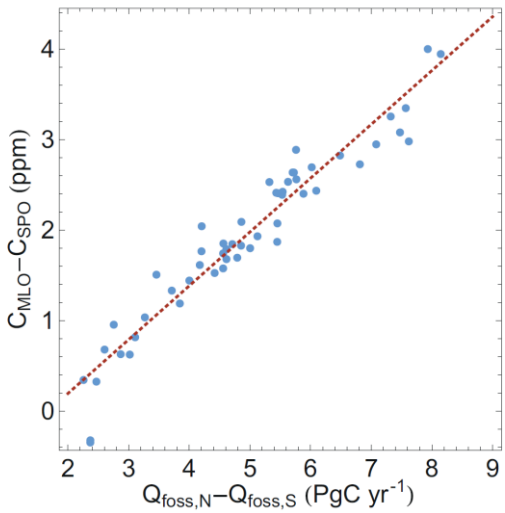

The North-South gradient in atmospheric CO_2 increases in parallel with fossil fuel emissions. Blue points: Annually averaged CO_2 concentration difference between the station Mauna Loa in the Northern Hemisphere and the station South Pole in the Southern Hemisphere (vertical axis; versus the difference in fossil fuel combustion CO2 emissions between the hemispheres. Dark red dashed line: regression line fitted to the data points. (IPCC, WGI, 2013, Figure 6.13)

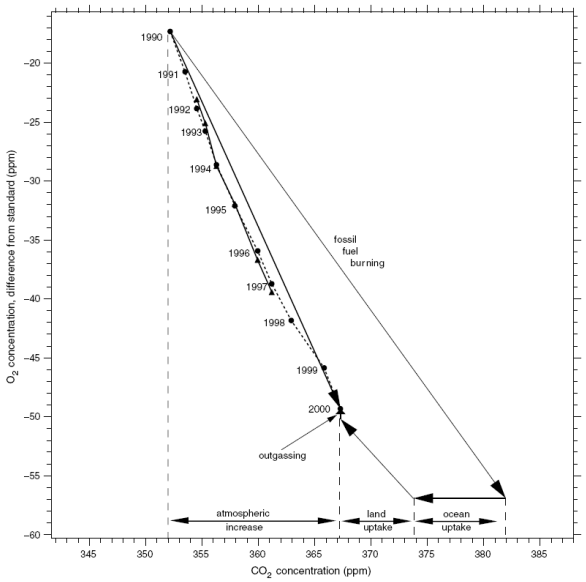

Figure 2.5: Determining the terrestrial and oceanic C sink. The figure shows the relationship between changes in atmospheric CO_2 (x-axis) and O_2 (y-axis). The points represent the measured atmospheric concentrations between 1990 and 2000 (annual value). The effect of fossil fuel burning is based on the relatively well known stoichiometric O_2:CO_2 ratios of coal, oil and gas. The uptake by the land biosphere and the ocean results from these known stoichiometric O_2:CO_2 ratios, which is represented by the slope of the arrows.

Box 2.4

O_2 and CO_2: Measuring changes in atmospheric O_2 is a formidable challenge as changes are small compared to the atmospheric O_2 content. The ratio O_2/N_2 is measured to achieve the required precision. Changes in the O_2/N_2 ratio are governed by changes in the O_2 concentration as the atmospheric N_2 concentration is almost constant. Usually, measurements are expressed relative to a standard in units of „per meg“:

$$\delta\left(\frac{O_2}{N_2}\right)=\left(\frac{(O_2/N_2)_{sample}}{(O_2/N_2)_{reference}}-1\right)\cdot 10^6 \quad \text{(per meg)}$$

4.8 per meg are equivalent to 1 ppm; the oxygen content of the air is 20.95 % and 1/20.95 = 4.8. We write a budget equation for atmospheric O_2 that corresponds to the budget equation for atmospheric CO_2. The following budget equation is approximately valid for *decadal* time scales:

$$\frac{dO_2}{dt}=-\alpha_f\cdot E+\alpha_b\cdot F_{a,b;net}$$

E und $F_{a,b;net}$ denote fossil emissions and the net carbon flux into the land biosphere. α_f and α_b are stoichiometric ratios that links O_2 consumption and CO_2 release from the processes of burning fossil fuel, photosynthesis and organic matter respiration on land. Possible net air-sea fluxes of oxygen in response to changes in ocean circulation, temperature and the marine biological carbon cycle are neglected in the above equation. Rearranging yields the net air-to-land biosphere flux:

$$F_{a,b;net}=\frac{1}{\alpha_b}\left(\frac{dO_2}{dt}+\alpha_f\cdot E\right)$$

The net air-to-sea flux can now be determined from the atmospheric CO_2 budget and we get:

$$F_{a,oc;net}=E-\frac{dNa}{dt}-F_{a,b;net}$$

Process (rough stoichiometric molecular formula)	Ratio of the O_2 and CO_2 fluxes
Photosynthesis and respiration on land $CO_2 + H_2O \leftrightarrow CH_2O + O_2$	$\alpha_b = 1.1$
Combustion of fossil fuels $CH_y + (1+y/4)\ O_2 \leftrightarrow y/2\ H_2O + CO_2$	$\alpha_f = 1.4$
Oceanic uptake of CO_2 $H_2O + CO_2 + CO_3^{--} \rightarrow 2\ HCO_3^-$	0
Oceanic photosynthesis and respiration $106\ CO_2 + 16\ NO_3^- + H_2PO_4^- + 17\ H^+ + 122\ H_2O$ $\leftrightarrow C_{106}\ H_{263}O_{110}N_{16}P + 138O_2$	

Table 2.3: Summary of important O_2 and CO_2-related processes. Marine organisms extract inorganic carbon and other nutrients (N, P, Fe) from the water and emit oxygen during photosynthesis. The classical Redfield ratios ($P:N:C:O_2=1:16:106:-138$) are used here. More recent analysis yield $P:N:C:O_2=1:16:117:-170$. The relative flux of CO_2 and O_2 between the ocean and the atmosphere depends on the carbonate chemistry and the rate of gas exchange and surface-to-deep transport and varies with time and space.

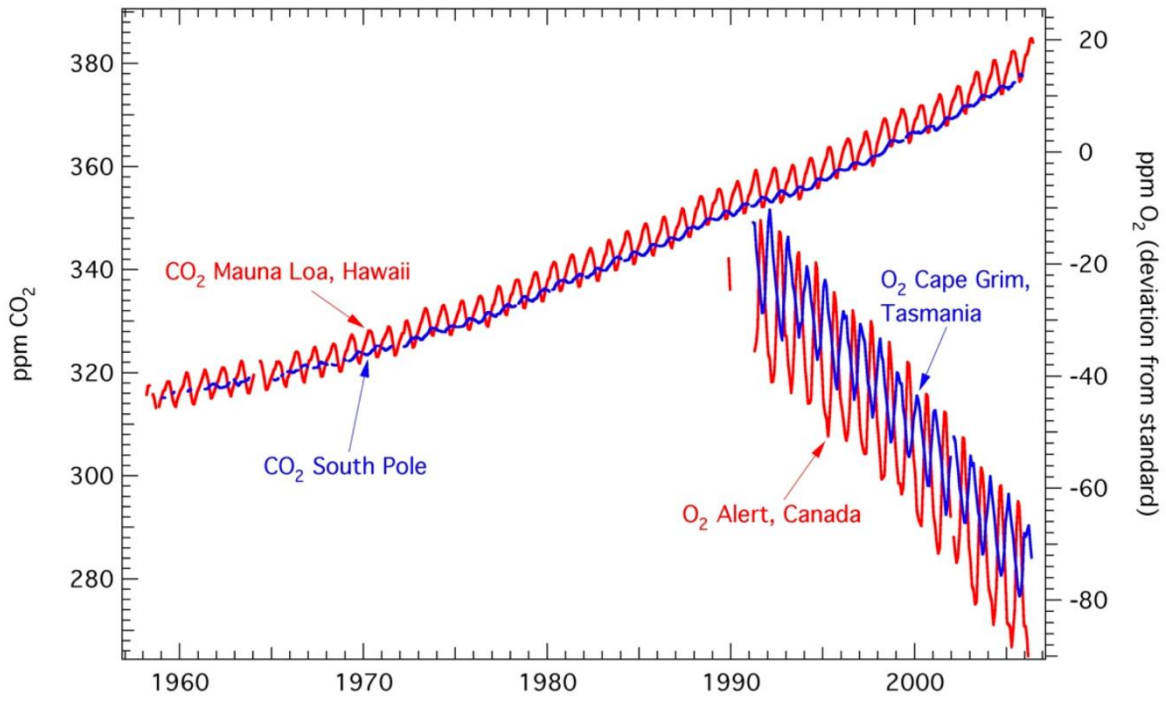

Figure 2.6: Increase in CO_2 and decrease in oxygen as measured on air samples.

Literature:

Reviews

Ciais, P., et al. (2013), Carbon and Other Biogeochemical Cycles, in *Climate Change 2013: The Physical Science Basis. Contribution of Working Group I to the Fifth Assessment Report of the Intergovernmental Panel on Climate Change*, edited by T. F. Stocker, D. Qin, G.-K. Plattner, M. Tignor, S. K. Allen, J. Boschung, A. Nauels, Y. Xia, V. Bex and P. M. Midgley, pp. 465-570, Cambridge University Press, Cambridge, United Kingdom and New York, NY, USA. http://www.ipcc.ch/report/ar5/wg1/

Denman, K.L., et al. (2007), Coupling between changes in the climate system and biogeochemistry, in Climate Change 2007: The Physical Science Basis. Contribution of Working Group I to the Fourth Assessment Report of the Intergovernmental Panel on Climate Change, edited by S. Solomon, et al., pp. 499-587, Cambridge University Press, Cambridge United Kingdom and New York, NY, USA.

Prentice, I. C., G. D. Farquhar, M. J. Fasham, M. I. Goulden, M. Heimann, V. J. Jaramillo, H. S. Kheshgi, C. LeQuéré, R. J. Scholes, and D. W. R. Wallace. 2001. The carbon cycle and atmospheric CO_2. Pp. 183–237 in Climate change 2001: The scientific basis (Contribution of Working Group I to the third assessment report of the Intergovernmental Panel on Climate Change), edited by J. T. Houghton, Y. Ding, D. Griggs, M. Noguer, P. van der Linden, X. Dai, K. Maskell, and C. A. Johnson. Cambridge: Cambridge University Press. http://www.proclim.ch/IPCC2001.html; http://www.ipcc.ch

Siegenthaler U. and Sarmiento J.L. Nature, 365, 119-125, 1993.

Tarnocai, C., et al. (2009), Soil organic carbon pools in the northern circumpolar permafrost region, Global Biogeochem. Cycles, 23, 1-11.

Other (Oxygen)

Keeling R. F., S. C. Piper and M. Heimann. Global and hemispheric CO_2 sinks deduced from changes in atmospheric O_2 concentration. Nature, 381, 218-221, 1996.

Plattner, G.-K., F. Joos, and T. F. Stocker. 2002. Revision of the global carbon budget due to changing air-sea oxygen fluxes. *Global Biogeochemical Cycles* 16:1096, doi:10.1029/2001GB001746.

3 The terrestrial biosphere

The terrestrial biosphere interacts with the physical climate system on different time scales and exchanges various important quantities with the atmosphere. Some important properties are:

- The **amount of carbon** stored in the land biosphere is ~5 times larger than the modern atmospheric C-Inventory and about 10 times smaller than the oceanic C-Inventory. Changes in the terrestrial carbon storage directly and quickly affect the atmospheric **CO_2** concentration. However, on time scales of hundred years, the majority of such a disturbance is absorbed by the ocean.
- The land biosphere regulates the evaporation of **H_2O**. Hence, it affects the energy balance of the earth surface, precipitation and runoff significantly.
- Emissions of methane (CH_4) and nitrous oxide (N_2O), volatile organic carbon (VOC) and aerosols affect the atmospheric concentrations of **greenhouse gases** and atmospheric **chemistry**.
- The surface property determines the flux of **momentum** (through friction between plants and air), as well as the **albedo** and thus the radiation balance.

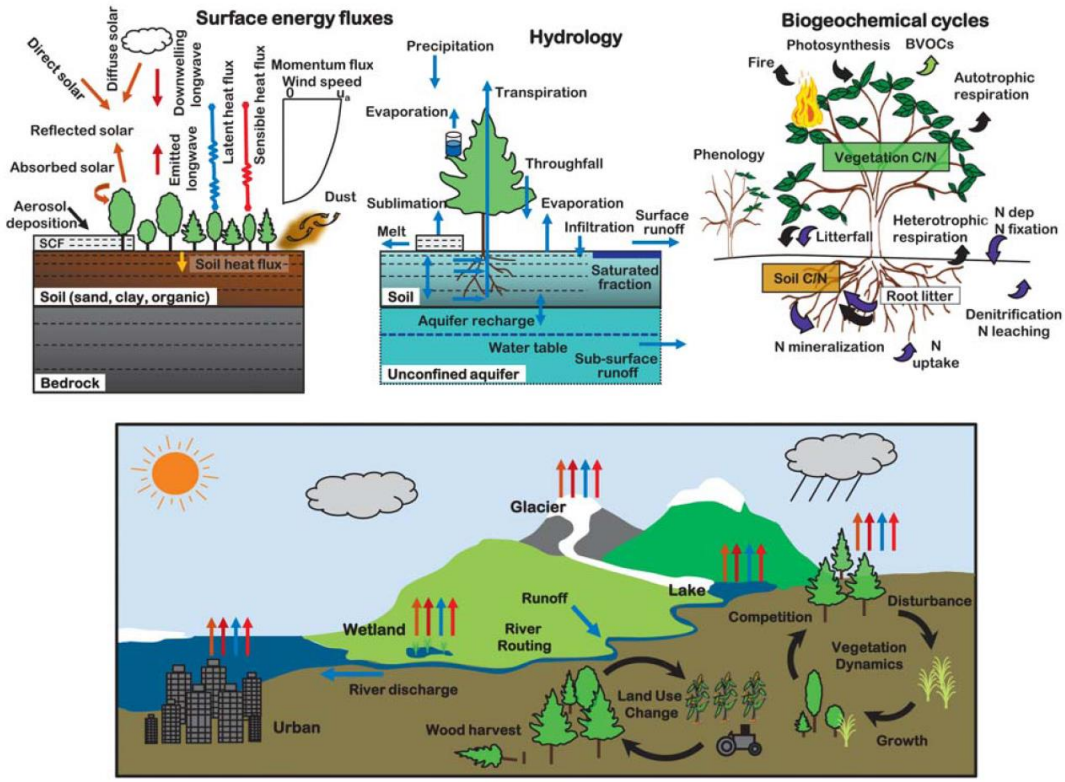

Figure 3.1 Schematic diagram of terrestrial processes represented in the National Centre for Atmospheric Research Community Land Model (CLM4). (Source: G. B. Bonan, iLEAPS Newsletter, No 10, Nov.2010).

The interaction between the atmosphere and the biosphere can roughly be split into three domains. On the **biophysical** level, the vegetation affects the surface heat balance, the albedo and the roughness (friction) and hence the transfer of momentum from the atmosphere to the ground. The plant actively regulates its stomatal conductance; thereby it controls the evaporation of water, and in turn influences the surface heat balance. On the **biogeochemical** level, it regulates the distribution of carbon and nutrients in the living vegetation, the litter layer and in the soil. The composition and structure of plant communities is described by the **terrestrial ecology**. The large range of relevant time scales is characteristic for a model that incorporates all three aforementioned levels: from milliseconds for photosynthesis to millennia for the residence time of inert soil carbon and pedogenesis. The genetic evolution of plants takes place on an even larger time scale.

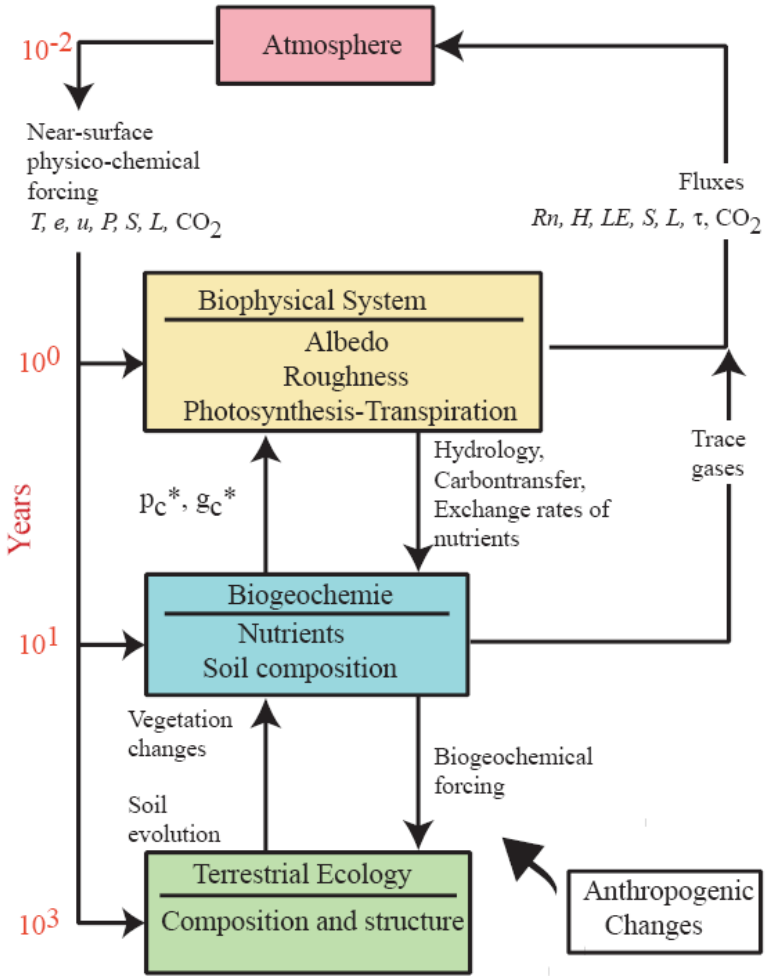

Figure 3.2: Decomposition of a biosphere-atmosphere model into three main domains that are roughly separated by their different time scales of exchange processes (given in years, left axis): biophysical model, biogeochemical model and terrestrial ecosystem model. The near-surface physical-chemical part is controlled by the air temperature (T), the partial pressure of water vapour in the air (e), precipitation (P), short- (S↓) and long-wave radiation (L↓) and the CO_2 mixing ratio. The photosynthetic capacity, p_c*, and the maximum stomatal conductance, g_c*, regulate the photosynthesis-transpiration system and hence the fluxes of water and CO_2. Important for the energy balance at the earth surface is the long-wave outgoing radiation, Rn, the fluxes of sensible heat, H, and latent heat, LE, as well as solar, S, and long-wave incident radiation, L. Interactions of wind and vegetation leads to a drag, , τ, onto the atmosphere that is proportional to the wind speed at the ground.

3.1 Vegetation zones

Biome classification: Structurally and functionally different ecosystems evolve under different climatic conditions. They are referred to as biomes. Different biome classifications are described in the literature, most of which distinguish 15 – 20 biome types. They agree about the nature and extent of easily identifiable biomes such as the tundra, deserts, broad- and needle-leafed forests or tropical moist forests. Differences in the characteristics of the biomes account for a majority of the spatial variation in carbon storage density. Table 3.1 illustrates the gradient of the carbon density from tropical to boreal forests and the differences between the carbon density of open shrub and grasslands and forests.

Biome types	area (10^{12} m^2)	Carbon density in the vegetation (kg m^{-2})	Carbon density in the soil (kg m^{-2})
Tropical moist forest	13.5	20.0	11.7
Tropical seasonal forest	8.3	16.0	11.7
Temperate evergreen forests	5.5	16.0	13.4
Temperate deciduous forests	6.1	13.5	13.4
Boreal forests	11.8	9.0	20.6
Tropical forest and shrub land	9.5	2.7	6.9
Temperate forest and shrub land	7.5	2.7	6.9
Tropical grasslands	14.3	1.8	4.2
Temperate Grassland	20.5	0.7	18.9
Tundra and alpine meadows	7.1	0.3	20.4.
Deserts	21.5	0.3	5.8
Cultivated land	2.7	0.5	6.0
Pastures	5.3	0.7	18.9
Total	133.4		

Table 3.1: Carbon density for year 1760 AD for different biome types, sorted by the carbon density in the vegetation (Emanuel et al, in Heimann M., NATO ASI Serie, 1991). The numbers are uncertain, as the classification is not always concise and the carbon density varies on small spatial scales.

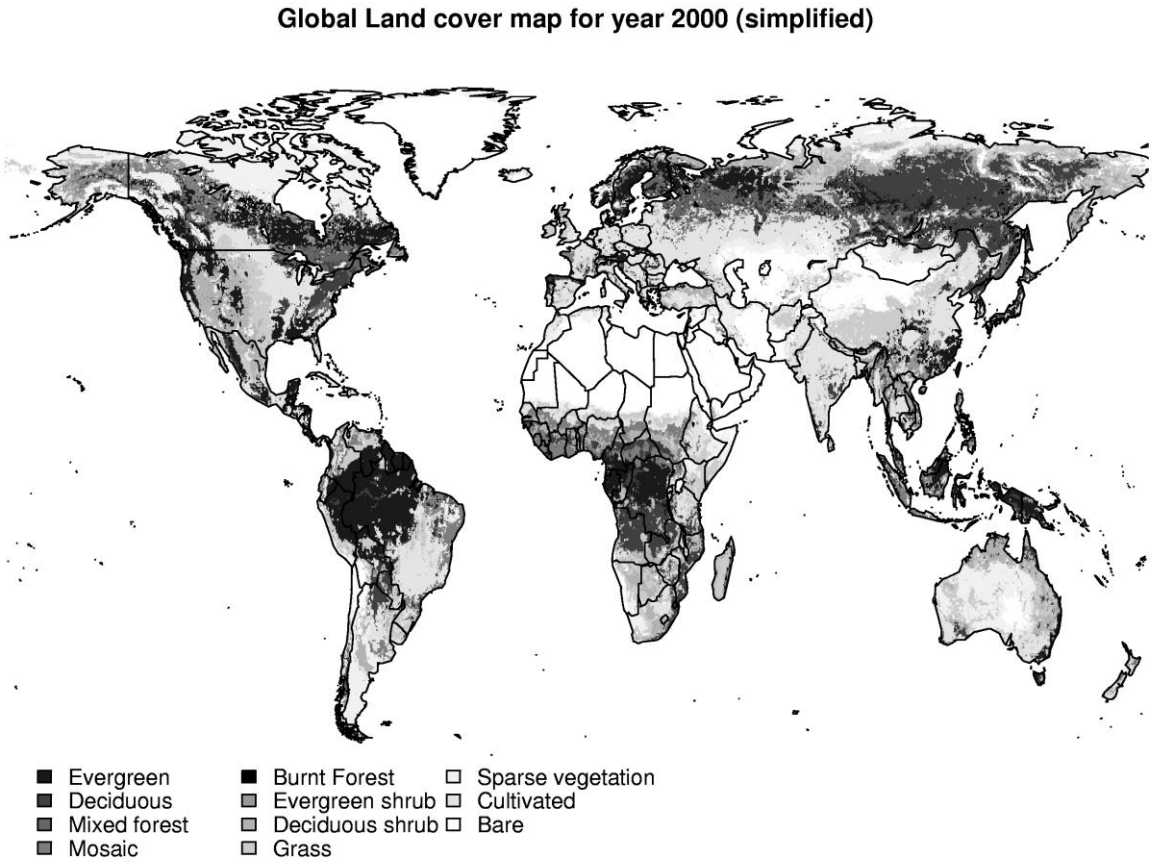

Figure 3.3: Distribution of the vegetation in year 2000 AD based on remote sensing and evaluated by the EU Joint Scientific Research Centre, ISPRA. Different regions were classified by local experts (30 teams in total). Each team used the VEGA2000 dataset which contained a daily global image of the vegetation sensor on board the SPOT 4 satellite. An interactive map can be found under:

http://www-gem.jrc.it/glc2000/interactive/glc2000_vgt.html

Area (10^{12} m^2)	Category
11.38	Tree Cover broadleaved evergreen
5.06	Tree Cover broadleaved deciduous closed
3.77	Tree Cover broadleaved deciduous open
9.00	Tree Cover needle-leaved evergreen
4.64	Tree Cover needle-leaved deciduous
4.08	Tree Cover mixed leaf type
0.58	Tree Cover regularly flooded fresh water
0.11	Tree Cover regularly flooded saline water
2.72	Mosaic: Tree Cover / Other natural vegetation
0.36	Tree Cover burnt
2.26	Shrub Cover closed-open evergreen
12.15	Shrub Cover closed-open deciduous
14.19	Herbaceous Cover closed-open
14.64	Sparse herbaceous or sparse shrub cover
1.23	Regularly flooded shrub and/or herbaceous cover
19.79	Cultivated and managed areas
2.54	Mosaic: Cropland / Tree Cover / Other natural vegegetation
1.67	Mosaic: Cropland / Shrub and/or grass cover
19.92	Bare Areas
15.10	Snow and Ice
0.05	Artificial surfaces and associated areas
0.01	No data
145.25	Total

Table 3.2: Land classification of the EU Joint Scientific Centre.

Outdated empirical relation between climate and vegetation: The relation between vegetation cover and climate has long been attracting the interest of climatologists and plant ecologists. Köppen (1936) developed a vegetation-based climatology. Climate categories are assigned to vegetation zones. The classification of climate zones is done according to the mean monthly temperature of the warmest ($T_{m,w}$) and the coldest ($T_{m,k}$) month and on the annual, r, and monthly sum of precipitation (P_m). Köppen distinguished for example between tropical rain climates ($T_{m,w} > 18^oC$) or boreal snow-forest climates ($T_{m,k} < -3^oC$ and $T_{m,w} > 10^oC$). As the classification of Köppen accounts for basic meteorological quantities, his vegetation-based classification allows a climatic classification of regions that lack measurements.

In the Anglo-Saxon region, an accordingly popular classification of climate and vegetation is the Holdrige life zone scheme. It is represented by a triangular diagram that corresponds to a linear projection of a two-dimensional climate space. The climate variables consist of the so-called annual "bio-temperature" and the mean annual precipitation. The so-called "potential evapotranspiration ratio" (PET ratio) is often used as the third axis. It corresponds to the difference of the two other variables. The "bio-temperature" is the normalized sum of the daily mean temperatures above 0^oC for one year:

$$T_{Bio} = \frac{\int dt \ \max(T, 0^{o}C)}{\int dt}$$

The triangular diagram consists of hexagonal cells to which names, such as ‘steppe’ or ‘rain forest’, are assigned.

The approaches of Köppen and Holdige are problematic and lack a sound scientific basis. For example, the chosen climate variables do not directly affect the vegetation, the zones are delimited by clear borders, seasonality is not accounted for and the classification relies on modern conditions. Changes in the interactions between climate and vegetation are only indirectly taken into account.

Modeling of biomes with „Plant Functional Types“: For the modeling of biomes it is important that the basic unit of a vegetation model is not the biome, but the plant. Biomes represent the coexistence of plants and the distribution of biomes must result from the distribution of plants. Important reasons exist for plants to be regarded as the basic unit of biome modeling. Crucial information about the mechanisms that lead to the biome distribution is taken from physiological work with different plant types. This data can be used to explicitly describe plants. Paleo-ecological analyses show that plant types respond to climate change individually. This means that a biome does not represent a fixed composition but rather that the composition varies with time and environmental conditions.

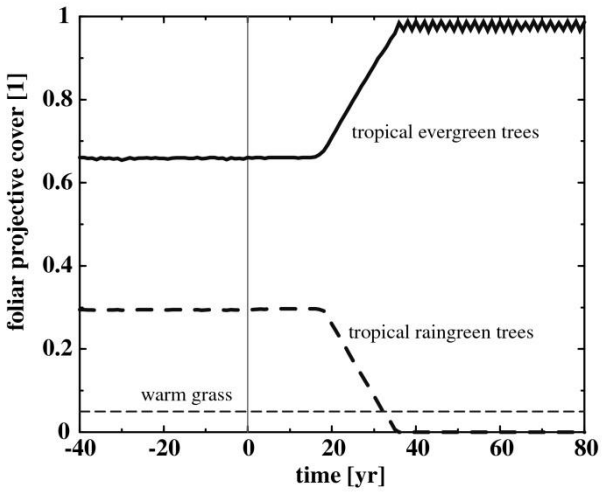

Figure 3.4: Changes in the simulated vegetation cover for a grid cell in the tropical rain forest (Lund-Potsdam-Jena DGVM). The vegetation cover is given for each PFT as a fraction of the grid area. Under pre-industrial atmospheric CO2 concentrations almost 70% of the area is covered by tropical evergreen trees and some 30% by tropical deciduous trees, while simulated grass cover is small. Evergreen forests require fewer resources to build up leaf mass, but suffer more under water stress during seasonal drought than deciduous trees. The atmospheric CO_2 concentration is abruptly increased to 500 ppm. The water-use efficiency increases under increased atmospheric CO_2 and hence evergreen trees gain an advantage over raingreen trees.

Biome models were developed in the 90’s based on this principle. Typical input quantities for such a model are fields of precipitation, temperature and cloud cover, as well as a map for the soil conditions. For practical reasons, models do not simulate single plant species but a

limited number of so-called *plant functional types* (PFTs). Prentice and colleagues developed a model in 1992 that simulates the distribution of 13 PFTs using threshold values for five bioclimatic indices: mean temperature of the coldest month (Tc), mean temperature of the warmest month (Tw), a moisture index, Growing Degree Days (GDD) relative to 0^{o}C and 5^{o}C. A plant type only occurs within its bioclimatic limits.

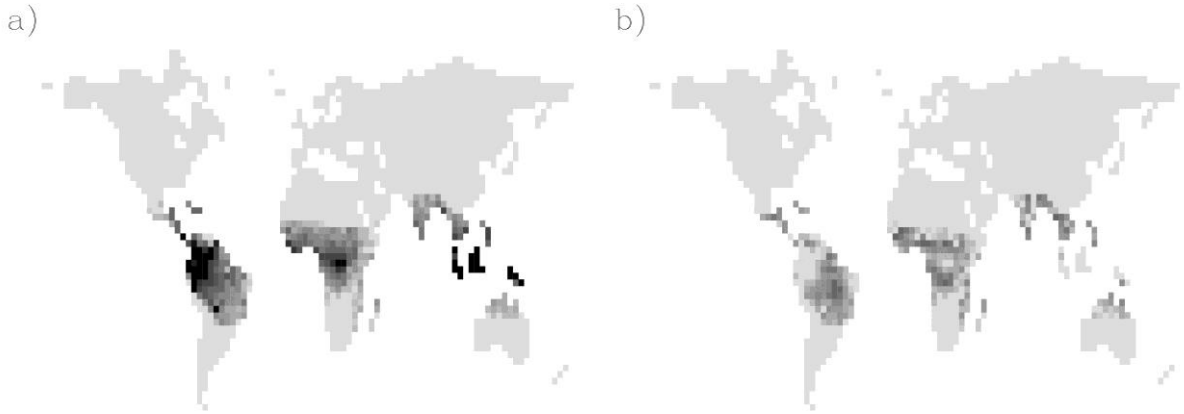

Figure 3.5: Plant cover in grid area fraction as simulated by the Lund-Potsdam-Jena DGVM for tropical broad-leaved trees. Evergreen trees (a) are in competition with deciduous trees (b).

Dynamic Global Vegetation Models (DGVMs), such as the Lund-Potsdam-Jena model, still contain such bioclimatic limits to describe the potential occurrence of PFTs. A crucial additional aspect is that different PFTs compete for resources such as nutrients or light. Decisive for its occurrence is thus not whether a PFT is located inside its bioclimatic limits, but whether it has a competitive advantage over other PFTs. In such models, physiological and phenotypical parameters are crucial for competitiveness. The optimal temperature for photosynthesis, and thus, for assimilation of carbon under different climatic conditions, is different for individual plant species. The root fraction at different depths, hence, the access to water varies between PFTs. Dominance supports the access to light (trees better than grass). Longevity of leafs and needles is crucial for the effort required to build up biomass (evergreen vs. deciduous plants).

Fluxes and inventories of carbon in PFTs and in the soil, as well as evaporation and soil water content are explicitly simulated in DGVMs. They aim at integrating the three levels: terrestrial ecology and biome dynamics, biochemistry (carbon pools and fluxes) and the physical interactions with the climate system, that are depicted schematically in **Figure 3.2**.

3.2 Fluxes and Inventories of carbon in the land biosphere

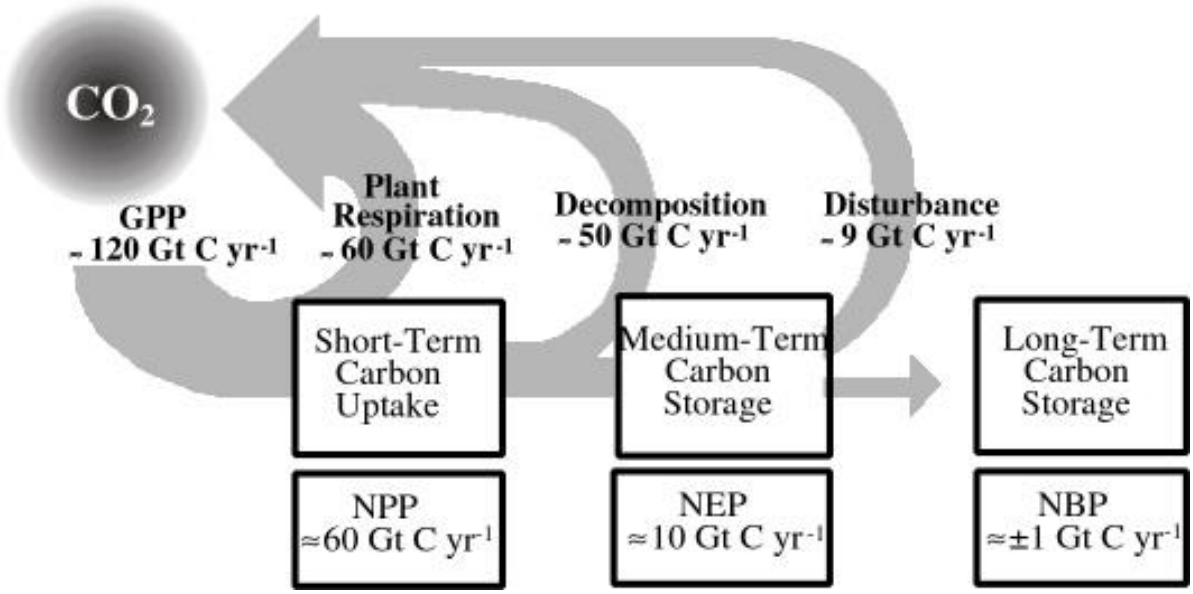

Figure 3.6: Global fluxes and reservoirs of carbon in the land biosphere.

The following carbon fluxes occur in an ecosystem:

- **Gross Primary Production, GPP:** Photosynthetically assimilated carbon
- **Autotrophic Respiration, AR (plant respiration):** Release of CO_2 by living plants (maintenance respiration, construction respiration; root respiration)
- **Net Primary Production, NPP:** NPP= GPP – AR; Carbon storage in living plants
- **Heterotrophic Respiration, HR:** Microbial decomposition of dead organic material.
- **Net Ecosystem Production (NEP):** NEP= NPP-HR; Carbon storage or -release of an "undisturbed" ecosystem. NEP can be derived from the measurements of CO_2 exchange fluxes with the atmosphere.
- **Disturbance, D:** Release of carbon due to fire, insect attack, herbivores, etc...
- **Net Biome Production, NBP:** NBP= NEP-D; annual carbon storage averaged over a large region.

On decadal time scales, the GPP is roughly compensated by the loss due to autotrophic and heterotrophic respiration and the fluxes resulting from disturbances. For this reason, at preindustrial times, the net flux of CO_2 between the atmosphere and the biosphere was near to zero and the atmospheric CO_2 concentration was almost constant. The net primary production of about 60 GtC/a is used for the buildup of leaf wood and root mass. The majority of assimilated carbon enters the litter pool after some time, where organic carbon is microbially mineralized to CO_2 or becomes soil organic carbon. The microbial decomposition of soil organic carbon also causes release of CO_2 to the atmosphere. A fraction of carbon stored in vegetation (and also in the soil) is directly or indirectly (release of CO and VOC) transformed to CO_2 or to coal by fires. A small fraction of organic carbon is washed into the ocean by rivers.
In models it is usually sufficient to simulate the most important fluxes and their disturbances. The formulation of a carbon balance of a system by measurements, however, also requires

accounting for small fluxes in order to capture the relatively small variations in NBP. For example, the export of C by rivers or the loss due to harvesting may play a crucial role for the computation of an ecosystem's NBP from observations.

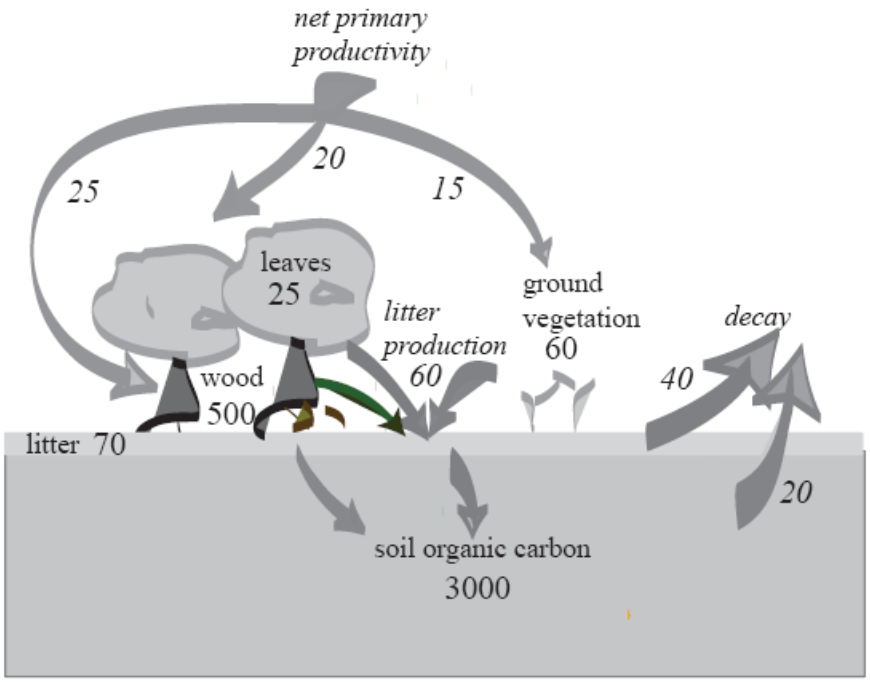

Figure 3.7: Terrestrial component of the global carbon cycle. The scheme illustrates the importance of organic carbon. Carbon inventories are given in GtC and fluxes (slanted) in GtC/a. Fire and other disturbance fluxes are neglected in this simplified scheme.

The amount of organic carbon in soils, litter and living vegetation is estimated at around 2500-3800 GtC. Less than a fifth of the terrestrial organic carbon is stored in living vegetation (incl. roots). Wood makes up 500 GtC, while leaves and ground vegetation account for some 100 GtC. The majority (2000-3000 GtC) of biospheric carbon mass consists of soil carbon. Litter (or detritus) is rapidly decomposed and contains only about 70 GtC.

As a comparison of Table 3.3 and Table 3.4 shows, estimates for the carbon storage in different biome types are uncertain. About half of the carbon stored in the vegetation is located in tropical forests, while the carbon content of vegetation in the savannahs, grasslands, deserts, agricultural lands and wetlands is small. In terms of the total amount of carbon, tropical forests play an important, but no longer a dominant role. Due to the slow decomposition rates in the soils of the mid and high latitudes, the total amount of carbon stored there is comparable to the amount in tropical rain forests. The carbon storage in temperate grasslands is comparable to the storage in temperate forests. In wetlands, the amount of soil carbon exceeds the soil carbon content in the living vegetation by a factor of more than 10.

Biomes	Area (10^6 km^2)	Carbon storage (GtC) Vegetation	Soils	Total
Tropical forests	17.6	212	216	428
Temperate forests	10.4	59	100	159
Boreal forests	13.7	88	471	559
Tropical savannah	22.5	66	264	330
Temperate grasslands	12.5	9	295	304
Deserts and semi-deserts	45.5	8	191	199
Tundra	9.5	6	121	127
Wetlands	3.5	15	225	240
Arable land	16.0	3	128	131
Total	*151.2*	*466*	*2011*	*2477*

Table 3.3: Amount of carbon stored in vegetation and in the upper meter of soils for present time. After IPCC Special Report on Land Use, Land Use Change, and Forestry, Cambridge University Press, 2000.

A recent estimate quantifies the carbon stored in the northern permafrost region to about 1700 GtC (Tarnocai et al., GBC, 2009). This corresponds to roughly 50% of the estimated global belowground organic carbon pool.

The area of all soils in the northern permafrost region is approximately 18,782 10^3 km^2, or approximately 16% of the global soil area. In the northern permafrost region, organic soils (peat-lands) and cryoturbated permafrost-affected mineral soils have the highest mean soil organic carbon contents (30 – 70 kg m^{-2}). Carbon pools are estimated to be 190 GtC for the 0–30 cm depth, 500 GtC for the 0–100 cm depth, and 1000 GtC for the 0–300 cm depth. Carbon pools in layers deeper than 300 cm were estimated to be 400 GtC in yedoma deposits and 240 GtC in deltaic deposits. In total, the northern permafrost region contains approximately 1700 GtC of organic carbon, of which approximately 88% occurs in perennially frozen soils and deposits.

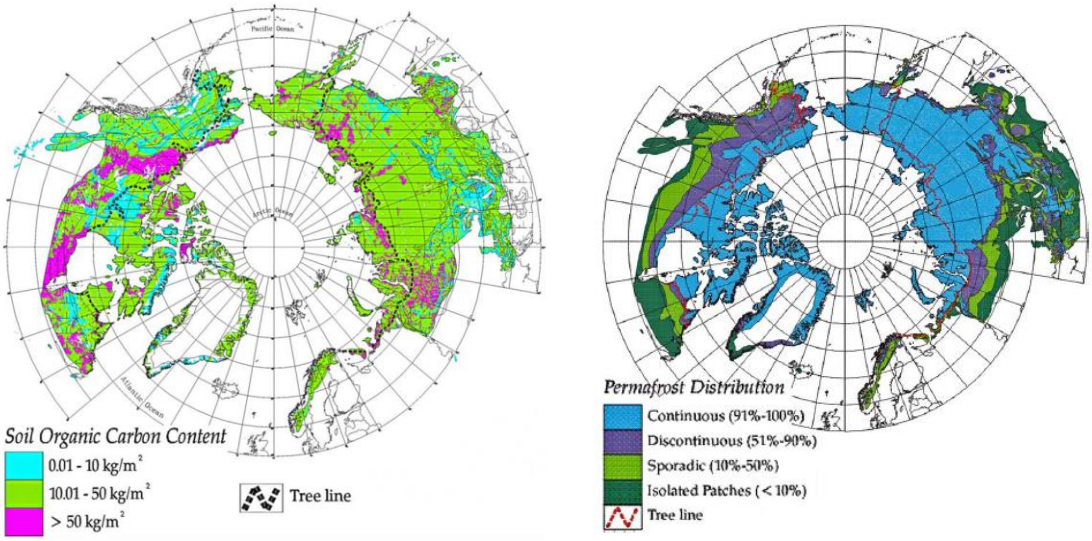

Figure 3.8: Soil organic carbon content and permafrost distribution after Tarnocai, GBC, 2009.

Estimates for the net primary production are considerably uncertain. Tropical and subtropical areas have the highest NPP, as shown in Table 3.4.

Biomes	Area (10^6 km^2)	Carbon storage (GtC) Vegetation	Soil	NPP (GtC a^{-1})
Tropical forests	17.5	340	692	20.1
Temperate forests	10.4	139	262	7.4
Boreal forests	13.7	57	150	2.4
Arctic tundra	5.6	2	144	0.5
Mediterranean Bushland	2.8	17	124	1.3
Arable land	13.5	4	248	3.8
Tropical savannahs	27.6	79	345	13.7
Temperate grasslands	15	6	172	5.1
Deserts	27.7	10	208	3.2
Total	*149.3*	*652*	*2,344*	*57.5*
Wetlands			450	
Frozen soils	25.5		400	
Grand total	*174.8*	*652*	*3,194*	*575*

Table 3.4: Amount of carbon stored in vegetation and soils of up to a depth of 3 meters and net primary productivity, at present. After Sabine et al., In The global carbon cycle. C.B. Field, M.R.Raupach (Eds), 2004.

3.2.1 A simple model for the description of the carbon content in vegetation and soil

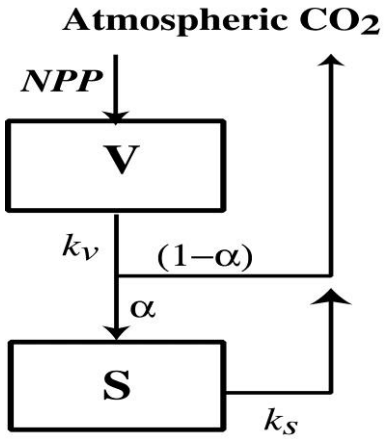

Figure 3.9: A 2-box model for the carbon storage in the land biosphere.

Let us consider the biosphere as a reservoir of two well-mixed boxes, representing the organic carbon content in the vegetation, V, and in the soil, S. The assimilation flux of C (NPP) enters the vegetation pool. The decay of C from the vegetation (leaf-shedding, branch-fall, death, fire, etc…) and from the soil pool is assumed to be proportional to the size of the respective carbon pool. A fraction, α, of the carbon flux from the vegetation enters the soil pool, while a fraction (1-α) is directly oxidized to CO_2 and is released to the atmosphere. The following three differential equations describe the change of the C-pool in the vegetation *(V)*, the soil *(S)* and the atmosphere-ocean system *(A)*:

$$\frac{dV}{dt} = NPP - k_V \cdot V = NPP - \frac{1}{\tau_V} \cdot V \qquad \text{Eq. 3.1}$$

$$\frac{dS}{dt} = \alpha \cdot k_V \cdot V - k_S \cdot S = \alpha \cdot \frac{1}{\tau_V} \cdot V - \frac{1}{\tau_S} \cdot S \qquad \text{Eq. 3.2}$$

$$\frac{dA}{dt} = -NPP + (1-\alpha) \cdot \frac{1}{\tau_V} \cdot V + \frac{1}{\tau_S} \cdot S \qquad \text{Eq. 3.3}$$

In the equations above, the decay rate, *k*, is replaced by the inverse of the mean residence time, τ:

$$k_i = \frac{1}{\tau_i} \qquad \text{Eq. 3.4}$$

.

When the above equations are solved at steady state (d/dt=0), we get the following solutions for the carbon pools of vegetation and soil:

$$V(t=\infty) = NPP \cdot \tau_V \qquad \text{Eq. 3.5}$$

$$S(t=\infty) = \alpha \cdot NPP \cdot \tau_S \qquad \text{Eq. 3.6}$$

These two solutions illustrate an important principle: The size of a certain carbon pool in steady state corresponds to the product of input and mean residence time:

mass = (input) x (mean residence time)

The global amount of carbon stored in soils is significantly larger than the amount of C in the vegetation, because $\alpha\tau_S >> \tau_V$. The smaller flux of C into the organic soil carbon pool is over compensated by the slower decay and the resulting longer residence time. For a mean residence time of carbon in the vegetation of τ_V=10 years and an NPP of 1 kg C m^{-2} a^{-1} we get a carbon storage of 10 kg C m^{-2} in the vegetation. For soils with a mean residence time of τ_S=100 years and α=0.3, the pool amounts to 30 kg C m^{-2}.

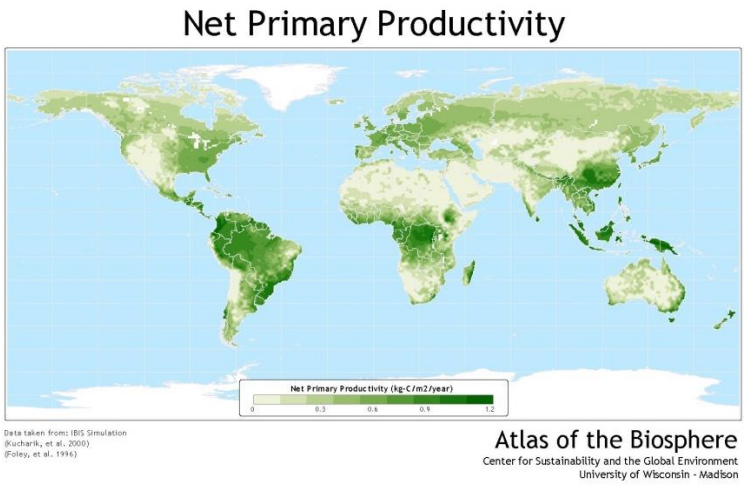

Figure 3.10: Geographical distribution of the net primary production (http://www.sage.wisc.edu/atlas/maps.php)

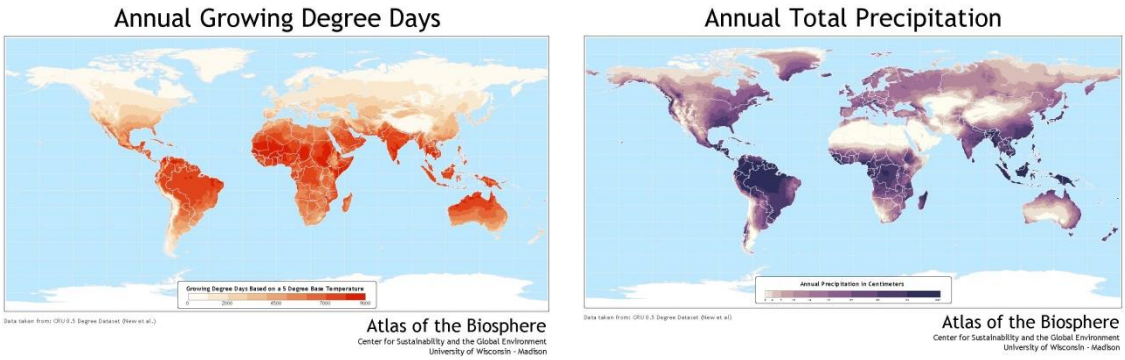

Figure 3.11: Geographical distribution of growing degree days (with respect to 5°C) and of annual precipitation (http://www.sage.wisc.edu/atlas/maps.php)

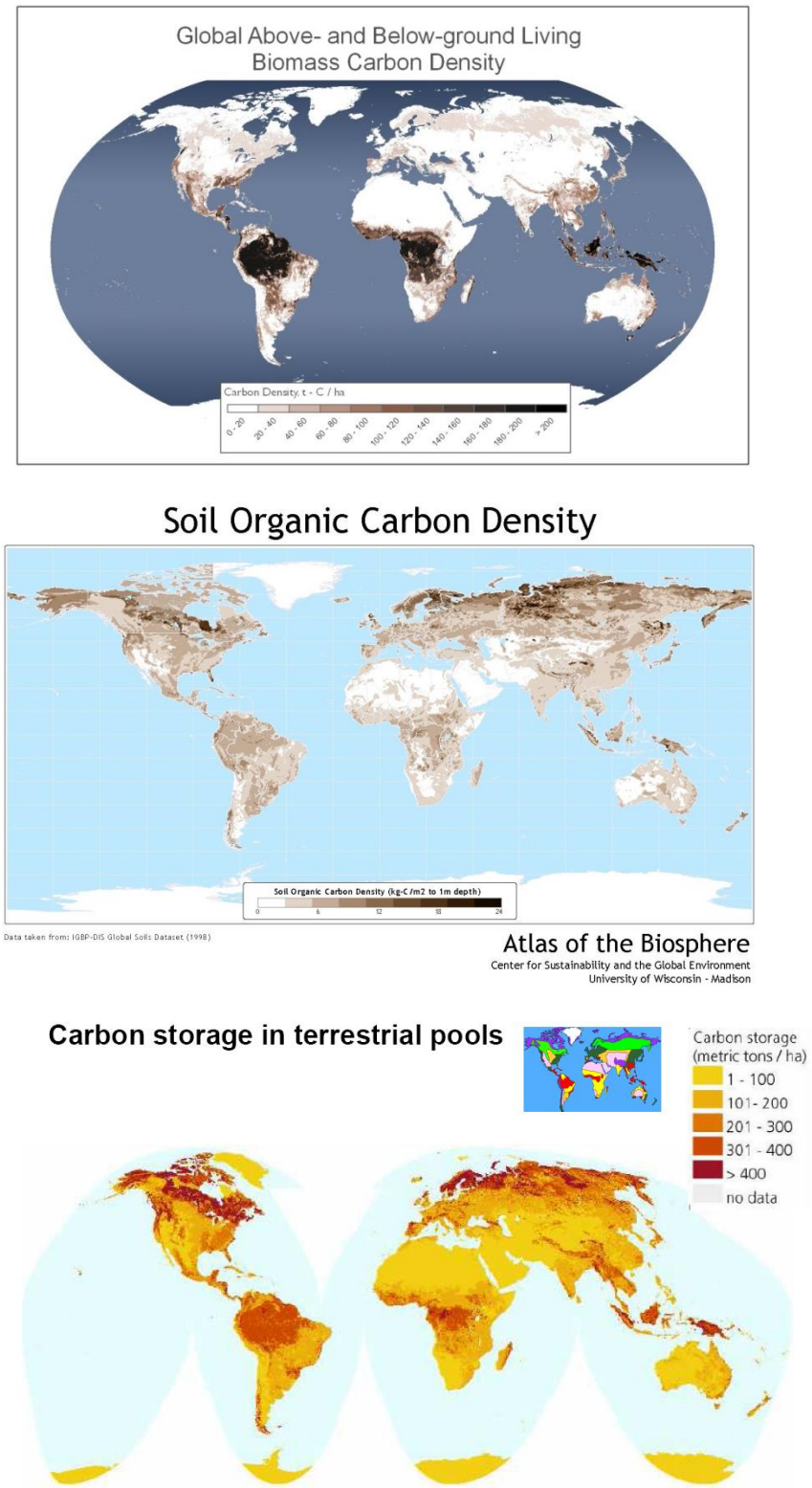

Figure 3.12: (top) Organic carbon in living vegetation (source: http://cdiac.ornl.gov/epubs/ndp/global_carbon/carbon_documentation.html#datafiles) , (middle) in soils (source: http://www.sage.wisc.edu/atlas/maps.php) and (bottom) in vegetation and soils (source: http://soils.usda.gov/use/worldsoils/mapindex/)

3.3 Biospheric processes

3.3.1 Photosynthesis

Photosynthesis is the conversion of light energy into chemical energy by living organisms. The raw materials are carbon, nitrogen, sulfur and other substances found in organic plant material. Approximately 50% of the solar radiation is available for photosynthesis (PAR: Photosynthetic Active Radiation).

There are two photosynthetic pathways: C_3 and C_4. The majority of land plants and all marine phytoplankton use the C_3 pathway. The following equation is a simplification of the photosynthesis reaction:

$$CO_2 + H_2O + hf \longrightarrow CH_2O + O_2 \qquad \text{Eq. 3.7}$$

Photosynthesis is very strongly influenced by the nourishment level of the plant, age of the leaves, physiology and under which light and temperature conditions that plant grows.

For example, the photosynthesis rate per leaf surface area is higher in plants that grew under strong light conditions compared to those that grew under weak conditions.

3.3.2 Respiration

Respiration is the decomposition of organic material. The simplified equation is:

$$CH_2O + O_2 \longrightarrow CO_2 + H_2O \qquad \text{Eq. 3.8}$$

Respiration is carried out by plants and soil. Approximately 50% of the assimilated C is returned to the atmosphere during plant respiration within hours to days (autotrophic respiration). Respiration in soil is carried out by roots (a part of autotrophic respiration) and the microbial decomposition of dead organic material (heterotrophic respiration). Soil respiration leads to very high CO_2 concentrations in subsurface air (1-2 orders of magnitude larger than in the atmosphere).

3.3.3 Regulation of photosynthesis and autotrophic respiration on the plant/leaf level

The net primary production (NPP, assimilation – respiration) is an important factor for the large scale characterization of the biosphere. With respect to the plant, photosynthesis and respiration are controlled by a number of factors (temperature, light, water, nutrients, CO_2, pollutants, etc). Gas (and water) exchange occurs through stomata, tiny pores found on the down side of a leaf.

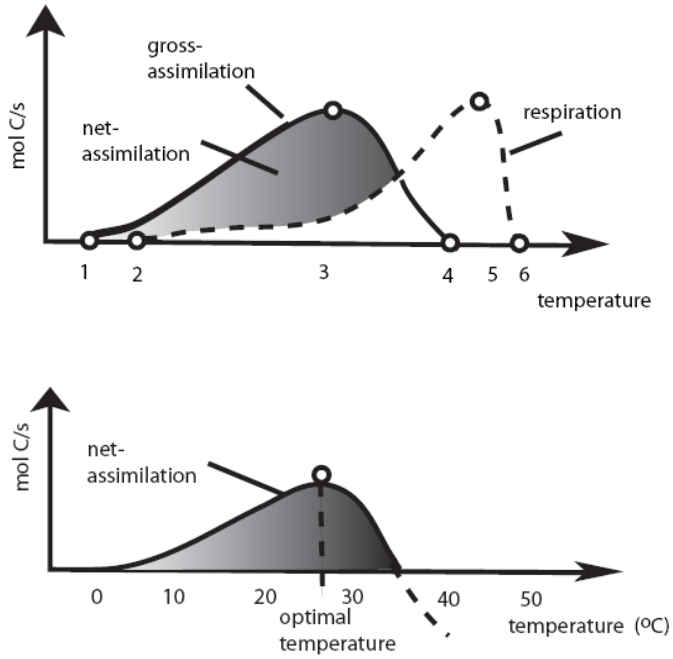

Main points:
1: minimum temperature for gross assimilation
2: minimum temperature for respiration
3: optimum for gross assimilation
4. maximum temperature for gross assimilation
5: optimum for respiration
6: maximum temperature for respiration

Figure 3.13: Qualitative dependence of photosynthesis (P), autotrophic respiration (R) and net primary production (P-R) on temperature, on the plant level.

The "fertilization effect" of an increased atmospheric CO_2 concentration may be parameterized with a simple relation between NPP and atmospheric CO_2 concentration:

$$NPP(t) = NPP(CO_{2,0}) \cdot (1 + \beta \cdot \ln \frac{CO_2(t)}{CO_{2,0}}) \qquad \text{Eq. 3.9}$$

β is a constant. The size of the fertilization effect in nature, however, is debated. Free air CO_2 enrichment (FACE) of trees show a sustained increase in NPP of about 23% when CO_2 is increased from 376 to 550 ppm.

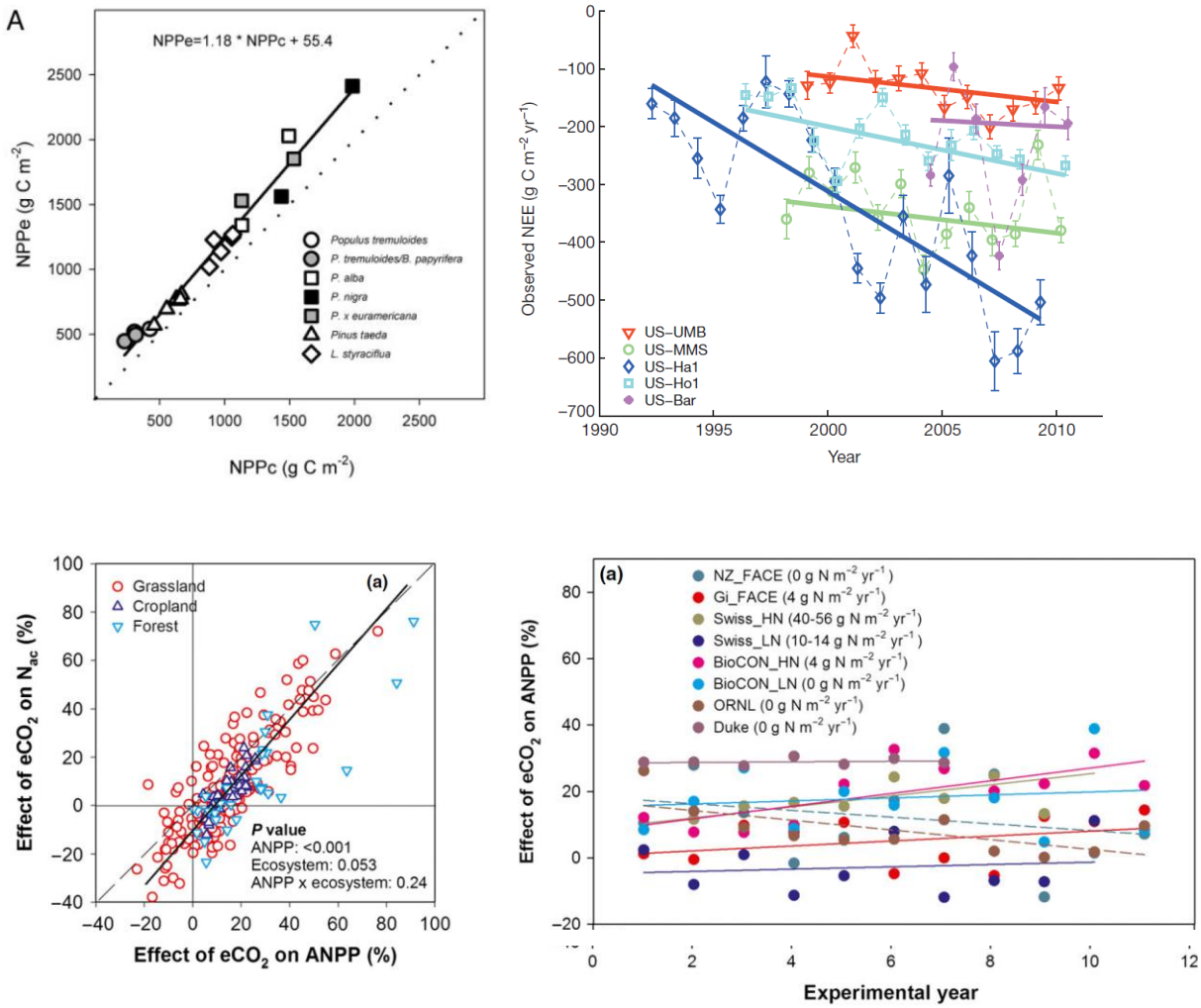

Figure 3.14: (upper right) Responses of NPP to elevated CO_2 in four free-air CO_2 enrichment (FACE) experiments in forests. NPP increases by 23% when CO_2 concentration is increased from 376 to 550 ppm in the forest stands. Shown is the regression of NPPe (elevated CO2 of 550 ppm) as a function of NPPc (control CO_2 of 376 ppm). The intercept is not significantly different from 0; the slope is significantly different from 1. Data are included only from years after LAI was no longer increasing. The dotted line represents the 1:1 relationship (Norby et al., PNAS, 2005).
(upper left) Long-term increase in net ecosystem carbon uptake (NEE) at five natural forest sites in the northeastern USA from eddy covariance flux measurements (negative sign= flux into land) (Keenan et al., Nature 2013).
(lower left) Relationship between effects of elevated CO_2 (eCO_2) on annual aboveground net primary production (ANPP) and corresponding nitrogen acquisition (Nac) (Feng et al., *Global Change Biology*, 2015)
(lower right) Effect of elevated CO_2 (eCO2) on above ground NPP in relation to the number of years of experimental CO2 exposure at each FACE site. Annual N fertilization amounts are given in the figure legend.

3.3.4 Regulation of the heterotrophic respiration

At least on the seasonal scale, the heterotrophic respiration (HR) by bacteria depends on temperature and humidity in the soil. The composition of organic compounds (lignin content) also affects HR. The decay of organic soil carbon is slow in dry and cold regions. Remember that the amount of stored carbon is proportional to the product of input and mean residence time. The high carbon density in soils of the high and mid-latitudes is thus a result of the

slower decay at low temperatures. The relatively small amount stored in tropical soils is due to the rapid decay of dead organic material in warm and moist regions.

Rustad, Oecologia, 2001, presented results from a meta-analysis to synthesize data on the response of soil respiration, net N mineralization, and aboveground plant productivity to experimental ecosystem warming at 32 research sites representing four broadly defined biomes, including high (latitude or altitude) tundra, low tundra, grassland, and forest. Warming methods included electrical heat-resistance ground cables, greenhouses, vented and unvented field chambers, overhead infrared lamps, and passive nighttime warming. Although results from individual sites showed considerable variation in response to warming, results from the meta-analysis showed that, across all sites and years, 2–9 years of experimental warming in the range 0.3–6.0°C significantly increased soil respiration rates by 20%. The authors have also found significant increases in net N mineralization rates by 46% and plant productivity by 19%. The response of soil respiration to warming was generally larger in forest ecosystems compared to low tundra and grassland ecosystems, and the response of plant productivity was generally larger in low tundra ecosystems than in forest and grassland ecosystems. With the exception of aboveground plant productivity, which showed a greater positive response to warming in colder ecosystems, the magnitude of the response of these three processes to experimental warming was not generally significantly related to the geographic, climatic, or environmental variables evaluated in this analysis. This underscores the need to understand the relative importance of specific factors (such as temperature, moisture, site quality, vegetation type, competitive status, land-use history, etc.) at different spatial and temporal scales, and suggests that we should be cautious in "scaling up" responses from the plot and site level to the landscape and biome level.

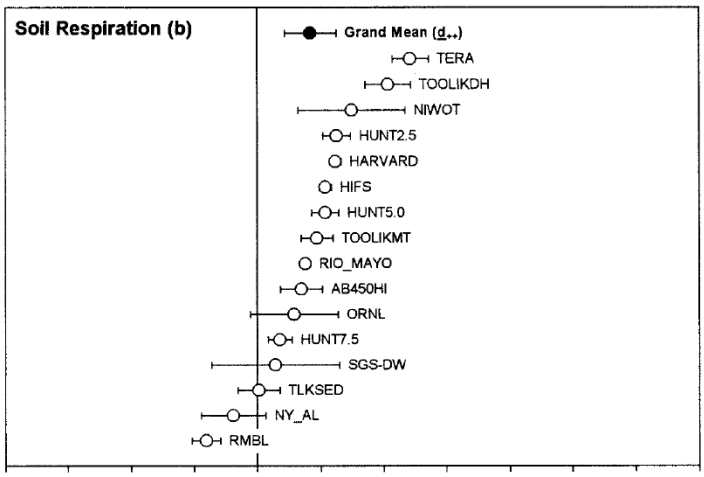

Figure 3.15: Response of soil respiration under experimental warming at different sites from Rustad et al., Oecologia, 2001.

Models incorporate the complex responses found in the field in a highly parameterized way. The decay rate of dead organic carbon, *k*, can be parameterized:

$$k = k_{10} \cdot r_{temp} \cdot r_{moist} \qquad \text{Eq. 3.10}$$

Where, k_{10} denotes the decay rate at 10°C and 100% water saturation of the soil. r_{temp} and r_{moist} are factors describing the relationship of the decay rate vs. temperature and soil moisture, respectively. It must be noted that this description represents a parameterization for a complex bacterial process

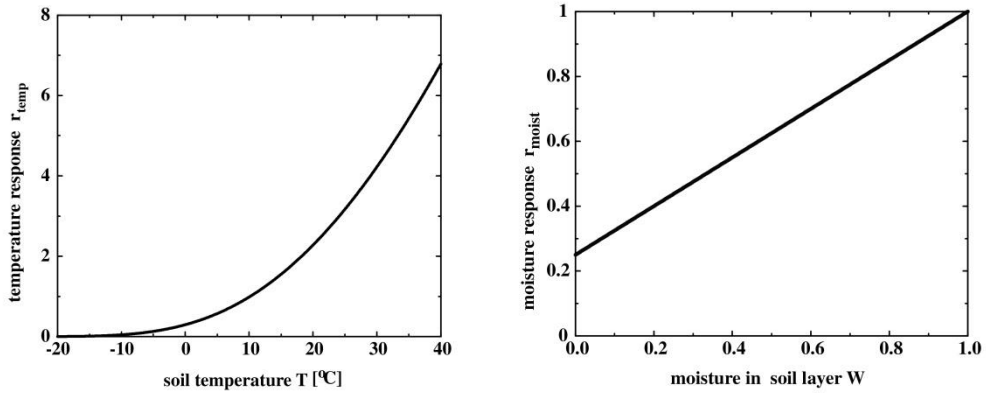

Figure 3.16: Dependence of the decay rate of dead organic material on the soil temperature (r_{temp}) and soil water saturation (r_{moist}) as incorporated in a model.

For the dependence of the bacterial decomposition on soil temperature, T_S, an exponential relationship is commonly assumed.

$$r_{temp} = \exp\left(308.56 \cdot \left(\frac{1}{56.02} - \frac{1}{T_S - 45.87^{o}\mathrm{C}}\right)\right) \text{ for } T_S < 45^{o}\mathrm{C} \qquad \text{Eq. 3.11}$$

Above a critical threshold value of the soil temperature, which lies around 45°C, soil bacteria die as decay shuts down.

The dependence on soil moisture is often assumed to be proportional to the saturation, *W*:

$$r_{moist} = 0.25 + 0.75 \cdot W \qquad \text{Eq. 3.12}$$

The temperature dependence of *k* is often represented by a so-called **Q_{10} factor.** Q_{10}=2 means that for an increase in temperature by 10 °C, the decay rate, *k*, increases by a factor of 2.

$$k(T) = k_{10} \cdot Q_{10}^{(T - 10^{o}C)/10^{o}C} \qquad \text{Eq. 3.13}$$

For **anaerobic conditions** (no oxygen available), e.g. in peats, swamps or rice paddies, decomposition processes are completely different. Instead of CO_2, methane is produced by bacterial activities. Above relations are not applicable anymore. It is one of the current challenges to quantify how changes in wetlands will affect future climate through the release of methane and CO_2.

3.3.5 Seasonal changes of NPP, heterotrophic respiration and atmospheric CO_2

The strong temperature dependence of HR and the temperature and light dependence of NPP result in a pronounced seasonality in both terms. There are also seasonal changes in the net rate of CO_2 emissions to the atmosphere.

This results in a seasonal signal in the NEP (NPP-HR), which has a yearly average of about zero. In an unperturbed, mature ecosystem NPP and HR compensate each other over the course of a year, unless there are disturbances such as fires or insect attacks.

$$\frac{dc_a}{dt} = const \cdot (HR - NPP) \quad \Rightarrow \quad c_a(t) = c_a(0) + const \cdot \int dt(HR - NPP) \qquad \text{Eq. 3.14}$$

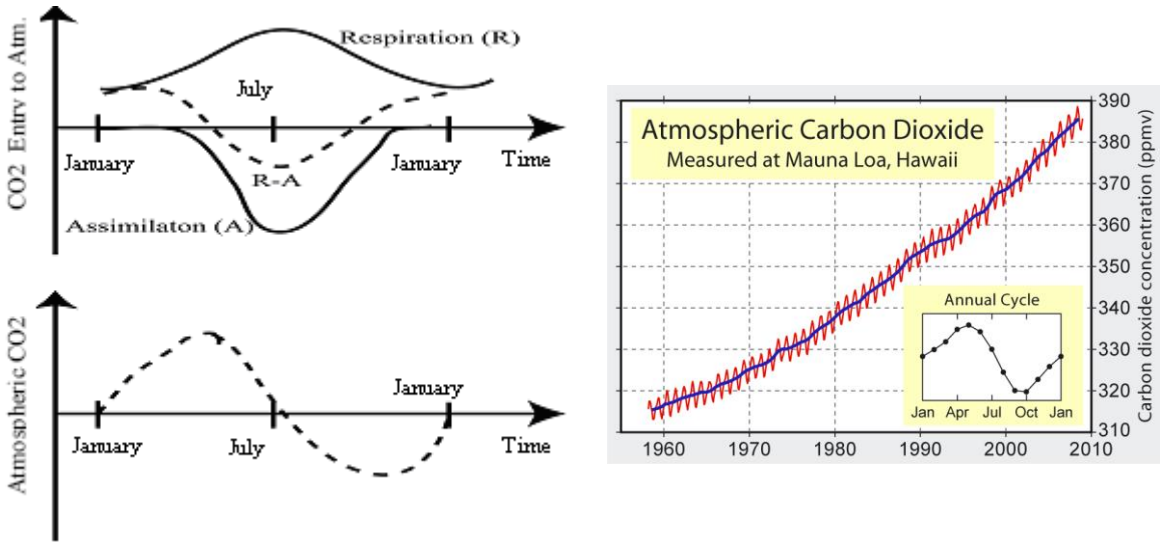

Figure 3.17: HR occurs throughout the year, but reaches its peak during the summer. NPP occurs mainly in summer (left). This yields a peak in the spring in CO_2 in the Northern Hemisphere (below).

3.3.6 An estimate of potential changes in terrestrial carbon storage for a doubling of atmospheric CO_2

In the following, we will do a rough estimate of the effect of a doubling of the atmospheric CO_2 concentration on the amount of carbon stored in the land biosphere. To this end, we apply the 2-Box model that was introduced in Section 3.2.1. Let us consider the differences in carbon storage between a "preindustrial steady state" in vegetation, V_0, and soil, S_0, and after a new equilibrium has been reached, V_1 and S_1. For the preindustrial state we assume the following global pool sizes:

Vegetation carbon: V_0 = 500 GtC
Litter and soil carbon: S_0 =2000 GtC
Atmospheric CO_2: $CO_{2,0}$= 280 ppm

Recall that according to Eqs. 3.5 and 3.6, for a box-model at steady state we can write:

Mass=input x residence time

a) CO_2 fertilization effect: We describe the change in NPP by:

$$\frac{NPP_1}{NPP_0} = 1 + g \qquad \text{Eq. 3.15}$$

According to Eqs. 3.5 and 3.6, carbon storage in vegetation and soil becomes:

$$\frac{V_1}{V_0} = \frac{S_1}{S_0} = \frac{V_1 + S_1}{V_0 + S_0} = \frac{NPP_1}{NPP_0} = 1 + g \qquad \text{Eq. 3.16}$$

Let us postulate a CO_2 fertilization effect (Eqn. 3.9) with β=0.3. It follows that the net primary production increases by 20% for a doubling of CO_2.

$$1 + g = \frac{NPP(2xCO_{2,0})}{NPP(CO_{2,0})} = 1 + \beta \cdot \ln\frac{2CO_{2,0}}{CO_{2,0}} = 1 + 0.3 \cdot \ln 2 = 1.2 \qquad \text{Eq. 3.17}$$

Hence, the vegetation and soil pool each increase by 20% as well (100 GtC+400 GtC=500 GtC):

b) Accelerated respiration: The increase of the CO_2 concentration is assumed to lead to a temperature increase: $\Delta T_{2x}=3^oC$. We assume that the Q_{10} factor is 2 for the heterotrophic respiration and the increase in mean surface temperature is 10^oC. This results in a decreased mean residence time of C in the soil by also about 20%:

$$\frac{\tau_{S,1}}{\tau_{S,0}} = \frac{k_0}{k_1} = Q_{10}^{-\Delta T_{2x}/10^{o}\mathrm{C}} = 2^{-0.3} = 0.81 \qquad \text{Eq. 3.18}$$

Due to the enhanced respiration, the soil pool alone will decrease by about 20% or 400 GtC.

c) For a combination of a) and b) we obtain the following equation for soil carbon:

$$\frac{S_1}{S_0} = \frac{NPP_1}{NPP_0} \cdot \frac{\cdot \tau_{S,1}}{\cdot \tau_{S,0}} = (1+g) \cdot Q_{10}^{-\Delta T_{2x}/10^{o}\mathrm{C}} \qquad \text{Eq. 3.19}$$

The relative change in C-storage is equal to:

$$\frac{V_1 + S_1}{V_0 + S_0} = (1+g) \cdot \frac{V_0}{V_0 + S_0} + (1+g) \cdot Q_{10}^{-\Delta T_{2x}/10^{o}\mathrm{C}} \cdot \frac{S_0}{V_0 + S_0} \qquad \text{Eq. 3.20}$$

Using the parameter values as above, we obtain a decrease of soil carbon by 2%, or 38 GtC, and still an increase in the vegetation by about 20%, or 104 GtC.

Finally, the net change in carbon storage amounts to:

$$(V_1 + S_1) - (V_0 + S_0) = 66 \text{ GtC} \qquad \text{Eq. 3.21}$$

In the example above, important factors, such as the change in NPP and plant distribution due to climatic change are neglected. The example illustrates that changes in C-storage in the terrestrial biosphere is the sum of sink and source processes.

3.3.7 A conceptual model for the terrestrial sink flux

In Chapter 2, it was demonstrated that a terrestrial sink flux on the order of 1-2 GtC a^{-1} compensates for the release of carbon due to deforestation and land use change. In the following we will examine the behavior of the terrestrial sink flux (after Thompson et al., 1997). First we consider the direct effect of an increased CO_2 concentration on the NPP. Second, we describe the carbon content in the biosphere by a single well-mixed box. The goal is to estimate the potential C-flux into the biosphere induced by the fertilization effect, $F_{a,b,fert}$. Thus, it is implicitly postulated that the terrestrial sink is dominated by fertilization effects and not by other factors, such as climate change, re-growth of forests at mid-latitudes, etc.

The balance equation for the terrestrial C-storage, *C*, reads:

$$\frac{dC}{dt} = NPP(t) - \frac{1}{\tau}C(t) \qquad \text{Eq. 3.22}$$

the net primary production shall be described as:

$$NPP = NPP_0\,(1 + g(t)) \qquad \text{Eq. 3.23}$$

$g(t)$ is the relative increase in NPP:

$$g(t) = \frac{\delta NPP}{NPP_0} \qquad \text{Eq. 3.24}$$

C: carbon content in the biosphere
NPP_0: preindustrial NPP
$\delta NPP = NPP - NPP_0$
τ: residence time of organic carbon; here, assumed to be constant over time.

For the preindustrial steady state, dC/dt = 0, we write:

$$C_0 = NPP_0 \cdot \tau \qquad \text{Eq. 3.25}$$

Linear relation of NPP vs. time:

We assume that the NPP increases linearly with time:

$$g(t) = r \cdot t \qquad \text{for } t>0 \qquad \text{Eq. 3.26}$$

Where the relative increase in NPP, *r*, is assumed to be constant:

$$r = \frac{1}{NPP_0}\frac{dNPP}{dt} \qquad \text{Eq. 3.27}$$

The balance equation becomes:

$$\frac{dC}{dt} = NPP_0 \cdot (1+rt) - \frac{C}{\tau} \qquad \text{Eq. 3.28}$$

And the solution for the terrestrial C-storage is:

$$C(t) = NPP_0 \cdot \tau \cdot (1+rt) - NPP_0 \cdot r \cdot \tau^2 \cdot (1 - \exp\frac{-t}{\tau}) \qquad \text{Eq. 3.29}$$

The heterotrophic respiration is:

$$R_h = \frac{C}{\tau} = NPP_0 \cdot (1+rt) - NPP_0 \cdot r \cdot \tau \cdot (1 - \exp\frac{-t}{\tau}) \qquad \text{Eq. 3.30}$$

for $t >> \tau$ and with $g=rt$ we get:

$$C(t) \approx \mathrm{NPP_0} \cdot \tau \cdot (1+\mathrm{rt}) - \mathrm{NPP_0} \cdot \mathrm{r} \cdot \tau^2 \approx NPP_0\, \tau\, (1+g) \qquad \text{Eq. 3.31}$$

The additional carbon storage is equal to the product of residence time and the increase in NPP:

$$\delta C = C(t) - C_0 \approx NPP_0\, \tau\, g \qquad t >> \tau \qquad \text{Eq. 3.32}$$

The heterotrophic respiration amounts to:

$$R_h = NPP_0 \cdot (1+rt) - NPP_0 \cdot r \cdot \tau \qquad t >> \tau \qquad \text{Eq. 3.33}$$

This means that the heterotrophic respiration becomes smaller than the NPP by a constant factor (for constant τ).

For the sink flux we obtain:

$$\frac{dC}{dt} = NPP_0 \cdot \tau \cdot r - NPP_0 \cdot \tau \cdot r \cdot \exp\frac{-t}{\tau} = NPP_0 \cdot \tau \cdot r \cdot (1 - \exp\frac{-t}{\tau}) \qquad \text{Eq. 3.34}$$

and for $t >> \tau$, the sink flux turns to:

$$\frac{dC}{dt} = NPP_0 \cdot r \cdot \tau \qquad t >> \tau \qquad \text{Eq. 3.35}$$

(This corresponds to the difference between NPP and the heterotrophic respiration)

Next, we consider the initial transient and calculate the time, $t(f)$, required to attain the fraction f (2/3) of the maximum sink flux.

$$f\, NPP_0\, \tau\, r = NPP_0\, \tau\, r\, (1 - \exp(-t/\tau)) \qquad \text{Eq. 3.36}$$

$t(f) = -\tau \ln(1-f)$ accordingly, $t(f=2/3) \cong \tau$ Eq. 3.37

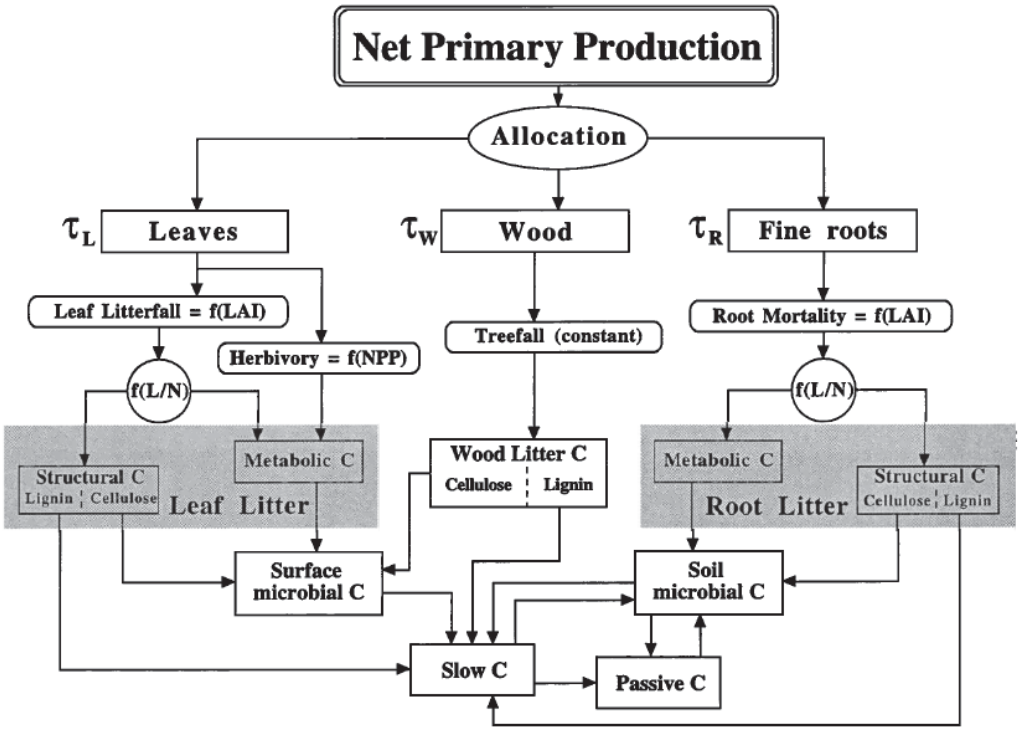

Figure 3.18: The flux of carbon in the living biomass, litter and organic soil matter as described by the Carnegie-Ames-Stanford Approach (CASA) biosphere model (Thompson, GBC, 1996).

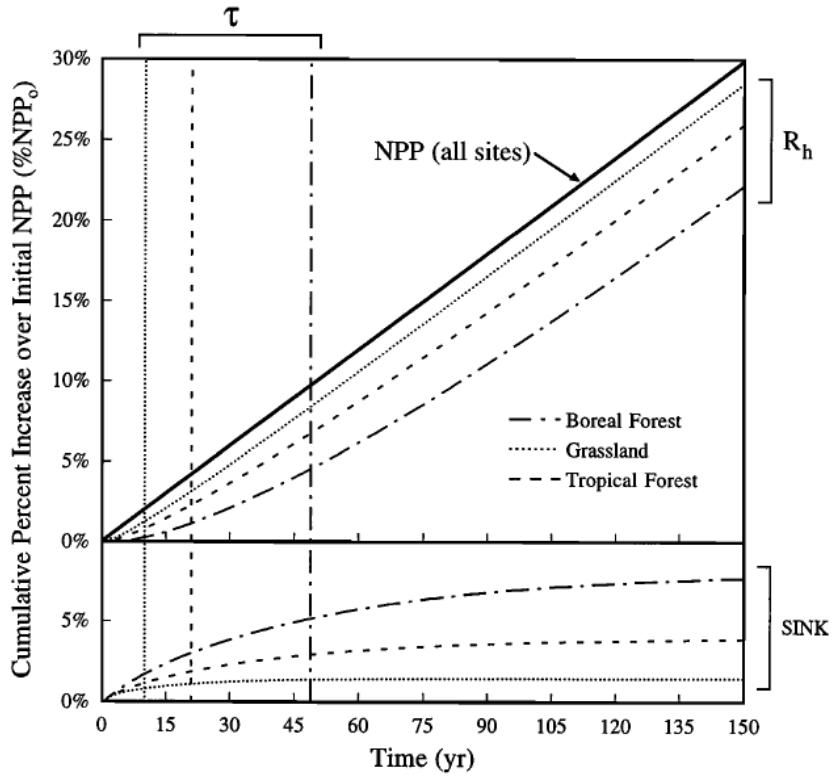

Figure 3.19: Heterotrophic respiration, R_h, and the carbon sink for a linear increase in NPP by 2% a^{-1} for three different grid cells in the CASA model. The mean residence time, τ, is depicted for each cell by a vertical line that crosses the time axis at τ. NPP, R_h and the sink flux are given as percentage of the initial annual NPP (Thompson, GBC, 1996).

Generalization: Strictly speaking, above equations are only valid for a linear increase in NPP with time. For the case NPP varies slowly with respect to the mean residence time, we can replace the constant rate of increase of the NPP, r, by the time derivative of g. Thus, we obtain the sink flux induced by the fertilization effect as a **first-order approximation**.

$$F_{a,b,\,fert}(t) \cong NPP_0 \cdot \tau \cdot \frac{dg(t)}{dt} \qquad \text{Eq. 3.38}$$

In other words, the sink flux at time *t* is proportional in the first-order approximation to the product of the preindustrial assimilation rate, the relative increase in NPP at time *t* and the actual mean residence time of organic C in the biosphere.

Finally, we estimate the time at which the **sink flux** reaches its **maximum**. Therefore, we take the time derivative of the sink flux and set it to 0. Neglecting transient and non-linear effects, we obtain:

$$\frac{dF_{a,b,\,fert}}{dt} = NPP_0 \cdot \tau \cdot \frac{d^2 g}{dt^2} \qquad \text{Eq. 3.39}$$

Hence, the sink flux maximum is at

$$d^2g/dt^2 \approx 0 \qquad \text{Eq. 3.40}$$

For a first-order linear increase of NPP with the atmospheric CO_2 concentration, the sink flux attains a maximum when the second time derivative of the atmospheric CO_2 concentration vanishes.

$$\frac{d^2 CO_2}{dt^2} \approx 0 \qquad \text{Eq. 3.41}$$

The present considerations are also valid in first-order for the uptake of anthropogenic CO_2 by the ocean. Oceanic uptake is also driven by the increase in atmospheric CO_2 concentrations.

Figure 1.10 illustrates that the total anthropogenic emissions (increase of carbon in the atmosphere plus biosphere plus ocean) for different stabilization scenarios are roughly located at the point of inflection of the CO_2 path.

One important question remains: How large is the increase in NPP required to be in order to explain the implied terrestrial sink as it is derived from observations. Thompson et al., applied the CASA model at a resolution of $1^{o}x1^{o}$ to explore this problem.

The historical terrestrial sink fluxes were estimated with an ocean model ("de-convolution", see Chapter 2) and the estimated "land use emissions" are derived. The increase in NPP that is required to explain the sink flux, is then calculated with the CASA model.

It follows, that the global NPP is required to have increased by about 20% until 1990 in order to explain the postulated sink flux merely by changes in NPP. Assuming that the global sink flux had only taken place in tropical forests, NPP is required to have increased by 30% in this region. According to the CASA model, grasslands are hardly able to represent a relevant sink region because the mean C-residence time in this vegetation type is too small.

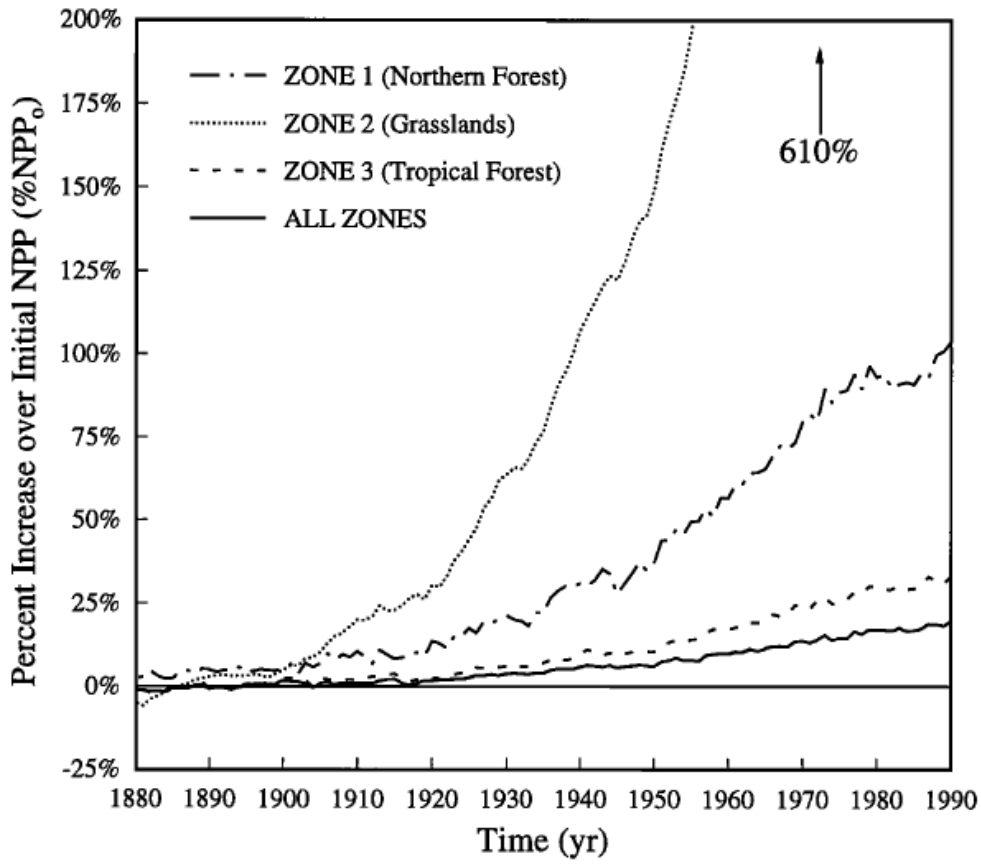

Figure 3.20: Cumulative changes in NPP required to explain the terrestrial sink flux.

3.4 Photosynthesis-Transpiration

In this section we will treat processes controlling the **assimilation of C** in the leaf and the **transpiration of water** from the leaf to the atmosphere.

Photosynthesis is the assimilation of carbon, nitrogen, sulphur and other substances into plant material using energy and light.

The radiation usable for photosynthesis (PAR: Photosynthetically active radiation) makes up about 50% of the solar incoming radiation.

The exchange of CO_2, O_2 and H_2O between the leaf and the atmosphere is conducted through the stomatal openings. The plant is able to actively control the stomatal openings. The water vapor pressure at the cell walls inside the stomata is equal to the saturation pressure. In order to avoid drought-related damages to the cell, the plant needs to close the stomatal openings when the evaporation of water exceeds the supply from the roots into the leaf.

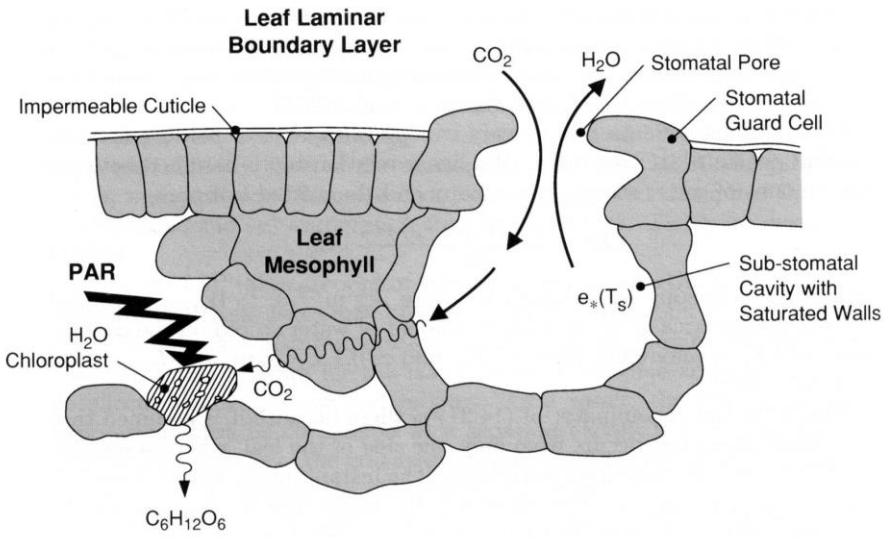

Figure 3.21: Schematic cross section of a leaf. The plant is able to control the opening of the stomatal pore and can thus regulate the exchange of CO_2 and H_2O. The vapor pressure in the sub-stomatal cavity is close to the saturation vapor pressure because the cells contain water. Under water stress, the plant has to close the stomatal pores, whereby the transfer of CO_2 and the photosynthesis is shut down.

A prediction of the theory detailed in the following sections is that an increase in CO_2 causes an increase in productivity, an increase in water use efficiency, and an increase in green foliage cover in warm, arid environments. Recent observations appear to support this (e.g. Keenan et al.,,Nature 2013, Donohue et al., Geophys. Res. Letter, 2013). For example, Satellite observations, analyzed to remove the effect of variations in precipitation, show that cover across warm arid environments has increased by 11% suggesting that the anticipated CO_2 fertilization effect is occurring alongside ongoing anthropogenic perturbations to the carbon cycle and that the fertilization effect is now a significant land surface process (Donohue et al., GRL, 2013).

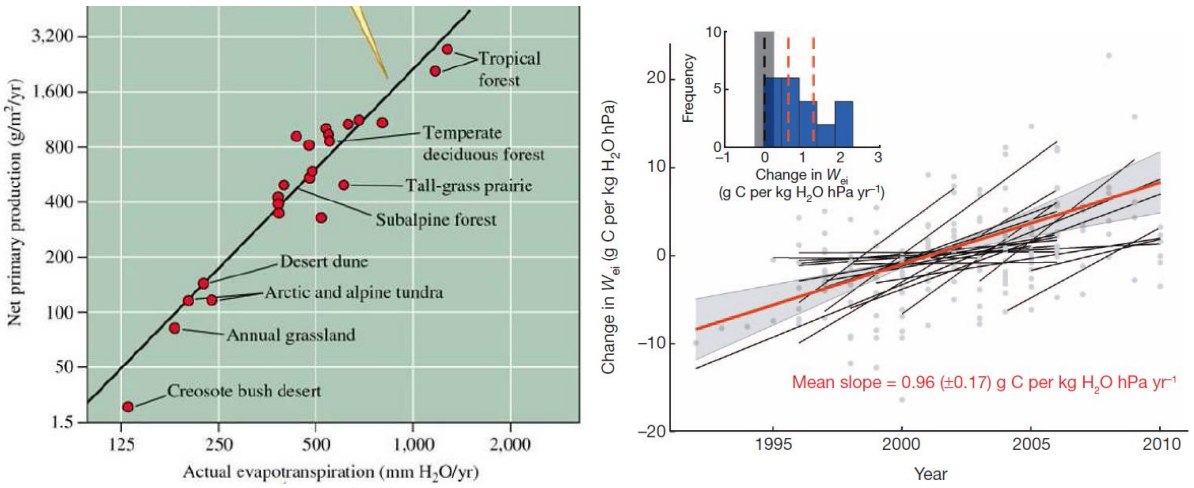

Figure 3.22: (left) Net primary productivity is very closely related to evapotranspiration. This has considerable implications, for example, for agriculture; as growing plants for food requires water.
(right) Observation-based long-term change in forest water-use efficiency. The annual change in water use efficiency, ΔWei (gC per kg H2O hPa) is calculated using daytime fluxes from summer months at individual sites.ΔWei is normalized to meanWei at each site. The red line represents the mean trend over all sites, extrapolated over the entire measurement period. The grey area highlights trends within one standard deviation about the mean trend. Individual site observations and trends are given as grey dots and black lines respectively (from Keenan et al, Nature, 2013).

So-called C3 plants assimilate carbon using the C3-photosynthesis path, while C4 plants follow the C4 path. We will discuss in the following sections the C3 pathway in more detail as this is followed by the majority of the plants on land and primary producers in the ocean.

3.4.1 Simplified description of photosynthesis in C3 plants

Biochemical knowledge may be summarized by a few equations that characterize the processes that control the assimilation rate of carbon on the stomata level. For C3 plants they are:

1) Carboxylation rate, Vc, of ribulose-biphosphate (RuP_2), with excess RuP_2
2) ratio of oxygenation (photo-respiration) to carboxylation
3) regeneration rate of ribulose-biphosphte (RuP_2), J*, *i.e.* the rate of electron transport induced by light absorption (photophosphorylation) and required to regenerate RuP_2.
4) "dark" respiration

Ribulose-1,5-bisphosphate (RuBP) is the molecule which carbon dioxide reacts with in photosynthetic carbon fixation. The enzyme ribulose bisphosphate carboxylase oxygenase (RuBiSCO) catalyzes the reaction of RuBP with CO_2

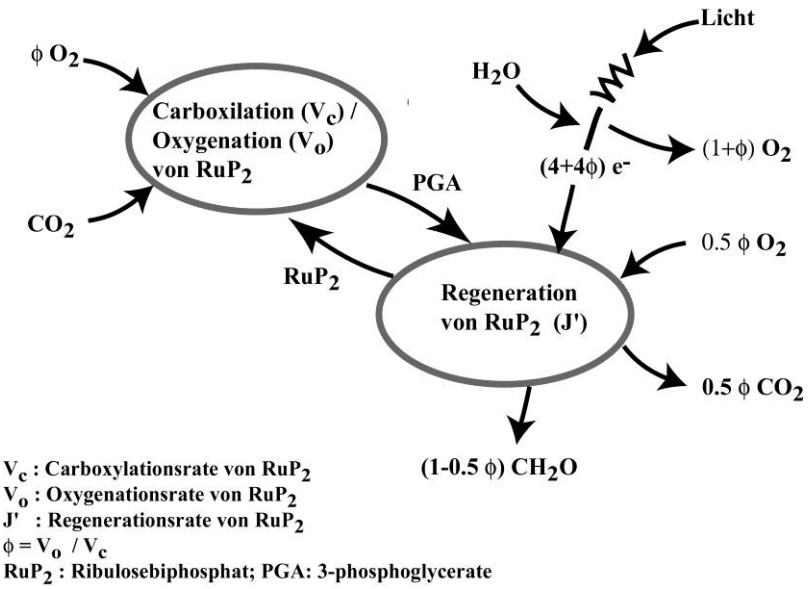

Figure 3.23: Simplified scheme of the cycles of photosynthetic reduction of CO_2 and photorespirational oxidation of carbon, RuP_2: Ribulosis biphosphatse; PGA: rate of 3-phosphoglyce.

Two competing processes, the carboxylation and the oxygenation of ribulosis-biphosphate can be described by the following kinetic rates:

Vc : Rate of carboxylation of RuP_2 (CO_2 assimilation)
Vo : Rate of oxygenation of RuP_2 (photo-respiration of CO_2).
Φ : ratio of the reaction rates:

$$\Phi = \frac{Vo}{Vc} \qquad \text{Eq. 3.42}$$

The stoichiometry of the complete reaction is:

$$(1\text{-}0.5\,\Phi)\ (CO_2 + H_2O + \text{light}) \rightarrow (1\text{-}0.5\,\Phi)\ (CH_2O + O_2) \qquad \text{Eq. 3.43}$$

Additionally, release of CO_2 takes place in the mitochondria: „dark respiration“,
Rd: rate of dark respiration

The assimilation rate of CO_2 is given as:

$$A = Vc - 0.5Vo - Rd = Vc(1 - 0.5\Phi) - Rd \qquad \text{Eq. 3.44}$$

3.4.1.1 Limiting the rate of assimilation

The assimilation rate of CO_2 is limited by the reaction rate of the carboxylation/oxygenation reaction under excess of ribulosis-biphosphate, or by the regeneration rate of ribulosis-biphosphate:

$$Vc = \min\{Wc, J^*\} \qquad \text{Eq. 3.45}$$

Wc: rate of carboxylation of RuP_2 under excess RuP_2 (high concentrations)
J*: regeneration rate of RuP_2

Case 1: RuP_2-saturated

RuP_2 occurs at high concentrations (saturation). The limiting step is the reaction rate of carboxylation/oxygenation.

Carboxylation rate:

$$Vc = Wc = Vc,\max \quad \frac{pCO2}{pCO2 + Kc(1 + pO2/Ko)} \qquad \text{Eq. 3.46}$$

Oxygenation rate:

$$Vo = Wo = Vo,\max \frac{pO2}{pO2 + Ko(1 + pCO2/Kc)} \qquad \text{Eq. 3.47}$$

$pCO2, pO2:$	partial pressure of CO_2 and O_2 inside the stomatal cavity of the leaf
$Vc,\max, Vo,\max:$	maximum rate of carboxylation and oxygenation, respectively
$Kc, Ko:$	Michaelis-Menten constants

Ratio of oxygenation vs. carboxylation:

We obtain the following ratio between oxygenation vs. carboxylation (generally valid):

$$\Phi = \frac{Vo,\max}{Vc,\max}\frac{pO2}{pCO2}\frac{Kc}{Ko} \qquad \text{Eq. 3.48}$$

CO_2 compensation point

Γ^*: CO_2 compensation point (A=0) of RuP_2 for saturation concentrations and $Rd = 0$

The CO_2 concentration inside the stomatal cavity becomes $pCO_2^* = \Gamma^*$ under the (theoretical) assumption that the stomatal pore is closed and the assimilation rate is set to 0. For the assimilation it follows from Eq. 3.44 that:

$$Vc = 0.5Vo \qquad \text{Eq. 3.49}$$

and the compensation point, using Eqn. 3.48, is equal to:

$$\Gamma^* = pCO2^* = 0.5\frac{Vo,\max}{Vc,\max}\frac{Kc}{Ko}pO2 \qquad \text{Eq. 3.50}$$

The CO_2 compensation point is thus primarily a function of temperature, T, due to the temperature dependence of the reaction constants.

The ratio between oxygenation and carboxylation can be formulated as a function of $\Gamma*$ and $pCO2$:

$$\Phi = \frac{Vo}{Vc} = \frac{2\Gamma*}{pCO2} \qquad \text{Eq. 3.51}$$

and the assimilation rate becomes:

$$A = Vc(1 - \frac{\Gamma*}{pCO2}) - Rd \qquad \text{Eq. 3.52}$$

The ratio $\frac{\Gamma*}{pCO2}$ corresponds to the ratio of photo-respiration vs. carboxylation.

Case 2: RuP_2-limited

The limiting step for carboxylation/oxygenation is the rate of RuP_2 regeneration.

The potentially possible electron transport depends on the incident light:

$$J = J_{\max} \frac{I}{I + 2.1 \cdot J_{\max}} \qquad \text{Eq. 3.53}$$

J: potential e^- transportation rate
$J_{\max}$: maximum possible e^- transportation rate under light saturation
I: photosynthetically active radiation

The e^- transportation rate for the regeneration of RuP_2 amounts to:

$$J = (4.5 + 10.5\frac{\Gamma*}{pCO2}) \cdot Vc \qquad \text{Eq. 3.54}$$

By combining the above equations, we obtain the maximum possible regeneration rate for RuP_2, and hence the carboxylation under light limitation:

$$Vc = J* = \frac{J_{\max} \cdot I}{I + 2.1 \cdot J_{\max}} \cdot \frac{1}{4.5 + 10.5\Gamma* / pCO2} \qquad \text{Eq. 3.55}$$

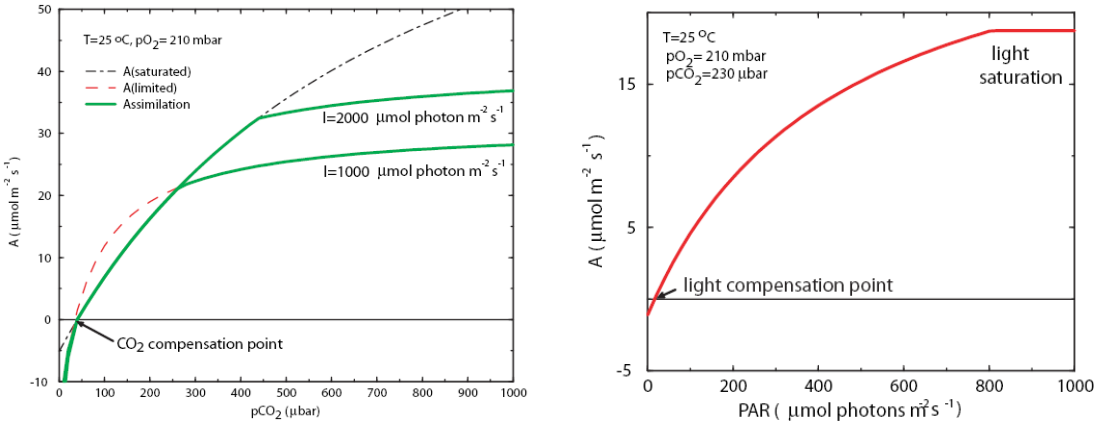

Figure 3.24: C-assimilation as a function of the CO_2 partial pressure inside the stomatal cavity (left) and the photosynthetically active radiation (PAR/I; right) for 0.45 g chlorophyll per m^2 leaf area.

3.4.1.2 Summary

The assimilation rate, *A*, on the leaf level can be characterized by the following equations:

$$A = Vc(1 - \frac{\Gamma *}{pCO2}) - Rd \qquad \text{Eq. 3.56}$$

$$\Gamma * = 0.5 \frac{Vo,\max}{Vc,\max} \frac{Kc}{Ko} pO2 \qquad \text{Eq. 3.57}$$

RuP$_2$-saturated: $$A = Vc,\max \frac{pCO2 - \Gamma *}{pCO2 + Kc(1 + pO2/Ko} - Rd \qquad \text{Eq. 3.58}$$

RuP$_2$-limited: $$A = \frac{J_{\max} \cdot I}{I + 2.1 \cdot J_{\max}} \cdot \frac{pCO2 - \Gamma *}{4.5 pCO2 + 10.5\Gamma *} - Rd \qquad \text{Eq. 3.59}$$

Note: *pCO2* is the partial pressure inside the *stomatal cavity* and is generally smaller than the CO_2 partial pressure in the surrounding atmosphere. The partial pressure inside the stomatal cavity is described as:

$$pCO2(\text{sto}) = \lambda \cdot pCO2(\text{atm}) \qquad \text{Eq. 3.60}$$

The ratio between the CO_2 partial pressure in the stomatal cavity and the surrounding atmosphere varies with the assimilation rate and the stomatal pore opening.

3.4.1.3 Temperature dependence of the model parameters

The temperature dependence of $Kc, Ko, Vc;\max, Vo;\max, Rd$ is**:**

$$\text{parameter} = \text{parameter}(298\text{K}) \exp(\frac{(T - 298\text{K})E}{298\text{K} \cdot RT}) \qquad \text{Eq. 3.61}$$

T: leaf temperature R: gas constant
E: activation energy per mol

The temperature dependence of J_{max} is

$$J_{\max} = B \exp\{-E/RT\}/(1 + \exp\{(ST - H)/RT\}) \qquad \text{Eq. 3.62}$$

Typical values for 0.45 g(chlorophyll)per m^2 leaf area and T=25 C:
Kc 460 µbar
Γ* 31 µbar
Ko 330 mbar
Vcmax 220 µmol g(Chl)$^{-1}$ s^{-1} (=98 µmol m^{-2} s^{-1})
Jmax 470 µmol g(Chl)$^{-1}$ s^{-1} (=210 µmol m^{-2} s^{-1})
Rd 2 µmol g(Chl)$^{-1}$ s^{-1} (=1 µmol m^{-2} s^{-1})

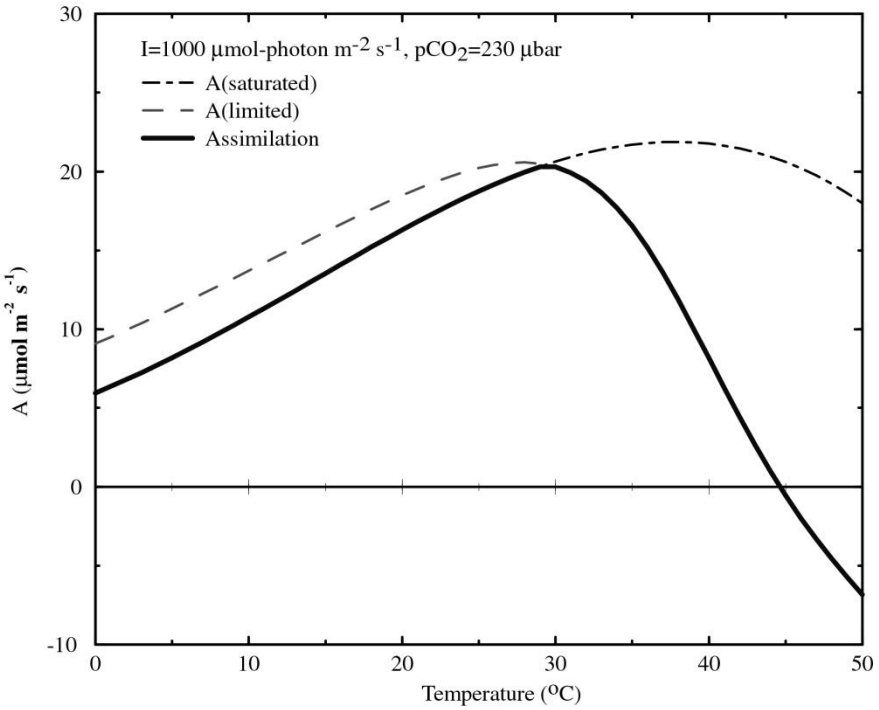

Figure 3.25: C-assimilation as a function of temperature inside the leaf for 0.45 g(Chlorophyll) per m^2 leaf area.

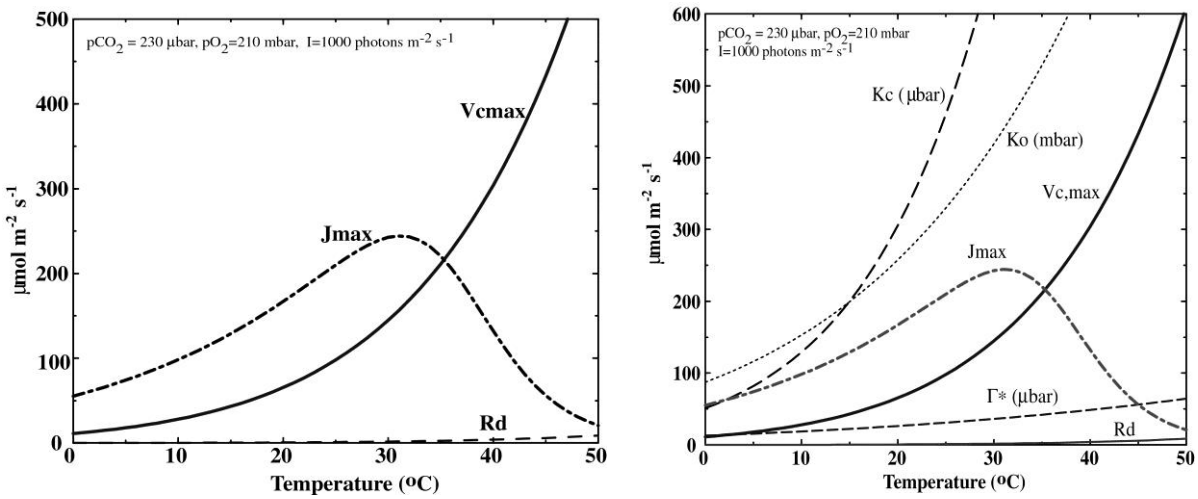

Figure 3.26: Temperature dependence of important reaction constants and parameters describing the photosynthesis.

3.4.1.4 Long-term effect of environmental conditions on photosynthesis

Photosynthesis on the leaf level is strongly affected by the availability of nutrients, leaf age and the physiology and under which light- and temperature conditions the plant has been growing. For example, $J\max$ and $Vc\max$ are higher for plants that grows under intense light.

This adaptability of plants and the numerous processes involved makes it difficult to estimate the effects of changing environmental conditions (CO_2, T, N, etc…) on the production of an ecosystem.

3.4.1.5 Production on the plant level

In order to obtain the assimilation of CO_2 on the plant level, the assimilation, A, on the leaf level has to be integrated over the entire plant. The form of the equations for a single leaf is usually conserved and empirical coefficients are used for Vcmax and Jcmax.

The gross synthesis is: $Agross = A + Rd$,
Integrated over a plant/ecosystem and over time, we obtain the gross primary production, GPP:

$$GPP = \int dplants \int (A + Rd)dt \qquad \text{Eq. 3.63}$$

The net primary production, NPP, is obtained by subtracting "maintenance" and "growth" respiration:

$$NPP = GPP - Rm - Rg \qquad \text{Eq. 3.64}$$

A possible description for the maintenance respiration, *Rm*, is that *Rm* is assumed to be proportional to the mass of carbon, *M*, in leafs, sapwood and fine roots, as well as to the N:C ration and a function of temperature:

$$Rm \sim M \cdot (N/C) \cdot f(T) \qquad \text{Eq. 3.65}$$

Growth respiration, *Rg*, is roughly:

$$Rg = 0.25 \cdot (GPP - Rm) \qquad \text{Eq. 3.66}$$

3.4.2 Transpiration and CO_2 assimilation

On the level of the leaf or the stomata, assimilation and transpiration are coupled by the diffusion of H_2O und CO_2 across the stomatal pores. The plant is able to control the stomatal pore opening. In order to avoid damages, the stomatal openings are closed when the transpiration rate becomes too high. The transpiration, E, is proportional to the difference in water vapor pressure between the stomatal cavity and the environment, ν, and to the stomatal conductance for H_2O, g:

$$E = \nu \cdot g \qquad \text{Eq. 3.67}$$

with

$$\nu = \frac{e(\text{sto}) - e(\text{atm})}{p(\text{atm})} \qquad \text{Eq. 3.68}$$

e(sto) and e(atm) denote the water vapor pressure in the stomatal cavity and in the ambient air. e(sto) corresponds to the saturation vapor pressure at the leaf temperature. The normalization of the water vapor gradient with the atmospheric pressure, p(atm), largely cancels the dependence on the altitude as well as the temperature dependence of the diffusion for the estimation of g. Hence, g is only to be affected by stomatal properties.

The assimilation of CO_2, A, is proportional to the CO_2 flux into the leaf:

$$A = \frac{g}{1.6} \cdot (CO_2(\text{atm}) - CO_2(\text{sto})) = \frac{g}{1.6} \cdot CO_2(\text{atm}) \cdot (1-\lambda) \qquad \text{Eq. 3.69}$$

where (g/1.6) is the stomatal conductance for CO_2 (in ppm) and λ is the ratio of the CO_2 partial pressure between the stomatal cavity and the atmosphere:

$$\lambda = \frac{\text{pCO}_2(\text{sto})}{\text{pCO}_2(\text{atm})} = \frac{\text{CO}_2(\text{sto})}{\text{CO}_2(\text{atm})} \qquad \text{Eq. 3.70}$$

The instantaneous “water-use efficiency” amounts to:

$$\frac{A}{E} = \frac{CO_2(\text{atm}) \cdot (1-\lambda)}{1.6\nu} \qquad \text{Eq. 3.71}$$

The above equation describes the increase in **water use efficiency** with the **atmospheric CO_2 concentration** for a fixed stomatal pore opening and fixed chlorophyll content. Higher atmospheric CO_2 concentrations not only favor higher assimilation rates of C but also lead to a lower loss of water by the plant and thus to **lower fluxes of latent heat.**

3.4.2.1 Transpiration efficiency, W, on the plant level

W represents the ratio between increase in biomass (NPP) and loss of water on the plant level (or ecosystem level). The instantaneous transpiration efficiency is modified by the loss of CO_2 due to the autotrophic respiration (given in percent of GPP), $\sigma(CO2)$, and by the additional loss of water during the night, $\sigma(H2O)$:

$$W = \frac{CO_2(\text{atm})(1 - CO_2(\text{innen})/CO2(\text{atm})}{1.6\nu} \cdot \frac{1-\sigma(CO_2)}{1+\sigma(H_2O)} \quad \text{Eq. 3.72}$$

W and A/E are given in units of [ppm/ppm].

3.4.3 Coupling of photosynthesis, evapotranspiration and soil water content

3.4.3.1 General concepts:

Evapotranspiration: Sum of evaporation and transpiration of plants in mm/day.
Potential Evaporation or Evapotranspiration, PET:
maximum possible evaporation: evaporation of a wet surface under given atmospheric conditions (rel. humidity, wind, temperature, roughness…)
Actual Evapotranspiration, AET:
actually occurring evapotranspiration.
Available Water Capacity, AWC:
available pore space for water in the soil
Relative soil water content, W:
soil water content as percent of AWC.

3.4.3.2 A model

In the following, we develop a model that couples the equations for assimilation (section 3.4.1) and the equations for the diffusion of CO_2 into and of H_2O out of the stomatal cavity (section 3.4.2) as well as the water consumption from the soil into the leaf. The idea is that assimilation is maximized if water is not limiting and reduced under water stress.

Let us denote the maximum possible water supply from the soil to the stomata by *S* and the flux of water that would diffuse through the stomata under ample water supply by *D* (for demand). The actual flow of water, *AET,* is now assumed to be the minimum value of *S* and *D*:

$AET=min\{S,D\}$ Eq. 3.73

The maximum possible water supply, S, is assumed proportional to the soil water content in the root area. The parameter *Emax* and the soil water content (as percentage) are known.

$$S = Emax\ W \qquad \text{Eq. 3.74}$$

As a next step, the potential conductance of the canopy under ample water supply is estimated. From Eq. 3.69 it follows:

$$g(\text{pot}) = \frac{1.6 \cdot A(\lambda\text{opt})}{CO_2(\text{atm}) \cdot (1 - \lambda\text{opt})} \qquad \text{Eq. 3.75}$$

The parameter λ_{opt} represents the "optimum" ratio of the CO_2 partial pressure inside and outside the leaf. Typically, λ_{opt} is set to 0.8. The assimilation $A(\lambda opt)$, is calculated as the integration of the assimilation rate over the vegetation cover (different PFTs) and the day or month following the equations summarized in Section 3.4.1.2. $CO_2(atm)$ is also assumed to be known, hence *g(pot)* can be calculated according to the Eq. 3.75

The potential conductance becomes zero when environmental conditions do not allow any assimilation despite optimum water supply, for example during the night (no light). The potential conductance is large when the ambient CO_2 content is very small. Then, the plant needs to open the stomatal pores in order to allow sufficient diffusion of CO_2 into the leaf.

The transpiration of water under optimum conditions, "demand" *D*, can reach *PET* (= evaporation from a wet surface). The following equation for *D* accounts for this boundary condition:

$$D = PET \cdot (1 - \exp\{-g(pot)/gm\}) \qquad \text{Eq. 3.76}$$

Where, *gm* is an empirical parameter, PET is known. *D* can thus be computed.

Now, the value obtained for the H_2O demand is compared to the value for the supply, S. In case enough water can be transported from the roots into the leaf, the actual conductance, *g(act)*, is set equal to the potential conductance:

$$g(act) = g(pot) \quad \text{for } S > D \qquad \text{Eq. 3.77}$$

In case of water scarcity, the amount of water transpired is constrained by the transport rate from the root into the leaf. At maximum, the transpiration can reach the supply, *S*. We set *D*=*S* and replace g(pot) by g(act) in Eq. 3.76 and solve for the actual stomatal conductance:

$$g(act) = gm \cdot \ln\{1 - \frac{S}{PET}\} \quad \text{for } D > S \qquad \text{Eq. 3.78}$$

Eq. 3.69 is still valid, hence:

$$A(\lambda) - g(act) \cdot CO_2(atm) \cdot (1-\lambda) \cdot \frac{1}{1.6} = 0 \qquad \text{Eq. 3.79}$$

This equation is used to calculate the actual photosynthesis rate *A* and the ratio of inner and outer CO_2 partial pressure λ for a given water supply and water content. *g(act)* und *CO2(atm)* are known. λ is varied until the above relation is satisfied. $A(\lambda)$ is calculated according to the equations in section 3.4.1.2

Above relations describe how the C-assimilation is regulated by soil moisture and evaporation of water. The soil water content itself is regulated by the evapotranspiration, precipitation, snow melting, percolation into deeper layers and runoff. For W<1 we write in a simplified form:

$$AWC \cdot \frac{dW}{dt} = precipitation + meltwater - AET\,[\text{mm/day}] \qquad \text{Eq. 3.80}$$

Above equations describe the feedback between soil water content, actual evaporation, and carbon assimilation for individual plant species or PFTs.

Photosynthesis/transpiration affects the local energy balance. The radiation absorbed by photosynthesis is not anymore available to the environment. The transpiration of water requires energy. The latent heat flux is:

$$LE = L \cdot AET \qquad \text{Eq. 3.81}$$

where L is the latent heat of evaporation for water (L=2'528 kJ kg^{-1}).

3.4.4 Synopsis

The evolution of PFTs, carbon storage and the atmospheric CO_2 on annual to centennial time scales yields the long-term interaction between climate and vegetation.

The coupling of a water-photosynthesis-soil water module to an atmospheric circulation model describes the feedback between evaporation (AET), precipitation, heat balance, soil water content, gross carbon assimilation and hence the short-term (seconds-day) interactions of vegetation and climate.

Surface roughness and albedo associated with different plant types (tree vs. grass) also affect the atmospheric heat balance and the circulation.

The coupling of the water-photosynthesis-soil water content-atmosphere module with the simulation of functional plant types (PFTs) and the equations for autotrophic and heterotrophic respiration (carbon fluxes and nutrient fluxes) yields the carbon storage in the vegetation and in the soil on time scales of days to millennia.

3.5 Evaluation of terrestrial models

Terrestrial models can be tested against different observations and measurement data. In this chapter we compare model results with data of some selected examples. Model results are produced by the Lund-Potsdam-Jena Dynamic Global Vegetation Model (LPJ-DGVM), which describes the three different levels of vegetation dynamics, carbon- and nutrient cycles and photosynthesis-transpiration, and by other spatially explicit terrestrial models. Furthermore, we compare the output of a soil model with observations.

The local seasonal cycle of carbon storage can be derived by measurements of the CO_2 flux between the atmosphere and a local ecosystem. So-called "flux-towers" are used to measure the wind and concentration of gases with a high temporal resolution.

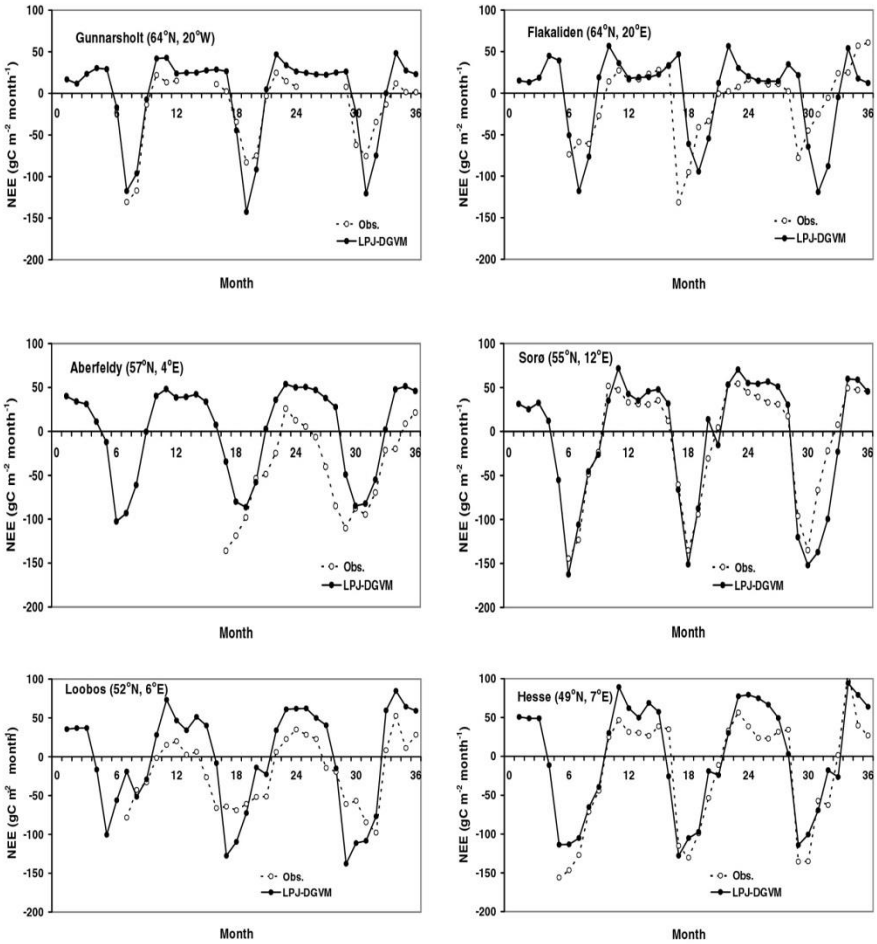

Figure 3.27: Comparison between the simulated and observed net ecosystem exchange of C (NEE). The simulation is done by the LPJ-DGVM (Lund-Potsdam-Jena Dynamic Global Vegetation Model, Sitch et al., 2003).

A further test for terrestrial models is the comparison between the modeled **global or regional sinks** and the corresponding reconstructions. The long-term global terrestrial sink flux, for example, can be derived from measurements of the O_2:N_2 ratio in the atmosphere (see Chapter 2) or calculated with an ocean model. Regional sink fluxes are estimated with an atmospheric transport model from the distribution of the atmospheric CO_2 concentration.

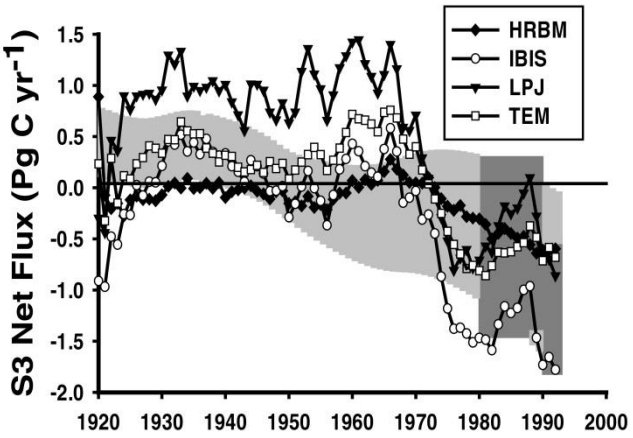

Figure 3.28: Comparison between the modeled evolution of the net flux into the biosphere of four different terrestrial models and the corresponding reconstructions. The light grey band depicts the estimated net flux (± 1 standard deviation) derived by a deconvolution of the measured atmospheric CO_2 and $13CO_2$ concentration. Dark bands represent the net flux into the biosphere as reconstructed from O_2/N_2 data. For the model simulations, the increase in atmospheric CO_2, climate change and land use change were accounted for (McGuire et al., 2001).

Interannual variations of the global terrestrial C-storage remain after subtracting the mean temporal trend of atmospheric CO_2 data. An alternative method is to derive the net fluxes into the ocean and biosphere from measurements of the atmospheric ratio of the two stable C isotopes 13C:12C.

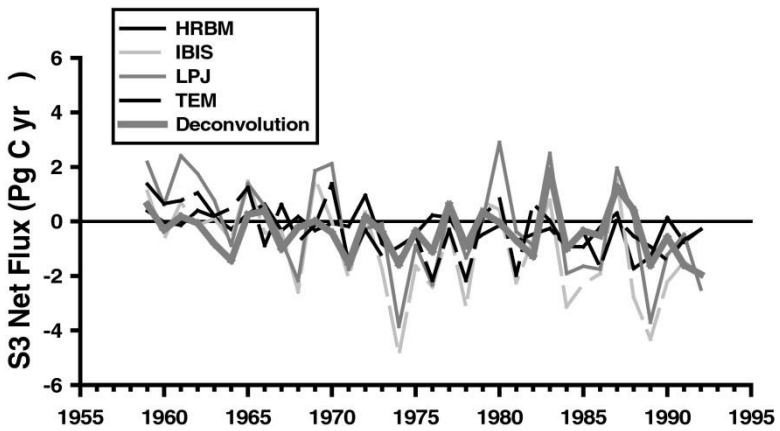

Figure 3.29: Reconstructed and modeled variation of the annual global carbon uptake/release by the land biosphere. The reconstructed values were derived by subtracting the ocean carbon uptake and the fossil emissions from the annual increase in the atmospheric C-content (McGuire et al., 2001).

The **seasonal cycle of atmospheric CO_2 concentrations** is measured continuously at different stations around the globe. The seasonal CO_2 variation, especially in the northern hemisphere, is primarily controlled by the seasonal uptake and release of C by the terrestrial biosphere. The regional net fluxes are prescribed as boundary conditions in an atmospheric transport model and the resulting seasonal variations are compared to CO_2 measurement data. Most of the stations are so-called free air stations which measure the tropospheric background concentration. The comparison between data and model results is thus representative on a continental scale.

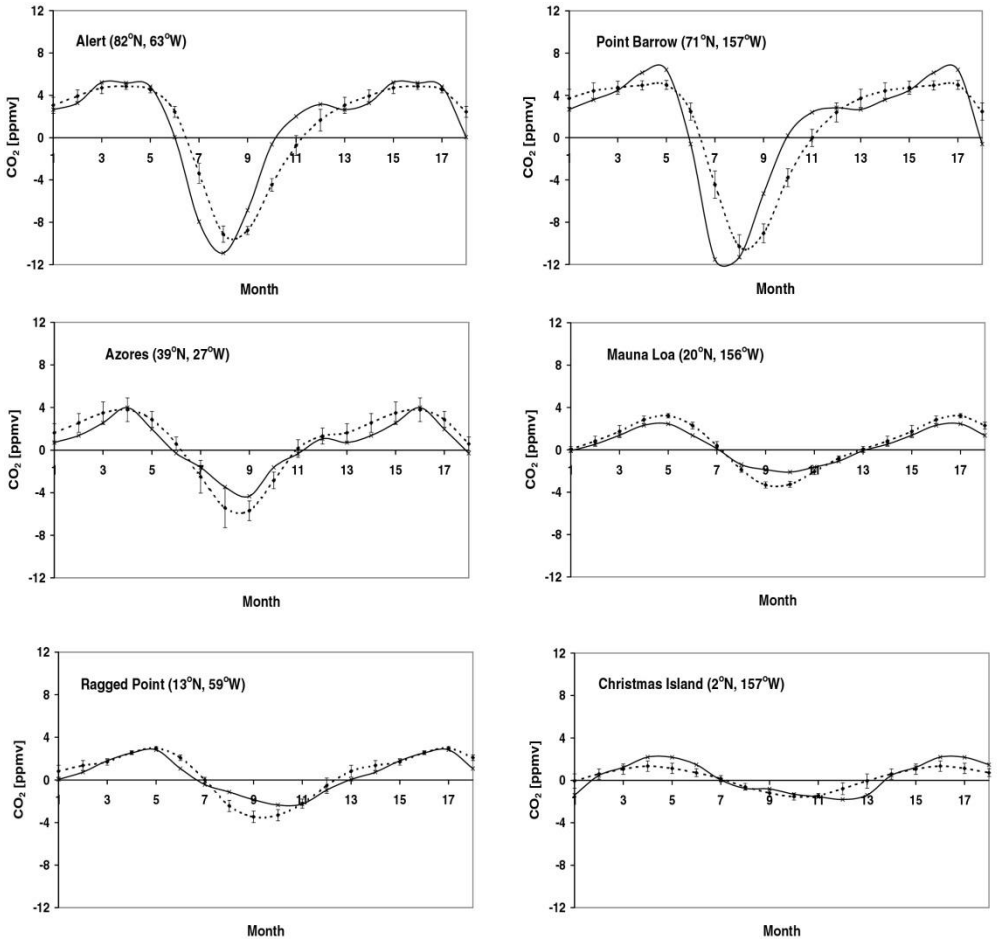

Figure 3.30: Observed seasonal variation of the atmospheric CO_2 concentration and modeled concentrations (solid line). The C-exchange fluxes as simulated by the LPJ-DGVM were prescribed in an atmospheric transport model (Sitch et al., 2003).

The **amplitude of the seasonal CO_2 variation** has increased since the beginning of the first atmospheric measurements on Mauna Loa, Hawaii. The increase points to an increased C-exchange with the land biosphere. Terrestrial models are expected to explain this increase.

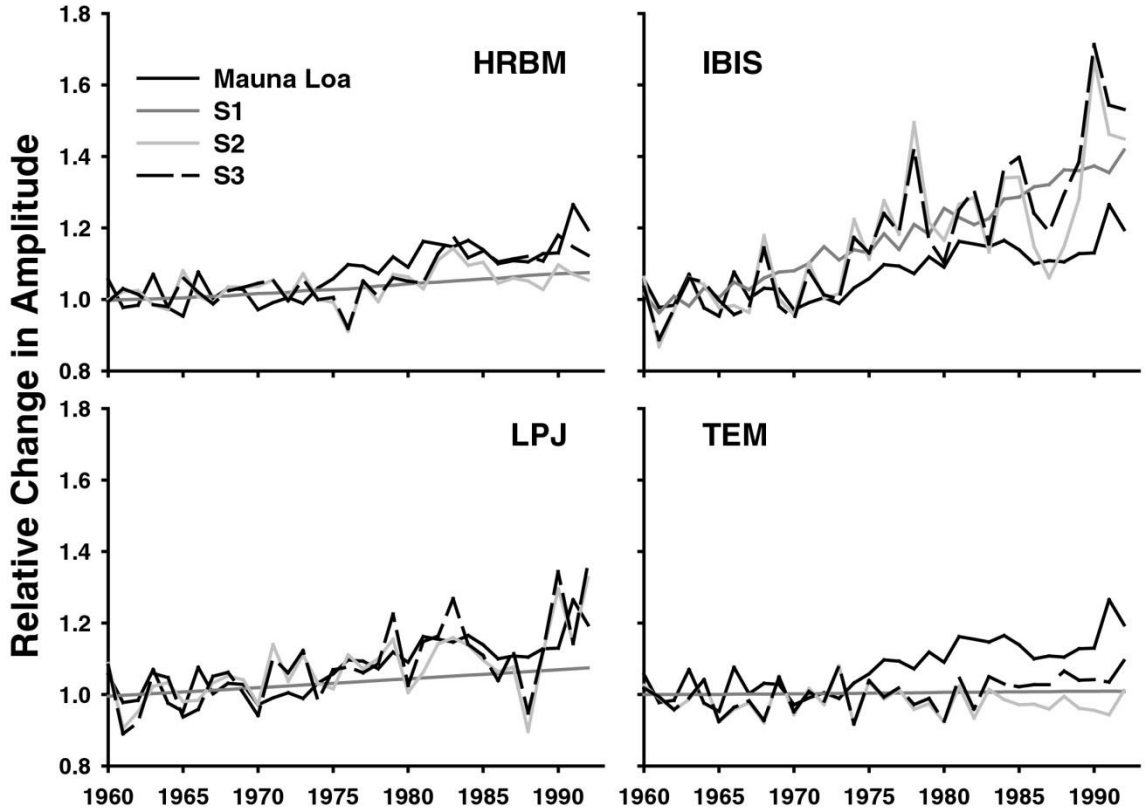

Figure 3.31: Trend in the amplitude of the seasonal CO_2 variation on Mauna Loa, Hawaii, between 1960 and 1992, derived from observations and computed from the NPP and heterotrophic respiration fluxes of four different terrestrial models. In simulation S1 only the atmospheric CO_2 increase was prescribed in the models; in simulation S2, the atmospheric CO_2 increase plus climate variability is accounted for; in simulation S3, atmospheric CO_2 increase, climate variability plus land use change is considered. The models agree that CO_2 fertilisation and land use change increase the amplitude (McGuire et al., 2001).

Bomb-produced ^{14}C and the mean residence time of organic carbon in the soil: As emphasized in previous sections, the mean residence time of organic carbon in the soil, τ, is of high importance for the terrestrial C-storage. Above-ground nuclear bomb tests in the 50s and 60s of the 20th century produced relatively large amounts of the radioactive ^{14}C isotope ($^{14}C : {}^{12}C \approx 10^{-12}$). The atmospheric $^{14}C : {}^{12}C$ ratio increased by about 80% between 1950 and 1963. Bomb-produced atmospheric ^{14}C enters the ocean and the biosphere. The radioactive decay plays a minor role on decadal time scales (half life: 5500 years). The bomb signal can be detected in the ocean as well as in the biosphere. Measurements on the $^{14}C : {}^{12}C$ ratio of organic carbon or on the respiration flux allow an estimate for the residence time of C in the soil and a verification of the time scales used in models. Unfortunately, only few $^{14}C : {}^{12}C$ measurements on the soil carbon are available.

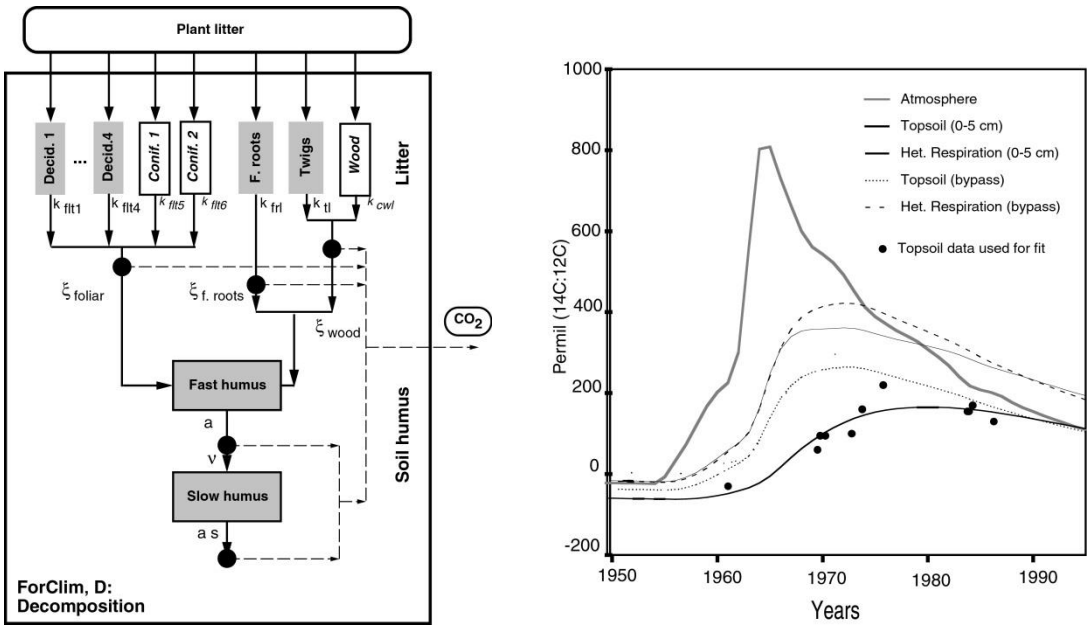

Figure 3.32: Schematic depiction of the carbon pools and fluxes in the ForClim model (left). Observed evolution of the $^{14}C : {}^{12}C$ ratio in the troposphere an in the organic C-pool of the upper soil layer in Meathop Wood (England) (right). The model is driven with the observed atmospheric $^{14}C : {}^{12}C$ values and observed input fluxes into the litter reservoirs (leaf shedding). The model ForClim reproduces the observed values in the soil well when 68% of the organic carbon have a mean residence time of 25 years ("fast humus" reservoir) and 32% have a mean residence time of 3500 a ("slow humus" reservoir). Furthermore, the modeled $^{14}C : {}^{12}C$ ratio of the heterotrophic respiration flux and results without litter pools are shown (Perruchoud et al., 1999).

Modeled hydrological quantities such as the runoff of water or the soil moisture can also be compared to observations. The temporal evolution of the soil moisture is affected by the transpiration.

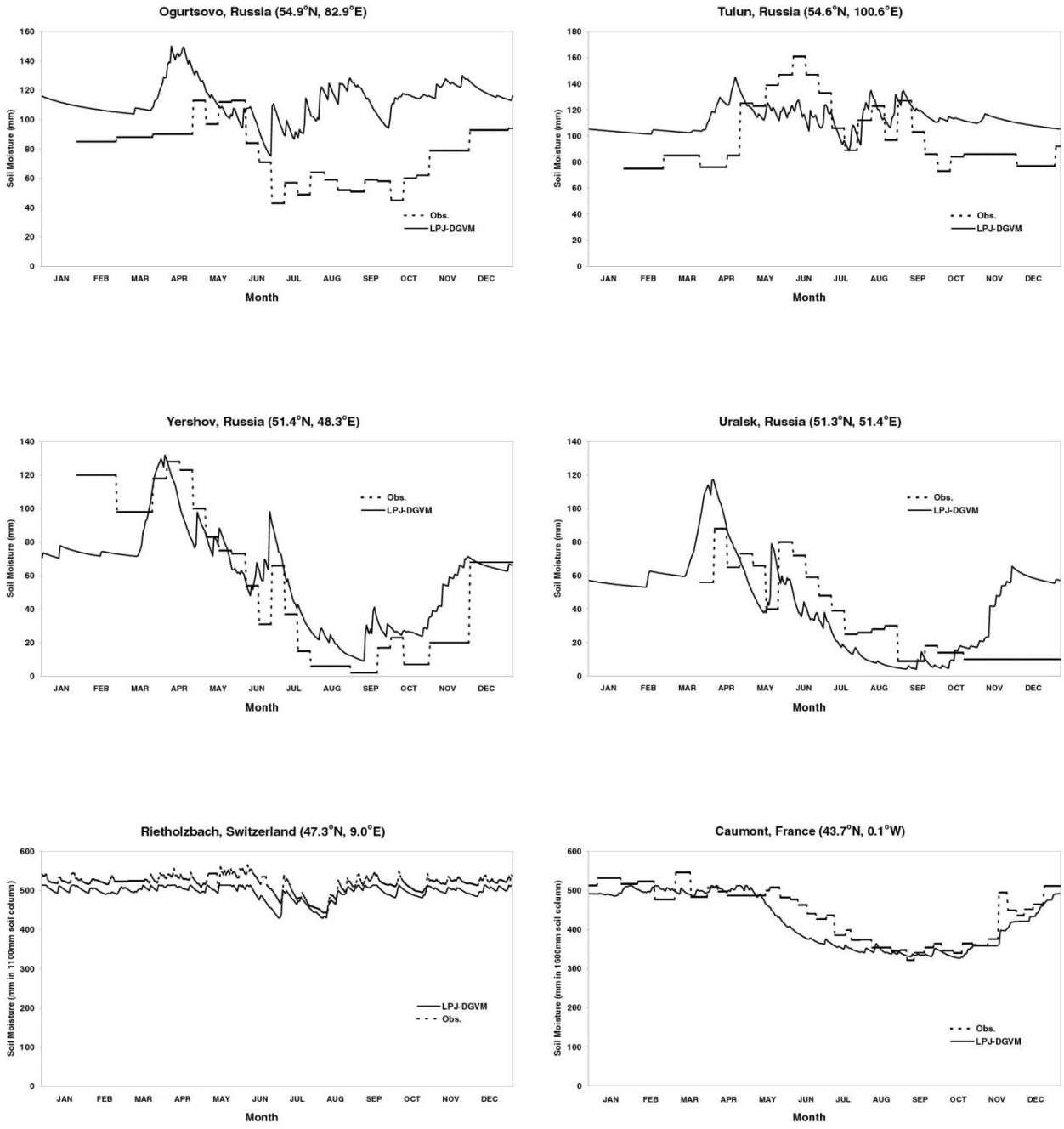

Figure 3.33: Observed and simulated soil moisture at different locations, as modeled by the LPJ-DGVM (Sitch et al., 2003).

3.6 Land Use Activities

Past and current land use and land use changes (LULUC) contribute to the ongoing anthropogenic climate change (IPCC, AR4, Chapter 2). LULUC activities continue to cause large emissions of carbon dioxide and other greenhouse gases to the atmosphere and alter surface properties such as albedo and water vapor exchange. Presently, about 40% of the world's land surface (excluding deserts, barren, and ice covered land) is used as cropland or pasture.

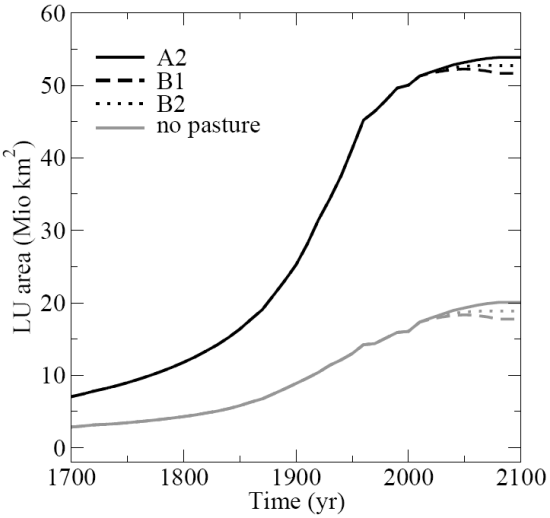

Figure 3.34: Expansion of cropland (grey) plus pastoral land and built-up area (black line).

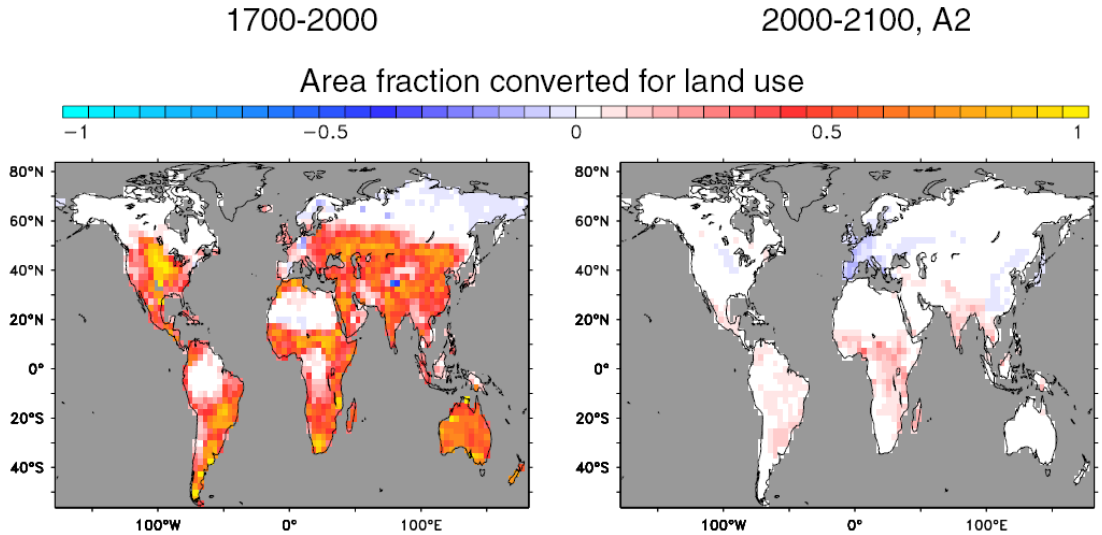

Figure 3.35: Area fraction converted for land use over the period 1700 to 2000 (left) and 2000 to 2100 under SRES scenario A2 (right).

A fundamental input for assessing LULUC impacts is spatially explicit and detailed fields that describe the spatio-temporal evolution of the area under land use. Traditionally, such data are gathered by the Food and Agricultural Organization (FAO) of the United Nations. Other maps have recently become available for cropland (Ramanakutti and Foley, 1999) and for cropland, pasture and built-up area (HYDE database) for the industrial period and more recently for the Holocene. Land use maps are also part of the output of some integrated assessment models used to develop mitigation and non-mitigation emission scenarios for the 21st century. In combination, these products provide the opportunity to study the evolution of land use, atmospheric CO_2 and climate over the industrial period and this century in a consistent way (Leemans et al, 2001).

Carbon emissions from LULUC have traditionally been estimated by a book-keeping method. Houghton, Tellus, 2003 used deforestation data from FAO and a response function that takes into account temporal delays between carbon emissions and uptake after deforestation or abandonment of used land. The book-keeping approach neglects any feedback between atmospheric CO_2, climate and carbon emissions from LULUC as well as changes in management practices such as fire suppression, thinning or grazing. The environmental feedbacks have been taken into account in a few global studies with terrestrial models either forced by prescribed climate fields and atmospheric CO_2 or run as a module in coupled carbon cycle – climate model.

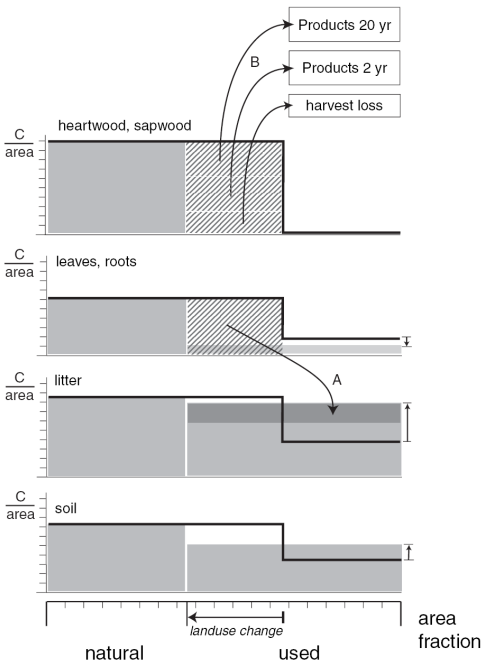

Figure 3.36: Fate of carbon when land is converted. A fraction of the carbon stored in the heartwood and sapwood of trees is transferred to product pools (paper, furniture …) and a portion is directly transferred to the atmosphere (harvest loss). Carbon in leaves and roots of living vegetation is transferred to the litter pool where it decays to soil organic matter and to CO_2 that escapes to the atmosphere. In book-keeping approaches, a specific response function is assumed that characterize the time scale over which carbon is transferred from the litter to the atmosphere and how vegetation re-grows after land is abandoned. In the BernCC model, the turnover of litter and soil carbon is mechanistically simulated and depends on the environmental conditions such as temperature and soil moisture.

Estimates of carbon emissions due to LULUC are uncertain. Carbon fluxes due to land use constitute the least well quantified flux in the global carbon budget. Land use emissions are estimated to be in the range from 5 to 27 GtC over the 1990 decade based on estimates from a range of studies and methodologically different approaches (IPCC Chapter 7). It is estimated that about a third (155 GtC) of total anthropogenic CO_2 emissions has been emitted through LULUC over the period 1850 to 2000. Houghton, 2003, estimated average tropical emissions of 2.2±0.6 GtC/yr for the nineties and negligible emissions from non-tropical areas. In contrast, De Fries et al. PNAS, 2002, obtained a tropical emission rate of 0.5 to 1.6 GtC/yr using the same book-keeping approach, but using satellite observations instead of FAO data. Archard et al. Science, 2002, independently estimated similarly low emissions in the tropics for the eighties and nineties as DeFries et al.

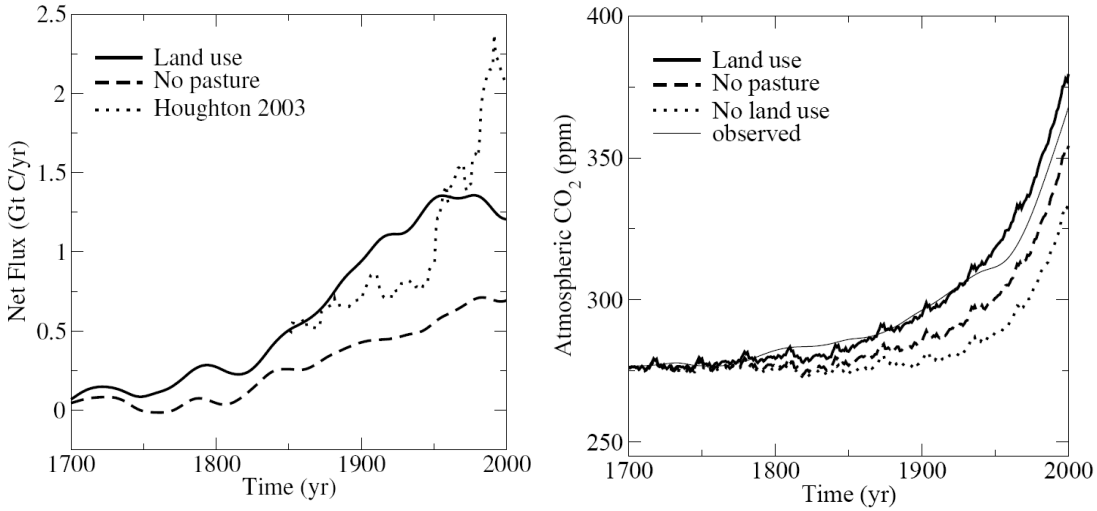

Figure 3.37: Estimated carbon emissions by land use and land use change from the book-keeping approach of Houghton applied to land cover data of the Food and Agriculture Organisation of the United Nations (FAO) (dash), and as simulated with the BernCC model with prescribed evolution of the area under pasture and cropland, including built-up (solid) and under pasture only (long-dash) from the HYDE3.0 database (left). Simulated atmospheric CO_2 for prescribed fossil carbon emissions and with and without prescribed land use (right).

Uncertainties in the quantitative understanding of carbon emissions from LULUC have negative consequences for the quantification of carbon cycle processes, the validation of carbon cycle models, and lead to uncertainties in projections of atmospheric CO_2 and climate change, and consequently, affect the formulation of emission mitigation strategies. Several lines of evidence suggest that terrestrial ecosystems have been a net sink for carbon in recent decades. This implies that sink processes compensate the CO_2 emissions from LULUC activities:

- If the CO_2 emissions from LULUC are large, this inferred terrestrial sink is large.
- If the CO_2 emissions from LULUC are small, then only a small sink is operating.

The mechanisms thought to be responsible for the inferred terrestrial carbon sink include enhanced growth through CO_2 fertilization and/or nitrogen deposition, but also woody

encroachment, forest re-growth and changes in management practices potentially not taken into account in current assessments of emissions from LULUC. As long as the magnitude and nature of the inferred current sink is not well-known it remains difficult to narrow uncertainties in projections of these potential sink processes and CO_2. For example, projected atmospheric CO2 for 2100 is up to 30% higher in simulations where CO_2 fertilization is not operating after year 2000 as opposed to simulations were CO_2 fertilization is continuing. Similarly, carbon emissions leading to stabilization must be about 30% lower in simulations without CO_2 fertilization than in simulations with CO_2 fertilization.

Traditionally, CO_2 emissions from LULUC are prescribed as an external source in coupled carbon cycle-climate model used to project future climate change. However, land carbon storage is overestimated in such simulations, since no correction is made for the increasing area under cultivation, where carbon turnover is faster and sink capacity reduced compared to area covered by forests.

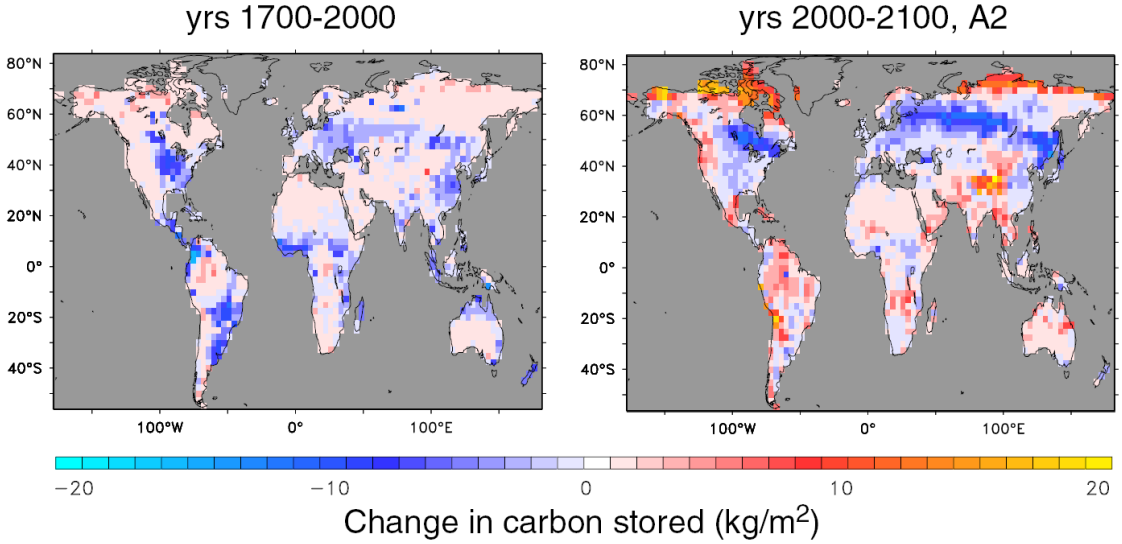

Figure 3.38: Changes in terrestrial carbon storage in the past and for the future under changing atmospheric CO_2, climate, and land use.

At Climate and Environmental Physics, we have applied the Bern Carbon Cycle-Climate (BernCC) model that includes the Lund-Potsdam-Dynamic Global Vegetation Model (LPJ-DGVM) complemented with a new module describing LULUC processes to address a range of LULUC related research questions. The most recent maps from the History Database of the Global Environment (HYDE3.0) and from the most recent post-SRES scenarios from the Institute of Applied System Analyses (IIASA, reference) are used to force the BernCC model.

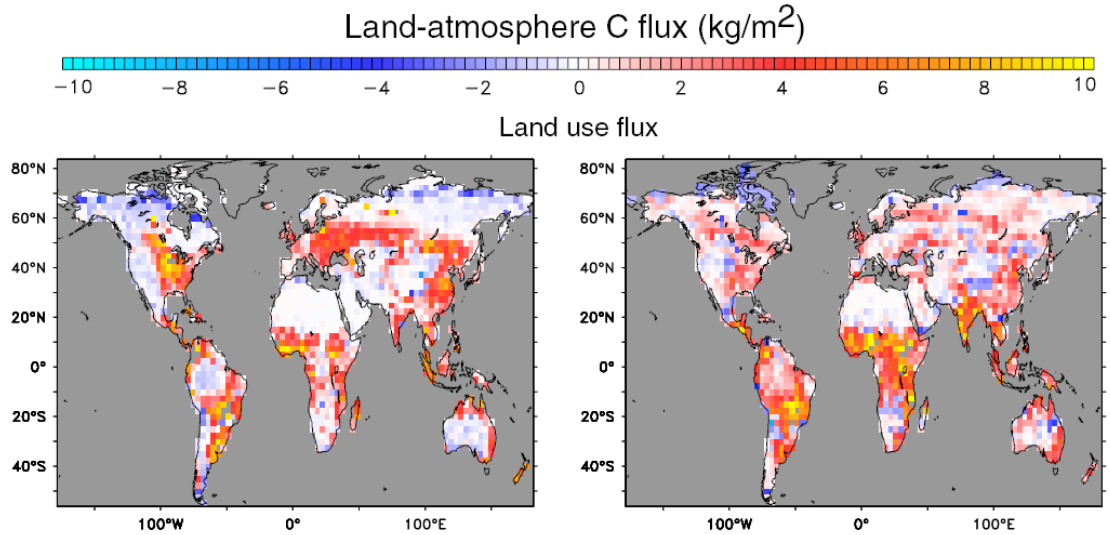

Figure 3.39: Cumulative carbon flux from land to the atmosphere in response to changes in land use as simulated with the BernCC model for the period 1700 to 2000 (left) and for this century (right). The flux is evaluated as the difference between a simulation with and without prescribed cropland and pasture expansion.

The land use flux simulated by the model can be attributed to different mechanisms.

- "Book-keeping flux": Carbon release as a direct consequence of land use change, as represented in statistical book-keeping models. The book-keeping models take into account conversion of carbon to product pools and direct release to the atmosphere during the land conversion process; transfer of carbon (slash, leaves, twigs) to litter and soils where the carbon decays following prescribed time scales; re-growth after land abandonment is assumed to follow a prescribed evolution. Changes in CO_2 and climate are by definition not included in the book-keeping approach.
- "Lost sinks": on converted areas, natural vegetation (mostly forest) is replaced by agriculture, which is less efficient as a CO_2-fertilised sink. This postulated flux is potentially important for the future.
- Fertilization and climate feedback: atmospheric CO_2 increases due to land use change. The higher CO_2 stimulates uptake in vegetation. Changes in climate are found to have a small net effect on simulated land use fluxes (but a substantial effect on simulated total land-atmosphere fluxes).

In the past, the book-keeping flux has been dominating, but the land-use fertilization feedback has reduced the total land use flux by about 30%. In the future, the "lost sink" mechanism dominates when industrial CO_2 emissions remain high and if CO_2 fertilization is indeed operating.

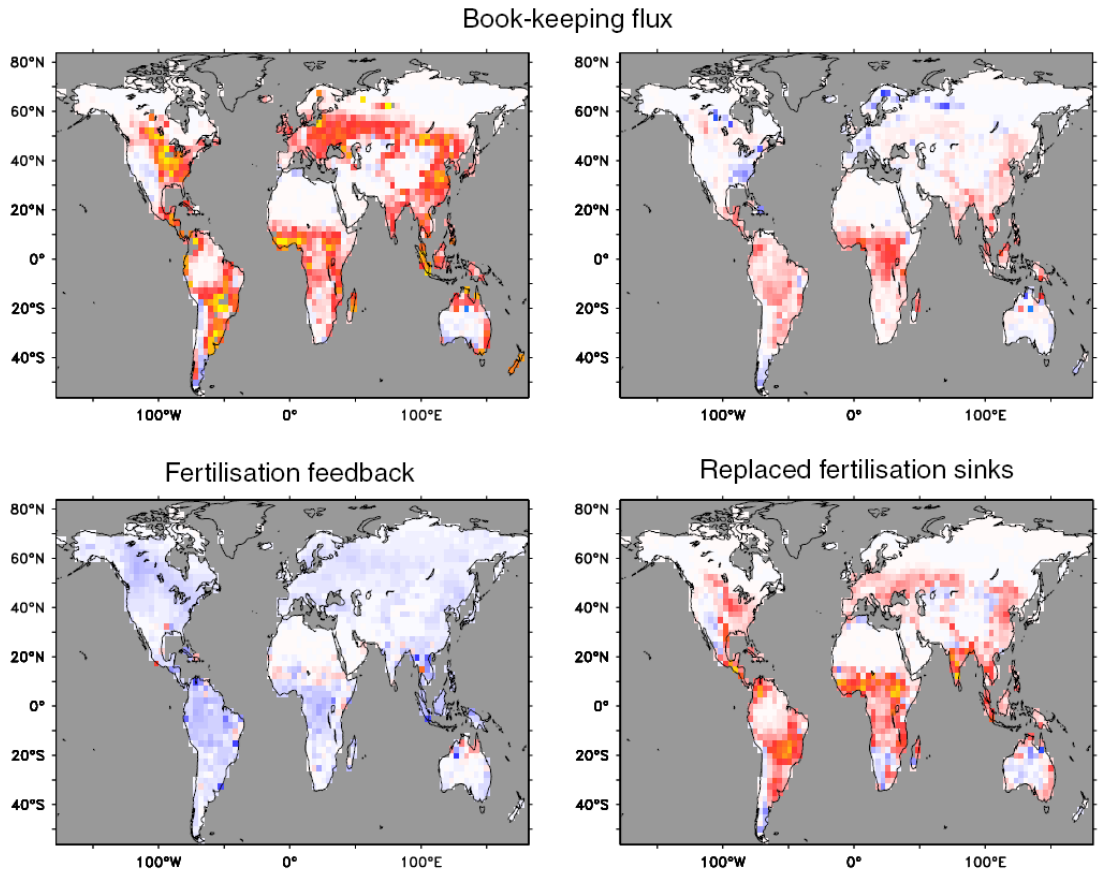

Figure 3.40: Attribution of carbon fluxes from land use to different mechanisms for the period 1700 to 2000 (left) and 2000 to 2100 (right). The upper row show the fluxes resulting from land conversion without taking into account other environmental factors such as CO_2 and climate change. The lower left panel shows how higher atmospheric CO_2 simulated with prescribed land use compared to a simulation without land use. This stimulates additional carbon uptake (blue) through increased CO_2 fertilization. The lower right panel shows how much less carbon is assimilated on agricultural land as compared to natural land under future rising CO_2.

Literature:

Age distribution: concepts and radiocarbon

Bolin B, Rodhe H (1973) A note on the concepts of age distribution and transit time in natural reservoirs. *Tellus*, 25, 58-62.

Trumbore SE, Chadwick OA, Amundson R (1996) Rapid exchange between soil carbon and atmospheric carbon dioxide driven by temperature change. *Science*, 272, 393-396.

D. Perruchoud, F. Joos, A. Fischlin, I. Hajdas, and G. Bonani. Evaluating time scales of carbon turnover in temperate forest soils with radiocarbon data. *Global Biogeochemical Cycles* , 13, 555-573, 1999.

Land use and land cover:

Achard, F., H.D. Eva, H.-J. Stibig, P. Mayaux, J. Gallego, T. Richards, and J.-P. Malingreau. 2002. Determination of deforestation rates of the world's humid tropical forests. *Science* 297, 999-1002.

DeFries, R.S., R.A. Houghton, M.C. Hansen, C.B. Field, D. Skole, J. Townshend. 2002. Carbon emissions from tropical deforestation and regrowth based on satellite observations for the 1980s and 90s. *Proceedings of the National Academy of Sciences* 99, 14256-14261.

Global Land Cover 2000 database. European Commission, Joint Research Centre, 2003. http://www-gem.jrc.it/glc2000.

Houghton, R.A. Revised estimates of the annual net flux of carbon to the atmosphere from changes in land use: 1850-1900. *Tellus*, 51B, 298-313, 1999.

Ramankutty, N., and J.A. Foley. 1999. Estimating historical changes in global land cover: Croplands from 1700 to 1992. *Global Biogeochemical Cycles* 13, 997-1027.

Strassmann, K. M., Joos, F. & Fischer, G. (2007) Simulating effects of land use changes on carbon fluxes: past contributions to atmospheric CO_2 increases and future commitments due to losses of terrestrial sink capacity. *Tellus B* 60B: 583-603.

Photosynthesis and transpiration

Collatz GJ, Ribas-Carbo M, and Berry JA (1992) A coupled photosynthesis - stomatal conductance model for leaves of C_4 plants. *Australian Journal of Plant Physiology*, 19, 519-538.

DeLucia EH, Hamilton JG, Naidu SL et al. (1999) Net primary production of a forest ecosystem with experimental CO_2 enrichment. *Nature*, 284, 1177-1179.

Donohue, R. J., Roderick, M. L., McVicar, T. R., and Farquhar, G. D.: Impact of CO2 fertilization on maximum foliage cover across the globe's warm, arid environments, Geophysical Research Letters, 40, 3031-3035, 10.1002/grl.50563, 2013.

Farquhar GD, von Caemmerer S Berry JA (1980) A biochemical model of photosynthetic CO_2 assimilation in leaves of C_3 species. *Planta*, 149, 78-90.

Keenan, T. F., Hollinger, D. Y., Bohrer, G., Dragoni, D., Munger, J. W., Schmid, H. P., and Richardson, A. D.: Increase in forest water-use efficiency as atmospheric carbon dioxide concentrations rise, Nature, 499, 324-327, 10.1038/nature12291

Monteith, JL (1995) Accomodation between transpiring vegetation and the convective boundary layer. *Journal of Hydrology*, 166, 251-263.

Models:

Cox PM, Betts RA, Jones CD, Spall SA, and Totterdell JJ (2000) Acceleration of global warming due to carbon-cycle feedbacks in a coupled climate model. *Nature*, 408, 184-187.

Cramer W, Bondeau A, Woodward FI, Prentice IC, Betts RA, Brovkin R, Cox PM, Fisher V, Foley JA, Friend AD, Kucharik C, Lomas MR, Ramankutty N, Sitch S., Smith B., White A., Young-Molling C (2001) Global response of terrestrial ecosystem structure and function to CO_2 and climate change: results from six global dynamic vegetation models. *Global Change Biology.*, 7, 357-373.

D. McGuire, S. Sitch, J. S. Clein, R. Dargaville, G. Esser, J. Foley, M. Heimann, F. Joos, J. Kaplan, D. W. Kicklighter, R. A. Meier, J. M. Melillo, B. Moore III, I. C. Prentice, N. Ramankutty, T. Reichenau, A. Schloss, H.Tian, L. J. Williams, U. Wittenberg. Carbon balance of the terrestrial biosphere in the twentieth century: Analyses of CO_2, climate and land-use effects with four process-based ecosystem models. *Global Biogeochemical Cycles*, 15, 183-206, 2001.

Haxeltine A , Prentice IC (1996) BIOME 3: an equilibrium terrestrial biosphere model based on ecophysiological constraints, resource availability and competition among plant functional types. *Global Biogeochemical Cycles*, **10**, 693-703.

Joos F, Prentice IC, Sitch S, Meyer R, Hooss G, Plattner G-K, Gerber S, Hasselmann K (2001) Global warming feedbacks on terrestrial carbon uptake under the Intergovernmental Panel on Climate Change (IPCC) emission scenarios. *Global Biogeochemical Cycles*, 15, 891-907.

D. W. Kicklighter, M. Bruno, S. Doenges, G. Esser, M. Heimann, J. Helfrich, F. Ift, F. Joos, J. Kaduk, G. H. Kohlmaier, A. D. McGuire, J. M. Melillo, R. Meyer, B. Moore III, A. Nadler, I. C. Prentice, W. Sauf, A. L. Schloss, S. Sitch, U. Wittenberg, and G. Würth. A first order analysis of the potential role of CO_2 fertilization to affect the global carbon budget: A comparison study of four terrestrial biosphere models. *Tellus* , Ser. B, 51, 343 - 366, 1999.

Sitch S, Smith B, Prentice IC, Arneth A, Bondeau A, Cramer W, Kaplan JO, Levis S, Lucht W, Sykes MT, Thonicke K,Venevsky S (2003) Evaluation of ecosystem dynamics, plant geography and terrestrial carbon cycling in the LPJ dynamic global vegetation model. *Global Change Biology*, **9**, 161-185.

Thompson, M. V. J. T. Randerson, Malmström and C. B. Field. (1996) Change in net primary production and heterotrophic respiration: how much is necessary to sustain the terrestrial carbon sink, *Global Biogeochemical Cycles*, 10, 711-726.

4 Tracer transport in the ocean

The ocean is a key reservoir for the climate system and the carbon cycle:

- The ocean is the largest of the three rapidly exchanging reservoirs and plays a central role in the global carbon cycle. It controls the atmospheric CO_2 concentration on time scales of several millennia. The ocean contains 60 times the amount of inorganic carbon of the atmosphere. On an even longer time scale, the interaction between ocean sediments (carbonates) and the erosion of carbonate- and silicate rocks on land controls the total amount of C in the three reservoirs atmosphere-biosphere-ocean.
- The distribution of carbon in the ocean is controlled by the interaction of physical processes such as the circulation, chemical processes such as the solubility of CO_2 and the carbonate chemistry in water and biological processes such as the production and decay of organic material, and also calcite and aragonite ($CaCO_3$)
- The oceanic carbon cycle is tightly coupled to the nutrient cycles of iron, phosphate, nitrate, oxygen and some other elements.
- The ocean is the source of life. Photosynthesis is older than $3 \cdot 10^9$ a. Originally, its occurrence was restricted to the sea because the UV radiation on land was inhibiting the development of living organisms when the ozone layer did not exist. The O_2 partial pressure was very low for a long time and the current atmospheric O_2 content was not reached until 2 to 0.5 billion years BP. The majority of atmospheric oxygen was produced by photosynthesis, thus by the production of organic material. However, free O_2 is only conserved when organic material is not oxidized. For each mol of net produced O_2, 1 mol C_{org} (organic carbon) has to enter the sediments in a non-oxidized state.

In this chapter, we present a qualitative discussion on the transport and transport time scale in the ocean. Two reasons are:

- The transport from the surface to the deep is the limiting step for the uptake of anthropogenic CO_2.
- The ocean circulation plays a significant role for the natural C-cycle and past atmospheric CO_2 and climate variations.

Tracers in the ocean allow us to estimate transport rates and water mass distributions. Measured tracer distributions are thus a crucial source of information and enable us to make a quantitative analysis of the role of the ocean in the climate system.

Stable tracers without sources and sinks in the ocean (salt and temperature) reveal the distribution of water masses but do not contain direct temporal information.

- The concentration of nutrients and oxygen is affected by photosynthesis in the surface ocean and re-mineralization of biogenic material, and can yield information about the combined effect of physical transport and biological activity.

- Thanks to their natural decay, radioactive tracers contain temporal information. ^{14}C and ^{39}Ar, of which the sources are located in the atmosphere, penetrate the ocean. At the same time, their concentration declines with time (radioactive decay).
- Transient anthropogenic tracers with varying and known atmospheric history also contain temporal information. Prominent examples of tracers that enable a reconstruction of the vertical transport in the upper ocean on time scales of decades are ^{3}H, or ^{14}C, ^{85}Kr from the nuclear industry, freons (CFCs), and ^{13}C from fossil fuels.

4.1 Transient tracers: How fast does the atmospheric disturbance penetrate the ocean?

4.1.1 The ^{14}C signal of above-ground nuclear bomb tests

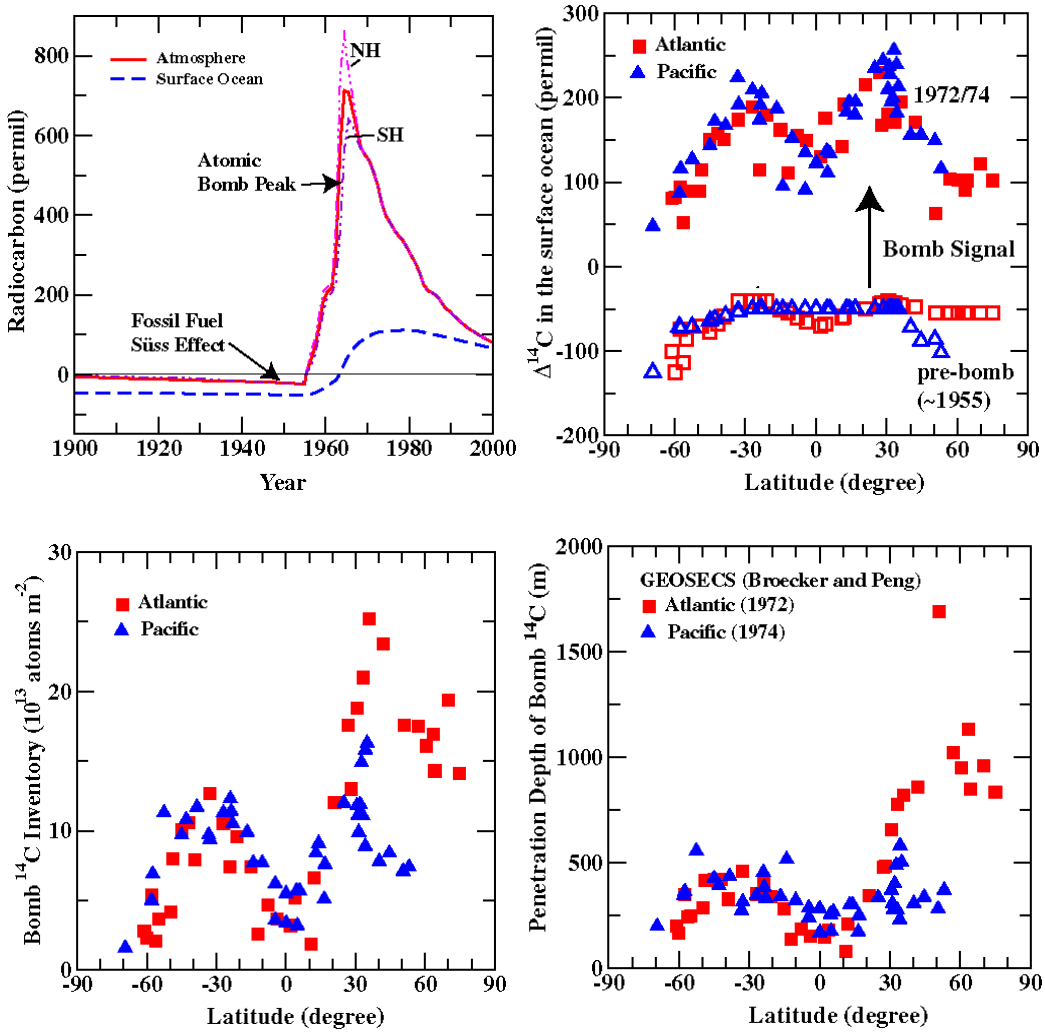

Figure 4.1: The observed signal of above-ground atomic bomb tests. After the test ban of 1963, atmospheric $\Delta^{14}C$ values decline because the signal is taken up by the ocean and the land biosphere.

Due to nuclear bomb tests in the 50s and 60s, the atmospheric ^{14}C:^{12}C ratio roughly doubled (the total amount of C was not affected, since ^{14}C:$^{12}C \sim 10^{-12}$. The signal of this perturbation is

clearly visible in the upper thermocline. Thus, it can be said that the uppermost layers of the ocean, up to a few hundreds of meters, are mixed within decades. For bomb-produced ^{14}C the radioactive decay is insignificant and the amount of bomb-produced ^{14}C may be assumed to be constant (until today). Bomb-produced $^{14}CO_2$ penetrates the ocean analogous to CO_2. In the 1970s and again in the 1990s, the distribution of the ^{14}C:^{12}C ratio was systematically recorded.

Commonly, the penetration depth into the ocean is quantified by the Mean Penetration Depth, z_{pen}: Let us consider the case of an exponential decline of the tracer concentration in the ocean, C, with depth z:

$$C(z) = C_{surf} \cdot \exp(-\frac{z}{z_{pen}})$$

The inventory per unit area (column inventory), I, amounts to:

$$I = C_{surf} \cdot z_{pen}$$

For generalization, we also define for the non-exponential case:

$$z_{pen} = \frac{I}{C_{surf}} \qquad \text{Eq. 4.1}$$

The regional distribution of the penetration depth exhibits maxima in the Northern Atlantic and between 30°S and 60°S (Figure 4.1). In this region, we expect the largest inventory of anthropogenic CO_2.

The penetration depth of bomb-produced ^{14}C was about 340 m in the 1974. This penetration depth provides a lower bound for the penetration and thus the uptake of anthropogenic CO_2 by the ocean, because the atmospheric CO_2 increase occurred over a longer time period than the change in the atmospheric ^{14}C:^{12}C ratio.

GEOSECS EXPEDITION	Mean Penetration Depth of Bomb ^{14}C (m)
Atlantic (1972/3)	414
Pacific (1973-4)	311
Indian Ocean (1977-8)	309
Global Ocean (1972-8)	344

Table 4.1: Mean penetration depth of bomb-produced ^{14}C.

4.1.2 Penetration of Chlorofluorocarbons into the ocean

Due to processes related to industrial production, CFCs have been emitted to the atmosphere since the 1930s. Many of these compounds have no (or very limited) natural sources. The atmospheric concentrations of different CFCs have seen a pronounced increase (Figure 4.2). A corresponding increase takes place in the ocean.

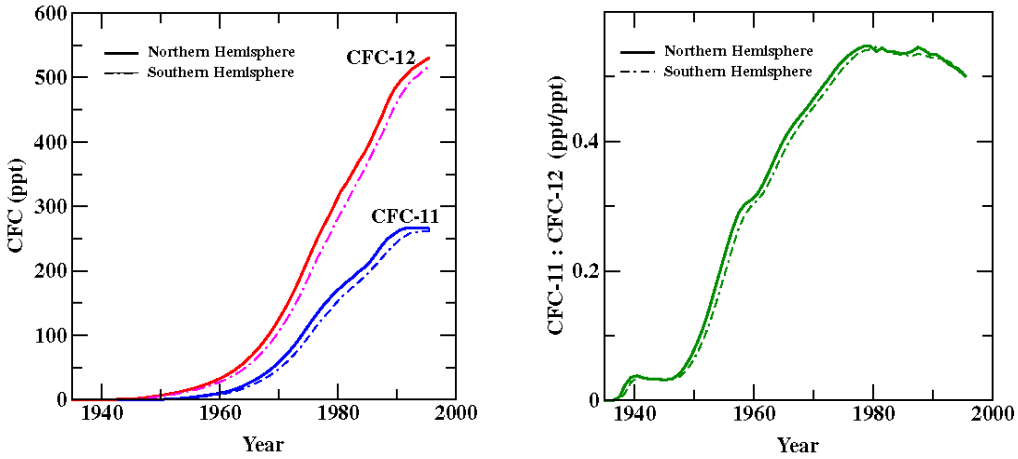

Figure 4.2: Observed increase of CFC-11 and CFC-12 in the atmosphere (left). CFC-11 and CFC-12 do not have any natural sources and have been produced industrially since the end of the 30s. The ratio of CFC-11 to CFC-12 has increased roughly linearly until around 1980 (right). This allows us to attribute an "age" to measured CFC ratios in the water.

The typical time scale for attaining an equilibrium between the mixed layer and the atmosphere is about 1 month for CFCs. Thus, the CFC concentration in the surface ocean is typically almost at equilibrium with the atmospheric concentration. Consequently, the CFC distribution in the ocean is primarily a function of known quantities (atm. concentration, solubility) and transport rates. These tracers are ideal to study oceanic transport processes and the penetration of an atmospheric disturbance into the ocean on time scales of decades.

The atmospheric ratio of CFC-11 to CFC-12 increased until the beginning of the 80s. As a first order approximation, the attribution of measured CFC ratios in the thermocline to the according atmospheric ratio yields the point in time at which the water left the surface (CFC-age).

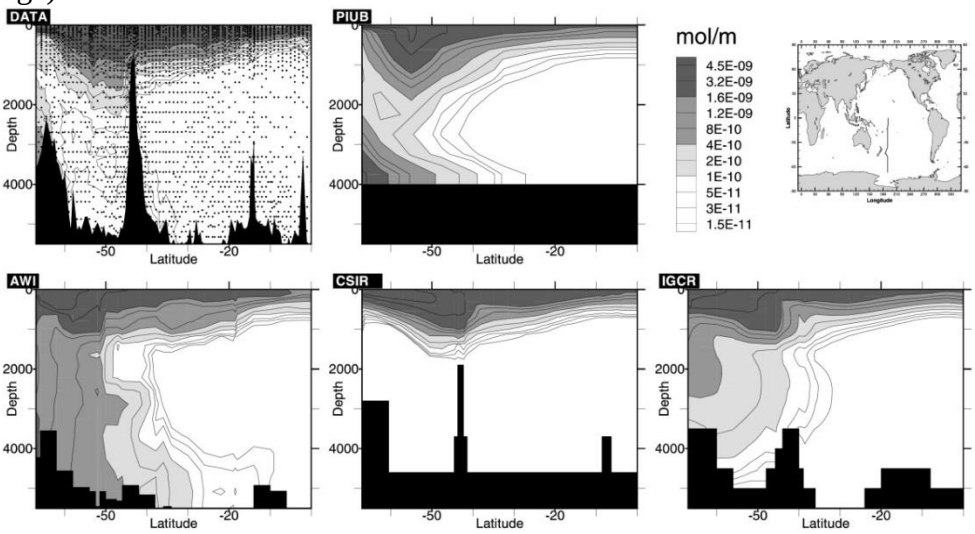

Figure 4.3: Measured and modelled distribution of CFC-11 along the WOCE section P15s in the western Southern Pacific. The data reveals that in southern latitudes, CFC-11 penetrates to a depth of up to 4000 meters. The model of the Physics Institute of the University of Berne (PIUB) and the models of the AWI and the IGCR exhibit a strong penetration of CFC into depth, while the CSIRO model is too strongly stratified.

In the past years, the distribution of CFC-11 and CFC-12 was systematically recorded by the World Ocean Experiments (WOCE). This allows a thorough test of ocean models as it was conducted by the Ocean Carbon Model Inter-comparison Project (OCMIP).

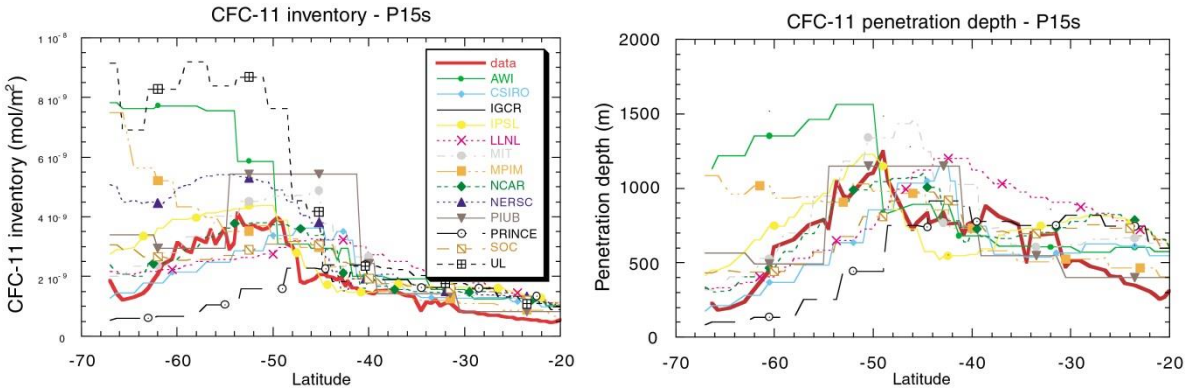

Figure 4.4: Inventory and penetration depth of CFC-11 across the WOCE section P15s in the Southern Pacific.

Like for bomb-produced ^{14}C, the largest inventories and penetration depths are localized in the Southern Ocean between 30°S and 60°S and in the northern North Atlantic. Since the penetration of anthropogenic CO_2 is analogous to the penetration of bomb-produced ^{14}C and CFCs, the largest inventories of anthropogenic CO_2 are expected in the same regions.

4.1.3 The oceanic increase in DIC during the past 200 years: regional distribution

Reconstructions of the increase in DIC since the beginning of the industrialization are derived from the WOCE data and shown in Figure 4.5. A particularly high amount of anthropogenic CO_2 can actually be found in the North Atlantic and between 30°S and 60°S in the well-ventilated Antarctic Intermediate Water (AAIW). The globally integrated change of the oceanic carbon inventory has been estimated from tracer data to about 118 GtC for the year 1994.

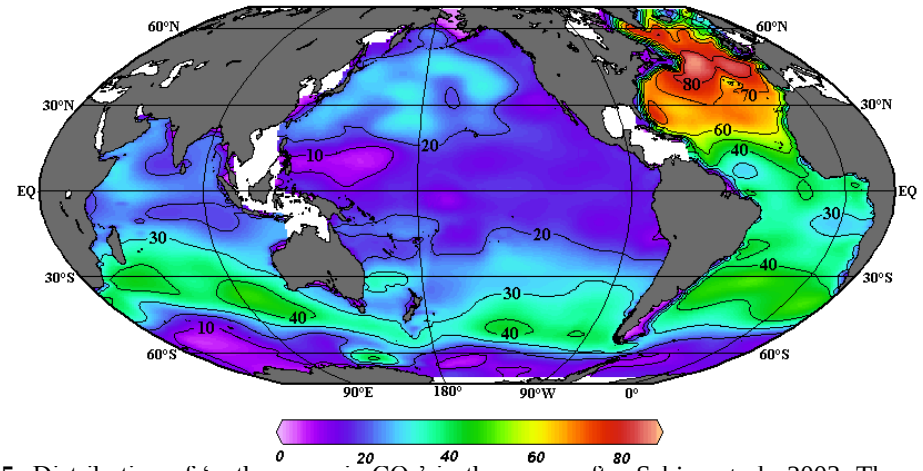

Figure 4.5: Distribution of 'anthropogenic CO_2' in the ocean after Sabine et al., 2003. The map illustrates the reconstructed increase in DIC in mol per m^2.

4.2 Stable tracers and the distribution of water masses

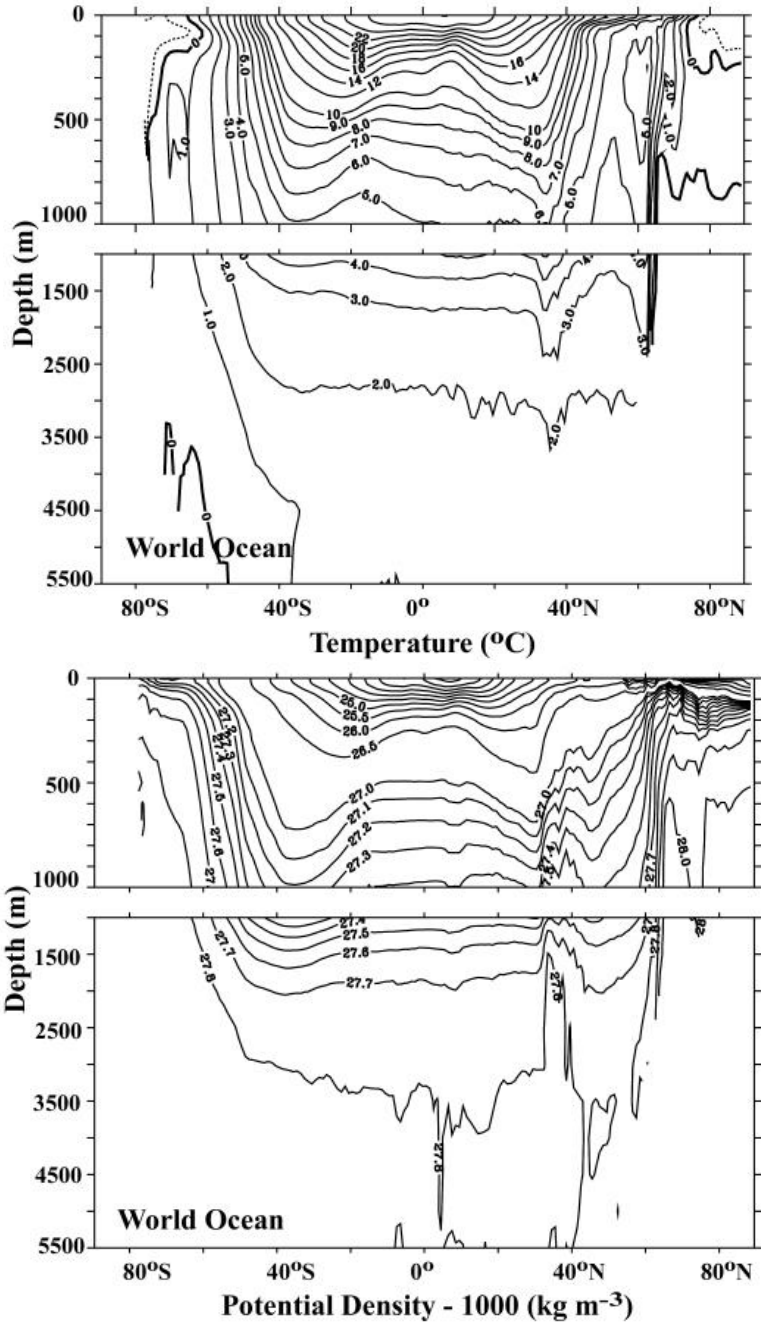

Figure 4.6: Annual mean zonal distribution of temperature (°C) (above) and potential density, ρ_θ (kg m^{-3}), (below) in the global Ocean.

Stable tracers such as salt and temperature (and thus density) as well as tracers that are tightly linked to the carbon cycle (O_2, DIC, P, Alk) contain information about the distribution of water masses in the ocean. The deep ocean is cold hence; it is fed by water that originates from the high latitude (cold) surface ocean. In contrast, the warm surface water of the tropics and subtropics is not transported very deep. Around 75% of the ocean volume is in contact

with the atmosphere by an area of only 4% of the ocean surface. Therefore, the high latitudes are of fundamental significance for long-term changes in the marine C-cycle and climate. The southern ocean plays a crucial role in different hypotheses that aim at explaining the observed increase by 80 ppm during the 5000 years of the glacial-interglacial transition.

For energetic reasons, the water exchange preferentially occurs along surfaces of equal density (isopycnals). They are, as a first-order approximation, equal to the surfaces of equal temperature.

In the *deep* Ocean, concentrations of inorganic carbon, phosphate, nitrate and other nutrients increase from the Northern Atlantic to the Southern Ocean. The highest concentrations are found in the Northern Pacific. The associated circulation is characterized by the simplistic but popular image of the **conveyor belt**.

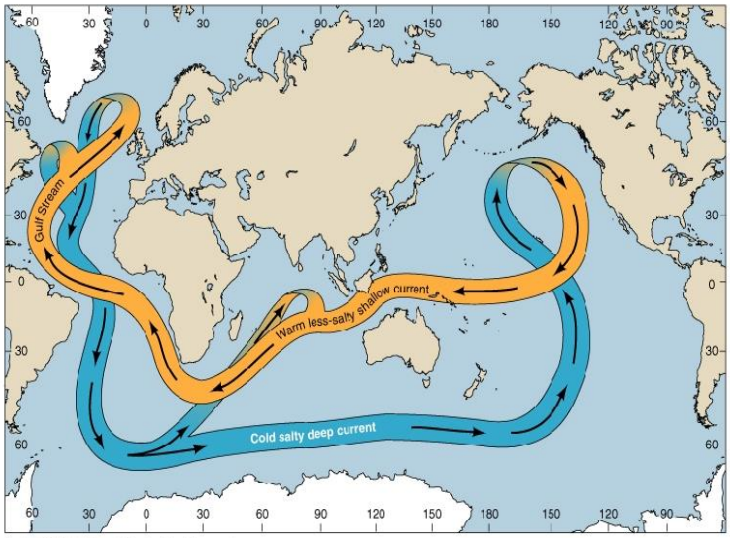

Figure 4.7: The current thermo-haline circulation is illustrated by the strongly simplified image of an oceanic conveyor belt. Cold water sinks in the Northern Atlantic, flows southwards in the deep ocean (dark/blue branch), is recycled in the southern Ocean and up-wells in the Pacific and Indian Ocean. At the surface, the water is heated up and flows back to the Northern Atlantic for the reason of mass conservation (bright/red branch).

In the surface ocean, nutrients are converted to organic material by algae; part of it sinks to depth and is re-mineralized to inorganic nutrients in the water column. This leads to an increase in nutrient concentrations as the amount of time the water spends at depth increases. In the image of the conveyor belt, nutrient-poor water sinks in the North Atlantic and flows into the southern ocean and from there into the Northern Pacific and into the Indian Ocean. On its way, it transports the nutrients that percolate from the upper ocean layers.

The conveyor belt scheme is a sketch highlighting an important characteristic of the thermo-haline (density driven) circulation. However, in reality, the deep circulation is much more complicated and sketches such as Figure 4.7 must not be over-interpreted.

The temperature, salinity and nutrient distributions allow oceanographers to identify typical water masses. We, briefly, discuss here the water masses in the Atlantic. North Atlantic Deep Water (NADW), which is formed in the Labrador, Greenland, Iceland and Norwegian Seas, flows southward and penetrates the Atlantic between 2000 and 4000 m depth. At the continental shelf of Antarctica, dense saline water sinks and flows northwards below the NADW as Antarctic Bottom Water (AABW). A cold but relatively fresh layer, Antarctic Intermediate Water (AAIW), pushes from the south towards the Equator at intermediate depths.

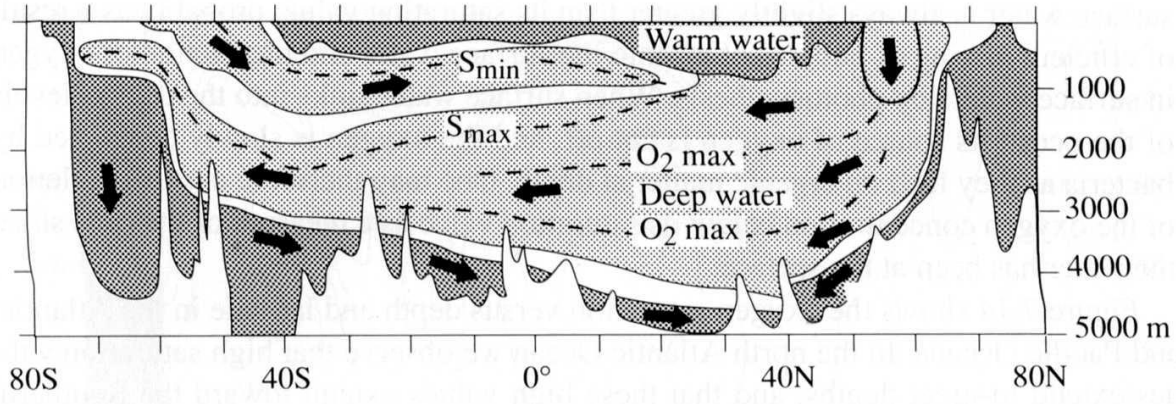

Figure 4.8: Current distribution of water masses in the Atlantic.

4.3 The radioactive carbon isotope ^{14}C: How quickly does the ocean mix?

^{14}C is formed in the atmosphere from nitrogen by cosmogenic radiation and decays in the climate system with a mean life time, λ^{-1}, of 8267 years. $^{14}CO_2$ enters the surface ocean by gas exchange and is transported downwards. After a water parcel has left the mixed layer, the ^{14}C:^{12}C ratio (~10^{-12}) continuously decreases due to radioactive decay. The (fractionation-corrected) ^{14}C:^{12}C ratio, *R*, of inorganic carbon is hence a measure for the age of the water mass, or the time elapsed since the water has left the surface. From the decay equation:

$$\frac{d^{14}R}{dt} = -\lambda \cdot {}^{14}R \qquad \text{Eq. 4.2}$$

the age, τ, of the respective water mass follows:

$$\tau = \frac{1}{\lambda} \cdot \ln \frac{{}^{14}R_{Surface}}{{}^{14}R} \qquad \text{Eq. 4.3}$$

$^{14}R_{Surface}$ denotes the ^{14}C:^{12}C ratio of the water when it is leaving the surface.

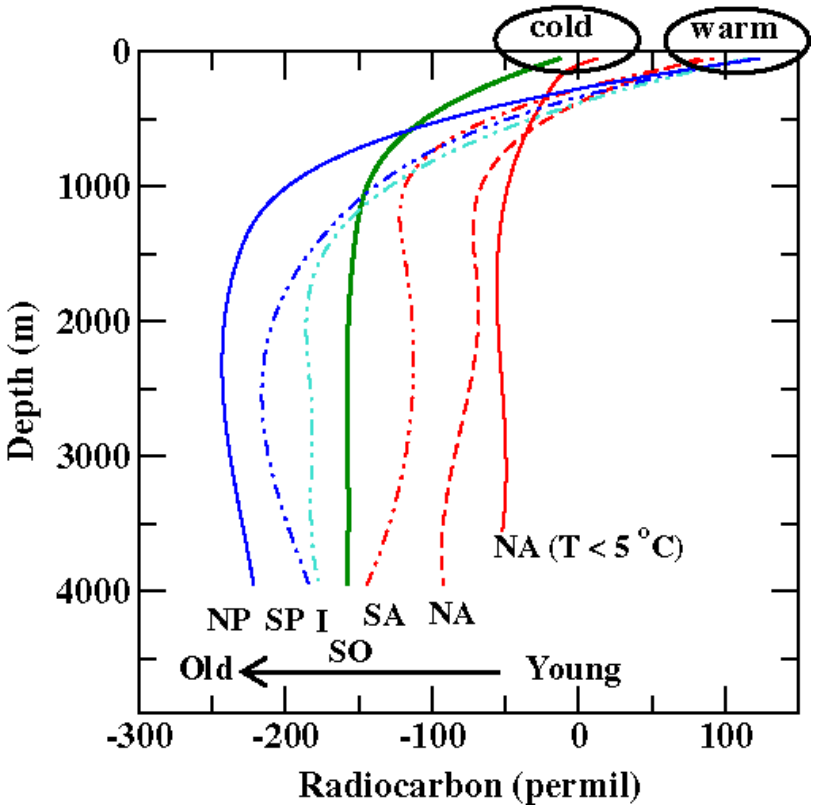

Figure 4.9: Profiles of $\Delta^{14}C$ in different ocean basins (NA: North Atlantic, SA: South Atlantic, SO: Southern Ocean, I: Indian Ocean, SP: South Pacific, NP: North Pacific) from the GEOSECS data. The profiles represent mean values for areas with a surface temperature of more than 5 °C and less than 5 °C, respectively. At depth, the water age decreases from the North Atlantic to the North Pacific. At the surface, the D14C values are lower in the cold than in the warm regions. This points to an enhanced vertical exchange at high latitudes.

The deviation of the $^{14}C : {}^{12}C$ ratio of a sample from a standard ratio is commonly quantified in units of permils. As a first-order approximation, it takes 8.3 years to deplete the $^{14}C : {}^{12}C$ ratio by 1 permil. At preindustrial times, the mean ratio in the surface layer was at -50 permils. The deep water masses in the North Pacific with a $^{14}C : {}^{12}C$ ratio of up to -240 permils are hence, of a nominal ^{14}C age of 1500 years. The mean $^{14}C:{}^{12}C$ ratio of the deep ocean is -160 permils. This implies that it takes in the order of 1000 years to bring the deep ocean into equilibrium after an atmospheric perturbation.

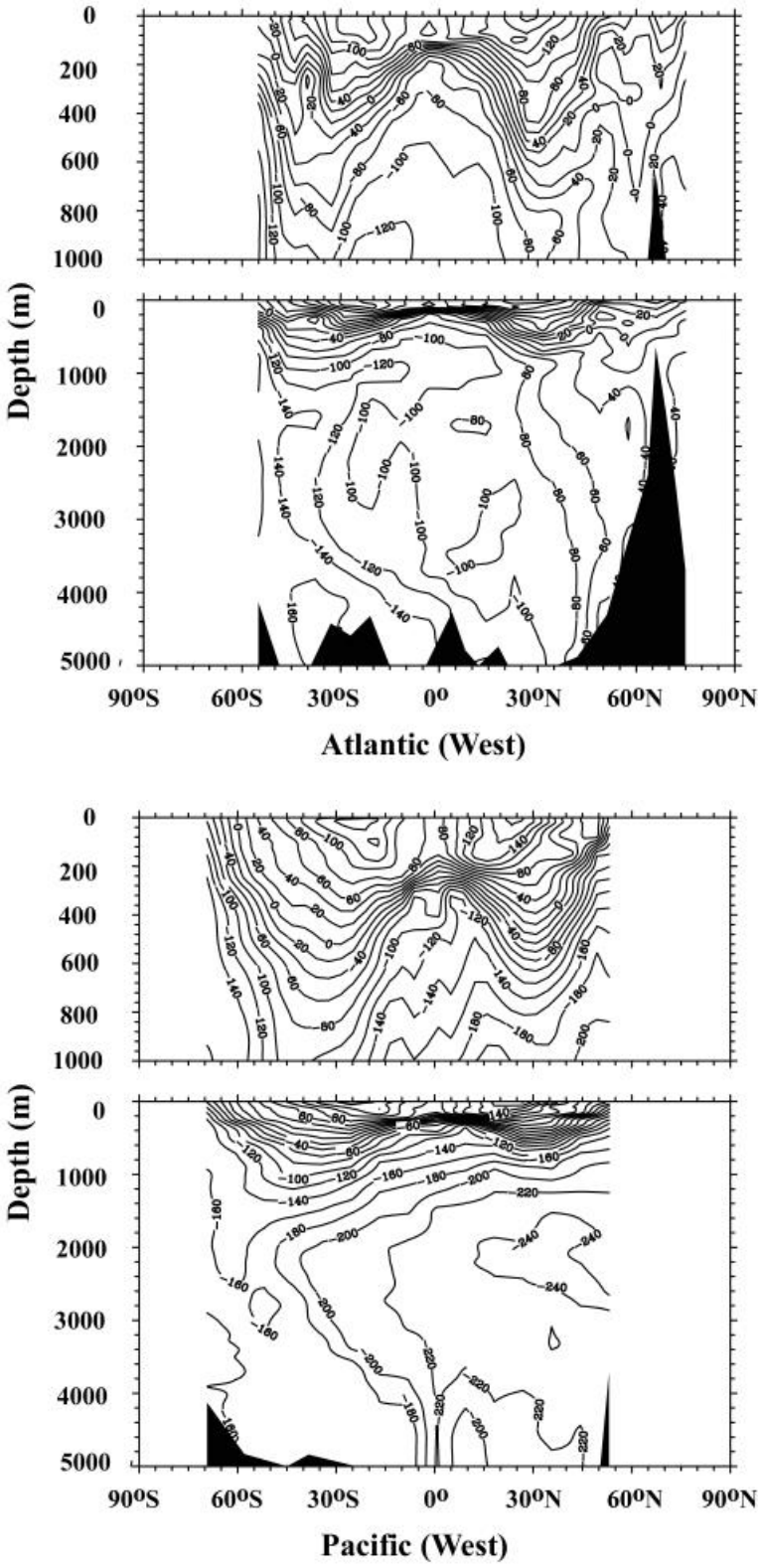

Figure 4.10: Distribution of the radioactive carbon isotope ^{14}C in the Ocean (in permils) in the year 1972 (Atlantic) and 1974 (Pacific).

5 Uptake of anthropogenic CO_2 by the ocean

In this chapter we will treat the uptake of anthropogenic CO_2 by the ocean. More specifically, we want to discuss the processes that allow us to simulate the uptake of anthropogenic CO_2 by the ocean over the industrial period and in the future.

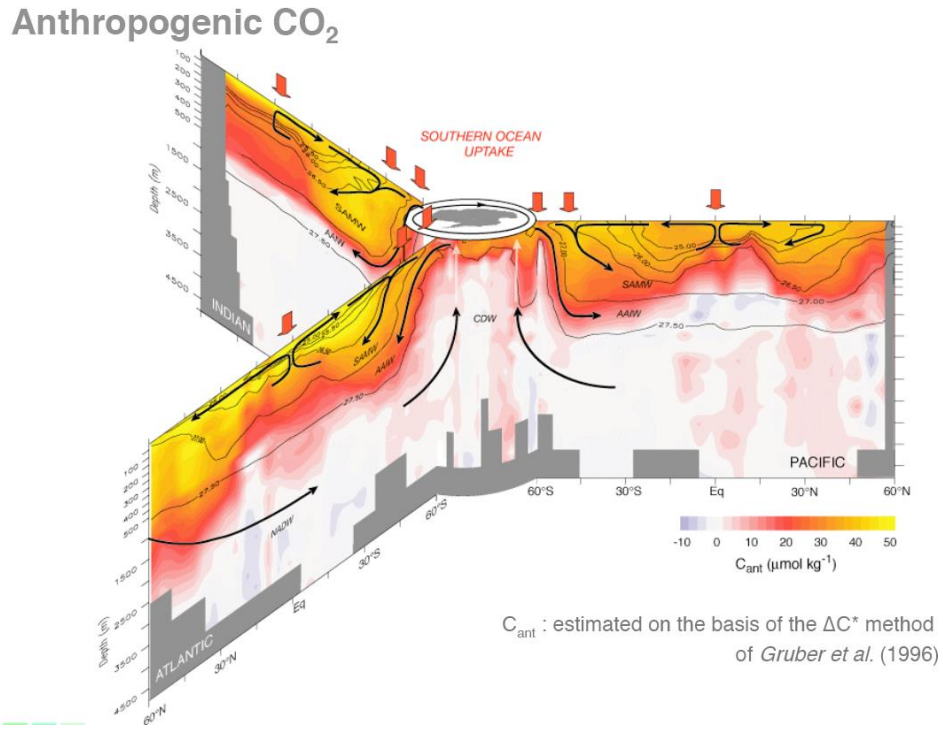

Figure 5.1: Reconstructed distribution of anthropogenic carbon in the ocean.

5.1 Processes and models

On time scales of less than 1000 years, the oceanic uptake of anthropogenic CO_2, or CO_2 from terrestrial sources, is controlled by the following three processes:

1. Gas exchange between the atmosphere and the ocean
2. Carbonate chemistry in the sea water
3. Transport to depth by advection, convection and diffusion

- The equilibration of the surface layer with the atmosphere takes place on a typical time scale of 1 year.
- Together with the ocean volume, the carbonate chemistry controls the uptake capacity of the ocean. The relevant chemical reactions take place nearly instantaneously. Recall that the dissolved inorganic carbon (DIC=$[CO_2]$ + $[HCO_3^-]$ + $[CO_3^{2-}]$) occurs mainly in the form of bicarbonate ($[HCO_3^-]$).
- The limiting step for the uptake of anthropogenic CO_2 is the transport of excess CO_2 into the deep ocean with typical time scales of decades (thermocline) to centuries (deep sea).

5.1.1 CO_2-exchange flux atmosphere-ocean

The net gas flux from the atmosphere into the ocean is proportional to the difference in concentration between the air and water. The CO_2 concentration in the surface water of the ocean is often expressed as a partial pressure (pCO_2; units e.g. μatm, where 1 μatm ≈ 1 ppm on sea level). For the gas exchange flux per unit area into the ocean, we write:

$$F = k_l \cdot \alpha \cdot (pCO_{2,a} - pCO_{2,s}) = k_l \cdot (c_a - c_s)$$
$$F = k_g \cdot (pCO_{2,a} - pCO_{2,s}) \qquad \text{Eq. 5.1}$$

where k_l = transfer coefficient relative to the concentration in the fluid phase, *kg* = transfer coefficient relative to the partial pressure, α = Bunsen coefficient (solubility), $pCO_{2,a}$ = partial pressure of CO_2 in the atmosphere, $pCO_{2,s}$ = actual partial pressure in the ocean that corresponds to the hypothetical partial pressure of CO_2 in the air which is assumed to be at equilibrium with the CO_2 concentration in the water.

Solubility of gases

Here we will express the concentrations as follows:

p(i)	partial pressure of the gas i in the air (gaseous phase),	[p] = atm
c_w	concentration of the dissolved gas in water,	$[c_w] = \frac{\text{ml(Gas; STP)}}{\text{l (water)}}$
c_g	concentration of the gas in gas phase,	$[c_g] = \frac{\text{ml(Gas; STP)}}{\text{l (air)}}$

note: STP = Standard Temperature and Pressure (0°C, 1 atm)
1 ml (gas;STP) = (1/22,400) mol = $4.46 \cdot 10^{-5}$ mol.
Sometimes, c_w is expressed as [mol/l (water)] and c_g in [mol/l(gas)] *(c_g=n/V=p/(RT))*

Partial pressure and molar ratio

The concentrations of atmospheric gases are commonly expressed as molar ratio (number of gas molecules per number of air molecules) in dry air, χ'. (Sometimes, the partial pressure in dry air is used) The partial pressure (μatm) and χ' (ppm) are related as follows:

$$p(i) = \chi'(i) \cdot \left(1 - \frac{p(\mathrm{H_2O})}{P_{atm}}\right) \cdot P_{atm} \qquad \text{Eq. 5.2}$$

where p_{atm} and $p(H_2O)$ are the total partial pressure in gas phase and the partial pressure of water vapor.

Above the ocean surface, the air is saturated with water. The water vapor pressure at saturation is around a few percents of the atmospheric pressure. It is a function of salinity S (permil) and temperature (K) and after Weiss and Price (1980):

$$p(\mathrm{H_2O}) = \exp\left[24.4543 - 67.4509 \cdot (100/T) - 4.8489 \ln(T/100) - 0.000544 \cdot S\right] \qquad \text{Eq. 5.3}$$

The concentration of a gas dissolved in water is proportional to the concentration of the gas in air. The concentration of a gas in the gas phase and in the liquid phase can be expressed in different units, and different definitions to describe the equilibrium partition between the gas and liquid phase are used. In the following we discuss the functions describing the solubility of a gas in sea water. We start with the Bunsen-coefficient.

Bunsen-coefficient, fugacity and solubility of non-ideal gases

The Bunsen coefficient α for an ideal gas is defined as:

$$C_W(i) = \alpha\, p(i) \qquad \text{Eq. 5.4}$$

$$\text{units: } [\alpha] = \frac{\mathrm{ml(Gas;\ STP)/l(water)}}{\mathrm{atm}}$$

α depends on the temperature and the salt content of water but it is nearly independent from the partial pressure of the gas.

The above relation is valid for ideal gases and is sufficient for noble gases or O_2 and N_2. Gases, such as CO_2, N_2O or CFCs, have a non-ideal behavior. Instead of the partial pressure, *p(i)*, the **fugacity**, *f(i)*, has to be used in the equation above. We write:

$$f(i) = p(i) \cdot \exp\left[(V(i) - V_{ideal}(i)) \cdot \frac{P}{RT}\right] \qquad \text{Eq. 5.5}$$

and

$$c_w = \alpha \cdot f \qquad \text{Eq. 5.6}$$

V(i) is the real molar volume of the gas i in units of $m^3\ mol^{-1}$ and $V_{ideal}(i)$ is the molar volume of an ideal gas. The difference between the partial pressure and the fugacity is about 0.4% for

CO_2 and corresponds to 1.4 ppm. Depending on the application this may be significant since, on the global average, a difference between the fugacity of 1.4 ppm roughly corresponds to a net flux of 1 GtC yr^{-1}. For practical reasons, the correction resulting from the non-ideality and of the water vapor in air is directly incorporated into the solubility function, $F_{sol}(i)$, and we obtain:

$$c_w(i) = F_{sol}(i) \cdot \chi' \cdot p_{atm} \qquad \text{Eq. 5.7}$$

Where $F_{sol}(i)$ is a function of temperature and salinity.

Henry's Law for the volumetric solubility

For certain applications, another formulation is more convenient: Concentrations in air and water are of the same units in order for the solubility to become dimensionless. This yields the Henry's Law:

$$c_w = s\, c_g \qquad \text{Eq. 5.8}$$

units: $$[s] = \frac{\text{ml(gas; STP)/l(water)}}{\text{ml(gas; STP)/l(gas)}}$$

We call s the (volumetric) solubility. Bunsen coefficient and volumetric solubility are related according to:

$$s = \alpha \cdot \frac{T}{273.2K} \cdot \frac{1}{1000} \cdot \frac{atm}{ml(Gas;\ STP)/1(Gas)} \qquad \text{Eq. 5.9}$$

Gas	**Relative molecular mass**	**Bunsen coefficient** $\alpha\left(\frac{\text{ml(gas;STP/1(water))}}{\text{atm}}\right)$		**s**
		0° C	24° C	24° C
He	4	7,8	7,4	$0{,}80 \cdot 10^{-2}$
Ne	20	10,1	8,6	$0{,}94 \cdot 10^{-2}$
N_2	28	18,3	11,8	$1{,}28 \cdot 10^{-2}$
O_2	32	38,7	23,7	$2{,}58 \cdot 10^{-2}$
Ar	40	42,1	26,0	$2{,}83 \cdot 10^{-2}$
Kr	84	85,6	46,2	$5{,}03 \cdot 10^{-2}$
Xe	131	192	99	$10{,}8 \cdot 10^{-2}$
CO_2	44	1437	666	0,725

Table 5.1: Solubility in sea water (at 35‰ salinity).

From Table 5.1 we can draw the following conclusions:

- The solubility of noble gases increases with increasing molecular mass.

- In general, the solubility decreases with increasing temperature. This effect is stronger for the noble gases (and CO_2) compared to the lighter gases. The volumetric solubility for CO_2 is close to 1, while for the other gases listed it ranges between 10^{-2} and10^{-1}.

Example: How much dissolved CO_2 is contained in the ocean?

We aim at estimating the ratio of dissolved CO_2 ($[CO_2]$) versus the atmospheric CO_2 inventory. We apply the Henry's Law and consider the atmosphere and the ocean as two well-mixed boxes that are in equilibrium.

We define the atmospheric scale height, h_{atm}, and the associated volume, $V_{atm,}$ in such a way, that the atmospheric mass is equal to the mass contained by the volume V_{atm} at a uniform pressure of 1 atm (sea level). We put $V_{atm} = A\, h_{atm}$, with A = Earth surface and $h_{atm} \approx 8$ km = equivalent height of the atmosphere (≈ e-folding altitude of atmospheric air pressure).

Then, the amount of CO_2 in the atmosphere, N_{atm} , and in the ocean, N_o, is linked by the following equations:

$$N_{atm} = V_{atm}\, c_g \qquad \text{and} \qquad N_o = V_o\, c_w = V_o\, s\, c_g$$

Therefore:

$$\frac{N_o}{N_{atm}} = s\frac{V_o}{V_{atm}}, \qquad \text{and} \quad V_O = A_O\, h_O$$

where $A_O = 0{,}7\, A$, $h_O \approx 4$ km, $s = 1.5$ (deep sea is cold!):

$$\frac{N_o([CO_2])}{N_{atm}(CO_2)} = s\frac{0{,}7A\ h_o}{A\ h_{atm}} \approx 1.5 \cdot \frac{0{,}7 \cdot 4\text{km}}{8\text{km}} \approx \frac{1}{2} \qquad \text{Eq. 5.10}$$

The amount of CO_2 in the ocean in the form of dissolved CO_2 would be only about 50 % of the atmospheric amount if ocean water was saturated with respect to the atmospheric CO_2 concentration everywhere. As mentioned above, the majority of inorganic carbon in the ocean is not present as dissolved CO_2, but as bicarbonate. The observed ratio of dissolved inorganic carbon (DIC) to the atmospheric CO_2 is:

$$\frac{N_o(DIC)}{N_{atm}(CO_2)} \approx \frac{38000\ \text{GtC}}{600\ \text{GtC}} \approx \frac{63}{1} \qquad \text{Eq. 5.11}$$

We can now derive a rough estimate of the ratio between dissolved CO_2 and DIC:

$$\frac{[CO_2]}{DIC} \approx \frac{1}{126} \approx 1\,\%$$

Gas transfer rate

An estimate for the mean global transfer rate from the marine ^{14}C inventory

In this section, we want to derive a rough first estimate of the mean global gas exchange rate and discuss associated time scales utilizing the ^{14}C inventory method. Radioactive carbon ^{14}C is produced in the atmosphere by spallation of nitrogen by cosmic radiation and decays with a mean life time, λ^{-1}, of 8267 years. At an approximate steady-state, the flux of ^{14}C into the ocean has to be equal to the decay rate of ^{14}C in the ocean (and in the sediments). The flux is expressed with the mean CO_2 concentration and the mean isotope ratio, *R*, in the atmosphere (subscript: a) and in the surface ocean (s):

$$^{14}F_{a,s} = A_o \cdot k_l \cdot [CO_2]_s \cdot (R_a - R_s) \qquad \text{Eq. 5.12}$$

The decay corresponds to the product of the ^{14}C content in the whole ocean (o) and the decay rate, λ:

$$^{14}F_{decay,o} = \lambda \cdot \left(V_o \cdot (\overline{DIC_o \cdot R_o})\right) \qquad \text{Eq. 5.13}$$

where $V_o = A_o\, h_o$ corresponds to the ocean volume and the product ($DIC_o \times R_o$) to the mean ^{14}C concentration. It then follows,

$$k_l \cong \lambda \cdot h_o \cdot \frac{DIC_o}{[CO_2]_s} \cdot \frac{R_o}{R_a - R_s} \approx \frac{1}{8267\ \text{a}} \cdot 3800\ \text{m} \cdot \frac{2.2\ \text{mol m}^{-3}}{0.01\ \text{mol m}^{-3}} \cdot \frac{0.84}{1-0.95} \qquad \text{Eq. 5.14}$$

$$k_l \approx 20\ \text{cm h}^{-1} \approx 1750\ \text{m a}^{-1}$$

This transfer rate is based on dissolved CO_2 , $[CO_2]$. Since only about 0.5% of the DIC in the surface ocean is in the form of $[CO_2]$, the transfer rate with respect to DIC is smaller by a factor of 200.

$$k_l(\text{DIC}) = k_l \times \frac{[CO_2]_s}{DIC_s} \approx 1750\ \text{m a}^{-1} \cdot \frac{0.01\ \text{mol m}^{-3}}{2.0\ \text{mol m}^{-3}} \approx 8.75\ \text{m a}^{-1} \qquad \text{Eq. 5.15}$$

The observed inventory of bomb-produced ^{14}C in the ocean is also consistent with these estimates.

Exchange time for the wind-mixed layer and the atmosphere

The time until the amount of DIC in the wind-mixed surface layer, N_s, with depth h_s, exchanges with the atmosphere is equal to:

$$\tau_s(DIC) = \frac{N_s(DIC)}{F_{as}(CO_2)} = \frac{A_o \cdot h_s \cdot DIC_s}{A_o \cdot k_l \cdot [CO_2]} = \frac{h_s}{k_l(DIC)} \approx \frac{75\ m}{8.75\ m\ a^{-1}} \cdot \approx 8.5\ a \qquad \text{Eq. 5.16}$$

Hence, the carbon in the wind-mixed surface layer typically exchanges with the atmosphere within decades. The carbon content of the atmosphere roughly corresponds to an ocean layer of 68 m thickness at a mean concentration of 2.0 mol-C m^{-3}. We define an atmospheric equivalent height, H_{atm}, so that:

$$N_{atm} = A_o\, H_{atm}\, DIC_s \qquad \text{Eq. 5.17}$$

And we obtain numerically that:

$$H_{atm} = \frac{N_{atm}}{A_o \cdot DIC_s} = \frac{594 \cdot 10^{15}\ \text{g-C} \cdot \frac{1}{12.01\ \text{g-C mol}^{-1}}}{3.62 \cdot 10^{14}\ m^2 \cdot 2.0\ \text{mol m}^{-3}} \approx 68\ m \qquad \text{Eq. 5.18}$$

The residence time of CO_2 in the atmosphere with respect to gas exchange with the ocean amounts to:

$$\tau_{atm} = \frac{h_{atm}}{k_l(DIC)} \approx \frac{68\ m}{8.75\ m\ a^{-1}} \cdot \approx 8\ a \qquad \text{Eq. 5.19}$$

Formulations for the gas transfer rate as a function of temperature and wind speed

To evaluate local gas and CO_2 exchange fluxes, a globally averaged value for the gas transfer rate is not sufficient. Measurements of gas transfer in wind tunnels and ship-based measurements show a strong dependence of the gas transfer rate on the wind speed, typically 10 m above the water surface, U_{10}, and the Schmidt number, *Sc*. The Schmidt number represents the ratio of kinematic viscosity of the fluid and the molecular diffusivity of the exchanging gas. It allows the comparison of transfer rates of different gases and different fluids. Literature contains numerous propositions for the formulation of gas transfer rates as a function of wind speed and the Schmidt number. A typical formulation is:

$$k_l = k(Sc = 660) \cdot \left(\frac{Sc(T)_{liquid;gas}}{660}\right)^{-0.5} \qquad \text{Eq. 5.20}$$

It is apparent that the gas transfer rate *k* and hence k_l is highly uncertain and the different proposed formulations differ considerably. A fundamental problem of quantifying the gas transfer coefficient in the real ocean precisely is its large spatial extent that cannot be simulated in wind tunnels and the large range of wind speeds. Of course, it is particularly difficult to obtain exact values for high wind speeds. At high wind speeds, the breaking of waves and the inclusion of air bubbles in the water become important.

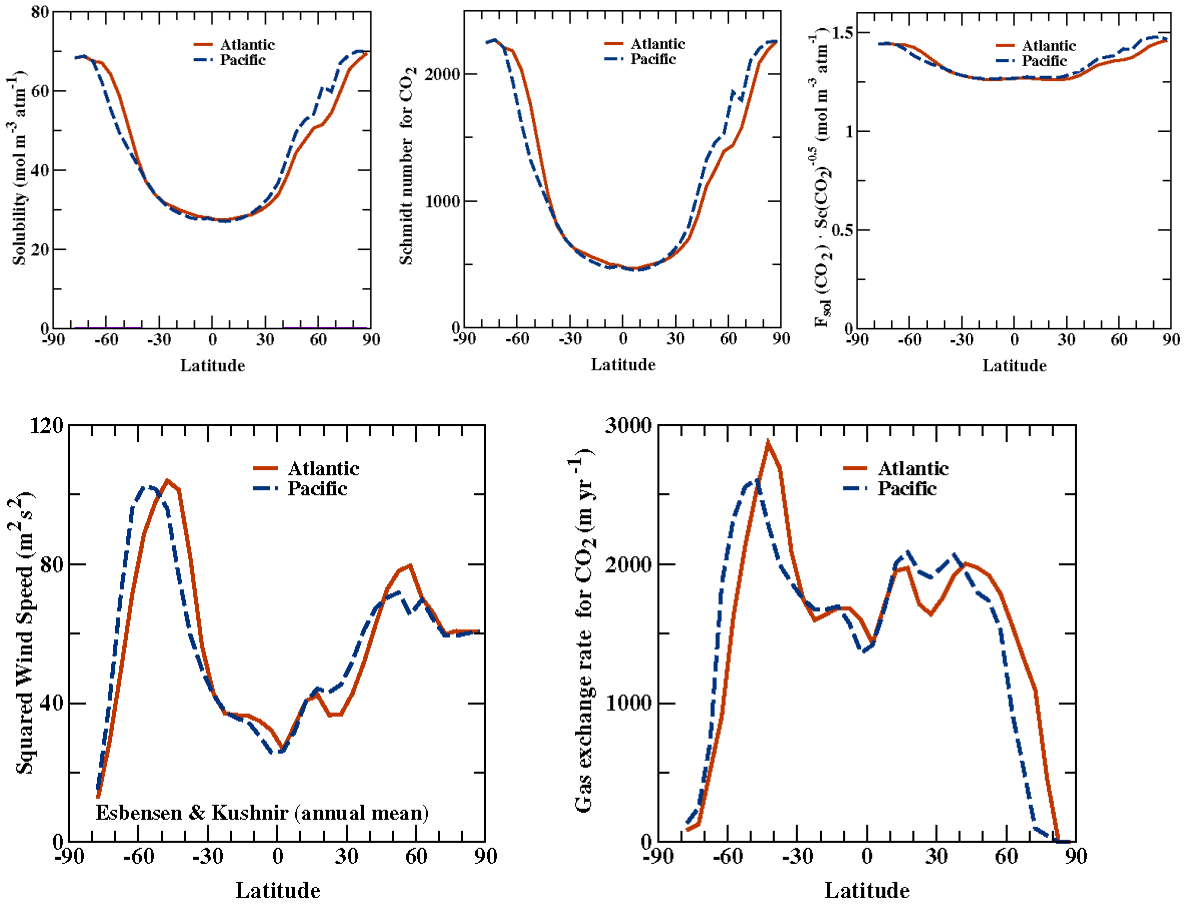

Figure 5.2: Gas exchange rates for CO2 and their terms as a function of latitude in the Atlantic and Pacific. Zonal annual mean values are shown. Gas exchange rates were calculated according to Wanninkhof, 1992: kg= 0.39 u2 (660/Sc)0.5 Fsol.

	equation	Global C-flux [GtC yr^{-1}]
Liss&Merlivat, 1986	k=0.17 U_{10}; U_{10}<3.6 m s^{-1} k=2.85 U_{10}-9.65; 3.6 m s^{-1}<U_{10}<13 m s^{-1} k=5.9 U_{10}-49.3; U_{10}<13 m s^{-1}	-1.0
Wanninkhof, 1992 [W/92]	k=0.39 U_{10}^2 (long-term mean wind) {k=0.31 U_{10}^2 (actual wind)}	-1.8
Wanninkhof&McGillis, 1999 [W&M/99]	k=1.09 U_{10} – 0.333 U_{10}^2+0.078 U_{10}^3 (long-term mean wind) {k=0.0283 U_{10}^3(actual wind)}	-3.0
Nightingale et al, 2000	k=0.333 U_{10} + 0.222 U_{10}^2	-1.5
NCEP-41 year mean wind	k=0.39 U_{10}^2; [W/92]	-2.2
NCEP 6-hours mean wind	k=0.31 U_{10}^2; [W/92]	-1.7
NCEP 6-hours mean wind	k=0.0283 U_{10}^3; [W&M/99]	-2.3

Table 5.2: Global carbon flux from the atmosphere out of the ocean, calculated from the pCO_2 climatology (Monthly values; Takahashi et al.) and – if not stated otherwise – with monthly wind values (NCEP) for the year 1995.

Combining the formulations for the gas transfer rate with observed wind data and observed pCO_2 values in the water and in the atmosphere allows us to estimate the local, regional and global fluxes for carbon between the atmosphere and the ocean. Different formulations yield a range for the net carbon flux from the atmosphere into the ocean of 1 GtC yr^{-1} to 3 GtC yr^{-1} for the year 1995.

The quadratic relation of Wanninkhof, 1992, as well as the relation of Wanninkhof and McGillis was scaled such that the global mean transfer rate succeeds in representing the global uptake of bomb-produced ^{14}C. In spite of this global condition, considerable uncertainties remain for the global net atmosphere-to-ocean flux as derived from measurements of the air-se partial pressure difference.

It might be worthwhile to note that uncertainties in the gas exchange rate play a minor role in modeling the uptake of anthropogenic CO_2, as surface-to-deep transport is the limiting step. However, as stated above these uncertainties are relevant for the quantification of the flux between the atmosphere and the ocean from measurements and also for modeling carbon isotopes.

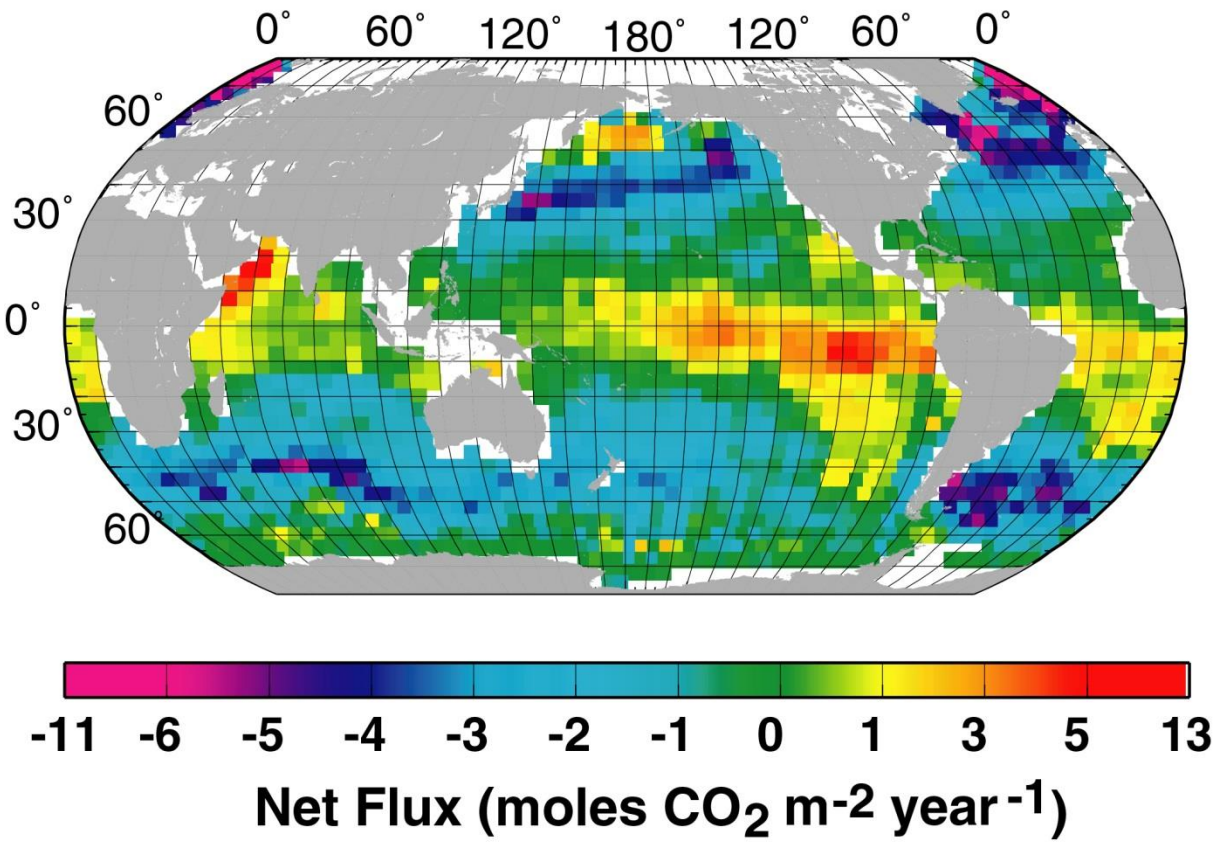

Figure 5.3: The net CO_2 flux across the ocean surface, as calculated from a climatology of the CO_2 partial pressure in the surface ocean. (positive values mean out-gassing to the atmosphere).

5.1.2 Carbonate chemistry

The chemistry of the ocean is changing in response to rising atmospheric CO_2. In the following sections we discuss the associated chemical processes in more detail.

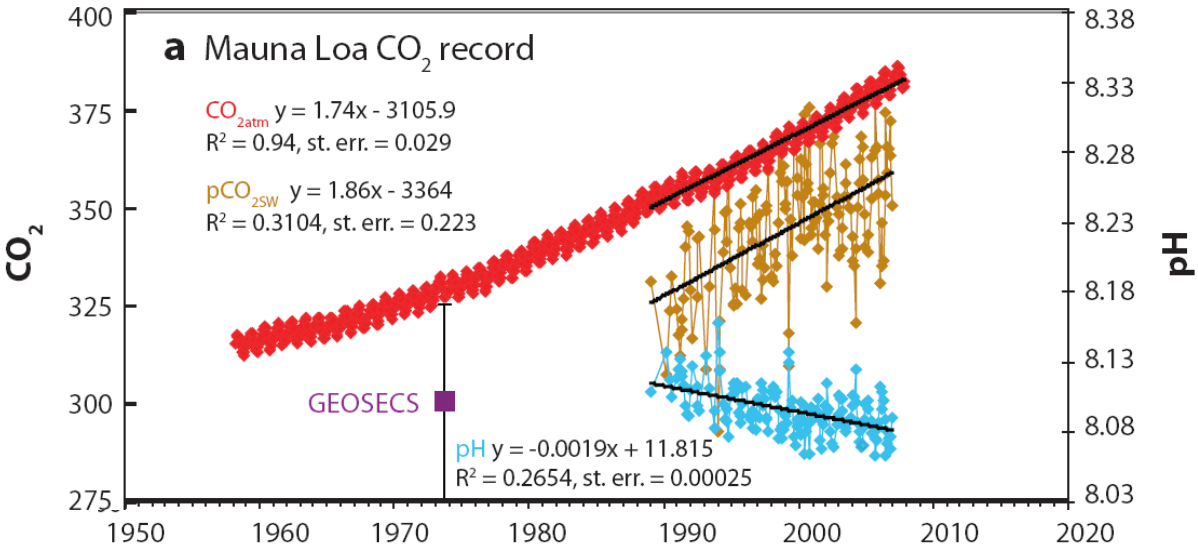

Figure 5.4: Changes in atmospheric CO2 at Mauna Loa (red) and of the pCO2 (brown) and pH (blue) in surface water at ocean station ALOHA in the subtropical Northern Pacific. The ocean becomes less alkaline with the uptake of CO_2 and the drop in pH.

Total dissolved inorganic carbon, DIC

Carbon in the ocean is most abundant in the form of dissolved inorganic carbon. The sum of the three inorganic components bicarbonate (HCO_3^-; ca. 90%), carbonate (CO_3^{2-}; ca. 10%) and dissolved CO_2 (ca. 0.5%) are represented by $\sum CO_2$ or DIC (dissolved inorganic carbon).

Dissolved CO_2 reacts with H_2O to form carbonic acid, H_2CO_3, which then dissociates rapidly to HCO_3^- and CO_3^{2-} (bicarbonate und carbonate ions). The corresponding chemical equilibria are:

$$CO_2 + H_2O \leftrightarrow H_2CO_3 \leftrightarrow H^+ + HCO_3^- \qquad \text{Eq. 5.21}$$

The concentration of H_2CO_3 is very low, ~$2 \cdot 10^{-3}$ times the CO_2-concentration, and it can hardly be measured. Thus, H_2CO_3 is usually included in dissolved CO_2: $[H_2CO_3^*]=[CO_2]+[H_2CO_3]$. Often $[H_2CO_3^*]$ is simply written as $[CO_2]$.

$$HCO_3^- \leftrightarrow H^+ + CO_3^{2-} \qquad \text{Eq. 5.22}$$

The associated equilibrium constants are ([X] = concentration of X):

1. dissociation constant of carbonic acid:

$$K_1 = \frac{[H^+]\cdot[HCO_3^-]}{[H_2CO_3 *]} \qquad \text{Eq. 5.23}$$

$0°C:\quad 6.33\cdot10^{-7}\ mol/kg$

$30°C:\quad 10.47\cdot10^{-7}\ mol/kg$

2. dissociation constant of carbonic acid:

$$K_2 = \frac{[H^+]\cdot[CO_3^{2-}]}{[HCO_3^-]} \qquad \text{Eq. 5.24}$$

$0°C:\quad 6.53\cdot10^{-10}$ mol/kg

$30°C:\quad 10.78\cdot10^{-10}$ mol/kg

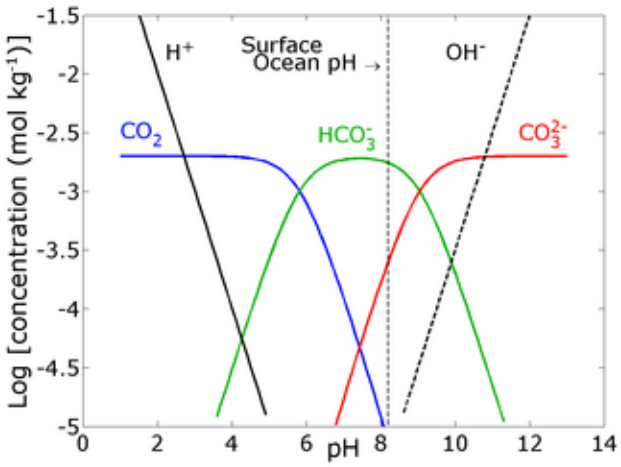

Figure 5.5: Concentrations in the carbonate system versus pH for sea water.

H_2CO_3 is a very weak acid: Its dissociation constant, hence the relative abundance of the different species, depends on the concentration of hydrogen ions, H^+, which are commonly represented by the pH.

$pH = -\log a_H$ (log: to the basis 10) Eq. 5.25

a_H is the concentration (more precisely: the activity) of hydrogen ions H^+. Pure water has pH ≈ 7, sea water: pH ≈ 8. From Eq. 5.23 we obtain $[H_2CO_3^*] / [HCO_3^-] = [H^+]/K_1$, meaning that the larger the hydrogen ion concentration (the lower the pH), the larger the ratio of $[H_2CO_3^*]/[HCO_3^-]$. In an acidic fluid (pH < 7), the chemical balance is shifted towards dissolved CO_2,

while in an alkaline fluid it is shifted towards CO_3^{2-}. With pH ~8 for sea water and values of the dissociation constants at 30°C, we get:

$$\frac{\left[HCO_3^-\right]}{\left[H_2CO_3^*\right]} = \frac{K_1}{\left[H^+\right]} \sim \frac{10^{-6}}{10^{-8}} = 100 \qquad \text{Eq. 5.26}$$

$$\frac{\left[CO_3^{--}\right]}{\left[HCO_3^-\right]} = \frac{K_2}{\left[H^+\right]} \sim \frac{10^{-9}}{10^{-8}} = 0.1$$

The ratio in sea water is hence

$$[H_2CO_3^*]:[HCO_3^-]:[CO_3^{2-}] = 1:90:10 \qquad \text{Eq. 5.27}$$

Alkalinity and other acid-base pairs in sea water

In order to calculate the dissociation of CO_2 in sea water, the equilibria of other acid-base pairs have to be taken into account. For a generalized acid-base reaction we write:

$$HA \leftrightarrow A^- + H^+ \qquad \text{Eq. 5.28}$$

and for the dissociation constant:

$$K = \frac{a_H \cdot \left[A^-\right]}{[HA]} \approx \frac{\left[H^+\right] \cdot \left[A^-\right]}{[HA]} \qquad \text{Eq. 5.29}$$

Commonly, the value of the dissociation constant is given as a logarithm to the base 10. To be precise, not the concentration, but the activity of H^+ is to be used in the above equation.

Particularly the boric acid, silica, and phosphoric acid are important for the carbonate system in the ocean. For the boric acid we write:

$$B(OH)_3 + H_2O \leftrightarrow B(OH)_4^- + H^+ \qquad \log K = -8.7 \qquad \text{Eq. 5.30}$$

The reactions for silicic acid are:

$$Si(OH)_4 \leftrightarrow SiO(OH)_3^- + H^+ \qquad \log K = -9.5 \qquad \text{Eq. 5.31}$$

$$SiO(OH)_3^- \leftrightarrow SiO(OH)_2^{2-} + H^+ \qquad \log K = -12.6 \qquad \text{Eq. 5.32}$$

The second reaction can be neglected in the ocean, since $SiO(OH)_2^{2-}$ in the ocean at pH~8 is practically non-existent.

Autoprotolysis of water is accounted for with:

$$H_2O \leftrightarrow OH^- + H^+ \qquad \log K = -14 \qquad \text{Eq. 5.33}$$

The concentration of total boron scales well with salinity, S:

Total-Bor = $[H_3BO_3] + [H_4BO_4^-] = 416\ \mu mol\ kg^{-1}\ S/35$ Eq. 5.34

Unlike boric acid, silicic acid is recycled through the biological cycle because it is used by organisms for the buildup of opal (SiO_2). The concentration of dissolved silica is, as opposed to boric acid, dependent on the biological activity.

An important quantity that controls the acid-base properties of a fluid is the alkalinity for alkaline fluids (and the acidity for acidic fluids). Simply speaking, the alkalinity represents the amount of bases contained in a solution, or the amount of acids required to be added to a solution in order to attain a neutral pH (or the reference value for pH). The most important bases in sea water are bicarbonate and carbonate ions and we write for the **carbonate alkalinity**:

$$\mathrm{Alk-Carb} \approx 2\left[\mathrm{CO_3^{2-}}\right]+\left[\mathrm{HCO_3^-}\right] \qquad \text{Eq. 5.35}$$

The concentration of carbonate ions, $[CO_3^{2-}]$, is weighted with a factor two because; two H^+ ions are needed in order to form H_2CO_3. Accounting for all the other present acid-base pairs, especially the boric acid, we get the **total alkalinity** with respect to the seawater pH scale (reference compounds: H_2CO_3, H_2O, $Si(OH)_4$, $H_2PO_4^-$):

$$\begin{aligned} Alk = {} & 2\left[CO_3^{2-}\right]+\left[HCO_3^-\right]+\left[B(OH)_4^-\right]+\left[OH^-\right] \\ & +\left[SiO(OH)_3^-\right]+\left[HPO_4^{2-}\right]+2\left[PO_4^{3-}\right]-\left[H_3PO_4\right]-\left[H^+\right] \end{aligned} \qquad \text{Eq. 5.36}$$

Why is the quantity of alkalinity used? Alkalinity can easily be measured operationally and the alkalinity is a conserved quantity with respect to physical transport. Knowing the alkalinity and all dissociation constants, as well as the total amount of DIC, boric acid, etc., the partitioning of DIC and other acid-base pairs can be computed.

What role does the alkalinity play for CO_2 uptake? The total alkalinity is larger than the carbonate alkalinity and the uptake capacity of sea water for the acidic CO_2 is higher if the contribution of additional acid-base pairs is taken into account.

Alkalinity does not change with the uptake of CO_2 from the atmosphere. However, the formation or dissolution of calcite ($CaCO_3$) changes the alkalinity.

How can we compute the pCO2 partial pressure or the amount of carbonate ions given this information? It is common to measure the total concentration of DIC, phosphate, silicate, temperature and salinity in combination with the alkalinity or to simulate their transport with a model. Considering (i) the dissociation constants, (ii) the total concentrations and (iii) the alkalinity, we can formulate a system of equations and compute the dissociation of different acid-base pairs. These equations are non-linear. The solutions are usually found by an iterative numerical method. The temperature- and pressure dependence of the constants has to be considered as well.

Relationship between DIC and the CO_2 partial pressure

pCO_2 increases when the water takes up more CO_2. At the same time, pH decreases and the ratios of $CO_3^{=}/CO_2$ and HCO_3^-/CO_2 decrease (see **Figure 5.5**); hence DIC does not increase proportionally to pCO_2. The relative increase of ΣCO_2 is smaller than that of pCO_2. This fact is represented by the **buffer factor** ξ:

$$\xi = \frac{\Delta pCO_2}{pCO_{2o}} \Big/ \frac{\Delta \Sigma CO_2}{\Sigma CO_{2o}} \qquad \text{Eq. 5.37}$$

where $\Delta pCO_2 = pCO_2 - pCO_{2o}$ and $\Delta\Sigma CO_2 = \Sigma CO_2 - \Sigma CO_{2o}$. pCO_{2o} and ΣCO_{2o} are undisturbed (e.g. preindustrial) values. ξ can be derived from the carbonate equilibria and the dissociation equilibria of H_2O and other acid-base pairs.

Typical values:	warm surface sea water:	ΣCO_2 = 1980 µmol/kg,	ξ = 9
	cold surface sea water:	ΣCO_2 = 2160 µmol/kg,	ξ = 14
	mean value for the ocean:		ξ = 10

Until 1990, the atmospheric CO_2 content increased by about 25%, hence DIC increased only by about 2.5% = 50 µmol kg^{-1} (assuming the surface waters and the atmosphere to be in equilibrium).

The relation between the partial pressure and DIC is **non-linear**. With increasing pCO_2 less CO_2 is dissolved in the water as DIC. In other words, the uptake capacity of the ocean decreases relatively, with the increasing amounts of atmospheric perturbation.

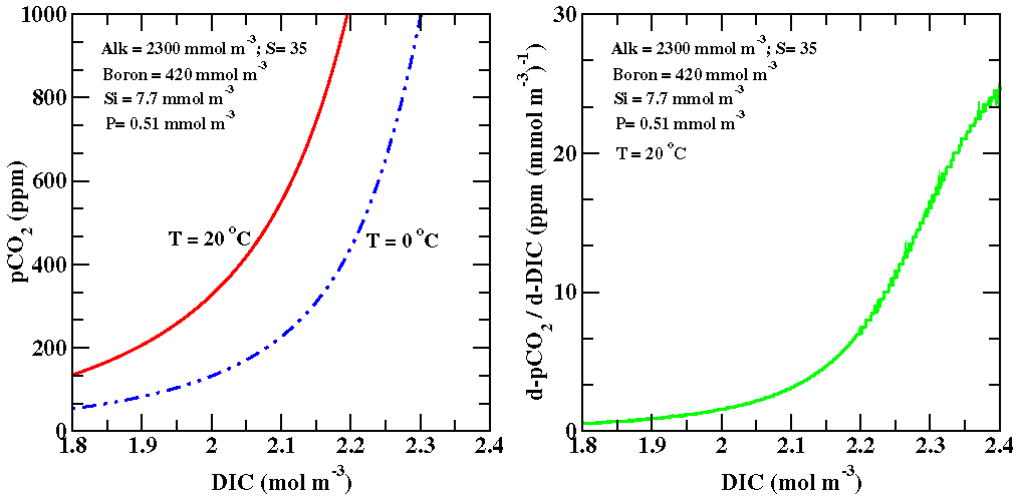

Figure 5.6: The CO_2 partial pressure (left) and the derivative of pCO2 by DIC (right) as a function of DIC.

Equilibration time of the wind-mixed layer for a disturbance in atmospheric CO_2

Next, we compute the time scale for the equilibration of the surface layer with respect to an atmospheric perturbation. For this, we consider a step change in the atmospheric partial pressure at time t=0 and monitor how the partial pressure and the perturbation in DIC evolves in the surface layer when considering air-sea exchange as the sole transport process. We will find that the time scale to equilibrate the surface with the atmosphere is smaller than the exchange time scale for the total amount of DIC in the surface layer. This is a consequence of the buffer factor.

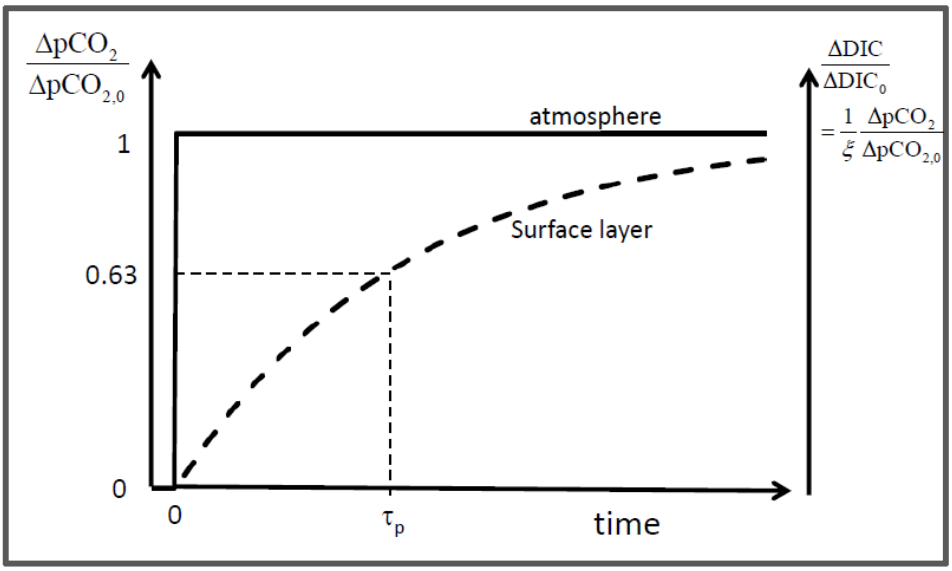

Figure 5.7: Illustration how the (well-mixed) surface ocean (dash) responds to a step change in the atmospheric CO_2 partial pressure (solid) when considering air-sea exchange as the sole transport process.

We consider the change of the DIC perturbation over time, ΔDIC, in a well-mixed box of depth h_s and area A_o, which only exchanges with the atmosphere:

$$A_o \cdot h_s \cdot \frac{d\Delta DIC}{dt} = A_o \cdot k_g \left(\Delta pCO_{2,a} - \Delta pCO_{2,s} \right)$$

We divide by a reference concentration of DIC, DIC_0, and expand the right-hand side of the equation with the reference partial pressure, $pCO_{2,0}$:

$$\frac{d}{dt}\frac{\Delta DIC}{DIC_0} = \frac{1}{h_s \cdot DIC_0} k_g \cdot pCO_{2,0} \left(\frac{\Delta pCO_{2,a}}{pCO_{2,0}} - \frac{\Delta pCO_{2,s}}{pCO_{2,0}} \right)$$

The first term on the right-hand side is equal to $1/\tau_s(DIC)$. We replace the relative change in partial pressure of the surface ocean using the buffer factor and obtain:

$$\frac{d}{dt}\frac{\Delta DIC_s}{DIC_0} = \frac{1}{\tau_s(DIC_0)}\cdot\left(\frac{\Delta pCO_{2,a}}{pCO_{2,0}} - \xi\frac{\Delta DIC_s}{DIC_0}\right) = \frac{\xi}{\tau_s(DIC_0)}\left(\frac{1}{\xi}\frac{\Delta pCO_{2,a}}{pCO_{2,0}} - \frac{\Delta DIC_s}{DIC_0}\right)$$

We may set $x=\Delta DIC/ DIC_{0;}$ $c=1/\xi\ \Delta pCO_2,a/pCO2,_0$ and $\tau_p=\xi/\ \tau_s(DIC_0)$ and write:

$$\frac{d}{dt}x = \frac{1}{\tau_p}\cdot(c-x)$$

For the boundary conditions: x(t=0)=0 and setting c constant for t>0 we obtain the following solution:

$$x(t) = c\left(1-\exp\left(\frac{-t}{\tau_p}\right)\right) \quad \text{or} \quad \frac{\Delta DIC_s(t)}{DIC_0} = \frac{1}{\xi}\frac{\Delta pCO_{2,a}}{pCO_{2,0}}\cdot\left(1-\exp\left(\frac{-t}{\tau_p}\right)\right)$$

Thus, τ_p is the (e-folding) time scale for the equilibration of the surface DIC concentration by air-sea exchange to reach equilibrium after an atmospheric perturbation:

$$\tau_p = \frac{\tau_s(DIC_0)}{\xi} = \frac{8.5\ a}{9}\cdot \approx 1\ a \qquad \text{Eq. 5.38}$$

This means that for a typical time scale of the anthropogenic CO_2 increase of about 30 years and due to the slow exchange of the surface with the deep ocean, the perturbation in the surface ocean (not the deep sea!) is close to equilibrium with the atmospheric perturbation.

Relationships between CO_2 partial pressure and temperature, alkalinity and salinity

Changes in environmental conditions, most notably temperature, salinity, and alkalinity, affect pCO_2, and thus air-sea fluxes and atmospheric CO_2, even if DIC is kept fixed. The chemical constants and the CO_2 partial pressure depend on temperature as well as on salinity. The following relations are useful to make a first-order estimate of the effects of a change in the environmental variables:

$$\frac{\frac{\Delta pCO_2}{pCO_2}}{\Delta T} = 0.0423K^{-1} \qquad \text{Eq. 5.39}$$

$$\frac{\frac{\Delta pCO_2}{pCO_2}}{\frac{\Delta S}{S}} = 0.94 \qquad \text{Eq. 5.40}$$

Partial pressure changes with changing alkalinity.: $$\frac{\frac{\Delta pCO_2}{pCO_2}}{\frac{\Delta Alk}{Alk}} = -9.4 \qquad \text{Eq. 5.41}$$

Gas exchange of $CaCO_3$ does not change the alkalinity. However, alkalinity decreases with the formation of $CaCO_3$ from CO_3^{2-} and Ca^{2+}. It can be shown that:

$$[CO_2][CO_3^{2-}] \approx \text{constant} \qquad \text{Eq. 5.42}$$

Thus, the formation of $CaCO_3$ does not lower the partial pressure of CO_2, as it may be expected from the employment of carbon (Figure 5.6). On the contrary, it increases the partial pressure. The lowering of the alkalinity by lowering $[CO_3^{2-}]$ dominates the change in partial pressure (Figure 5.8). The cycling of calcium carbonate will be discussed later.

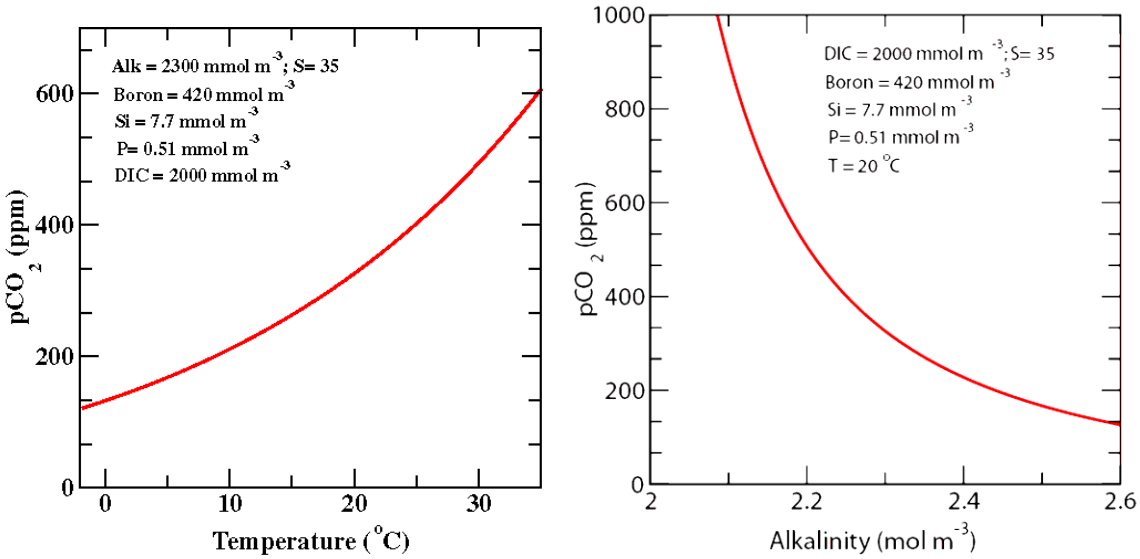

Figure 5.8: The CO_2 partial pressure as a function of water temperature and alkalinity.

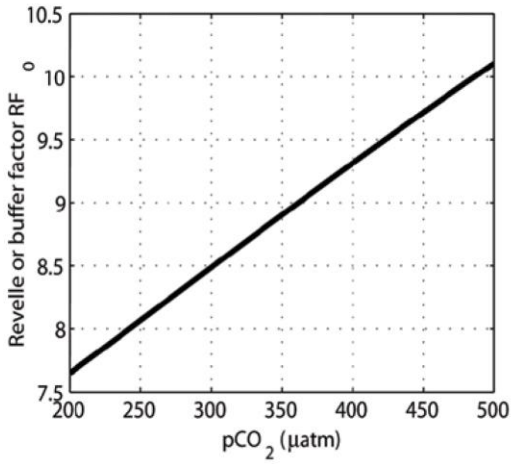

Figure 5.9: The carbon chemistry is non-linear. The Revelle Factor increases with increasing atmospheric CO_2. This means that the uptake capacity of the ocean is, relatively, less for high CO_2 emissions. Here the Revelle factor is shown for a temperature of 25°C, salinity of 35 psu, and total alkalinity of 2.3 mol/m^3.

5.1.3 Long-term CO_2 uptake by the ocean

Question: What fraction of anthropogenic CO_2 will remain in the ocean after equilibrium is reestablished?

Preindustrial amounts of CO_2 (or ΣCO_2) in the atmosphere and ocean:

N_a = 594 GtC (at 280 ppm); N_o = 37'400 GtC = 63 · N_a

New equilibrium: x = relative increase in the atmosphere, $\Delta N_a = x \cdot N_a$. Applying the buffer factor yields:

Increase of the DIC content in the ocean: $\frac{\Delta N_o}{N_o} = \frac{1}{\xi}\frac{\Delta N_a}{N_a} = \frac{1}{\xi}\frac{\Delta pCO_2}{pCO_{2,0}} = \frac{x}{\xi}$

Fraction of the added amount that remains in the atmosphere in equilibrium:

$$\frac{\Delta N_a}{\Delta N_a + \Delta N_o} = \frac{xN_a}{xN_a + (x/\xi)N_o} = \frac{1}{1+\frac{N_o}{\xi N_a}} = \frac{1}{1+6.3} = 14\% \quad \text{Eq. 5.43}$$

The DIC reservoir in the ocean is 60 times larger than the atmospheric reservoir, but the oceanic capacity to absorb CO_2 at steady state is only 6 times larger than that of the atmosphere. Due to the long mixing time of the deep ocean (10^2 - 10^3 yr) the deep ocean takes up CO_2 very slowly and a new steady state will be reached only after approximately 1000 years; thus a significant portion of CO_2 remains in the atmosphere for a long time. A larger fraction of the CO_2 will be taken up by the ocean through ocean-sediment interactions (after thousands of years), or when natural variations in CO_2 are superimposed onto the system.

5.1.4 Uptake of anthropogenic CO_2: A simple model

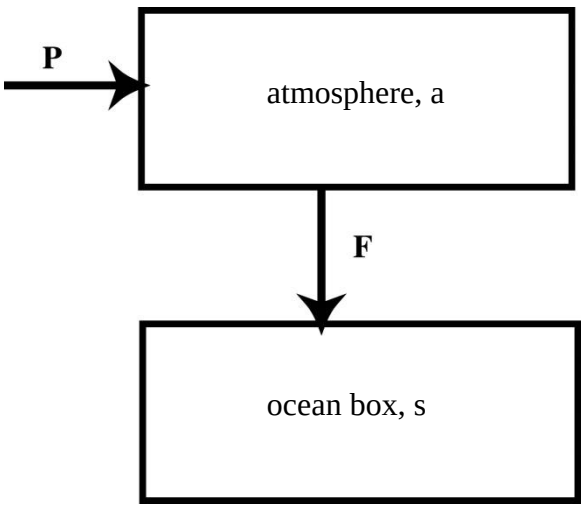

A portion of anthropogenic CO_2 is absorbed by the ocean. We can construct a two box model to consider the case.

The uptake of CO_2 is controlled by (1) gas exchange between the atmosphere and the ocean, (2) mixing of surface waters into the deep (more difficult to represent).

To simplify, we assume that the ocean box is well-mixed, with a thickness that is equivalent to the penetration depth of anthropogenic CO_2. Based on model calculations, we assume this depth to be 500 m (Amount of carbon: $N_{oc,0}$ = 5,000 GtC).

CO_2 is produced due to human activities (production rate P) and emitted to the atmosphere; a portion enters the ocean (net flux F). We want to calculate what the perturbation is in both reservoirs.

Terms:		
	$N_a = N_{a0} + n_a$	Amount in the atmosphere; $n_a(t)$ = perturbation
		N_{a0} Preindustrial atmospheric content
	$N_{oc} = N_{oc,0} + n_{oc}$	Amount in the ocean
	F	net air-to-sea flux

Budgets:

$$\frac{dN_a}{dt} = \frac{dn_a}{dt} = P - F \qquad \text{Eq. 5.44}$$

$$\frac{dN_{oc}}{dt} = \frac{dn_{oc}}{dt} = F \qquad \text{Eq. 5.45}$$

Air-sea exchange and atmospheric residence time

To solve the two differential equations 5.44 and 5.45, we need to express the net air-to-sea flux F as a function of the atmospheric, n_a, and oceanic, n_{oc}, perturbations.

Net gas exchange flux (k = gas exchange coefficient, A_{oc} = ocean area):

$$F = A_{oc}\, k\, (pCO_{2,a} - pCO_{2,oc}) = A_{oc}\, k\, (\Delta pCO_{2,a} - \Delta pCO_{2,oc}) \qquad \text{Eq. 5.46}$$

The right hand side of the equation (after the second equal sign) is valid because the preindustrial state was approximately a steady state: $pCO_{2a0} = pCO_{2oc,0} = pCO_{20}$ (also $F_{0,net} = 0$). For the perturbation, the following is valid:

$$\frac{\Delta pCO_{2a}}{pCO_{20}} = \frac{n_a}{N_{a0}}, \qquad \frac{\Delta pCO_{2,oc}}{pCO_{20}} = \xi \frac{n_{oc}}{N_{oc0}} \qquad \text{Eq. 5.47}$$

Also:

$$F = A_{oc} k \left(\frac{n_a}{N_{a0}} pCO_{20} - \xi \frac{n_{oc}}{N_{oc0}} pCO_{20} \right) = F_0 \left(\frac{n_a}{N_{a0}} - \xi \frac{n_{oc}}{N_{oc0}} \right) \qquad \text{Eq. 5.48}$$

$F_0 = A_{oc}\, k\, pCO_{20}$ is the preindustrial gross gas exchange flux, where

$$\tau_{a,oc} = \frac{N_{a0}}{F_0} \approx 7{,}5 yr \qquad \text{Eq. 5.49}$$

$$F = \frac{1}{\tau_{a,oc}} \left(n_a - \xi \frac{N_{a0}}{N_{oc0}} n_{oc} \right) \qquad \text{Eq. 5.50}$$

$\tau_{a,oc}$ is the average lifetime of a CO_2 molecule in the atmosphere with respect to exchange with the ocean at preindustrial times.

Airborne fraction

We can now solve the system of the differential equations 5.44 and 5.45 numerically, for any value of emission, *P*. In the following, an analytical solution is presented for exponentially increasing emissions, roughly approximating the real emission history. The production rate, *P(t)*, increases exponentially with time:

$P(t) = P_1 \cdot e^{\mu t}$ Eq. 5.51

where $\mu \approx 1/30a$

The same time dependence is also valid for the perturbation: $n_a = n_{a1}.e^{\mu t}$, $n_{oc} = n_{oc1}.e^{\mu t}$, because the differential equations are linear. Substituting them in equations 5.45 and 5.50 yields:

$$\frac{dn_{oc}}{dt} = F: \quad \mu n_{oc} = \frac{1}{\tau_{a,oc}}\left(n_a - \xi \frac{N_{a0}}{N_{oc0}} n_{oc}\right)$$

or,

$$n_{oc} = \frac{n_a}{\tau_{a,oc}\mu + \frac{N_{ao}}{N_{oc0}}\xi}$$ Eq. 5.52

Numerical:

N_{a0} = 594 GtC, N_{oc0} = 5000 GtC, μ = 1/30a, $\tau_{a,oc}$ = 7,5a, ξ = 10: n_{oc} = 0.70 n_a

Relationship to production: The sum of the perturbations is equal to the total amount of CO_2 produced (= cumulative production):

$$P_{cum} = \int_{-\infty}^{t} P dt : \qquad n_a + n_{oc} = P_{cum} \quad n_a(1+0.7) = P_{cum}$$ Eq. 5.53

It follows

$$n_a = 0.59 P_{cum} \qquad n_{oc} = 0.41 P_{cum}$$ Eq. 5.54

Our simple model predicts an airborne fraction of anthropogenic CO_2 of 59 %.

The net CO_2 flux F is equal to the gross flux into the ocean minus the flux back into the atmosphere. Without this return flux, the ocean would take up significantly more CO_2. This becomes obvious when ξ is set to 0 in Eq. 5.52. Hence, $\Delta pCO_{2s} = 0$ (or $N_{s0} = \infty$), corresponding to a infinitely large ocean sink):

$$n_s = \frac{n_a}{\tau_{as}\mu} = 4.0 n_a, \qquad n_a = 0.20 P_{cum}, \qquad n_s = 0.80 P_{cum}$$

Air-sea disequilibrium

We can also say that the net flux is proportional to the pCO2-disequilibrium between surface water and atmosphere. Thus, we write Eq. 5.46 as:

$$F = A_s k\left(\Delta pCO_{2a} - \Delta pCO_{2s}\right) = A_s k \Delta pCO_{2a}\left(1 - \frac{\Delta pCO_{2s}}{\Delta pCO_{2a}}\right) \qquad \text{Eqn. 5.1}$$

The expression outside the parentheses on the right hand side is the atmosphere-ocean gross flux and the expression in the parentheses is the degree of disequilibrium. We obtain:

$$\frac{\Delta pCO_{2s}}{\Delta pCO_{2a}} = \frac{n_s \xi N_{a0}}{n_a N_{s0}} = 0.83$$

According to the simplified box model, the mean anthropogenic pCO_2 increase in the surface water corresponds to the 83% of the atmospheric increase.

Literature

Carbonate Chemistry

- http://www.eoearth.org/article/Marine_carbonate_chemistry
- Dickson, A.G., Sabine, C.L. and Christian, J.R. (Eds.) 2007. *Guide to best practices for ocean CO_2 measurements*. PICES Special Publication 3, 191 pp. **http://cdiac.ornl.gov/oceans/Handbook_2007.html**
- Millero, F. J., Thermodynamics of the carbon dioxide system in the oceans, Geochim. Cosmochim. Acta, 59, 661-677, 1995.
- Stumm, W. and J. J. Morgan, Aquatic Chemistry (3rd ed.), Wiley & Sons, New York, pp. 1022, 1996.
- Zeebe, R. E. and D. A. Wolf-Gladrow, CO_2 in Seawater: Equilibrium, Kinetics, Isotopes, Elsevier Oceanography Series, 65, pp. 346, Amsterdam, 2001.

6 The marine biological cycle

6.1 A geochemical perspective

This section focuses on the effect of the marine biota on the tracer distribution in the ocean and on the global carbon cycle. Organic matter, as well as $CaCO_3$ (calcite and aragonite) and silicate shells (SiO_2, Opal) are formed by biological activity in the surface ocean and are partly exported to the deep ocean where they are re-mineralized (Figure 6.1). First, we will address the cycle of organic matter.

The organic matter cycle and vertical gradients in nutrient concentrations

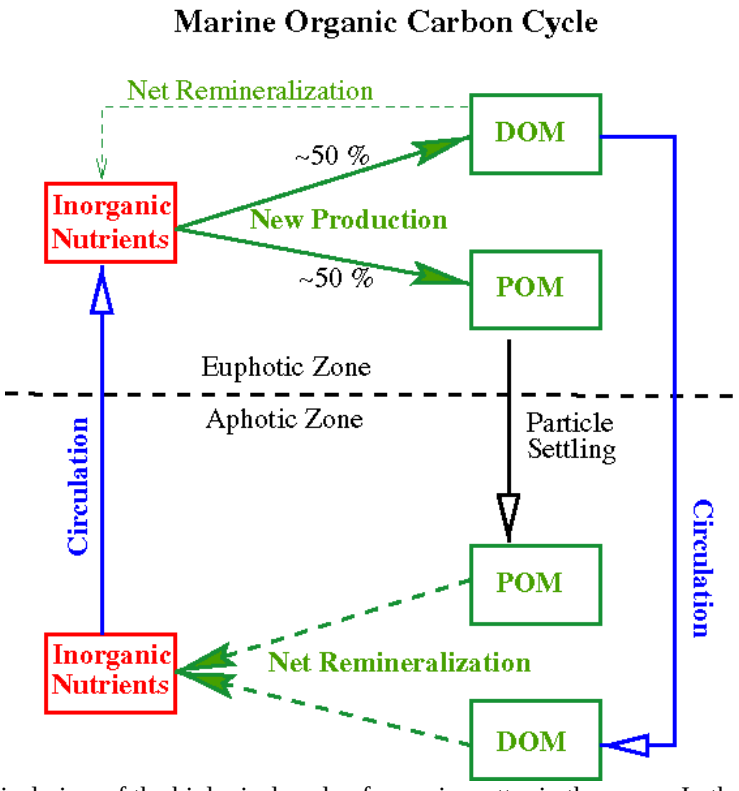

Figure 6.1: Geochemical view of the biological cycle of organic matter in the ocean. In the surface ocean, biological activity results in the conversion of nutrients to particulate organic matter (POM). From the surface ocean, POM is partly exported to the deep ocean where it is re-mineralized. This leads to a depletion of inorganic nutrients in the surface layer (euphotic zone) and to an enrichment of inorganic nutrients at depth.

The effects of the marine biology are reflected in the distribution of nutrient (N, P, C, etc…) and oxygen.

In a **dead ocean,** nutrients such as, nitrogen and phosphorus, as well as the alkalinity, would be almost **uniformly** distributed because their residence time in the ocean with respect to river inputs and sedimentation is significantly longer than the typical mixing time of the ocean, and because these tracers do not exchange with the atmosphere. The distribution of DIC would be highly correlated with the solubility of CO_2 in water and thus, with

temperature. In reality, strong vertical gradients of the distribution of phosphate, nitrate, DIC and alkalinity are observed. They can only be explained by the formation and re-mineralization of organic matter and carbonate shells.

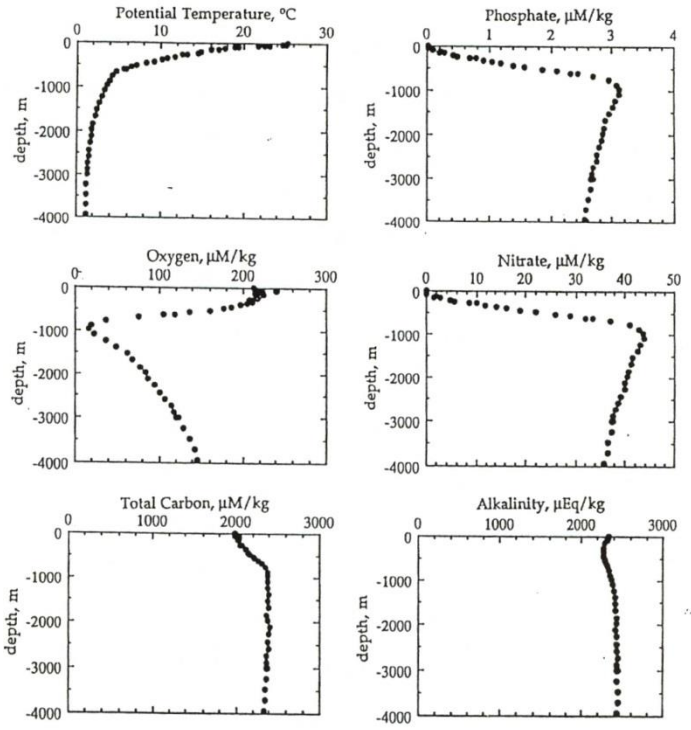

Figure 6.2: Vertical distribution of the potential temperature, phosphate (PO_4^{3-}), oxygen (O_2), nitrate (NO_3^-), dissolved inorganic carbon (DIC; $\sum CO_2$) and alkalinity in the Northern Pacific (GEOSECS station 212, 30 N, 160 W).

Dissolved C, P and N are depleted in the surface relative to the deep, because biogenic material is constantly exported from the surface to the deep. The transport by organic material corresponds to about 90 % of the export flux of biogenic carbon, the remainder is by carbonate shells. Dead organic matter is oxidized by bacteria mainly in the thermocline. This leads to DIC and NO_3 maxima and to an O_2 minimum at the depth of several hundred meters.

Nitrogen (nitrate) and phosphorus (phosphate) are limiting nutrients for plants. This means that only as long as N and P are available, organic material can be produced. The input of P and N to the surface is primarily through the exchange of water masses of the surface ocean with the Thermocline and the deep sea and only to a small extent by continental runoff. In vast parts of the ocean (Figure 6.3), especially at mid-latitudes, almost all available P and N are consumed by organisms. The biological productivity in such regions is limited by the availability of these elements and thus controlled by the water exchange of the surface with the deep ocean. In upwelling regions, for example in the Equatorial Pacific or along coastal regions, the biological productivity is high. In the Southern ocean, as well as in the Northern Pacific, P and N concentrations are considerably higher than elsewhere. In these regions, the productivity is controlled by other factors (light; other tracers: Fe).

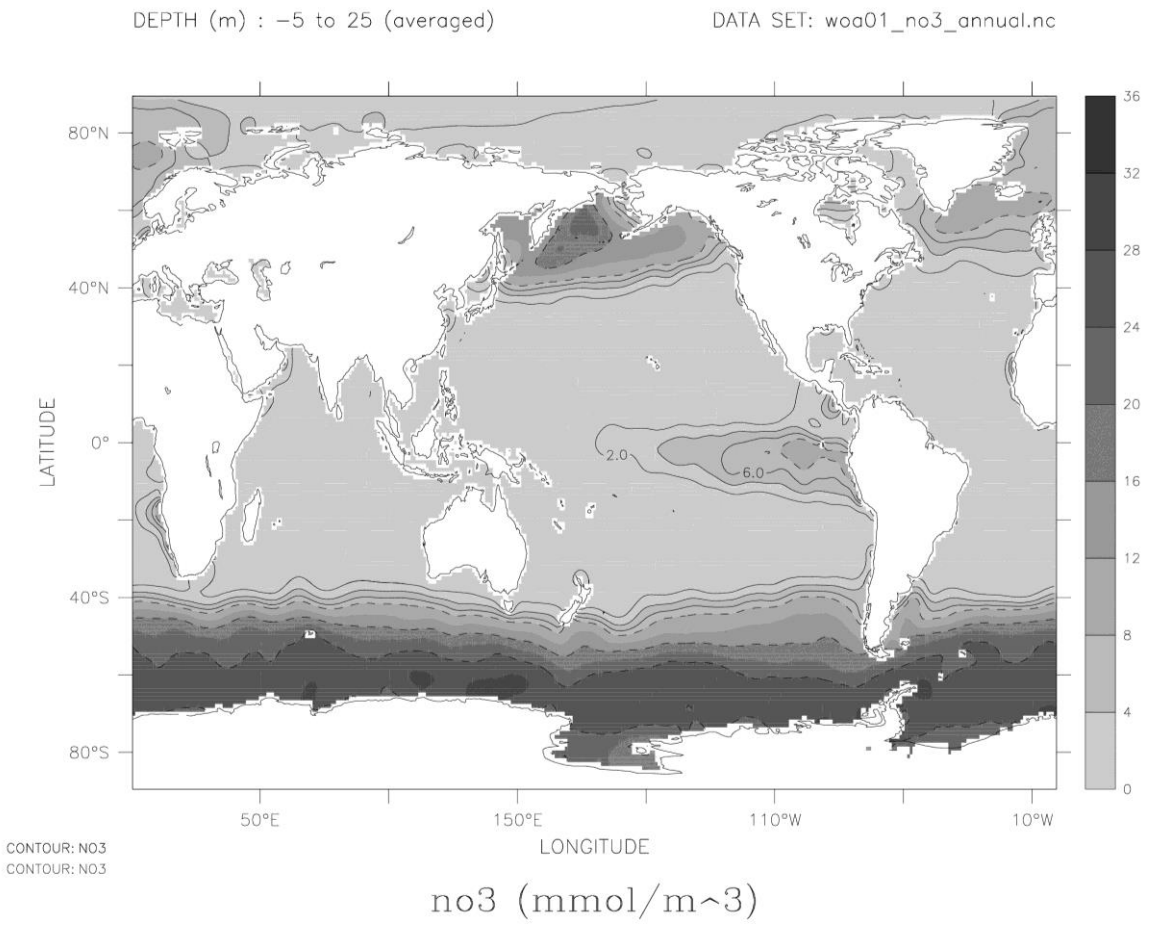

Figure 6.3: The concentration of nitrate in the uppermost 25 meters.

Redfield ratios: linear coupling between nutrients

The ratio of P : N : C: O_2 and to other nutrients is surprisingly constant in the deep ocean (> 400 m). This can be explained by the fact that over long time scales (year) and larg spatial scales (basin), nutrients are built into organic material at a roughly constant ratio, although very large differences exist between different organisms in terms of their chemical composition. These ratios are called **Redfield ratios**. For each mol of organic phosphorous re-mineralized below 400 meters, 16 mol of nitrogen and 120 mol of carbon are released and 170 mol of oxygen is consumed:

P : N : C: O2 = 1 : 16 : 120:-170 (Redfield ratios) Eq. 6.1

The ratios for trace elements to phosphorous are roughly:

P : Fe : Zn : (Cu, Mn, Ni, und Cd) = 1 : 0.005 : 0.002 : 0.0004 Eq. 6.2

For opal-building organisms growing under sufficient nutrient supply, the ratio of biogenic silica to nitrogen is:

$Si:N \approx 1:1$ Eq. 6.3

However, the Si:C and Si:N ratio can be much larger in case the growth of organisms is limited by low iron concentrations.

Concentration of nutrients is thus, roughly, linearly coupled through the activity of the marine biota.

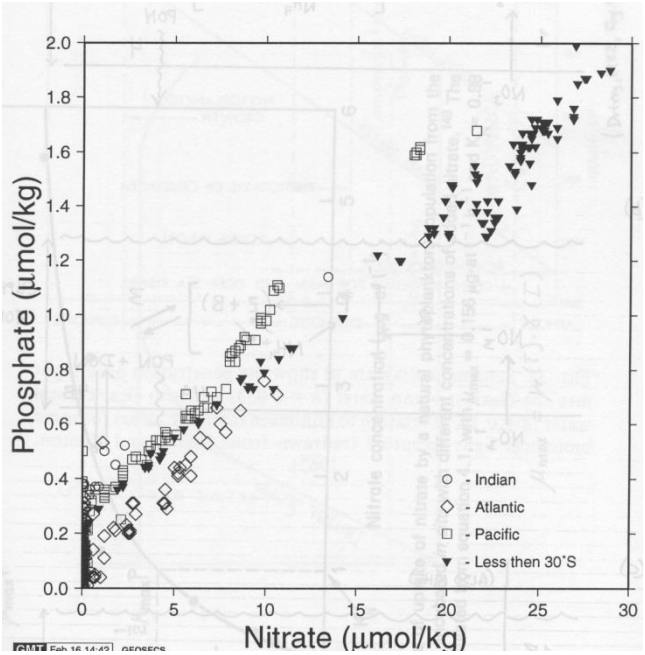

Figure 6.4: The ratio of nitrate to phosphate in the surface ocean.

Does the organic matter cycle affect atmospheric CO_2?

For an ocean in steady state, the fluxes related to the cycling of organic matter are roughly in balance. Thus, the organic matter cycle does not remove carbon from fossil fuel burning and other external sources from the atmosphere. However, the organic matter cycle affects the natural concentration of CO_2 and changes in the organic matter cycle can have an impact on atmospheric CO_2.

Without the flux of organic matter into depth, the DIC concentration and thus the partial pressure of CO_2, pCO_2, in the surface ocean would be noticeably higher. Model simulations of the oceanic C- and P-cycle indicate that for a dead ocean (no biology), the atmospheric CO_2 concentration would be about 450 ppm. In hypothetical simulations where the marine biology is able to deplete the macronutrients everywhere in the ocean, atmospheric CO_2 is around 230 ppm instead of the preindustrial 280 ppm.

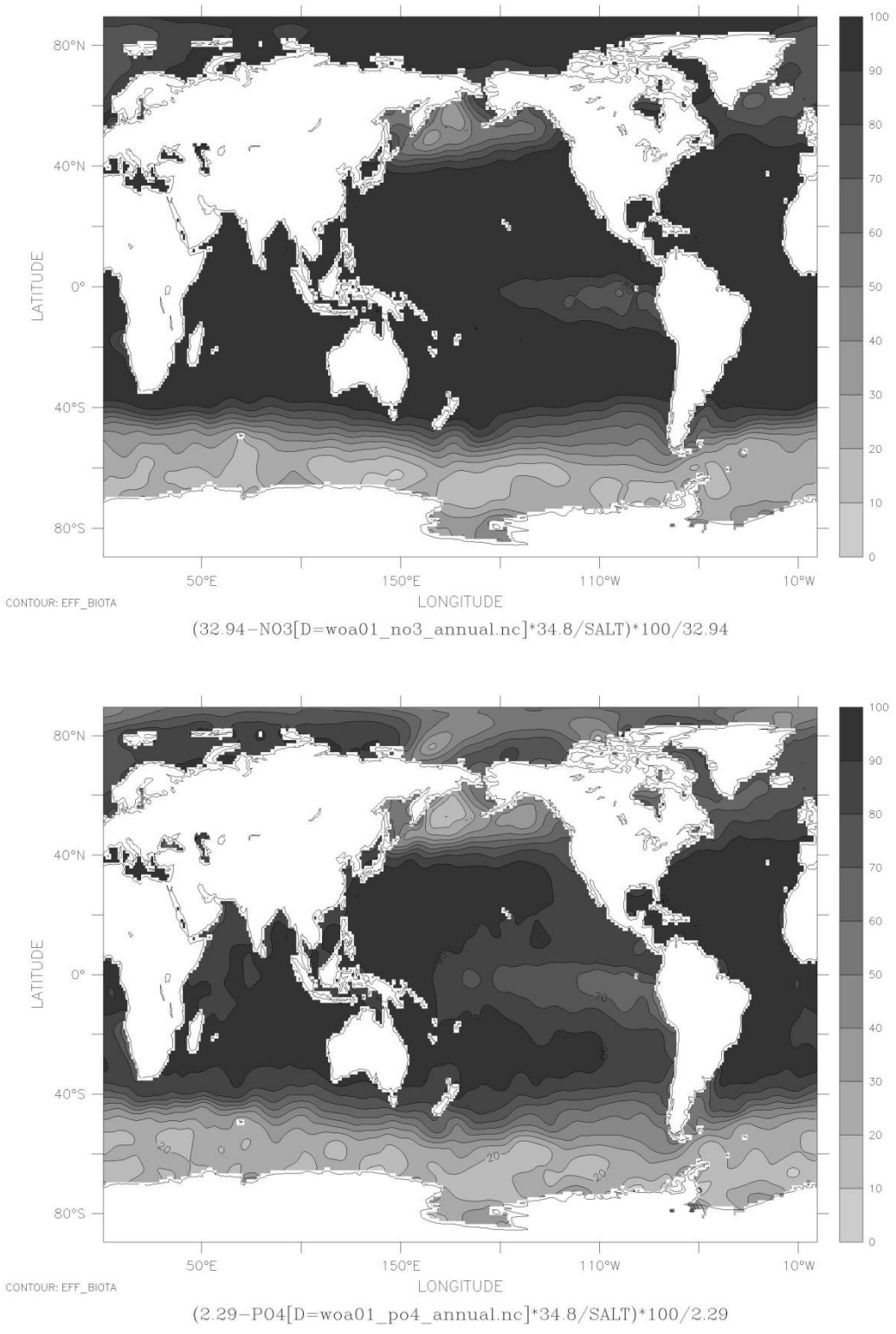

Figure 6.5: Efficiency of the marine biota in depleting nitrate (above) and phosphate (below) in the surface layer (as percentage).

How effectively are macro-nutrients used by marine organisms?

The sensitivity of atmospheric CO_2 to changes in the nutrient cycles, motivates a more thorough discussion of the biological cycle with respect to the nutrient depletion at the surface. We focus on the nutrient phosphate which is, neglecting inputs by rivers and sedimentation, only affected by processes within the ocean. In contrast to carbon, phosphate is not subject to gas exchange processes. Without the flux of organic matter to depth, the phosphate concentration would be similarly distributed as the salinity. Variations in the spatial distribution would merely be affected by evaporation and precipitation (as well as the small inputs from rivers and the dust deposition). Freshwater input lowers the concentration of tracers and salinity by dilution, while evaporation leads to enrichment. We correct the phosphate concentration for the input of freshwater by normalizing the concentration to the mean salinity of the ocean, 34.8 psu:

$$P_n(x,t) = P(x,t) \cdot \frac{34.8}{s(x,t)} \qquad \textbf{Eq. 6.4}$$

s is the salinity at the location x at time t and P_n is the normalized phosphate concentration.

Without the biological cycle, P_n would be uniformely distributed in the ocean and would be equal to the mean oceanic concentration $\overline{P}_n$ at all locations (P_n is a ratio and hence not a conserved quantity with respect to transport processes such as diffusive mixing or convection; here, the mixing effects are small and may be neglected). Now, we can describe the efficiency of the organic biological cycle with respect to the depletion of nutrients and DIC as follows:

$$Eff - Biota(x,t) = \frac{\overline{P}_n - P_n(x,t)}{\overline{P}_n} 100\% \qquad \textbf{Eq. 6.5}$$

P_n equal zero corresponds to an efficiency of 100 %. The Redfield coupling causes other elements, particularly DIC to be depleted in parallel to P when considering the action of the organic matter cycle in isolation. A 100 %-efficiency means that DIC and other nutrients can not be further depleted in the surface ocean by the cycling of organic matter. Other processes such as air-sea fluxes and the cycling of calcite affect DIC in addition.

As **Figure 6.5** illustrates, the marine biology is very efficient in depleting phosphate and nitrate at the surface in many regions. Particularly in the area of the subtropical gyres, the efficiency amounts to over 80 %. However, in the Southern Ocean, in the Northern Pacific, and in the Equatorial Eastern Pacific, high nutrient concentrations can still be found. Reasons for the sub-optimal efficiency in these areas will be discussed in the next sections.

Distributions of nutrients and the large-scale circulation

Figure 6.6 and Figure 6.7 shows the distribution of phosphate and inorganic carbon in different ocean basins. The depletion of phosphate and carbon in the warm surface ocean is clearly visible. Unlike phosphate, the carbon distribution is also controlled by the temperature (solubility depends on temperature), thus the distributions are not completely congruent. At depth, relatively low concentrations are found in the region of ‘young’ North Atlantic Deep Water, while maxima are located in the ‘old’ Northern Pacific.

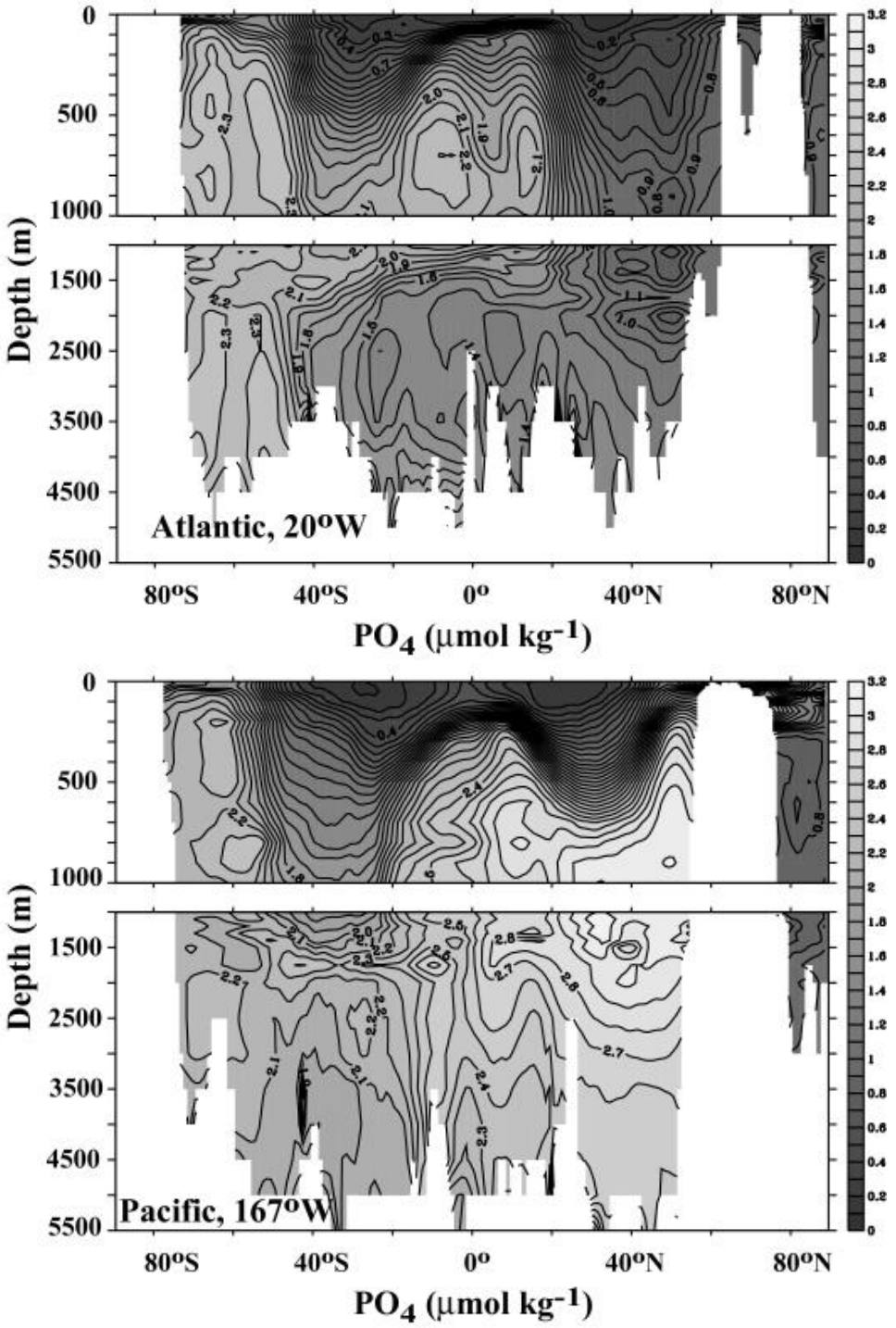

Figure 6.6: Distribution of the phosphate in the ocean. Except in the Southern Ocean and in upwelling regions, surface waters are depleted of nutrients due to biological activity. The nutrient concentration in the deep Pacific is significantly higher than in the deep North Atlantic.

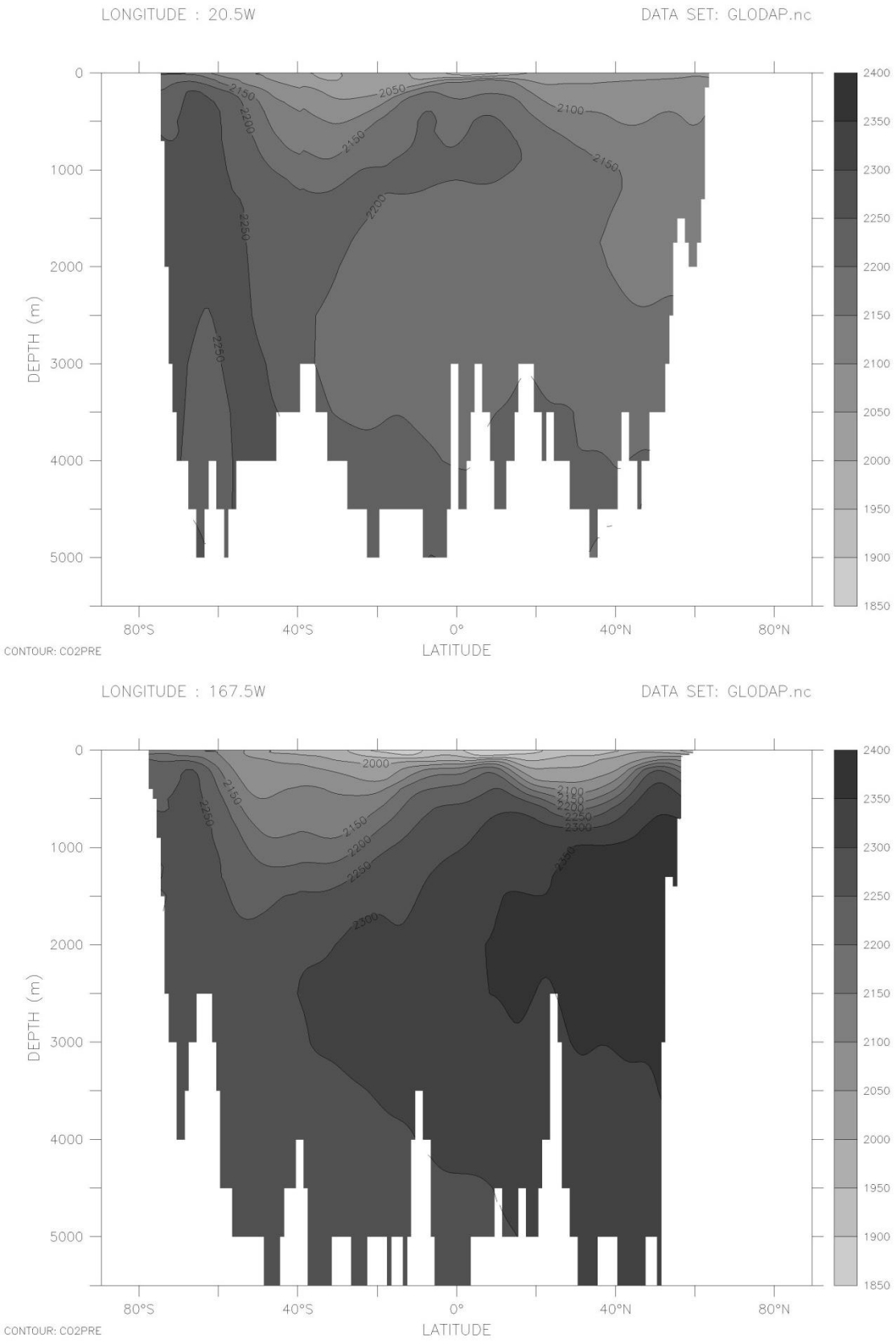

Figure 6.7a,b: Preindustrial reconstructed distribution of DIC in the Atlantic (top) and Pacific (bottom) Oceans.

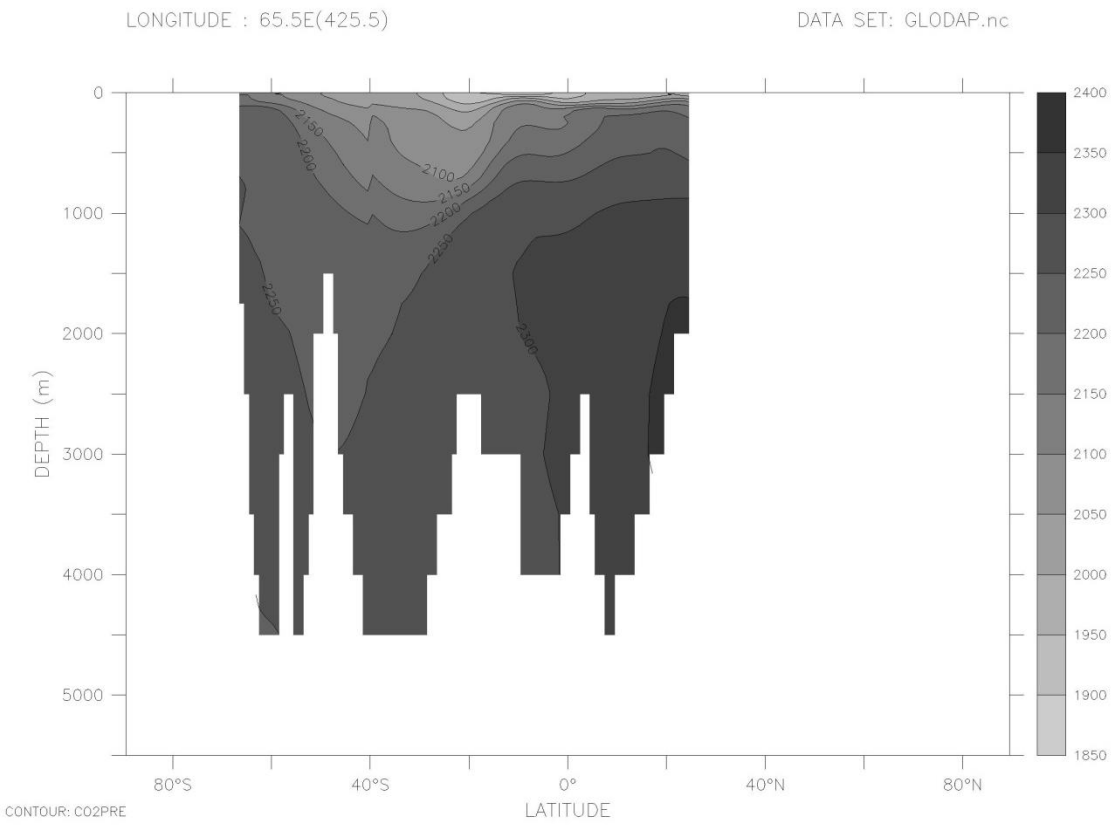

Figure 6.7c: Preindustrial reconstructed distribution of DIC in the Indian Ocean.

The gradients in nutrients from the deep North Atlantic to the deep North Pacific and deep Indian Ocean is similar to the deep-ocean gradient in radiocarbon (see chapter 4). The "older" the water, the more time was available to accumulate nutrients from re-mineralization and thus the higher the nutrient concentration.

The tight coupling between circulation, water age and biochemical tracers is most obvious when the $^{14}C/^{12}C$ ratio is plotted against the concentration of oxygen for North Atlantic Deep Water. High flow velocities directed to the south (Western Boundary Current) are found at the western bound of each basin. Consequently, the western Atlantic has a higher $^{14}C/^{12}C$ ratio and higher oxygen concentrations (lower nutrient concentrations) than the eastern Atlantic. In contrast, the eastern zones in front of Africa ($20^{o}N$) are less ventilated due to conservation of angular momentum (vorticity). In these 'eastern shadow zones' the oxygen concentrations are low and the water shows a high ^{14}C-age.

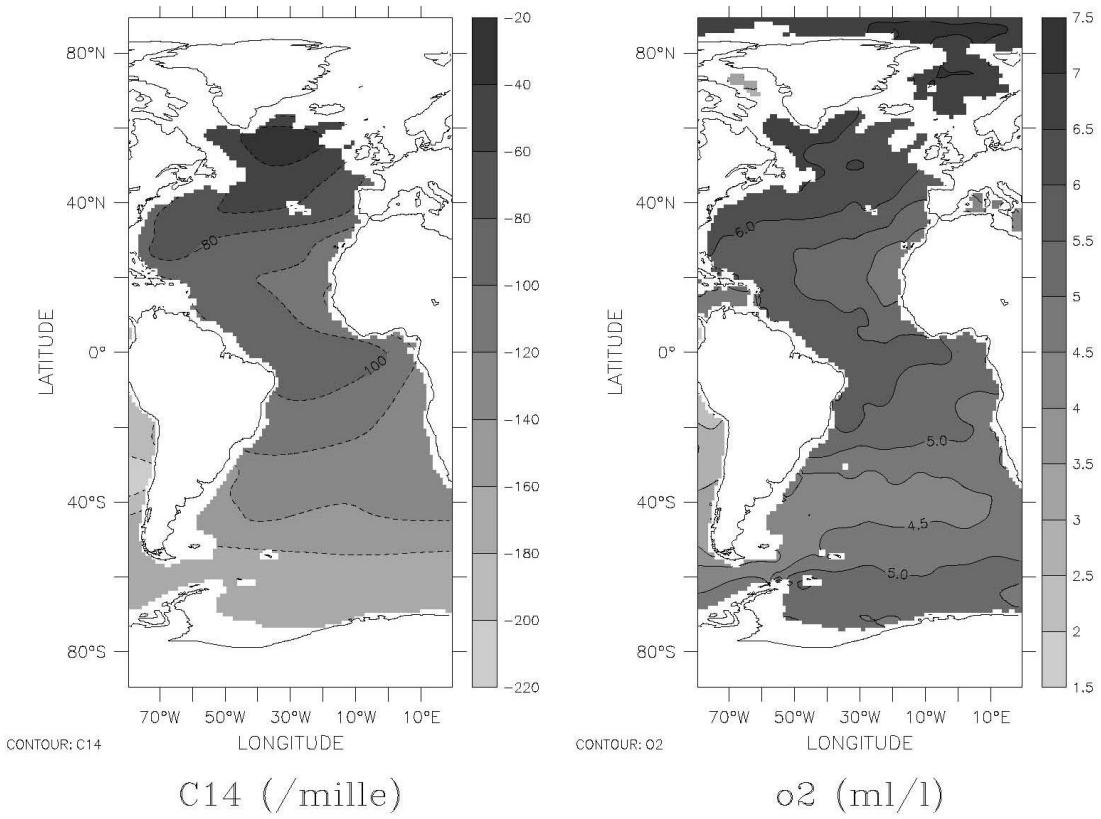

Figure 6.8: Distribution of $^{14}C/^{12}C$ (permil) and oxygen at a depth of 1750 m in the Atlantic.

6.2 Biological processes in the euphotic zone and re-mineralization of organic matter at depth

At first, some important classes of marine organisms are discussed.

Autotrophic organisms, such as phytoplankton, produce organic matter on their own using inorganic nutrients and light or chemical energy.
Heterotrophic organisms, such as bacteria, zooplankton or fishes gain energy and nutrients from existing organic material. Some hybrid forms, so-called mixotrophs, exist; they are able to function in an autotroph as well as in a heterotroph way.

Phytoplankton: As on land, the food web begins with organisms that are capable of producing organic matter by photosynthesis which requires light (‘marine plants’). The largest part of oceanic photosynthesis is realized by floating plants, called phytoplankton. They follow the C3 photosynthesis path discussed in section 3. The nutrient-poor open ocean is dominated by phytoplankton species of less than a few μm in diameter. Productive regions close to the coast are dominated by larger phytoplankton species, such as the silica shell-forming diatoms or the calcite shell-forming coccoliths. The primary production in the ocean is of roughly the same size as on land. However, the typical lifetime of plankton is on the order of some weeks. For this reason, only a small amount of carbon is stored in the form of plankton.

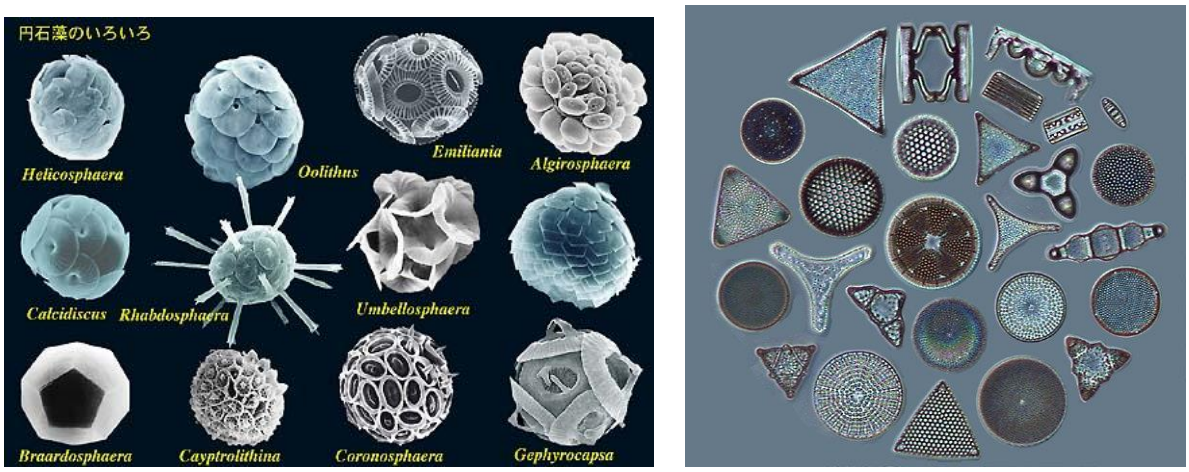

Figure 6.9: Many different species exist which form calcite shells (left) and opal shells (right).

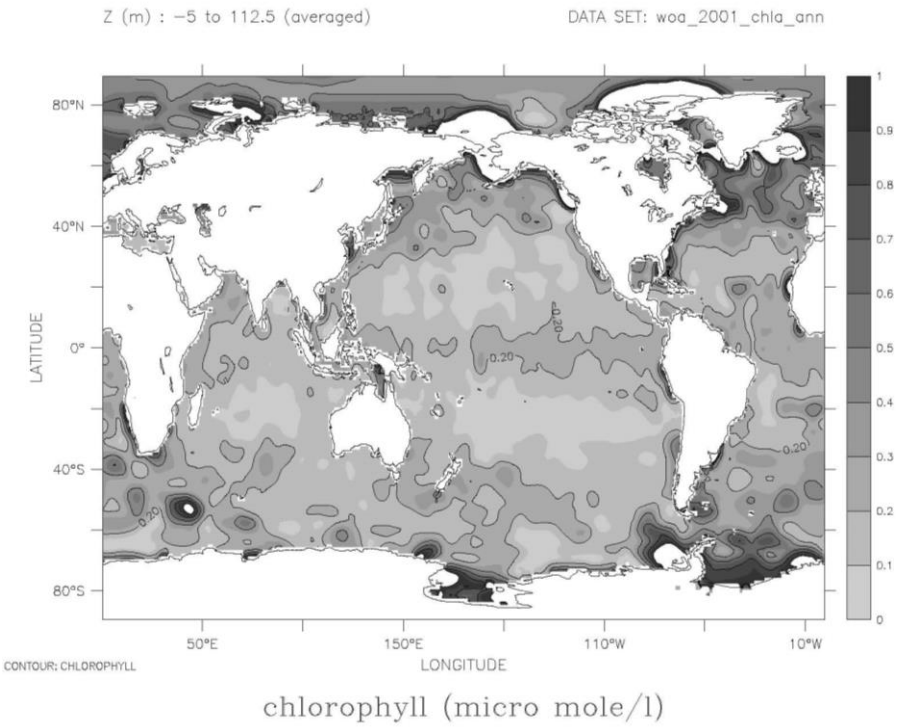

Figure 6.10: Chlorophyll distribution in the uppermost 115 m. The distribution was derived from remote sensing data.

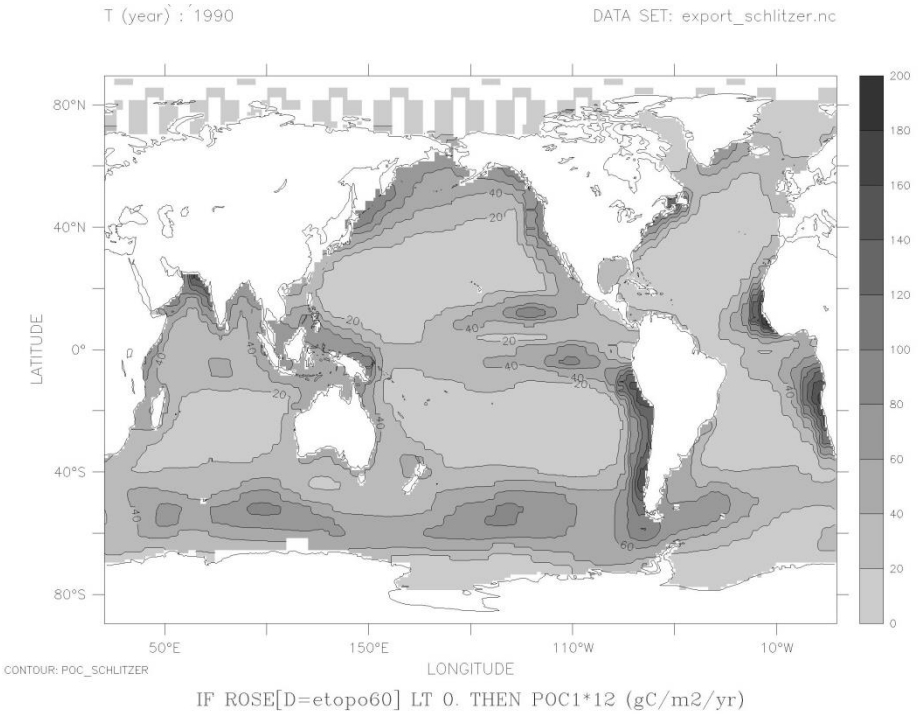

Figure 6.11: Export production of particulate organic carbon (POC). This estimate was derived from inverse modeling of the observed nutrient distribution. The global export production of POC amounts to 10 GtC per year. The export of dissolved organic carbon (DOC) is about 2 GtC per year. In total, about 12 GtC leave the surface ocean as organic matter each year.

The chlorophyll content in water can be measured with satellites. The chlorophyll content is a measure for the amount of phytoplankton. Regions of high productivity and high nutrient concentration are called **eutrophic**. The vast inner regions of the ocean with a low N- and P-content and low productivity are called **oligotrophic**.

The composition of phytoplankton is commonly described according to the Redfield ratios:

$$106\ CO_2 + 16\ HNO_3 + H_3PO_4 + 122\ H_2O = (CH_2O)_{106}(NH_3)_{16}(H_3PO_4) + 138\ O_2 \qquad \text{Eq. 6.6}$$

The corresponding ratios C:N:P:O_2=106:16:1:-138 diverge from the element ratios observed at depth. It must be noted that the Redfield concept of constant element ratios is only valid as a first-order approximation and that individual organisms may strongly differ in terms of the chemical composition.

Operationally (for measurements) phytoplankton is categorized into different size classes (from Picoplankton (0.2-2 μm) to Macroplankton (>2000 μm)).

Nitrogen-fixing organisms, such as Trichodesmium, consume N_2 (which makes up 80 % of air) for the synthesis of organic matter. This enables biological production in the surface water even in conditions where the water is completely depleted in nitrate and ammonium. Nitrogen-fixers clearly differ from phytoplankton in terms of their chemical composition. In particular, their N:P ratio is on the order of 40. Hence, considerably higher than the Redfield ratio of 16:1. The current marine N_2 fixation is about 130 TgN per year. This is sufficient to support about 10% of the export production.

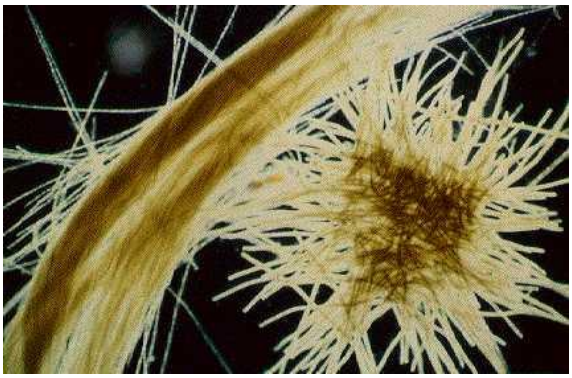

Figure 6.12: Marine Cyanobacteria, here “Trichodesmium”, are capable of fixing nitrogen from N_2. Hence, they consume N_2 in order to form organic matter.

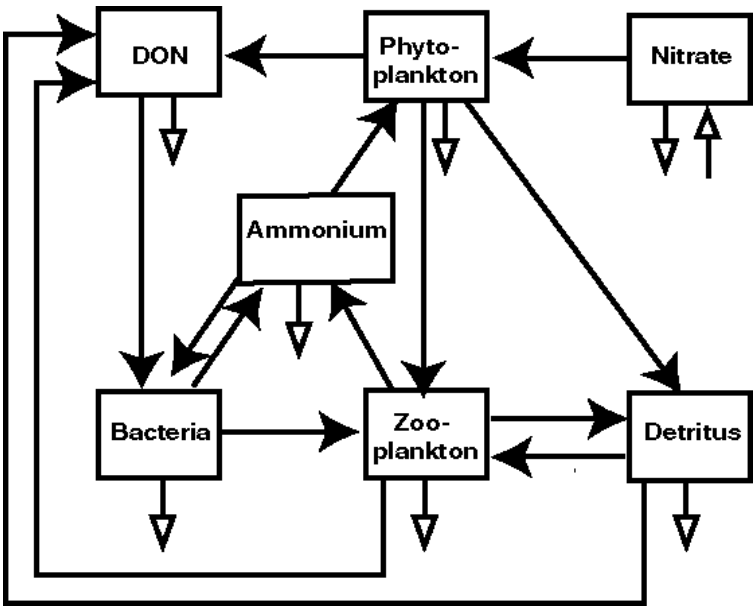

Figure 6.13: Scheme of the biological cycle of nitrogen in the surface ocean. Filled arrows represent material fluxes between pools in the euphotic zone. Open arrows represent the export from the euphotic zone to the thermocline. The *bacterial loop* begins with the consummation of DOM by bacteria and the production of ammonium, which is partly used by phytoplankton for primary production. It ends with the death of bacteria, e.g., caused by grazing of zooplankton. Ammonium is not transformed to nitrate at the surface because the required nitrifying bacteria are inhibited by light availability.

Zooplanktons are organisms that take up energy by consuming plants (herbivores) and meat. The grazing by zooplankton has three important effects: First, the amount of phytoplankton and bacteria is reduced. Second, zooplanktons excrete parts of the consumed food as particulate organic matter. Third, the metabolism of zooplanktons causes the release of ammonium that serves the phytoplankton as N-supply.

Bacteria consume organic matter produced by other organisms (heterotroph). They may also use inorganic nutrients for their metabolism (autotroph).

In the surface layer, bacteria are an important component for recycling organic matter, which is used for the production by autotrophic organisms. This is called the bacterial loop (Figure 6.13). At the surface, bacteria release ammonium and other substances due to the decomposition of dissolved organic matter, which then serve as nutrients for phytoplankton and thus enable photosynthesis. At the same time, bacteria compete for nitrogen with phytoplankton (NO_3, NH_4). It is unclear whether bacteria induce a net increase of photosynthesis, or whether they constrain the growth of phytoplankton by taking up nitrogen.

Bacterial activity influences the amount and the quality of organic matter exported to depth. Although the production of dissolved (DOM) and particulate (POM) organic matter through primary productivity is about equal, the export flux of organic matter out of the euphotic zone is dominated by the POM flux (globally: 10 GtC POM vs. 2 GtC DOM per year).

In the deep ocean and in sediments, bacteria decompose a large part of organic matter, and are thus responsible for the fact that only a few percents of the organic matter formed at the surface actually enter the sediments. In other words, bacteria are responsible for the re-mineralization of organic matter in the deep sea.

An important aspect is that most **nitrifying bacteria** are inhibited by light. During nitrification, ammonium is converted to nitrate in several steps. In the surface ocean, ammonium is not further reduced to nitrate by bacterial activity, while in the deep ocean, nitrifying bacteria convert ammonium to nitrate.

Particulate (POM) and dissolved (DOM) organic matter: Besides the living biomass, organic matter is also in the form of dead material. Operationally, dissolved organic matter (DOM), which passes a micro pore filter, and particulate matter, which is retained by a micro pore filter, are distinguished. Phytoplankton and zooplankton are sources of dead organic matter during their life time and at the time of death. Figure 6.14 depicts schematically the formation and decomposition of DOM. Additionally, oceans contain organic matter that is washed in from land by rivers (or by deposition). The mean life time of terrigenous DOM, washed into the Arctic sea by the great rivers, has been estimated to be about 7 years.

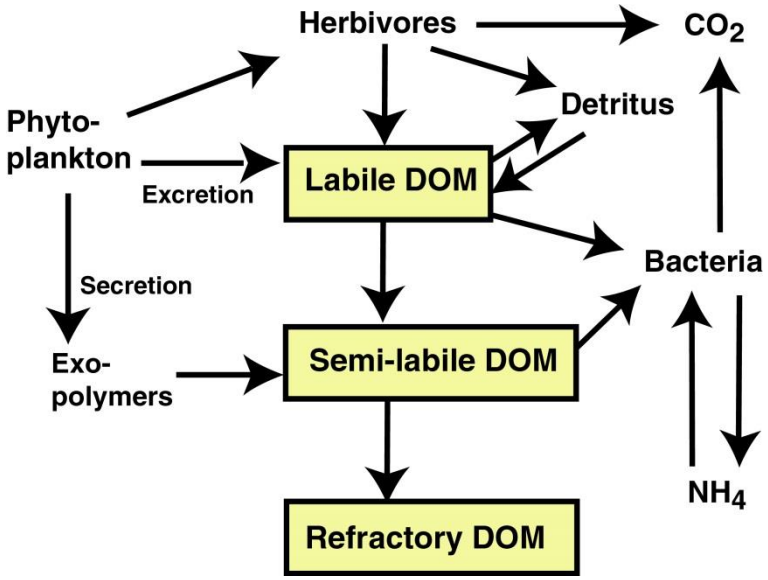

Figure 6.14: Three important components of dissolved organic matter (DOM) and processes associated with its formation and decomposition. Bacteria can also contribute to the formation of DOM by releasing enzymes that split up particulate organic matter into smaller compounds.

6.2.1 Limiting factors for biological production

Most of the relations for photosynthesis derived in the chapter on the land biosphere can also be applied to marine systems. However, the influence of light, nutrient availability, temperature and other environmental parameters on the growth of phytoplankton is often described in a parameterized form by a temperature-dependent growth rate, *V*, and factors that depend on the nutrient availability and light:

$$\frac{dPhyto}{dt} = V(T) \cdot \gamma(Nährstoffe) \cdot \gamma(Licht) \cdot Phyto - mortality \qquad \text{Eq. 6.7}$$

Typical values for the maximum specific growth rate, *V(T)*, are on the order of 1/(1-3 days).

Nutrients: Inorganic carbon and water are sufficiently available in the surface ocean, while N and P are strongly or completely depleted in large areas. Biological production is thus limited. N and P are called macro-limiting nutrients. On longer time scales, P is considered as the ultimately limiting nutrient; because some organisms (e.g. Trichodesmium) are capable of fixing nitrogen (they consume gaseous N_2 for the synthesis of organic matter). In contrast, the inventory of phosphate is controlled by the exogenous inputs. However, N is often completely depleted before P (see **Figure 6.5**).

Most of the phytoplankton species are capable of taking up N in the form of **nitrate (HNO_3)** and **ammonium (NH_4)**. However, the uptake of ammonium is energetically favorable, thus, ammonium is often rapidly consumed by the organisms and its abundance in the ocean is small. Therefore, the main effect of the occurrence of ammonium is the inhibition of nitrate uptake. This relation can be represented by an additive function that gives ammonium a stronger weight.

$$\gamma(N) = \frac{[NO_3^-]}{K_{NO_3^-} + [NO_3^-]} \cdot \exp(-a \cdot [NH_4^+]) + \frac{[NH_4^+]}{K_{NH_4^+} + [NH_4^+]} \qquad \text{Eq. 6.8}$$

The concentration of dissolved CO_2 is relatively low (see Chapter on carbonate chemistry) and the rate of photosynthesis is expected to be limited by CO_2. However, most organisms have developed ways to concentrate CO_2 in order to overcome this limiting factor.

In many areas, dissolved iron is present at very low concentrations and this iron deficit inhibits the growth of phytoplankton. For silicate shell-producing organisms, the concentration of silica has to be considered in addition. A possibilie way to describe this limitation is to include another Michaelis-Menten factor into the above equation. For example:

$$\gamma(Fe, Si) = \frac{[Fe]}{K_{Fe} + [Fe]} \cdot \frac{[Si(OH)_4]}{K_{Si(OH)4} + [Si(OH)_4]} \qquad \text{Eq. 6.9}$$

The Michaelis-Menten constants (or Monod constants) K are on the order of 0.1 mmol per m^{-3} for nitrate and ammonium, just about 1 mmol m^{-3} for silica and about 30 nmol m^{-3} for dissolved iron.

Light intensity is weakened by water and plankton and in clear water the incident light intensity is reduced to about 1 % at a depth of 100 m. At this point, photosynthesis is strongly reduced. The layer in which the light intensity is above 1 % is often referred to as the **euphotic zone**.

The light limitation for the growth of phytoplankton can also be described by a factor:

$$\gamma(I) = \frac{I}{\sqrt{I_k^2 + I^2}} \qquad \text{Eq. 6.10}$$

where I_k is a constant (on the order of 20 W m^{-2}) and I is the amount of light available for photosynthesis (Photosynthetically Active Radiation, PAR). PAR is about half of the incident light. Light is weakened by absorption and scattering in the water column and we use the Beer Law to derive the radiation at depth z:

$$\frac{dI(\lambda,z)}{dz} = -K(z,\lambda)\cdot I(\lambda,z) \qquad \text{Eq. 6.11}$$

The absorption generally depends on the depth and the wavelength of the light. In the case of a mean absorption coefficient that is constant with respect to depth, we obtain:

$$I(z) = I_0 \cdot \exp(-K \cdot z) \qquad \text{Eq. 6.12}$$

The absorption coefficient is a function of the phytoplankton content (*Phyto*) and of the content of other dimming particles:

$$K = k_{H_2O} + k_{Phyto} \cdot Phyto + k_{turbidity} \qquad \text{Eq. 6.13}$$

Accordingly, the mean penetration depth of light is:

$$z_{pen} = \frac{1}{K} \qquad \text{Eq. 6.14}$$

The attenuation coefficient of PAR for clear water, k_{H2O}, is about 0.04 m^{-1} (z_{pen}= 25 m) and hence only 1 % of the surface PAR is available at a depth of 115 m. 115 m is chosen as the nominal depth of the euphotic zone. k_{phyto} and $k_{turbidity}$ describe the light attenuation by phytoplankton and particles. The latter can be neglected except in coastal seas. The weakening by phytoplankton can be strong and k_{phyto} is on the order of 0.05 m^{-1} (mmol-N Phytoplankton m^{-3})$^{-1}$. At a phytoplankton concentration of 0.6 mmol-N m^{-3}, the 1 % level is reached at about a depth of 40 m. In coastal waters, where the concentration of phytoplankton, DOM and other particles is very high, the euphotic zone can be even shallower.

The size of the mixed layer strongly affects the mean amount of light available to photosynthesis. In this layer, water is constantly mixed by the action of winds. Most of the planktonic organisms are not capable of controlling their density actively and the mean residence time of an organism at a certain depth is roughly uniform across the entire mixed layer. The mean amount of light, $\bar{I}$, available to such organisms is thus equal to the mean radiation in the entire mixed layer:

$$\bar{I} = \frac{I_0 \cdot z_{pen}}{z_{ml}} \cdot (1 - e^{-z_{ml}/z_{pen}}) \cong \frac{I_0 \cdot z_{pen}}{z_{ml}} \qquad \text{Eq. 6.15}$$

In the open ocean, the mixed layer depth is almost always larger than the penetration depth of light (25 m) and the exponential term is close to 0. This means that the mean amount of light scales roughly linearly with the depth of the mixed layer. A shallow mixed layer allows a high mean radiation intensity, while a deep mixed layer inhibits high growth rates of phytoplankton due to a low average light intensity.

For clear water (z_{pen}=25 m) with I_0= 100 W m^{-2}, the mean light intensity for a 40 m (typical summer value), and a 200 m (high latitudes in winter) deep mixed layer amounts to:

$$\bar{I}(z_{ml} = 40 \text{ m}) = \frac{100 \text{ W m}^{-2} \cdot 25 \text{ m}}{40 \text{ m}} \cdot (1 - e^{(-40/25)}) = 50 \text{W m}^{-2}$$

$$\bar{I}(z_{ml} = 200 \text{ m}) = \frac{100 \text{ W m}^{-2} \cdot 25 \text{ m}}{200 \text{ m}} \cdot (1 - e^{(-200/25)}) = 12.5 \text{W m}^{-2}$$

With I_k= 20 W m^{-2}, the light factor in the growth equation for phytoplankton is:

$$\gamma(\bar{I}(z_{ml} = 40 \text{ m}, I_0 = 100 \text{ Wm}^{-2}) = \frac{\bar{I}}{\sqrt{I_k^2 + \bar{I}^2}} = \frac{50}{\sqrt{20^2 + 50^2}} = 0.92$$

$$\gamma(\bar{I}(z_{ml} = 200 \text{ m}, I_0 = 100 \text{ Wm}^{-2}) = \frac{\bar{I}}{\sqrt{I_k^2 + \bar{I}^2}} = \frac{12.5}{\sqrt{20^2 + 12.5^2}} = 0.53$$

The depth at which the mean photosynthesis rate in the mixed layer equals the Community Respiration (Respiration and loss by phytoplankton, zooplankton, bacteria, etc…) is denoted as the **critical depth**. The depth, at which the radiation allows just as much photosynthesis as the community respiration at the respective depth, is called the compensation depth and the corresponding radiation the "compensation irradiance" (without mixed layer, the ecosystem would exist only above this depth).

Zooplankton reduces the stocks of phytoplankton by grazing. This can significantly limit the accumulation of phytoplankton mass.

HNCL regions: In the so-called high nutrient-low chlorophyll regions (Southern Ocean, Northern Pacific and the eastern equatorial Pacific), biological productivity is obviously not limited by the availability of nitrogen and phosphate. Possible limiting factors for the growth of phytoplankton are a light deficit (primarily during winter at high latitudes), too low concentrations of biologically available iron or grazing of zooplankton.

6.2.2 Export Production

Export Production:

The fraction of production that leaves the euphotic zone in the form of organic matter is called the export production. Since the life time of phytoplankton and zooplankton is on the order of some weeks, the export production equals the so-called new production on the long-term average. The global export of particulate organic matter amounts to about 10±3 GtC. In addition, roughly 2 GtC are exported as DOM.

New and Recycled Production: Large parts of the ocean are nutrient-limited, meaning that the amount of phytoplankton will increase in case additional nutrients enter the surface ocean. The part of primary production that is enabled by the physical transport of nutrients to the

surface layer is called new production. Nutrients are also converted back to inorganic forms by processes of the food web. The primary production that is supported by the decomposition of organic matter in the surface layer itself is called recycled production. The total primary production is the sum of 'new' and 'recycled production'. The f-ratio represents the share of new production of the total production and depends on the systemic composition (species and amount of phytoplankton, zooplankton, etc):

$$f_{ratio} = \frac{\text{New Production}}{\text{Total Production}} \qquad \text{Eq. 6.16}$$

Globally, about half of the primary production leads to dissolved organic matter, majority of which is consumed by bacteria in the surface ocean. However, a considerable part is exported from the euphotic zone. Estimates yield that about 20 % of the total export of organic matter to depth consists of DOM. Diatoms with their opal shells make up a large part of the global export production and it is estimated that 50 % of the POM export is done by diatoms.

6.2.3 Re-mineralization of organic matter at depth

Remineralization of POM and DOM: Due to re-mineralization, the flux of particulate organic matter, F_{POC}, decreases with depth z. It is often parameterized as:

$$F_{POC}(z) = F_{POC}(z = 100\,m) \cdot \left(\frac{z}{100\,\text{m}} \right)^{-b} \qquad \text{Eq. 6.17}$$

The fit parameter, b, varies with location and time between 0.6 and 1.3. The mean over numerous observational stations is about 0.8. Only about 1 % of the POC flux leaving the euphotic zone reaches the ground of the ocean and enters the sediments. More complex models simulate the aggregation and gravitational settling of particles explicitly.

The labile part of dissolved organic matter (DOM) is converted to inorganic matter within weeks, while the so-called refractory DOM can have ^{14}C ages of up to a thousand years and more. Initially, the DOM concentration decreases rapidly with depth, but then stabilizes at a relatively high level. The rapid decrease is due to the decay of labile and semi-labile DOM, while refractory DOM is responsible for the relatively uniform background concentration. Often, the decay of (semi-labile) DOM is described as being proportional to the concentration of semi-labile DOM.

$$\frac{\text{dDOM}}{\text{dt}} = -\lambda_{\text{DOM}} \cdot \text{DOM} \qquad \text{Eq. 6.18}$$

The decay time of semi-labile DOM is on the order of some months to several years.

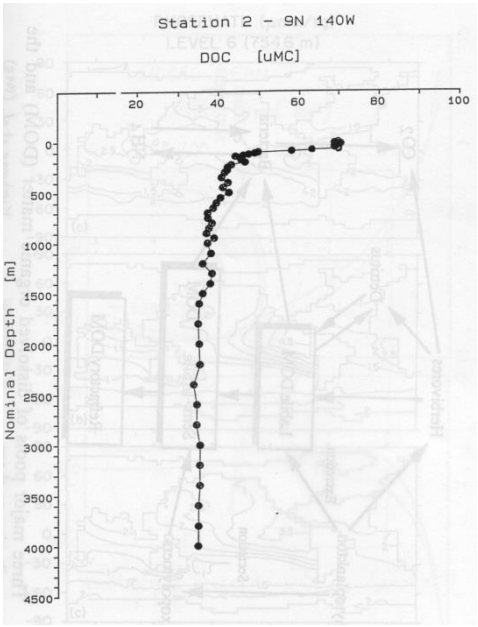

Figure 6.15: Decrease of dissolved organic carbon, DOC, with depth. DOC falls to the background concentration of long-living (refractory) DOC of 40 μmolC/kg within a few hundred meters.

6.2.4 Apparent Oxygen Utilization

Preformed and re-mineralized components: The observed distribution of a tracer can be split into a so-called preformed concentration and the amount ΔC_{remin} formed by re-mineralization:

$$C_{observed}(x,y,z,t) = C_{preformed} + \Delta C_{remin} \qquad \text{Eq. 6.19}$$

This corresponds in the simplest: A water parcel that leaves the surface at a concentration of $C_{preformed}$ and, in which concentration changes solely due to the re-mineralization process. In a more realistic case, water masses of different origin are mixed (different $C_{preformed}$). For oxygen, the re-mineralization component is quite easy to estimate. The oxygen concentration at the surface is close to saturation. Typically, it is 1-2% oversaturated. As a first approximation, $C_{preformed}$ can be estimated from the saturation concentration. The following re-mineralization component for oxygen follows:

$$\Delta O_{2,remin}\,(x,y,z,t) \approx [O_2\,(x,y,z,t)] - [O_2]_{sat} \qquad \text{Eq. 6.20}$$

The saturation concentration is calculated for the in-situ measured temperature and salinity (meaning at location x,y,z). Note that the solubility of oxygen depends non-linearly on T and S. Due to this non-linearity, mixing of saturated waters of different temperature results in a higher concentration than the saturation concentration at the mixing temperature. Hence, due to these non-linear mixing effects, the in-situ saturation concentration is only an approximation for $O_{2,prefomed}$. Nevertheless, it is a good one. A possible re-mineralization due to denitrification is not accounted for.

AOU: The term Apparent Oxygen Utilization (AOU) is often used. AOU is defined as follows:

$$AOU \equiv [O_2]_{sat} - [O_2\,(x,y,z,t)] \qquad \text{Eq. 6.21}$$

As a first approximation, AOU corresponds to $-\Delta O_{2,remin}$. From the Redfield ratios we can directly derive the re-mineralization components for P, N, C and Alk from the nitrification process. For example phosphate:

$$\Delta PO4,remin = r_{P:O2} \cdot (-AOU) \qquad \text{Eq. 6.22}$$

Figure 6.16 shows the observed distribution of oxygen and AOU in the Pacific. The oxygen concentrations are small in the thermocline of the Northern Pacific, thus at the "end of the Conveyor Belt Circulation". On the other hand, oxygen concentrations are high in the thermocline around 40°S. The thermocline at around 40°S is obviously well ventilated. Following the lines of equal temperature (~density) from the surface into the thermocline we observe a continuous increase of AOU with increasing distance from the surface. This corresponds to the image of a ventilation of the thermocline along surfaces of equal density and the water age increases with the distance from the 'outcrop region' (region where a surface of equal density meets the surface of the ocean). On its way away from the outcrop region, oxygen is consumed by re-mineralization and AOU increases.

The oxygen concentration is close to zero in the so-called Oxygen Minimum Zones, which are located at a depth of around 500 m in front of the coast of Latin America, in the California Current System and in the Arabian Sea (Figure 6.17). These zones are located in regions of high export production, or re-mineralization rates, resp. and of relatively high water age. Denitrification, and hence the production of N_2O, is increased in these regions.

Re-mineralization rates and oxygen utilization rates (OUR) can be estimated using water ages and considering the mixing ratio of different water masses.

Let us consider the situation in the deep Pacific. For simplification we assume that the water is transported from the Southern Ocean to the Northern Pacific only by advection and that the water masses do not mix. According to this model, the phosphate concentration and AOU of the water parcel increase due to re-mineralization of organic matter. AOU increases by about 100 mmol m^{-3} (1 ml/l = 44.6 mmol m^{-3}, Figure 6.16) and PO_4 by 0.6 mmol m^{-3} (Figure 6.6) between the deep (2000 m) Southern Ocean and the Northern Pacific. On the other hand, $\Delta^{14}C$ decreases by around 70 permils, which corresponds to an age increase by 560 years. This yields:

$$\frac{dPO_4}{dt} \approx \frac{0.6 \text{ mmol m}^{-3}}{560 \text{ a}} = 1\ \mu\text{mol m}^{-3}\ \text{a}^{-1} \qquad \text{Eq. 6.23}$$

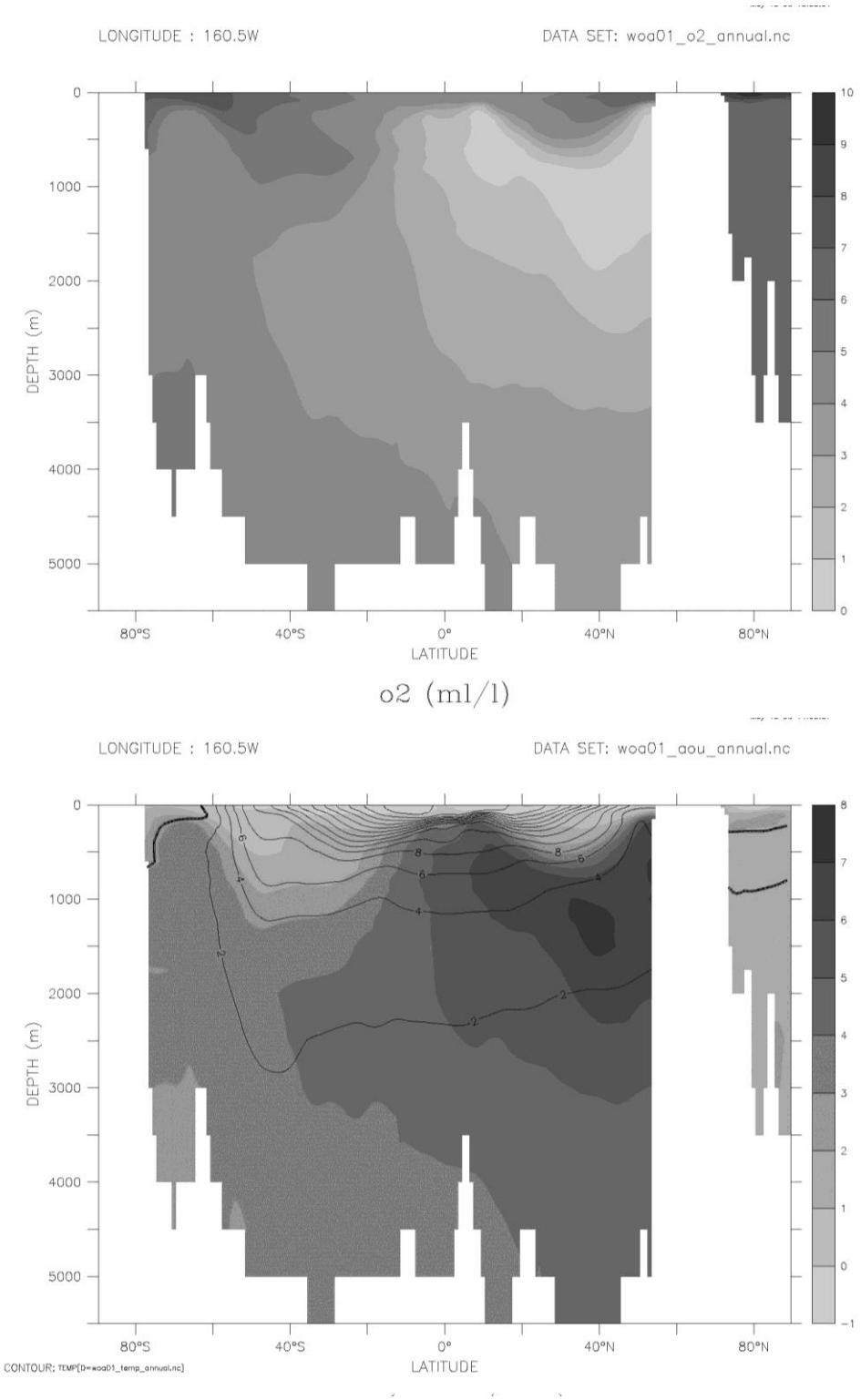

Figure 6.16: Concentration of oxygen (top) and apparent oxygen utilization (AOU) (bottom) in ml/l (1ml(STP)=44.6 µmol) along a transect in the Pacific at 160°W. In the lower figure, isotherms are additionally given as contour lines.

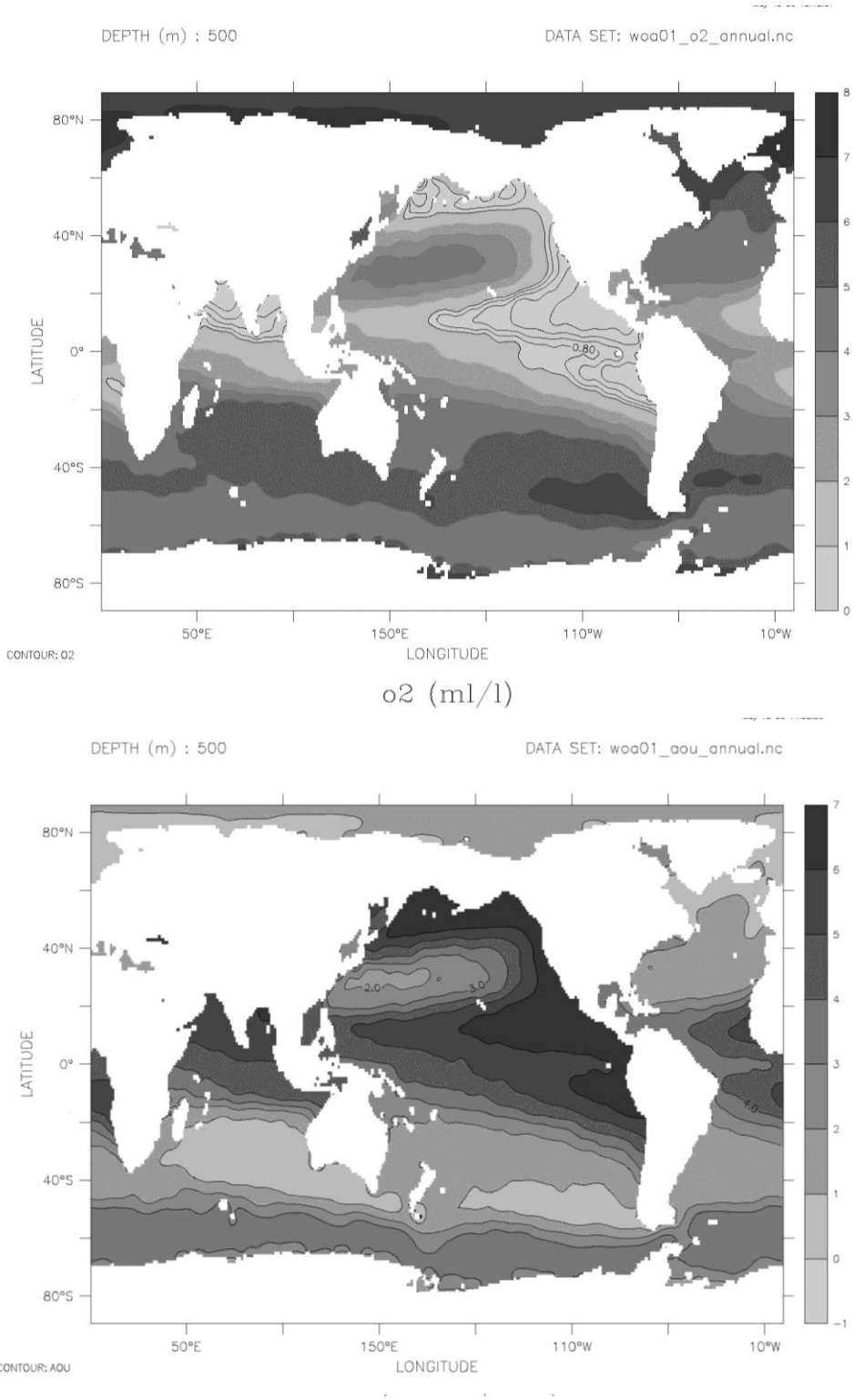

Figure 6.17: Distribution of oxygen (top) and AOU (bottom) at a depth of 500 m. The oxygen concentration is very low off the coasts of Latin- and Northern America, in the Northern Pacific and in the Arabian Sea. The concentration gradients of these oxygen minimum zones are highlighted by contour lines with a distance of 0.2 ml/l. These regions are characterized by a relatively high denitrification rate and a high N_2O production.

$$\frac{dO_2}{dt} \simeq -\frac{dAOU}{dt} \approx \frac{\text{-100 mmol m}^{-3}}{560\text{ a}} = -180\ \mu\text{mol m}^{-3}\ \text{a}^{-1} \qquad \text{Eq. 6.24}$$

Analogously, OUR can be estimated for the thermocline. Typically, OUR is on the order of 10 mmol m^{-3} a^{-1}, hence about two orders of magnitude larger than in the deep ocean. The majority of the re-mineralization occurs in the thermocline and less than 10% of the exported organic carbon is re-mineralized below 2000 m.

6.2.5 Nitrous Oxide (N_2O)

Decomposition of organic matter: In an oxygen-containing environment, the transformation of organic N to inorganic nitrate occurs in three steps:

$O_2 > 0$; dark:

Ammonification: organic N $\rightarrow$ NH_4^+ Eq. 6.25

Ammonium Oxidation: $3\ NH_4^+ + 3\ H_2O + 6\ CO_2 \rightarrow 3\ NO_2^- + 6\ H^+ + C_6H_{12}O_6$ Eq. 6.26

Nitrite Oxidation: $12\ NO_2^- + 6\ H_2O + 6\ CO_2 \rightarrow 12\ NO_3^- + C_6H_{12}O_6$ Eq. 6.27

The **nitrification** of ammonium to nitrate is done by different bacteria that gain energy for the buildup of organic matter (here denoted $C_6H_{12}O_6$) through this process. The most well-known are *Nitrosomonas spp*, which oxidize ammonium, and *Nitrobacter spp*, which oxidize nitrite (NO_2^-). The common re-mineralization process requires oxygen and is inhibited by light.

Under oxygen-depleted conditions, alternative bacterial processes for the decomposition of organic matter become important. Quantitatively important is the **denitrification**, where oxygen is replaced by nitrate as the oxidant:

$C_{106}H_{175}O_{42}N_{16}P + 104\ HNO3 \rightarrow 106\ CO_2 + 60\ N_2 + H_3PO_4 + 138\ H_2O$ Eq. 6.28

Thus, the denitrification causes nitrate to be converted to N_2 and organic matter to be decomposed. On the long term, the loss of nitrate has to be compensated by the formation of new nitrate. This is achieved by the nitrogen fixation in the euphotic zone. It is unclear as to what extent the current nitrate budget of the ocean is in an equilibrium state. The loss through denitrification is estimated to be about 70Tg N yr^{-1}.

Formation of N_2O: The conversion of organic matter causes a small amount of nitrogen to be released as nitrous oxide. N_2O is an important greenhouse gas. About a third of the natural sources for atmospheric N_2O are located in the ocean, and about 2/3 in the land biosphere. The formation of N_2O is associated with the oxidation of ammonium during the process of nitrification. N_2O is also formed during denitrification. N_2O is an intermediary product of denitrification. In case part of the produced N_2O escapes before the reduction to N_2 is completed, denitrification turns to a N_2O source. At the same time, denitrification can also act as a N_2O sink.

Isotope measurements on N_2O in the ocean point to the fact that nitrification is quantitatively the most important process for N_2O formation in the ocean. At relatively low oxygen concentrations, more N_2O tends to be produced from one mol of organic matter. Typically, this relation is parameterized in models by linking the N_2O production to the re-mineralization rate of oxygen and to the oxygen concentration

$$\text{Source } (N_2O) = (\varepsilon + \beta\, f(O_2)) \left.\frac{dO_2}{dt}\right|_{\text{Remin-Nitrification}} \qquad \text{Eq. 6.29}$$

With

$$f(O_2) = \frac{[O_2]}{O_{2max}} \qquad [O_2] < O_{2max}$$

$$f(O_2) = \exp\left(\frac{-k([O_2] - O_{2,max})}{O_{2,max}}\right) \qquad [O_2] > O_{2max}$$

Typically, k is 0.1 and $O_{2,max}$ about 1 10^{-3} μmol l^{-1} and ε is roughly 10^{-4}.

Consumption in anoxic regions is described by:

$$\text{Sink } (N_2O) = -k_{consumption}\,[N_2O] \qquad \text{Eq. 6.30}$$

N_2O is transported in the ocean and enters the atmosphere by gas exchange. There, N_2O is transformed to N_2, primarily by photochemical processes and has an atmospheric life time of 120 years.

Atmospheric N_2O variations during the last glacial period: During the last glacial and during the transition to the current warm period, the atmospheric concentration repeatedly fluctuated by about 20-30 ppm. These fluctuations are associated with a reorganization of the large-scale circulation of the Atlantic. Paleo data reveals that several times in the past the North Atlantic Deep Water Formation temporarily shut down and that the Atlantic was filled at depth with water from the Southern Ocean, and not with NADW. Model simulations (Figure 6.18) point to a direct coupling of these circulation changes with changes in the oceanic N_2O source. However, the largest part of the observed atmospheric variations is probably caused by changes in the terrestrial biosphere.

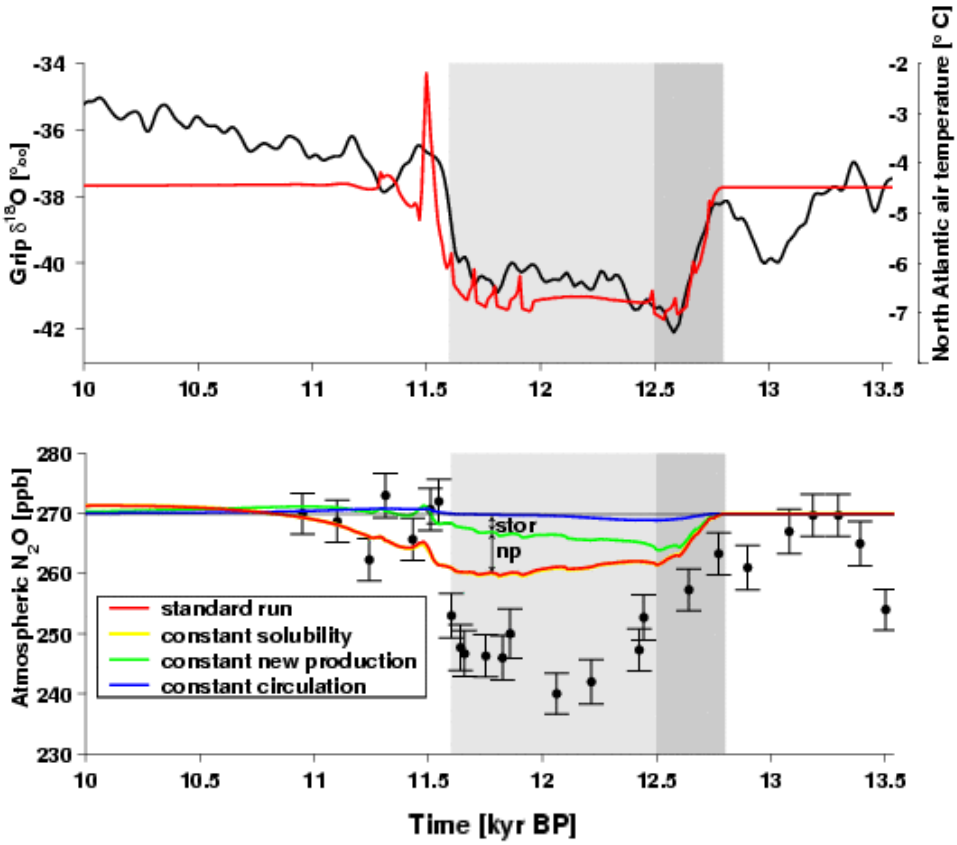

Figure 6.18: Comparison between observations and model results for the Younger Dryas, a cold phase (grey) during the transition from the last glacial to the current interglacial. The model ocean was disturbed by a prescribed freshwater input into the Northern Atlantic. This disturbance lead to a collapse of the North Atlantic deep circulation and a cooling in the north Atlantic region (above, left axis), which is comparable in length and strength with the variations of the oxygen isotope ^{18}O in Greenland, a temperature proxy. The figure below illustrates the evolution of the atmospheric N_2O measured in polar ice cores (symbols) and in the model. The modeled N_2O explains only part of the observed variation, because the land biosphere (not modeled) probably contributes to the atmospheric variations. The largest part of the ocean-caused changes is attributed to the reduction in the Export Production after the collapse of the NADW (np) and to the slower mixing of the Atlantic leading to an increased storage of N_2O in the ocean (stor), while changes in the surface temperature/solubility of N_2O play a minor role.

6.2.6 Calcium carbonate

The cycling of calcium carbonate ($CaCO_3$) plays a crucial role in the global carbon cycle when considering time scales longer than 1000 years. The marine $CaCO_3$ cycle regulates the alkalinity budget of the ocean. In the long run, the input of alkalinity from land is balanced by the loss of alkalinity due to sedimentation of $CaCO_3$.

The $CaCO_3$ cycle and ocean sediments have the following important effects:

1) An atmospheric CO_2 perturbation caused by an external input (extraction) of CO_2 into the system atmosphere-ocean (such as the emission of fossil CO_2 or the uptake/release from the land biosphere) is significantly reduced by the ocean-sediment interaction with a time scale of typically 5000 years.
2) An atmospheric CO_2 perturbation due to a change in the formation and the export of $CaCO_3$ out of the surface ocean is significantly enhanced by the interaction. Changes in the export production of $CaCO_3$ are thus able to strongly affect the atmospheric CO_2 concentration and potentially played an important role for the glacial-interglacial CO_2 variations.

The typical time scale for these interactions is considerably shorter (5000 years) than the residence time of alkalinity.

On time scales of more than 100'000 years, the atmospheric CO_2 concentration is regulated by the erosion of rocks and planetary outgassing of CO_2.

Formation of biogenic $CaCO_3$: The formation (dissolution) of 1 mol $CaCO_3$

$$Ca^{2+} + CO_3^{2-} \rightarrow CaCO_3 \qquad \text{Eq. 6.31}$$

causes 1 mol carbon and 1 mol calcium ions as well as 2 mols alkalinity to be extracted from (added to) the water column. Thus, the CO_2 partial pressure increases with the formation of $CaCO_3$.

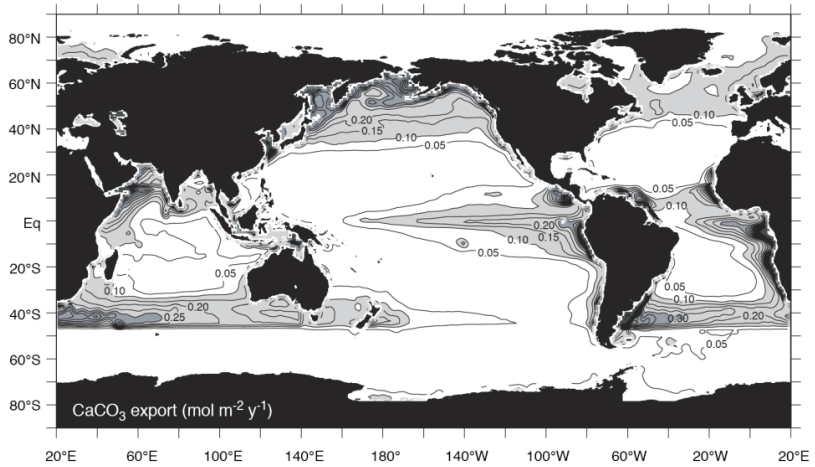

Figure 6.19: Estimated export of calcium carbonate out of the surface ocean (From Sarmiento and Gruber, 2006)

In the open ocean, three groups of organisms are mainly responsible for the formation of biogenic $CaCO_3$. We note that $CaCO_3$ is not precipitated spontaneously in the open ocean as the activation energy for the reaction is high. Two mineral forms of $CaCO_3$ can be distinguished: calcite (trigonal system) and aragonite (orthorhombic system). Calcite is more stable. Coccolithophorides are a group of phytoplankton organisms forming shells from calcite. The zooplanktonic group of foraminifera forms calcite shells, as well. Pteropods, a zooplankton group, form shells made of aragonite. It is estimated that about 70 to 90 % of the $CaCO_3$ export in today's oceans is in the form of calcite.

The marine $CaCO_3$ budget: Annually, about 1 GtC of $CaCO_3$ is formed in the euphotic zone by the marine biota and exported to the deep sea. About 0.7 GtC of it is dissolved in the open water column, the rest precipitates to the ground. Of this flux of 0.3 GtC a^{-1} about 0.1 GtC a^{-1} (10^{13} mol) enters the sediments on the long-term, while the rest is dissolved from the sediments into the water column.

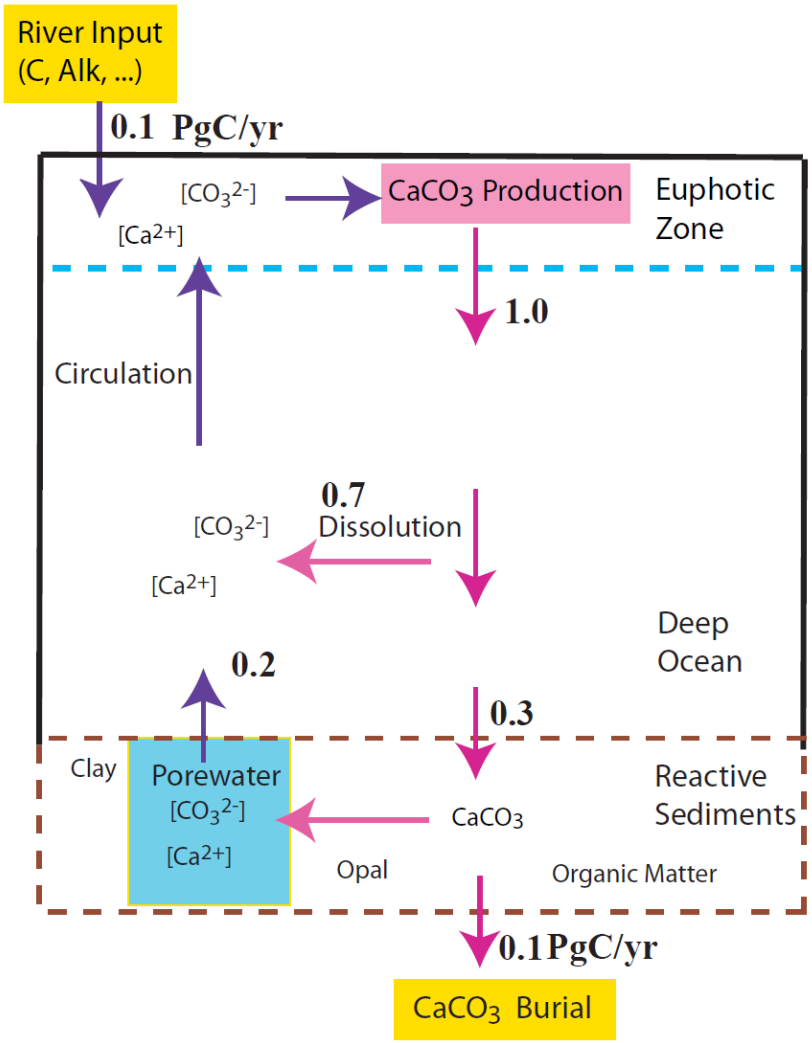

Figure 6.20: Schematic representation of the cycling of calcite. Fluxes are given in PgC/ yr. On the long-term average the input of carbon and alkalinity from land approximately equals the burial flux. Small imbalances in these two fluxes have altered atmospheric CO_2 in the past on time scales from millennia to millions of years.

Production by corals and marine plants growing on the ocean floor was neglected for this budget. It is estimated that some 0.3 GtC are produced by these systems. Corals predominantly produce aragonite or calcite with a high magnesium content; both structures have a higher solubility product than calcite and are thus less stable.

The loss of alkalinity due to $CaCO_3$ sedimentation ($2\ 10^{13}$ mol a^{-1}) is compensated by the input of alkalinity into the ocean by rivers, originating from the erosion on land. The residence time of alkalinity is about 100'000 years:

$$\tau = \frac{\text{Inventory}}{\text{Input}} = \frac{[\text{Alk}_{oc}] \cdot A_{oc} \cdot h_{oc}}{F_{river}(\text{Alk})} = \frac{2.3 \text{ mol m}^{-3} \cdot 3.62\ 10^{14} \text{ m}^2 \cdot 3800 \text{ m}}{2\ 10^{13} \text{ mol a}^{-1}} \approx 100'000 \text{ a}$$

Eq. 6.32

rain ratio: The export flux of $CaCO_3$ in the open ocean of 1 GtC a^{-1} corresponds to only ~8% of the total export of organic carbon (~10 GtC as POC, 2 GtC as DOC) from the surface ocean. The ratio of the flux of inorganic carbon in the form of $CaCO_3$ and organic carbon in the form of POC is often referred to as the rain ratio. For the export production:

$$r_{CaCO3:POC} = \frac{F_{Export}(\text{CaCO}_3)}{F_{Export}(\text{POC})} \approx 0.1$$

Eq. 6.33

The export rain ratio exhibits a relatively small spatial variability in the modern ocean. Thus, the pattern of the export production of $CaCO_3$ resembles the pattern of the export production of organic matter.

The export of 1 mol of $CaCO_3$ is directly associated with the export of roughly 1 mol of organic matter. This means that only about 7 percent of the export of organic matter is realized by calcite-forming organisms.

The carbon flux as organic matter is larger than as $CaCO_3$, in the upper ocean. However, the two fluxes become comparable in size in the deep ocean and the rain ratio is close to 1.

$$r_{CaCO3:POC} = \frac{F(\text{CaCO}_3, z = 4000 \text{ m})}{F\ (\text{POC}, z = 4000 \text{ m})} \approx 1$$

Solubility of $CaCO_3$: The chemical balance for the dissolution reaction of $CaCO_3$

$$CaCO_3 \leftrightarrow Ca^{2+} + CO_3^{2-}$$

Eq. 6.34

is defined by the solution product, K_{SP}:

$$K_{SP}^{CaCO3} = [CO_3^{2-}]_{sat} \cdot [Ca^{2+}]_{sat}$$

Eq. 6.35

where $[CO_3^{2-}]_{sat}$ and $[Ca^{2+}]_{sat}$ denote the saturation concentration of carbonate and dissolved calcium in equilibrium with the mineral calcite or aragonite. Aragonite has a roughly 50% higher solubility than calcite.

Variations in $[Ca^{2+}]$ in the ocean are less than 1%. The oceanic $[Ca^{2+}]$ amounts to about 0.01028 μmol kg^{-1}. For this reason, it is convenient to quantify the over- or under-saturation of $[CO_3^{2-}]$ with respect to calcite or aragonite:

$$\Delta CO_3^{2-}=[CO_3^{2-}]-[CO_3^{2-}]_{sat} \quad \text{Eq. 6.36}$$

As a measure for over- or under-saturation, the following factor is often used:

$$\Omega = \frac{[CO_3^{2-}]\cdot[Ca^{2+}]}{[CO_3^{2-}]_{sat}\cdot[Ca^{2+}]_{sat}} = \frac{[CO_3^{2-}]\cdot[Ca^{2+}]}{K_{SP}^{CaCO3}} \quad \text{Eq. 6.37}$$

Again, it is noted that the solubility and thus Ω are different for aragonite than calcite. Since the concentration of Ca^{2+} in the ocean is nearly constant, the following relationship is valid:

$$\Omega \cong \frac{[CO_3^{2-}]}{[CO_3^{2-}]_{sat}} \quad \text{Eq. 6.38}$$

The solubility products for aragonite and calcite increase with pressure. The pressure-dependence can be quantified from the molar volume, ΔV_i, and the compressibility, ΔK_i,:

$$\ln(K_i^p / K_i^{p0}) = \frac{\Delta V_i}{RT} P + \frac{0.5\Delta K_i}{RT} P^2 \quad \text{Eq. 6.39}$$

where P is pressure, K^p is the solubility product at pressure P and K^{p0} is the solubility product at pressure $p0$ = 1 atm. R and T are the gas constant and temperature.

The saturation concentration at the surface at 0^oC is 42 μmol kg^{-1} for calcite and 66 μmol kg^{-1} for aragonite. At a depth of 6000 m (6000 dbar) these concentrations rise to 124 and 184 μmol kg^{-1} (Figure 6.21).

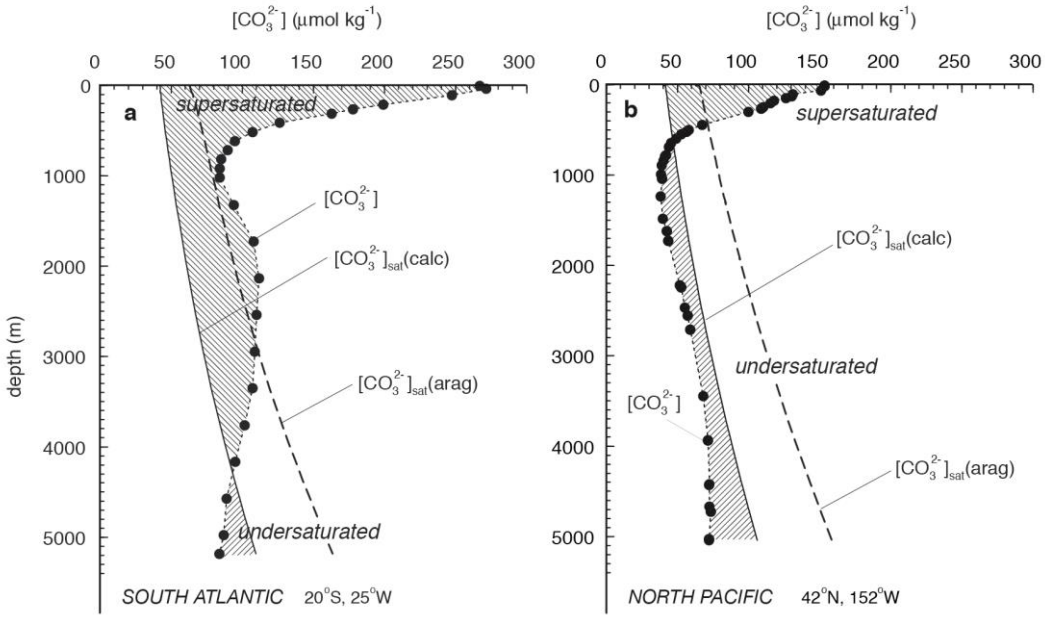

Figure 6.21: Variation of CO_3^{2-} (symbols) and the saturation concentration with respect to calcite (solid line) and aragonite (dashed lines) with depth (Sarmiento and Gruber, 2006).

The saturation horizon denotes the depth at which the CO_3^{2-} concentration is equal to the saturation concentration. As Figure 6.21 shows, the saturation horizon for calcite is around 4000 m in the Atlantic and much shallower in the North Pacific. We expect dissolution of $CaCO_3$ in undersaturated water. The dissolution rate of calcite (or aragonite) can be described by:

$$\frac{dCaCO_3}{dt} = -k_{CaCO3} \cdot [CaCO_3] \cdot (1-\Omega)^n \qquad \text{for } \Omega < 1 \qquad \text{Eq. 6.40}$$

The rate *k* and the exponent *n* are only roughly quantified. The distribution of alkalinity and other tracers point to the fact that $CaCO_3$ is also dissolved above the saturation horizon for calcite; this dissolution is possibly associated with bacterial processes. Therefore, an exponential decrease of the $CaCO_3$ flux with an e-folding depth of 3500 m is sometimes used to parameterize $CaCO_3$ dissolution:

$$F_{CaCO_3}(z) = F_{CaCO_3}(z_0) \cdot \exp((z - z_0)/3500\ \text{m}) \qquad \text{Eq. 6.41}$$

This yields also the re-mineralization rate for a given export production.

An important relation to understand, qualitatively, the effect of different processes − such as the formation and re-mineralization of organic matter and $CaCO_3$ − on the distribution of carbonate ions, sediment formation and atmospheric CO_2 is given by the following approximation from the carbonate chemistry:

$Alk \approx [HCO_3^-]+2[CO_3^{2-}]+..$

$DIC=[CO_2]+ [HCO_3^-]+[CO_3^{2-}] \approx [HCO_3^-]+[CO_3^{2-}]$

and hence:

$[CO_3^{2-}] \approx Alk\text{-}DIC$ Eq. 6.42

This simple qualitative equation is a powerful instrument for assessing the effects of changes in different processes. Next, we address the distribution of carbonate ions in the ocean.

Effect of the remineralisation of organic matter and dissolution of $CaCO_3$ on CO_3^{2-}: The remineralization of 1 mol-C of organic matter increases DIC by 1 mol, but lowers Alk due to the formation of nitrate by $r_{N:C}$=16/117=0.14 mol. Thus, the difference Alk-DIC decreases by 1.14 mol. In turn, the concentration of carbonate ions decreases according to the approximate equation above.

The dissolution of 1 mol $CaCO_3$ increases DIC by 1 mol and Alk by 2 mol and Alk-DIC is increased by about 1 mol. CO_3^{2-} . Thus, CO_3^{2-} increases when $CaCO_3$ dissolves

The concentration of carbonate ions is correlated with the concentration of nutrients. It is the highest at the surface and strongly declines in the thermocline because re-mineralization of organic matter lowers CO_3^{2-}. The re-mineralization rate of organic matter in the thermocline is about five times the rate of $CaCO_3$ re-mineralization and thus, the lowering influence of organic matter re-mineralization dominates on CO_3^{2-}. In the deep ocean, the ratio of the re-mineralization rates becomes about 1, and accordingly, CO_3^{2-} varies little. In this case, the effects of re-mineralization of organic matter and $CaCO_3$ compensate each other.

Due to the dominant influence of remineralization of organic matter on the CO_3^{2-} concentration, the saturation horizon for calcite (and aragonite) is high in the nutrient-rich Pacific and Indian Ocean and relatively low in the nutrient-poor Atlantic (Figure 6.21).

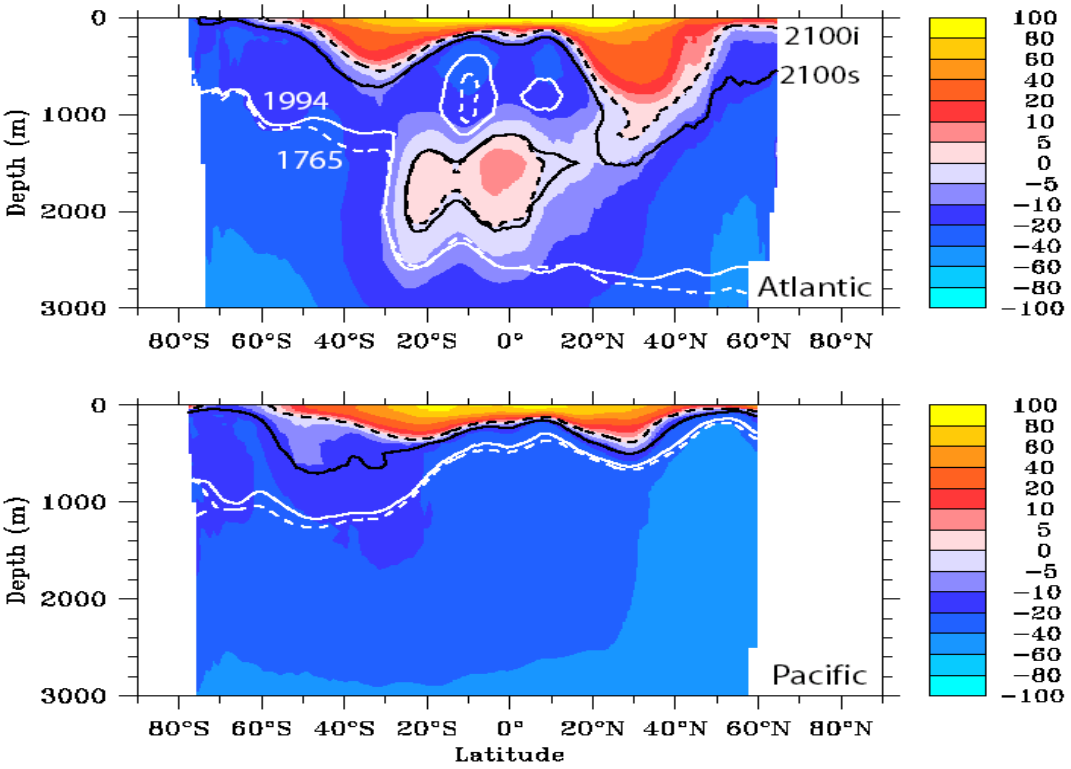

Figure 6.22: Carbonate ion concentration in the Atlantic and Pacific. Due to the invasion of anthropogenic CO_2, the depth of the saturation horizon with respect to aragonite has slightly increased between preindustrial (dashed white) and today (solid white). Until the end of this century, a dramatic increase is expected (black lines) unless fossil emissions are strongly reduced (Orr et al., Nature, 2005).

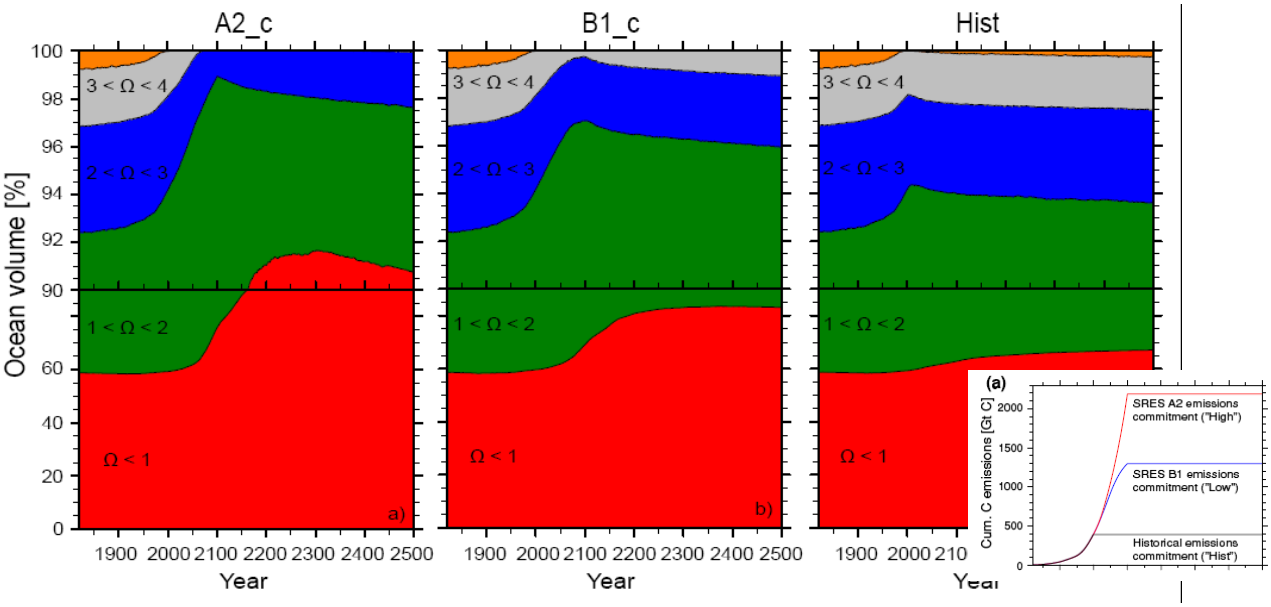

Figure 6.23: Simulated global annual mean changes in the entire ocean volume of supersaturated (Ω>1) and undersaturated (Ω<1) waters with respect to aragonite. The inset shows the evolution of cumulative carbon emissions for the three scenarios (after Frölicher and Joos, CD, 2010)

Effect of fossil CO_2 on CO_3^{2-}: The invasion of fossil CO_2 into the ocean increases DIC, but leaves Alk unaffected. Thus, uptake of fossil (or terrestrial) CO_2 causes a reduction in CO_3^{2-}. In turn, the invasion of the fossil CO_2 perturbation leads to a (transient) shift of the saturation horizon.

Models and data indicate that undersaturation with respect to Aragonite is imminent in the Arctic Ocean. The Southern Ocean will become, on average, undersaturated with respect to aragonite for a doubling of the atmospheric CO_2 concentration and undersaturated with respect to calcite for a quadrupling of the preindustrial CO_2 concentration.

Studies show that aragonite shells of pteropodes start to dissolve when water becomes under-saturated with respect to aragonite. This 'ocean acidification', in which the pH shifts to less alkaline values, poses a risks for calcifying organisms and therefore for the entire marine food web. Ocean acidification can also affect non calcifying organisms, e.g. through changes in acid-base physiology.

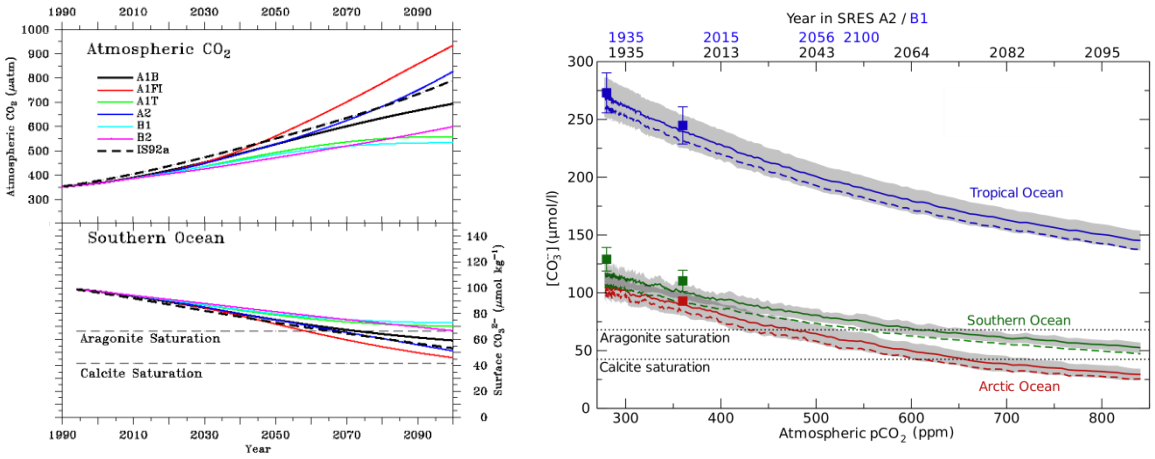

Figure 6.24: (left) Evolution of the CO_2 concentration in the atmosphere and the carbonate ion concentration in the Southern Ocean as computed with the Bern2.5D model (Orr et al., Nature, 2005). Additionally, saturation concentrations with respect to aragonite and calcite are given. (right) CO_3^{2-} as a function of atmospheric CO_2 and for three regions as computed with the NCAR carbon cycle-climate model (solid lines). Grey bands indicate spatial and temporal variability within a region and symbols denote data-based estimates (after Steinacher et al., Biogeosciences, 2009).

$CaCO_3$ sediments: $CaCO_3$ shells that are not dissolved enter the sediments together with other materials (silica, mineral particles, organic matter). The upper few cm of the sediment layer are porous and are in diffusive contact with the water above. Consequently, in the deep, under-saturated ocean, all of the $CaCO_3$ is dissolved, while in the sufficiently oversaturated water, $CaCO_3$ is conserved. In between, there is a transition zone in which the $CaCO_3$ content in the sediment decreases. The following discussion is related to calcite, which makes up about 90 % of the total $CaCO_3$ export.

The upper bound of the transition zone, where only very little $CaCO_3$ is dissolved, is referred to as the **lysocline**. The depth, at which practically all $CaCO_3$ is lost, is referred to as the **calcite compensation depth (CCD)**. At the CCD, the dissolution of $CaCO_3$ equals the deposition of $CaCO_3$. The zone between the lysocline and CCD is called the **transition zone**. The lysocline is located at about 4000 m depth in the Pacific and at 5500m in the Northern

Atlantic. The depth of the lysocline is roughly consistent with the depth of the saturation horizon and it appears that the chemical balance largely dominates the sedimentation of calcite.

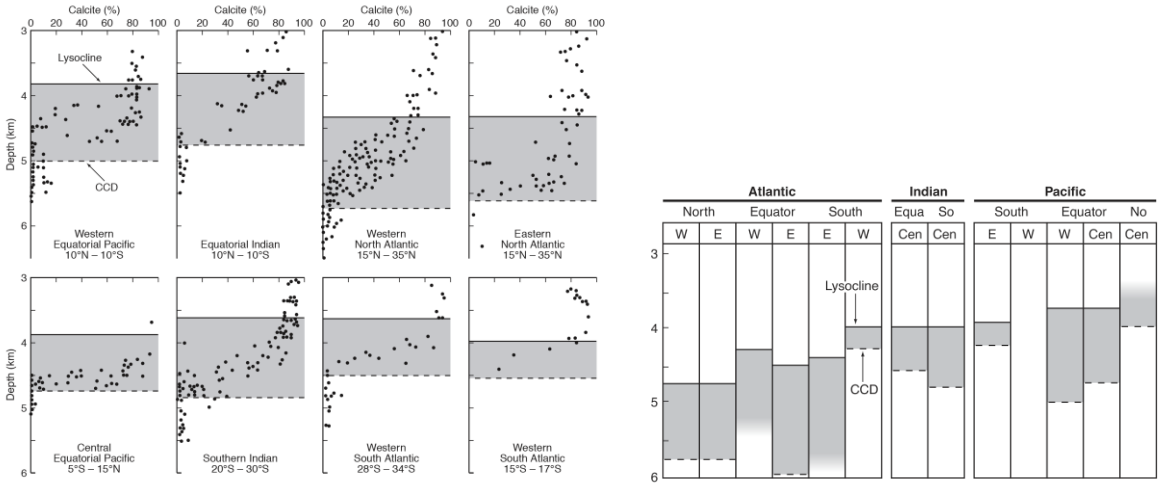

Figure 6.25: The relative fraction of $CaCO_3$ in the uppermost sediment layer as a function of the water depth for different ocean regions (after Broecker, 1982. Figure from Sarmiento and Gruber).

Dissolution of organic matter in sediments: The re-mineralization of organic matter is associated with the transfer of alkalinity. As discussed above, the carbonate ion concentration decreases in the order of 1 mol for each mol of organic carbon re-mineralized. Thanks to the re-mineralization of organic matter in the sediment layer, calcite can be dissolved within the sediments even if the ocean water above the sediment is oversaturated. Roughly equal amounts of organic carbon and calcite are deposited in the deep ocean and nearly all organic matter is re-mineralized. The lowering of the saturation state associated with organic matter re-mineralization is sufficient to dissolve large amounts of calcite.

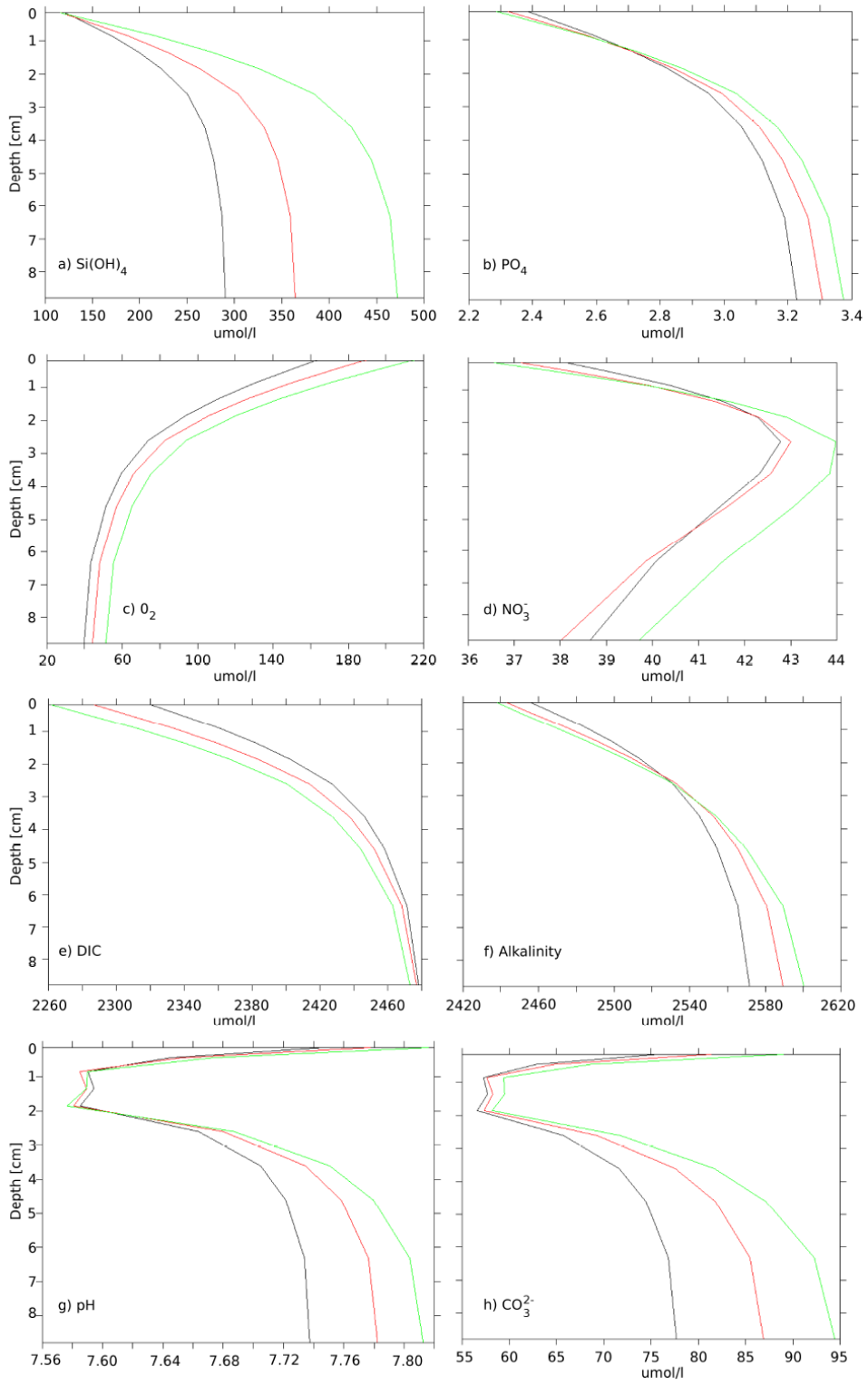

Figure 6.26: Global mean vertical profiles of pore water solutes as simulated with the Bern3D model and for three model setups (Tschumi, 2009)

Compensation of the anthropogenic perturbation by sediment interaction: The invasion of fossil CO_2 leads to a transient upward-shift of the saturation horizon and the lysocline. This causes the long-term balance between inputs from rivers and sedimentation to be disrupted. Less alkalinity is removed by sedimentation than supplied by rivers. The enhanced dissolution of calcite leads to an increase of alkalinity in the ocean until a new balance between input and sedimentation is attained.

An increase in alkalinity is associated with a decrease of the CO_2 partial pressure and thus an additional uptake of fossil CO_2. This sediment interaction causes a reduction of the airborne fraction of anthropogenic CO_2 to about 7% on a typical time scale of some 5000 years. Analogously, the atmospheric disturbance is decreased by the removal of CO_2 from the atmosphere (Figure 6.28). An example is the transition from the last glacial to the current interglacial when the carbon stocks in the terrestrial biosphere where growing.

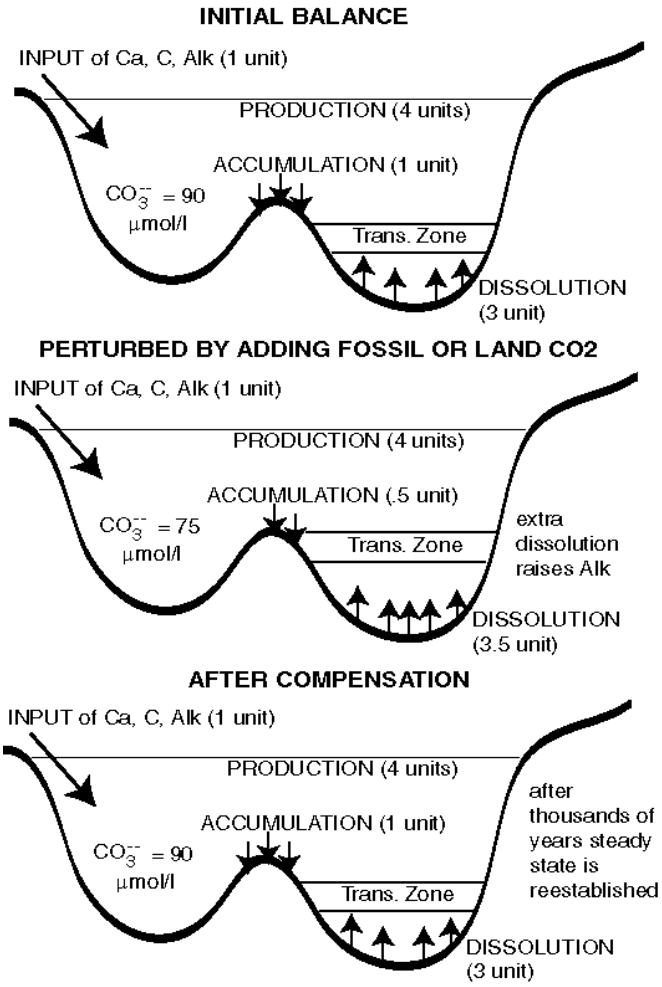

Figure 6.27: Simplified scheme of the compensation of fossil CO_2 by the dissolution of $CaCO_3$ from the sediments. (upper) In steady-state, the same amount of alkalinity enters the ocean from land as is removed by the sedimentation of $CaCO_3$. (middle) The uptake of fossil CO_2 temporarily lowers the CO_3^{--} content and the transition zone is lifted. This causes less alkalinity to be removed from the ocean than is added; and the alkalinity, as well as the CO_3^{-} concentration of the ocean increases until the initial balance between inputs and sedimentation is restored (lower).

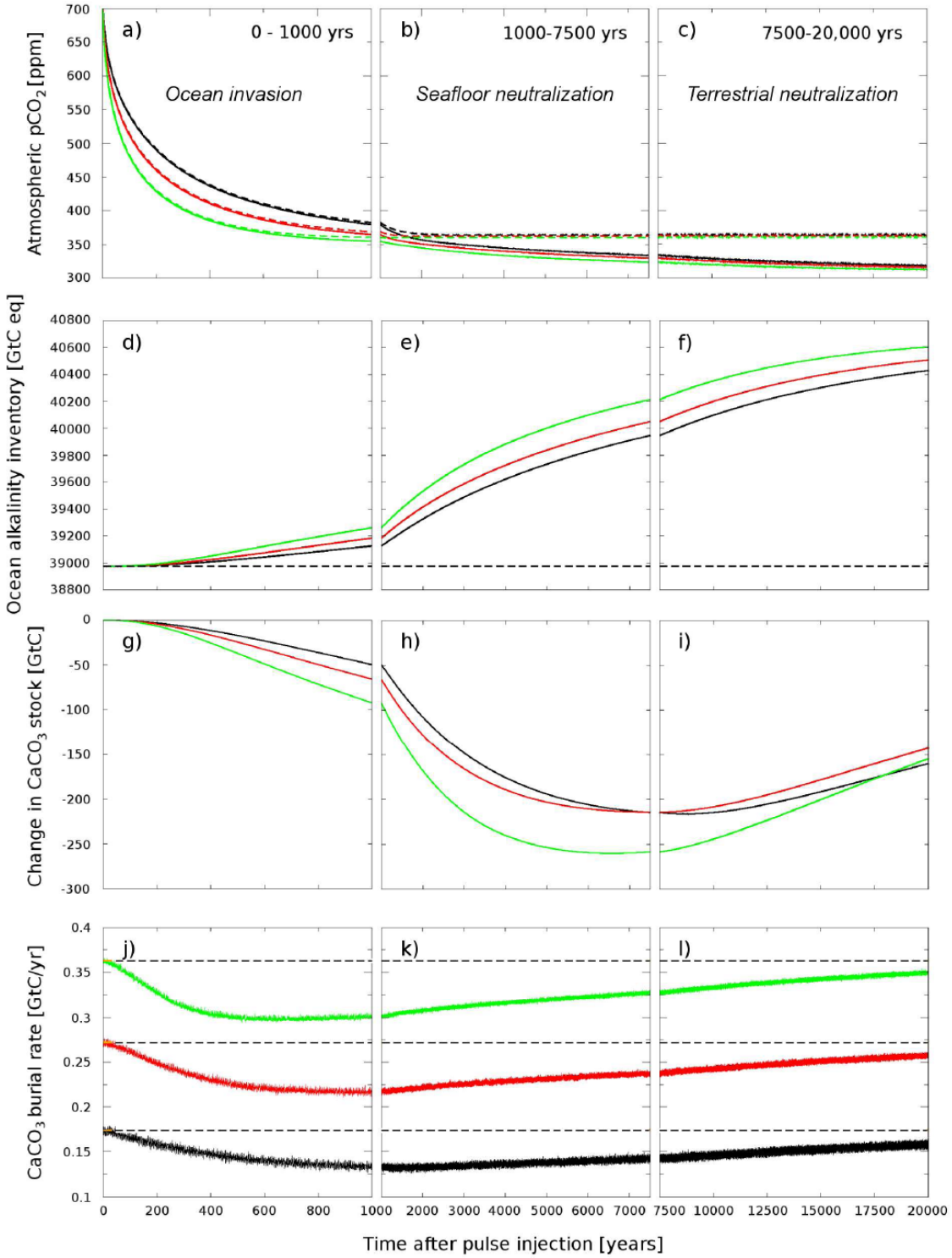

Figure 6.28: Model response to a 1000 GtC pulse injection into the atmosphere as simulated with the 3 setups of the Bern3D model (after Tschumi, 2009): The open system response (with sediment-interaction) is plotted as

solid lines, the closed system response (ocean only) as dashed lines. Black lines correspond to the low ocean diffusivity setup, red lines to medium diffusivity and green lines stand for the high diffusivity model. In panels (j-l) the black dashed lines indicate the rate of weathering input which is held constant during the experiments.

Effect of a perturbation in the export of calcite and organic matter: We are now able to examine the effect of a perturbation in the natural carbon cycle on the atmospheric CO_2 concentration. Figure 6.29 schematically illustrates the evolution of alkalinity, the DIC content, the lysocline depth and the CO_2 concentration in the atmosphere after a perturbation of the export flux of calcite with and without sediment compensation. It is assumed that all other conditions (circulation, temperature, etc…) remain fixed. The decreased export of calcite increases the alkalinity in the surface ocean. As a consequence, the CO_2 partial pressure in the surface ocean and in the atmosphere decreases. The DIC content of the ocean rises because carbon is taken up from the atmosphere. The reduced export of $CaCO_3$ leads to a reduced sedimentation of calcite in the first place. The alkalinity increases until the export of alkalinity by calcite sedimentation and the input from rivers are in balance again; the lysocline moves downwards. The increase in mean alkalinity in the ocean leads to a further rise of alkalinity in the surface ocean and thus to an additional decrease of the CO_2 concentration in the atmosphere. In this case, the sediment compensation enhances the initial perturbation in the CO_2 concentration.

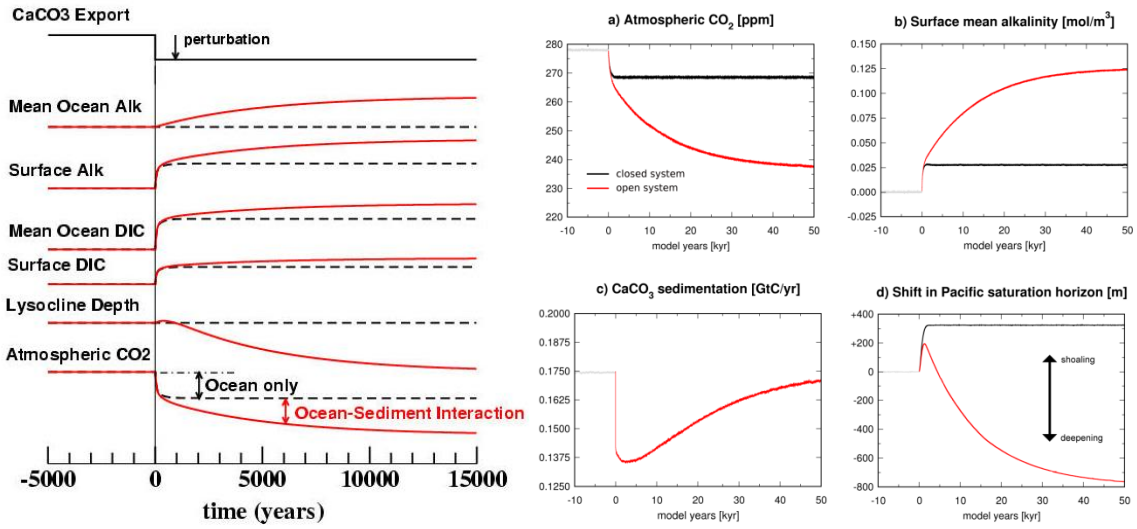

Figure 6.29: Evolution of alkalinity, the DIC content, the lysocline depth and the atmospheric CO_2 concentration after a perturbation in the export production of calcite. left: qualitative response after Sarmiento and Gruber, 2006; right: response as simulated with the Bern3D model for an instantaneous reduction in the $CaCO_3$ export by 20% at time 0.

6.3 Glacial-interglacial CO_2 variations

Atmospheric CO_2 varied between 172 and 300 ppm during the glacial-interglacial cycles for the last 800,000 years (Figure 6.30). We discuss first the general relationship between climate and atmospheric CO_2 during the last million years, before addressing the potential causes of the variations in CO_2. Some of the figures and text has been taken from the paleoclimate chapter of the IPCC Working Group I report, 2007.

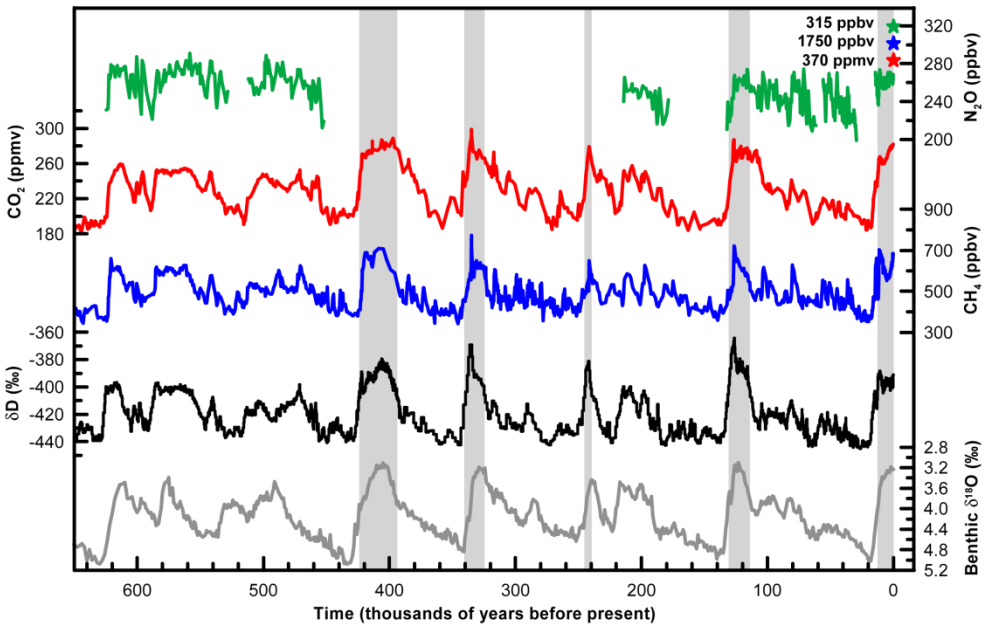

Figure 6.30: Variations of deuterium (δD), a proxy for local temperature, and the atmospheric concentrations of the greenhouse gases carbon dioxide, methane, and nitrous oxide derived from air trapped within ice cores from Antarctica and from recent atmospheric measurements. The shading indicates the last interglacial warm periods. Interglacial periods also existed prior to 450,000 years, but these were apparently colder than the typical interglacials of the latest Quaternary. The length of the current interglacial is, in the context of the last 650,000 years, not unusual. The stack of 57 globally distributed benthic $\delta^{18}O$ marine records, a proxy for global ice volume fluctuations, is displayed in the bottom part of the figure for comparison with the ice core data. Larger ice volume is expressed downwards. Note that the shaded vertical bars are based on the ice core age model (EPICA community members, 2004), and that the marine record is plotted on its original time scale based on tuning to the orbital parameters. The stars and labels indicate concentrations at year 2000.

Paleoclimatic records document a sequence of glacial-interglacial cycles over the past million years. The typical periodicity of large glacial-interglacial climate swings is around 100 kyr for the period of the past 430 ka, but there is also substantial climate variability on other orbital time scales, in particular the 41,000 kyr period of the variation in the tilt of the axis of the earth. A minor portion (20% on average) of each glacial-interglacial cycle was spent in the warm interglacial mode, which normally lasted about 10 to 30 kyr. There is evidence for longer interglacial periods between 430 and 740 ka, but these were apparently colder than the typical interglacials of the latest Quaternary. The Holocene, the latest of these interglacial periods, extends to the present.

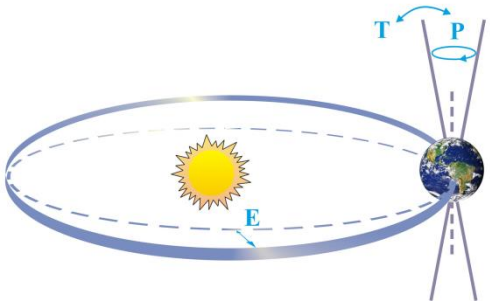

Figure 6.31: Schematic view of the Earth's orbital changes (Milankovic cycles) that drive the ice age cycles. "T" denotes changes in the tilt (or obliquity) of the Earth axis, "E" denotes changes in the eccentricity of the orbit (due to variations in the minor axis of the ellipse), and "P" denotes precession, i.e., changes in the direction of the axis tilt at a given point of the orbit.

Available evidence supports the view that glacial-interglacial cycles are driven by changes in the Earth's orbit around the sun, the so-called Milankovic cycles. These cycles change the amount of solar energy received at each latitude and in each season, but hardly affect the global annual mean. Many studies suggest that the amount of summer sunshine on northern continents is crucial. A low solar energy flux during northern hemisphere summers results in permanent snow cover and eventually the build-up of glaciers. Growing glacial surface area results in an increase in the reflection of solar radiation back to space and enforce the cooling.

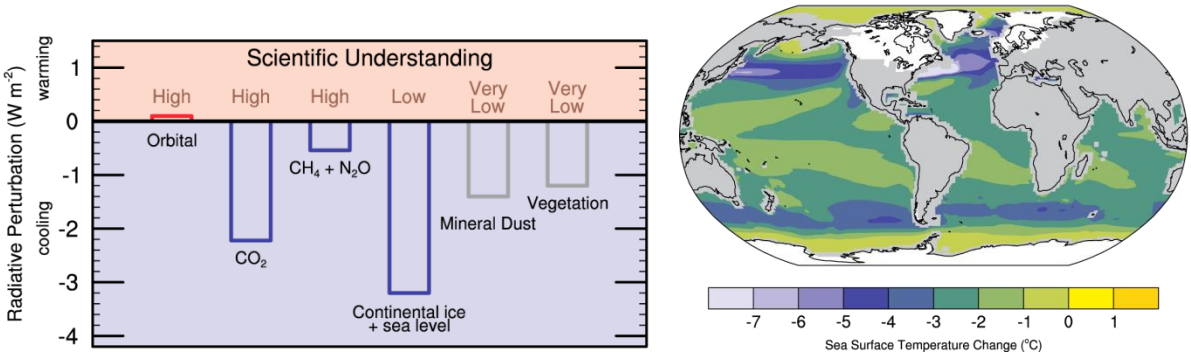

Figure 6.32: The Last Glacial Maximum climate (approximately 21kyrs ago) relative to pre-industrial (1750). left: Global annual mean radiative influences (W m^{-2}) of LGM climate change agents, generally feedbacks on glacial-interglacial cycles, but also specified in most AOGCM simulations for LGM. right: Multi-model average SST change for LGM PMIP-2 simulations by five AOGCMs (CCSM, FGOALS, HadCM, IPSL, and MIROC). Ice extent over continents is shown in white.

The ice core record indicates that greenhouse gases co-varied with Antarctic temperature over glacial-interglacial cycles, suggesting a close link between natural atmospheric greenhouse gas variations and temperature. Variations in CO2 over the last 420 kyr broadly followed Antarctic temperature, typically by several centuries to a millennium. During the last de-glaciation, and likely also the three previous ones, the onset of warming at both high southern and northern latitudes preceded by several thousand years the first signals of significant sea level increase resulting from the melting of the northern ice sheets linked with the rapid warming at high northern latitudes. The global mean sea level rose by around 120 to 140 m during the last transition and was primarily caused by the melting of northern hemisphere ice-

sheets that covered large parts of North America and Scandinavia during the last glacial maximum.

Although CO2 was likely not the primary cause for glacial-interglacial variations, it contributed significantly to the variations in the radiative balance of the surface-lower atmosphere system. The link between Antarctic temperature and CO_2 did not change on the glacial-interglacial time scale during the past 800 ka. This indicates a rather stable coupling between climate and the carbon cycle.

What Caused the Low Atmospheric CO_2 Concentrations During Glacial Times?
Ice core records show that atmospheric CO_2 varied in the range of 180 to 300 ppm over the glacial-interglacial cycles of the last 650,000 years (Petit et al., 1999; Siegenthaler et al., 2005a). The quantitative and mechanistic explanation of these CO_2 variations remains one of the big unsolved questions in climate research. Processes in the atmosphere, ocean, marine sediments, on land, and the dynamics of sea ice and ice sheets must be considered. A number of hypotheses for the low glacial CO_2 concentrations have emerged over the past 20 years, and a rich body of literature is available (Webb et al., 1997; Broecker and Henderson, 1998; Archer et al., 2000; Sigman and Boyle, 2000; Kohfeld et al., 2005). Many processes have been identified that could potentially regulate atmospheric CO_2 on glacial-interglacial time scales. However, existing proxy data to test these hypotheses are relatively scarce, uncertain, and their interpretation is partly conflicting.

Most explanations propose changes in oceanic processes as the cause for low glacial CO_2. The ocean is by far the largest of the relatively fast (<1000 yr) exchanging carbon reservoirs, and terrestrial changes cannot explain the low glacial values because terrestrial storage was also low at the Last Glacial Maximum. On glacial-interglacial time scales, atmospheric CO_2 is mainly governed by the interplay between ocean circulation, marine biological activity, ocean-sediment interactions, seawater carbonate chemistry, and air-sea exchange. Upon dissolution in seawater, CO_2 maintains an acid/base equilibrium with bicarbonate and carbonate ions that depends on the acid-titrating capacity of seawater, i.e., alkalinity. Atmospheric CO_2 would be higher if the ocean lacked biological activity. CO_2 is more soluble in colder than in warmer waters; therefore changes in surface and deep ocean temperature have the potential to alter atmospheric CO_2. Most hypotheses focus on the Southern Ocean, where a large volume-fraction of the cold deep-water masses of the world ocean are currently formed, and large amounts of biological nutrients (phosphate and nitrate) up-welled to the surface remain unused. A strong argument for the importance of Southern Hemisphere processes is the co-evolution of Antarctic temperature and atmospheric CO_2.

One family of hypotheses of low glacial CO_2 values invokes an increase or redistribution in the ocean alkalinity as a primary cause. Potential mechanisms are (i) the increase of $CaCO_3$ weathering on land, (ii) a decrease of coral reef growth in the shallow ocean, or (iii) a change in the export ratio of $CaCO_3$ and organic material to the deep ocean. These mechanisms require large changes in the deposition pattern of $CaCO_3$ to explain the full amplitude of the glacial-interglacial CO_2 difference through a mechanism called carbonate compensation (Archer et al., 2000). The available sediment data do not support a dominant role for carbonate compensation in explaining low glacial CO_2 levels. Furthermore, carbonate compensation may only explain slow CO_2 variation, as its time scale is multi-millennial.

Another family of hypotheses invokes changes in the sinking of marine plankton. Possible mechanisms include (iv) fertilization of phytoplankton growth in the Southern Ocean by increased deposition of iron-containing dust from the atmosphere after being carried by winds from colder, drier continental areas, and a subsequent redistribution of limiting nutrients, (v) an increase in the whole ocean nutrient content, e.g., through input of material exposed on shelves or nitrogen fixation, and (vi) an increase in the ratio between carbon and other nutrients assimilated in organic material, resulting in a higher carbon export per unit of limiting nutrient exported. As with the first family of hypotheses, this family of mechanisms also suffers from the inability to account for the full amplitude of the reconstructed CO_2 variations when constrained by the available information. For example, periods of enhanced biological production and increased dustiness (iron supply) are coincident with changes of 20 to 50 ppm. Consistently, model simulations suggest a limited role for iron in regulating past atmospheric CO_2 concentration (Bopp et al., 2002).

Physical processes are also likely to have contributed to the observed CO_2 variations. Possible mechanisms include (vii) changes in ocean temperature (and salinity), (viii) suppression of air-sea gas exchange by sea ice, and (ix) increased stratification in the Southern Ocean. The combined changes in temperature and salinity increased the solubility of CO_2, causing a depletion in atmospheric CO_2 of perhaps 30 ppm. Simulations with general circulation ocean models do not fully support the gas exchange-sea ice hypothesis. One explanation (ix) conceived in the 1980s invokes more stratification, less upwelling of carbon and nutrient-rich waters to the surface of the Southern Ocean, and increased carbon storage at depth during glacial times. The stratification may have caused a depletion of nutrients and carbon at the surface, but proxy evidence for surface nutrient utilization is controversial. Qualitatively, the slow ventilation is consistent with very saline and very cold deep waters reconstructed for the last glacial maximum (Adkins et al., 2002), as well as low glacial stable carbon isotope ratios (^{13}C /^{12}C) in the deep South Atlantic.

In conclusion, the explanation of glacial-interglacial CO_2 variations remains a difficult attribution problem. It appears to be likely that a range of mechanisms have acted in concert (e.g., Köhler et al., 2005). The future challenge is not only to explain the amplitude of glacial-interglacial CO_2 variations, but the complex temporal evolution of atmospheric CO_2 and climate consistently.